Universidade de Aveiro Departamento de Engenharia Mecânica
2006

Ricardo José Alves de Sousa

Desenvolvimento de um Elemento Sólido-Casca não Linear para Aplicação em Simulações de Conformação Plástica de Chapas Anisotrópicas

Development of a General Purpose Nonlinear Solid-Shell Element and its Application to Anisotropic Sheet Forming Simulation

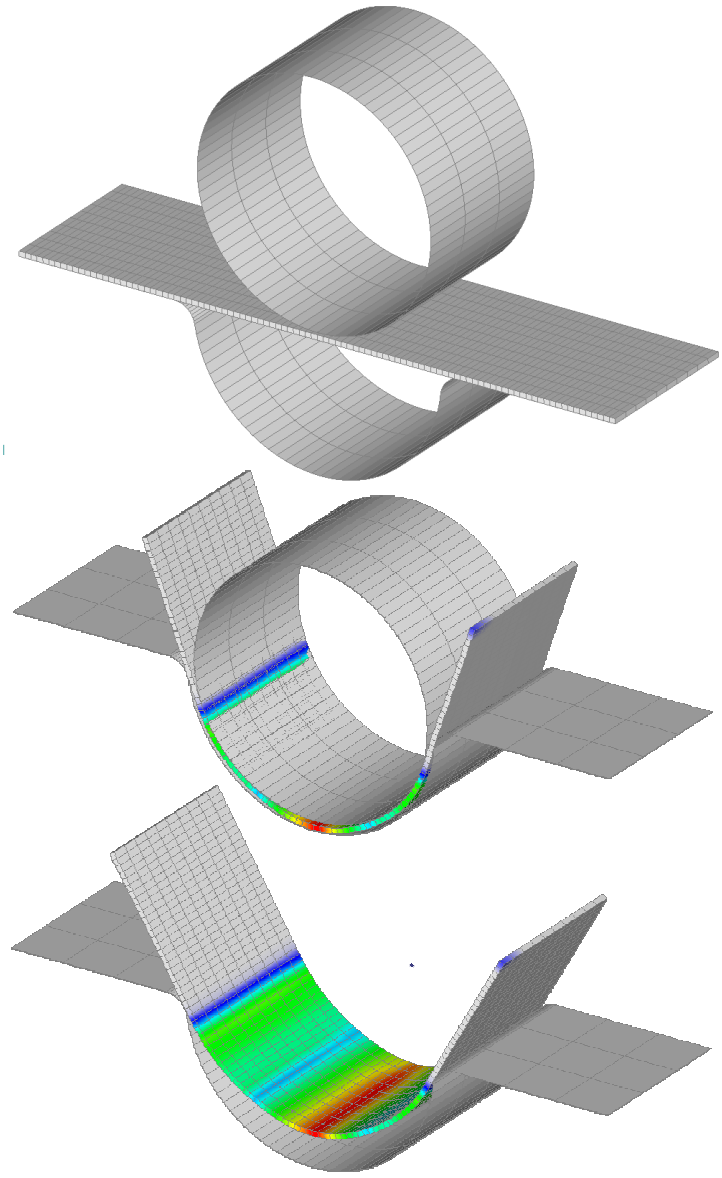

Universidade de Aveiro Departamento de Engenharia Mecânica
2006

Ricardo José Alves de Sousa

Desenvolvimento de um Elemento Sólido-Casca não Linear para Aplicação em Simulações de Conformação Plástica de Chapas Anisotrópicas

Development of a General Purpose Nonlinear Solid-Shell Element and its Application to Anisotropic Sheet Forming Simulation

Dissertação apresentada à Universidade de Aveiro para cumprimento dos requisitos necessários à obtenção do grau de Doutor em Engenharia Mecânica, realizada sob a orientação científica do Dr. Jeong-Whan Yoon, Cientista do Alcoa Technical Center, EUA / Professor Associado Convidado do Departamento de Engenharia Mecânica da Universidade de Aveiro e Professor José Joaquim de Almeida Grácio, Professor Catedrático do Departamento de Engenharia Mecânica da Universidade de Aveiro.

Dissertation presented to the University of Aveiro as a requirement to obtain the PhD Degree in Mechanical Engineering, and carried out under the scientific supervision of Dr. Jeong-Whan Yoon, Staff Cientist, Alcoa Technical Center, USA / Associate Professor, Department of Mechanical Engineering, University of Aveiro and Professor José Joaquim de Almeida Grácio, Full Professor, Department of Mechanical Engineering, University of Aveiro.

Bolsa de Doutoramento concedida pela Fundação para a Ciência e Tecnologia (FCT) referência POSI BD/12864/2003

PhD Scholarship granted by Fundação para a Ciência e Tecnologia (FCT) under POSI BD/12864/2003

Este trabalho é inteiramente dedicado à Susana, por todo o apoio e paciência.

"Experience is a hard teacher because she gives the test first, the lesson afterwards."
(Vernon Sanders Law)

"There are two things to aim at in life; first to get what you want, and after that to enjoy it. Only the wisest of mankind has achieved the second."
(Logan Pearsall Smith)

"An expert is a person who has made all the mistakes that can be made in a very narrow field."
(Niels Bohr)

O Júri

Presidente

EX.MO REITOR DA UNIVERSIDADE DE AVEIRO

DOUTOR DONG-YOL YANG
Full Professor, Korea Advanced Institute of Science and Technology (KAIST).

DOUTOR PAULO ANTÓNIO FIRME MARTINS
Professor Catedrático do Instituto Superior Técnico da Universidade Técnica de Lisboa.

DOUTOR JOSÉ JOAQUIM DE ALMEIDA GRÁCIO
Professor Catedrático da Universidade de Aveiro.

DOUTOR JOSÉ MANUEL DE ALMEIDA CÉSAR DE SÁ
Professor Associado da Faculdade de Engenharia da Universidade do Porto.

DOUTOR JEONG-WHAN YOON
Staff Cientist, Alcoa Technical Center (USA); Professor Associado Convidado da Universidade de Aveiro.

DOUTOR RUI PEDRO RAMOS CARDOSO
Professor Auxiliar da Universidade de Aveiro.

agradecimentos

O processo de investigação e desenvolvimento científico subjacente ao desenvolvimento de uma tese de Doutoramento é algo que requer, para o seu sucesso, o envolvimento e cooperação de um grupo de pessoas, que colaboram não apenas na vertente científica como também na pessoal.

Cumpre-me agradecer em primeira instância aos meus dois orientadores: To Dr. Jeong-Whan Yoon, thank you for introducing me in top class scientific research; thank you for being my advisor but at the same time a good friend; thank you for your patience, for dozens of phone calls and emails, sometimes to answer just a basic question.
Ao Professor José Grácio, agradeço a oportunidade que me deu de realizar este doutoramento; agradeço o modo caloroso como me recebeu no Departamento de Engenharia Mecânica da Universidade de Aveiro, contribuindo para a minha imediata integração; pelo dinamismo e motivação inigualáveis, sempre importantes nos momentos mais difíceis.

Ao colega e amigo Rui Cardoso, os mais sinceros agradecimentos. Sem a sua cooperação esta tese não existiria. Obrigado por me esclarecer todas as dúvidas, em qualquer hora ou lugar. Obrigado por me disponibilizar um código de elementos finitos verdadeiramente excepcional do qual pude tirar grande proveito, poupando horas, dias, meses de trabalho. Em suma, um verdadeiro Cérebro!

Ao colega e amigo Robertt Valente, obrigado por todo o apoio, científico e pessoal, pelos momentos de boa disposição, pelas conversas regadas a chá e café, pelo exemplo de calma e correcção. Ao meu colega de gabinete Fábio Simões, cuja amizade remonta aos tempos já longínquos da Universidade, obrigado pelo ambiente de trabalho diário fantástico, sem esquecer a imprescindível máquina de café e as boleias matutinas de Vespa.

Ao Professor Natal Jorge, da Universidade do Porto, os meus sinceros agradecimentos. Por toda a boa disposição, pela sua inesgotável fonte de ideias e por me ter iniciado na vida científica, muito obrigado!

To Dr. Fréderic Barlat and to Professor Wiktor Gambin, thank you for the few, but quite productive scientific discussions.

A todos os docentes, bolseiros e funcionários do Departamento de Engenharia Mecânica da Universidade de Aveiro, que todos os dias me proporcionam um ambiente de trabalho excepcional, deixo os meus sinceros agradecimentos.

Aos meus pais, que incondicionalmente me apoiaram, apoiam e apoiarão, sempre acreditando no meu potencial, do qual eu próprio às vezes duvido. Às minhas princesas, Susana e Íris, que constituem os pilares da minha vida, agradeço a alegria e motivação que me dão todos os dias.

palavras-chave

anisotropia, elementos finitos, aluminio, policristal, retenção, sólido-casca

resumo

A utilização dos métodos computacionais na Engenharia Mecânica tem assumido cada vez mais relevância, contribuindo para uma melhor compreensão dos processos de conformação plástica em chapa, especialmente aqueles que lidam com materiais anisotrópicos, como é o caso das ligas de alumínio. Dentre estes, o método dos elementos finitos (FEM) tem progredido substancialmente nas últimas duas décadas, em parte devido ao rápido desenvolvimento da arquitectura dos computadores. Para a correcta modelação dos processos de conformação plástica em chap: o desenvolvimento de um elemento finito preciso e eficiente, vocacionado para a modelação de estruturas com parede fina, como é o caso das chapas de metal; o estudo e implementação de modelos constitutivos, considerando a anisotropia material a três dimensões.

Assim, é proposto um novo elemento finito sólido-casca, suportando um número arbitrário de pontos de integração numérica ao longo da sua espessura. Devido à sua topologia sólida com oito nós físicos, esta formulação avalia naturalmente variações de espessura, contacto simultâneo em duas faces e modelos constitutivos tridimensionais, aspectos cruciais neste tipo de aplicações.

Do lado constitutivo, a caracterização de materiais anisotrópicos pode ser conseguida através de funções de cedência não quadráticas ou através de modelos policristalinos. A descrição matemática da anisotropia plástica é conveniente e computacionalmente eficiente devido ao facto de utilizar parâmetros mecânicos macroscópicos como dados de entrada. Por outro lado, a descrição policristalina é baseada em aspectos físicos micro-estruturais da deformação plástica, sendo a textura cristalográfica o principal dado de entrada para estes modelos. Assim, a rotação de cada um dos grãos é acompanhada individualmente e a anisotropia material é consequentemente evolucional. No entanto, quando comparado com os modelos fenomenológicos, os modelos policristalinos são computacionalmente intensivos e não passíveis de serem usados à escala industrial, em particular na análise de conformação em chapa. Neste trabalho, as duas alternativas são analisadas, mas devido ao seu carácter inovador, ênfase será dada a um modelo multi-escala optimizado, que utiliza o conceito da interacção dos sistemas de deslizamento ao nível do grão e uma transição micro-macro baseada na hipótese de que todos os grãos sofrem o mesmo nível de deformação macroscópico.

No final, os dois tópicos referidos (elemento finito e lei constitutiva) são consolidados num código de elementos finitos, sendo então validados e comparados com resultados experimentais ou numéricos, previamente publicados por outros autores.

keywords anisotropy, finite elements, aluminum, forming, spring-back, locking, solid-shell

abstract

The use of computational methods in Mechanical Engineering has gained more relevance, contributing to a better understanding of sheet metal forming processes, especially when dealing with anisotropic materials, such as aluminum alloys. Among them, the finite element method (FEM) has made significant progress during the last two decades, partly because of the rapid progress of computational environment. For a proper modeling of anisotropic forming processes, it is necessary to use accurate and efficient finite elements. The class of solid-shell finite elements has been appearing in the last years as an excellent alternative to shell elements to model thin-walled structures, presenting at the same time a number of advantages, namely the use of full constitutive laws and automatic consideration of double-sided contact. At the same time, it is important to utilize constitutive laws that describe the material anisotropy properly.

In this work, the main focus is given to the formulation of a new one point quadrature solid-shell finite element. As a distinctive feature, the formulation accounts for an arbitrary number of integration points through its thickness direction. Once it contains eight physical nodes, naturally evaluates thickness strain, double sided contact and full three-dimensional constitutive models, which are crucial aspects in this type of applications. Additionally, simulation of spring-back phenomena of a metal sheet can be made resorting only to a single layer of solid-shell finite elements containing several integration points through the thickness direction. On the constitutive side, anisotropic material modelling can be described utilizing non-quadratic mathematical yield functions or polycrystal models. Phenomenological description of plastic anisotropy is convenient and time-efficient since it is based on macroscopic mechanical properties of the material as input. On the other side, polycrystal description is based on the physical microstructural aspects of plastic deformation, being the crystallographic texture the main input to these models. However, compared to phenomenological approaches, despite having a more sounding theoretical basis, polycrystal models are computationally time-intensive and difficult to employ for large-scale industrial applications, particularly sheet forming analysis and design. Therefore, it is required to select an appropriate approach based on the problem characteristics. In this work, well-chosen anisotropic yield functions are reviewed. Additionally, the description of a time efficent grain-level single crystal model is carried out.

In the numerical tests, finite element development and constitutive modelling topics are consolidated in an in-house FEM code, being validated and compared with experiments or numerical results previously reported in the literature.

Table of Contents

List of Figures

List of Tables

Nomenclature

List of indices

${}^{n+1}_{n}\square$	Variable value between states (n) and (n+1)
${}^{n+1}\square$	Variable evaluated at state (n+1)
${}^{stb}\square$	Hourglass (stabilization) counterpart of a variable
$\square^{h}$	Finite element approximation of an entity
$\square^{(s)}$	Variable value at a given slip system (s)
$\square^{e}$	Stands for elastic
$\square^{p}$	Stands for plastic
$\square^{g}$	Variable value at a given grain (g)
$\square^{\text{int}}$	Stands for internal
$\square^{\text{ext}}$	Stands for external
$\square^{u+\alpha}$	Displacement and enhanced based variable (condensed)
$\square_{i}$	Variable evaluated at iteration (i)
$\square_{u}$	Displacement-based variable
$\square_{\alpha}$	Enhanced-based variable
$\square_{e}$	Variable in a finite element domain
$\square_{nlg}$	Geometrically nonlinear variable
$\square_{lg}$	Geometrically linear variable
$\square_{0}$	Stands for initial value or evaluated at the point ($\xi = \eta = \zeta = 0$)
$\square_{sym}$	Symmetric part of a tensor

$\square_{asy}$	Anti-symmetric part of a tensor
$\square_t$	Evaluated at the top surface of the solid-shell element
$\square_b$	Evaluated at the bottom surface of the solid-shell element
$\dot{\square}$	Time derivative (rate) of a variable
$\widehat{\square}$	Variable evaluated at the local corotational coordinate system
$\widetilde{\square}$	Enhanced assumed strain variable
$\breve{\square}$	Constrained variable
$\square^{\mathrm{T}}$	Transpose of a matrix

List of Symbols (Scalars and tensors)

$\boldsymbol{\alpha}$	Internal variables field of the EAS method
a	Phenomenological parameter used in yield functions
A, B, C	Voce-law parameters
$\mathbf{b}$	Body forces
$\mathbf{b}^*$	Left Cauchy-Green strain tensor
$\mathbf{b}^{(s)}$	Slip plane direction
$\mathbf{B}$	Strain-displacement matrix
$\mathbf{C}^*$	Right Cauchy-Green strain tensor
$\mathbf{C}_4$	Fourth order elastic constitutive tensor
$\mathbf{C}^e$	Second order elastic constitutive tensor
$C_i, \mathbf{C}', \mathbf{C}''$	Anisotropy coefficients
$\mathbf{D}$	Rate of deformation tensor
$\mathbf{d}$	Vector of displacement degrees of freedom
$\mathfrak{D}$	Directional derivative operator
δ_{ij}	Kronecker's Delta $\begin{cases} i = j \rightarrow \delta_{ij} = 1 \\ i \neq j \rightarrow \delta_{ij} = 0 \end{cases}$

δ	Infinitesimal operator for iterative variations
Δ	Finite operator for incremental variations
$\mathbf{e}_i$	Global Cartesian coordinate system
$\mathbf{E}$	Green-Lagrange strain tensor
$\mathbf{e}$	Almansi-Euler strain tensor
$\boldsymbol{\varepsilon}$	Generic strain tensor
$\overline{\varepsilon}^p$	Equivalent plastic strain
E	Young modulus
$\mathbf{F}$	Deformation gradient
$\mathbf{f}$	Force vector
ϕ, φ	Yield function
Φ	Plastic potential
$\mathbf{g}_a$	Covariant basis vector
$\mathbf{g}^a$	Contravariant basis vector
g	Hardening parameter
γ	Shear strain
Γ_σ, Γ_u	Control areas
H_{ab}	Hardening modulus
h	Hardening parameter
$\mathbf{I}_2$	Second order identity tensor
I	Incompressible deformations subspace
$\mathbf{J}$	Jacobian matrix
$\mathbf{K}^{uu}$	Displacement-based stiffness matrix
$\mathbf{K}^{u\alpha}, \mathbf{K}^{\alpha u}$	Coupled EAS-displacement-based stiffness matrices
$\mathbf{K}^{\alpha\alpha}$	EAS-based stiffness matrix
K, n'	Power-law hardening parameters
κ	Reference shear strain; Self-to-latent hardening ratio

$\mathbf{L}$	Velocity gradient
λ	Consistence parameter; plastic multiplier
m	Single grain Taylor factor
$\overline{m}$	Polycrystal Taylor factor
$\mathbf{m}$	Strain-rate (flux) vector
N_i	Linear shape functions
$\mathbf{N}$	Matrix containing the linear shape functions
$\mathbf{n}$	Normal vector
n^e_{nodes}	Number of nodes of a finite element
n_{grains}	Number of grains of a polycrystal
ν	Poisson ratio
$\mathbf{P}$	First Piola-Kirchhoff stress tensor
$\mathbf{P}_3$	Grains orientations matrix based on Roe's Euler angles
$\mathbf{p}$	Hydrostatic pressure
Π	Potential energy
$\mathbf{Q}$	Coupling matrix involving pressure and displacement fields
$\mathbf{r}^i$	Local orthonormal frame
$\mathbf{R}$	Rotation tensor
ρ	Density; Hardening function
$\mathbf{S}$	Second Piola-Kirchhoff stress tensor
$\mathbf{S}_3$	Stress tenor in 3×3 array form
$\mathbf{s}$	Deviatoric stress
$\boldsymbol{\sigma}$	Cauchy stress tensor
$\boldsymbol{\sigma}^{\mathrm{TR}}$	Trial elastic stress
$\overset{\mathrm{J}}{\boldsymbol{\sigma}}$	Jaumann objective stress rate of the Cauchy stress tensor
$\overset{\mathrm{G}}{\boldsymbol{\sigma}}$	Green-Naghdi-McInnis objective stress rate of the Cauchy stress

$\overline{\sigma}$	Effective stress
σ_Y	Yield stress
$\vartheta^{(k)}$	Bishop and Hill vertex number (k)
t	Time (instant)
$\mathbf{t}$	Traction forces
$\mathbf{T}$	Stress vector
${}^{l}_{c}\mathbf{T}$	Second order local/convective transformation tensor
$\boldsymbol{\tau}$	Kirchhoff stress tensor
$\tau^{(s)}$	Resolved shear stress of a slip system (s)
$\tau_c^{(s)}$	Critical resolved shear stress of a slip system (s)
$\mathbf{U}$	Right stretch tensor
U	Space of admissible solutions
$\mathbf{u} = (u, v, w)$	Displacement field
$\mathbf{V}$	Left stretch tensor
$\mathbf{v}$	Velocity tensor
V	Generic volume
$\mathbf{W}$	Spin rate tensor
W	Strain energy
$\mathbf{w}$	Plastic work
$\boldsymbol{\Omega}$	Rotation rate tensor
$\mathbf{x}_k = (x, y, z)$	Position vector of node k
$\boldsymbol{\Xi}$	Grain averaged stress value
$\boldsymbol{\psi} = (\xi, \eta, \zeta)$	Natural coordinate system
$\mathbf{Z}$	Matrix that transform the Cauchy stress into its deviator

ANS	-	Assumed Natural Strain
BCC	-	Body Centered Cubic
CRSS	-	Critical Resolved Shear Stress
EAS	-	Enhanced Assumed Strain Method
FC	-	Full Constrained (Taylor Model)
FCC	-	Face Centered Cubic
FEM	-	Finite Element Method
HCP	-	Hexagonal Close-Packed
MITC	-	Mixed Interpolation of Tensorial Components
RC	-	Relaxed Constrained (Taylor Model)
RESS	-	Reduced Enhanced Solid-Shell
RI	-	Reduced Integration
RSS	-	Resolved Shear Stress
SFE	-	Stacking Fault Energy
SRI	-	Selective Reduced Integration
TBH	-	Taylor-Bishop-Hill
VHW	-	Veubeke-Hu-Wazhizu

Chapter 1

Introduction

A proper modeling of realistic problems requires expertise in mechanical, metallurgical and computational fields. Nowadays, manufacturing industries are replacing the so-called conventional design, based on the experimental "trial-error" method, by computational procedures which require less time and money. The Finite Element Method has been proven to be quite successful in simulation of mechanical processes such as deep drawing (sheet metal forming), but the simulation accuracy is mainly dependent on two main issues: the finite element chosen to describe kinematics and the constitutive law employed to characterize the material response.
In the following paragraphs, a state of art review is given both on finite element technology and constitutive modeling of anisotropy, showing the developments carried out over the last decades and emphasizing the advantages and drawbacks of several methodologies.

1.1 State of art reviews

1.1.1 Solid Finite Elements for Sheet Metal Forming Simulation

The demand of an excellent compromise between accuracy and efficiency in finite element numerical simulations is considered a major milestone in computational mechanics field. Simulation of large-scale industrial problems still demands simple and robust finite elements, despite the quick development of computer's performance. In the field of sheet metal forming simulation, the studies on the development and application of low-order eight-node (brick) finite elements for thin-walled applications have been increasing for the optimal balance between accuracy and efficiency in numerical simulations. Particularly, the solid-shell

concept, based on the conventional solid element topology but with improved bending performance, has become popular. Solid-shell elements are kinematically similar to shell elements differing from the latter by the absence of rotational degrees-of-freedom, but keeping the three-dimensional structure of solid elements with eight physical nodes. A number of advantages encouraging the use of solid-shell elements can be listed by comparing these with conventional shell or classical continuum 3D elements:

- *Simpler procedure for configurations update without the inclusion of rotational degrees of freedom.* In fact, the presence of rotation-type degrees-of-freedom in general shell formulations requires a specific iterative update procedure for nonlinear analysis, since this class of variables are, by nature, non-additive;
- *The direct use of full three-dimensional constitutive laws without plane-stress assumptions on constitutive equations.* As a consequence, solid elements naturally account for thickness (strain) variations. For a conventional shell formulation, shell thickness variation is calculated in a post-processing manner after the plane-stress constitutive model is applied, due to zero nominal stress assumption in shell kinematics. Alternatively, the ability to account for thickness variations can be achieved with an additional stretch degree variable;
- *Accurate and automatic consideration of double-sided contact problems*, due to the presence of distinct physical nodes differentiating top from bottom surfaces;
- *Avoidance of numerical ill-conditioning effects*, typical in classical continuum (solid) elements when used in the modeling of thin structures like in sheet metal forming applications.

Focusing on 3D continuum elements, low order solid finite elements are highly prone to be affected by the so-called locking phenomena (Hughes, 2000). Overestimation of the stiffness matrix, due to the occurrence of locking, is the main source of poor results regarding this class of elements. Hauptmann et al. (2001) categorized several types of locking for solid and solid-shell elements (some of them

also affecting shell elements). In particular, for the case of sheet metal forming simulations involving plasticity and thin-walled geometries, distinct cases of locking are expectable and should be avoided, namely:

- *Volumetric locking*, as appearing due to the incompressible-type deformation in plasticity;
- *Transverse shear locking*, as occurring when thickness to length ratio tends to zero in bending-dominated problems;
- *Thickness locking*, which is related to an inefficient reproduction of the strain field along the thickness direction.

The *Reduced Integration* (RI) technique (Zienkiewicz et al., 1971) and the *Selective Reduced Integration* (SRI) technique (Hughes et al., 1977), were the first successful numerical solutions to alleviate locking pathologies. For low-order solid elements, both techniques correspond to the use of a lower quadrature rule (One Gauss point, located in the center of the tri-unit cube) rather than the full quadrature rule (2×2×2 Gauss points). While the RI scheme sooner resulted in non-physical (spurious) deformation patterns, SRI proved to be quite successful, although also affected by spurious modes, and being (to some extent) the predecessor of the *B-bar method* (Hughes, 1978; 1980). In the latter, shape functions derivatives related to the volumetric part of deformation were replaced by approximations resulting from a mixed formulation, without resorting to reduced integrations. Other formulations succeeded in using an augmented functional, when compared to the one obtained from displacement-based approaches, incorporating additional fields into the formulation and leading to the onset of general mixed methods. For the ***u/p*** *mixed formulation*, for instance, displacements are interpolated with functions providing C^o continuity requirement, while the pressure field is introduced via discontinuous functions between elements (Hughes, 2000; Zienkiewicz and Taylor, 2000).

Reduced integrated elements are especially attractive considering their computational efficiency. Nevertheless, due to the rank-deficiency generated, stabilization procedures are always required to avoid the appearance of spurious deformation modes, known as hourglass patterns. Consequently, reduced integrated

elements have been continuously developed combined with many stabilization schemes (possibly applied with shell or solid elements) through the last decades, as in the works of Belytschko et al. (1983; 1985; 1991; 1992; 1993; 1994; 2000), Liu et al. (1994; 1998) and Masud et al. (2000). Despite of these contributions, the one-point integration rule still gives rise to a critical drawback for the problems which require more than one integration point along the thickness direction, since the use of several elements' layers can cause a substantial decrease in computational efficiency and/or ill conditioning numerical problems.

Departing from previous mixed approaches, the *Enhanced Assumed Strain* (EAS) method was initially introduced by Simo and Rifai (1990). Within this formulation, the strain field is enlarged (under certain conditions) with the inclusion of an internal variable field, therefore resulting in additional deformation modes. The mathematical basis for such element formulation is given by the well-known Veubeke-Hu-Washizu three-field variational (Fraeijs de Veubeke, 1951). The EAS method has been widely applied for 2D, 3D, shell and solid-shell formulations successfully. A few examples of low order solid EAS elements are demonstrated in the works of Andelfinger and Ramm (1992), Simo et al. (1993), Korelc and Wriggers (1996), Rohel and Ramm, (1996), de Borst and Groen (1999), Kasper and Taylor (2000), Alves de Sousa et al. (2003a;b) or Fontes Valente et al. (2004a). Apart from accuracy issues, the computational inefficiency has proven to be the major disadvantage of solid EAS elements. In fact, the number of enhancing variables is seldom less than 10 (but reaching sometimes 30 or more), leading to hardly treatable stiffness matrices and heavy computational costs.

Still within the scope of the EAS method, but focusing on solid elements especially designed for shell-type applications, relevant lines of research in this field are given for instance by Schweizerhof and co-workers (Freischlager and Schweizerhof, 1996; Hauptmann and Schweizerhof, 1998; Hauptmann et al., 2000; Doll et al., 2000; Harnau and Schweizerhof, 2002) as well as Klinkel and Wagner (1997), Klinkel et al. (1999), Wagner et al. (2002) and Vu-Quoc and Tan (2003). In these works, not only the EAS method is used to tackle locking phenomena: the so-called *Mixed Interpolation of Components* (MITC), from the initial work of Dvorkin and Bathe

(1984) and the *Assumed Natural Strain* (ANS) approach firstly introduced in Park and Stanley (1986) are used mainly for transverse shear locking treatment. In fact, both techniques employ a set of additional sampling points in an element in order to obtain a substitute or complementary strain field leading to the fulfillment of the Kirchhoff-Koiter hypothesis in the thin shell limit. Also, in this group of solid-shell elements, stress is evaluated in two Gauss points through thickness direction (due to the use of a single layer of fully-integrated elements), which is commonly not enough to capture accurately bending effects due to the lack of integration points along the thickness direction.

In the scope of EAS and RI techniques, recent investigations proved that they can be combined to derive efficient and accurate solid-shell elements. Examples are the works of Puso (2000), Reese (2002; 2005; 2006), Reese et al. (2000) or Legay and Combescure (2003), which still have in its majority the common characteristic of using a fixed number of Gauss points through the thickness direction, which can be applied for linear elastic analyses with improved bending performance. Investigations carried out by Reese et al. (1999) and Reese and Wriggers (2000) have shown the importance of stabilization schemes in the EAS method: the hourglass instabilities can be avoided by a suitable form of stabilization. Therefore, a new class of eight-node solid-shell elements requiring only a single element layer, but including (user-defined) multiple integration points through thickness is highly desirable for nonlinear material modeling.

1.1.2 Anisotropic Plasticity

Historically, the studies on plastic anisotropy of metals have been categorized at two independent scales: continuum level phenomenological theory and micro level crystal plasticity theory. Both approaches have advantages. The classical mathematical theory allows for direct implementation into FEM codes, but there isn't a clear connection with the material micro-structure. On the other hand, in crystal plasticity such connection exists since texture is the main input to the models, but implementation into FEM codes is generally inefficient in terms of

CPU costs. Nevertheless, in the last two decades, the rapid improvement of computer's hardware, parallel processing and massive utilization of FEM techniques are continuously attracting the use of polycrystal models.

Barlat et al. (2002) stated that phenomenological models are possibly more accurate than polycrystal models when the strain amount is moderate, since mechanical data is used as input. However, polycrystal models are more accurate for the deformation accompanying texture evolution, since they can track the lattice rotation of each grain individually. Therefore, it is required to select an appropriate approach based on the problem characteristics.

1.1.2.1 Phenomenological approaches

The mathematical theory of plasticity starts from assumptions of phenomenological character based on experimental observation. Simplicity and accuracy are required in this field. Its foundations can be found in Hill (1950) and the extension to the case of finite deformations in MacMeecking and Rice (1975). At macroscopic level, and for a general stress state, plastic deformation is well characterized by means of a yield surface (or yield locus), a flow rule and a hardening law. The yield locus must be a convex surface in the stress space defining the boundary between elastic and plastic domains. Plastic anisotropy appears as an initial distortion of the yield surface shape due to yield stress and strain ratio directionalities. During plastic deformation, the yield locus is updated (expanded, moved, rotated) according to its associated hardening law. Finally, the flow rule determines the relation between strain rate tensor and stress tensor.

The mathematical description of a yield surface must follow experimental evidence. Bridgman (1923) observed that the hydrostatic pressure doesn't induce plasticity in general low porosity metals. Thus, only the second and third invariants of the stress tensor must be accounted for in the definition of a yield criterion. Drucker (1951) showed via a postulate that the yield surface must be convex for stability. However, Drucker postulate is a sufficient, but not a necessary condition for stability (Stoughton and Yoon, 2006). From the same postulate, it can be concluded that

the flow (or strain rate) vector is orthogonal to the plastic potential (or yield surface for associate flow rule).

Yield surfaces (stress potentials) are described by mathematical equations well-known as yield criteria. Roughly speaking, they are a fitting function of experimental data coming from mechanical tests. For isotropic materials, the phenomenological theory of plasticity has set its grounds in the works of Tresca (1864) and von Mises (1913). Hill (1948) extended Mises criterion to orthotropic materials originating the most popular anisotropic yield criterion, particularly for steel. In spite of some limitations to characterize aluminum alloys, the Hill'48 yield function offer ease of use and implementation and is available in the majority of FEM commercial codes.

Nevertheless, several scientists have proposed more sophisticated yield functions for anisotropic materials. Hill himself successively improved his criterion in subsequent works (Hill 1979; 1990) to better describe the "anomalous behaviour" of aluminum alloys. Bassani (1977) developed a family of yield functions depending only on four parameters, and Gotoh (1977) introduced a fourth-degree polynomial yield function. Another important research direction in the field was initiated by Hosford (1972) who introduced a non-quadratic yield function for isotropic materials, based on the results of polycrystal calculations. This criterion was later generalized by himself for anisotropic materials (Hosford, 1979). Budiansky (1984) prescribed a parametric expression in polar coordinates of the yield function. Barlat and Richmond (1987) introduced a non-quadratic function, including the shear stress components, later extended by Barlat and Lian (1989). In the nineties, yield functions emerged for any complex stress state: Barlat et al. (1991) developed a six-component yield function (Yld91), by using a linear transformation of the stress state; Karafillis and Boyce (1993) extended Yld91 criterion using a "weighted" linear transformation; Vegter et al. (1995) proposed a yield function with the aid of Bezier's interpolation.

On the other hand, Hill (1993) stated from experimental observation that none of the above referred yield criteria is able to represent the behaviour of a material exhibiting a tensile yield stress almost equal in value in the rolling and transverse

directions, while r-values vary strongly with the angle to the rolling direction. By doing so, Hill (1993) introduced a cubic yield criterion valid only when the principal stress axes and anisotropy axes are parallel. Yld96 (Barlat et al., 1997) modified Yld91 criterion by introducing both stress and strain directionalities into the formulation. Consequently, Yld96 is one of the most accurate yield functions for aluminum alloys' sheets, since it allows for the account of yield stress and r-value directionalities simultaneously. Though, it should be pointed out that there is no mathematical proof of convexity under full stress components. In this sense, Yoon et. al (2000a) and Barlat et al. (2003) proposed a plane stress yield function (Yld2000-2d) to alleviate the drawbacks of Yld96.

Recently, new yield functions continued to be proposed. Examples are Cazacu and Barlat (2001; 2003; 2004), providing a generalization of Drucker's criterion through general transformations operating on the second and third invariants of the stress tensor, allowing for its application to Hexagonal Close Packed (HCP) materials, which exhibit tension-compression yield asymmetry due to microstructural twinning. The drawback is that convexity conditions are difficult to verify. For this reason, a particular case of this theory, which consists of the linear transformation of stress components, has received particular attention in the last two years. Besides Barlat et al. (2003), Bron and Besson (2004) extended Karafillis and Boyce yield criteria based on the linear transformation concept.

With the exception of the yield function proposed by Bron and Besson (2004), the majority of the herein cited yield criteria were developed for plane stress states or do not fulfill the requirements for convexity. In this scope, it is worth to remark Barlat et al. (2005), which introduced a 3D yield function with 18 anisotropy coefficients respecting the convexity requirements (called Yld2004-18p) and applicable to aluminum alloys. The yield function requires experimental input data along every 15 degrees, but is able to capture accurately the r-value and yield stress directionalities for any kind of stress state.

1.1.2.2 Crystal plasticity approaches

The physical theory of plasticity provides a deeper insight into the understanding of anisotropic plastic deformation. It was started more than a century ago, when Ewing and Rosenheim (1899) showed that the plastic deformation of metals produces (on its surface) many parallel microscopic steps caused by the emergence of the so-called slip bands. Also, they observed that metal grains were an aggregate of crystals with approximate homogeneous lattice orientations. Thus, they concluded that plastic deformation was a result of simple shears along certain crystallographic planes into certain crystallographic directions. For some metals (later classified as Hexagonal Close Packed - HCP) they also noticed the particular deformation mode called twining.

Two decades later, Schmid (1924) and Taylor and Elam (1923; 1925) gave continuity to Ewing and Rosenheim's studies. Metals were separated into three main groups, the Face Centered Cubic, the Body Centered Cubic and Hexagonal Close-Packed, in a categorization still used nowadays (Figure 1-1). Firstly in the single crystal's domain, Schmid (1924) compared the mechanical behavior of FCC, BCC and HCP single crystals.

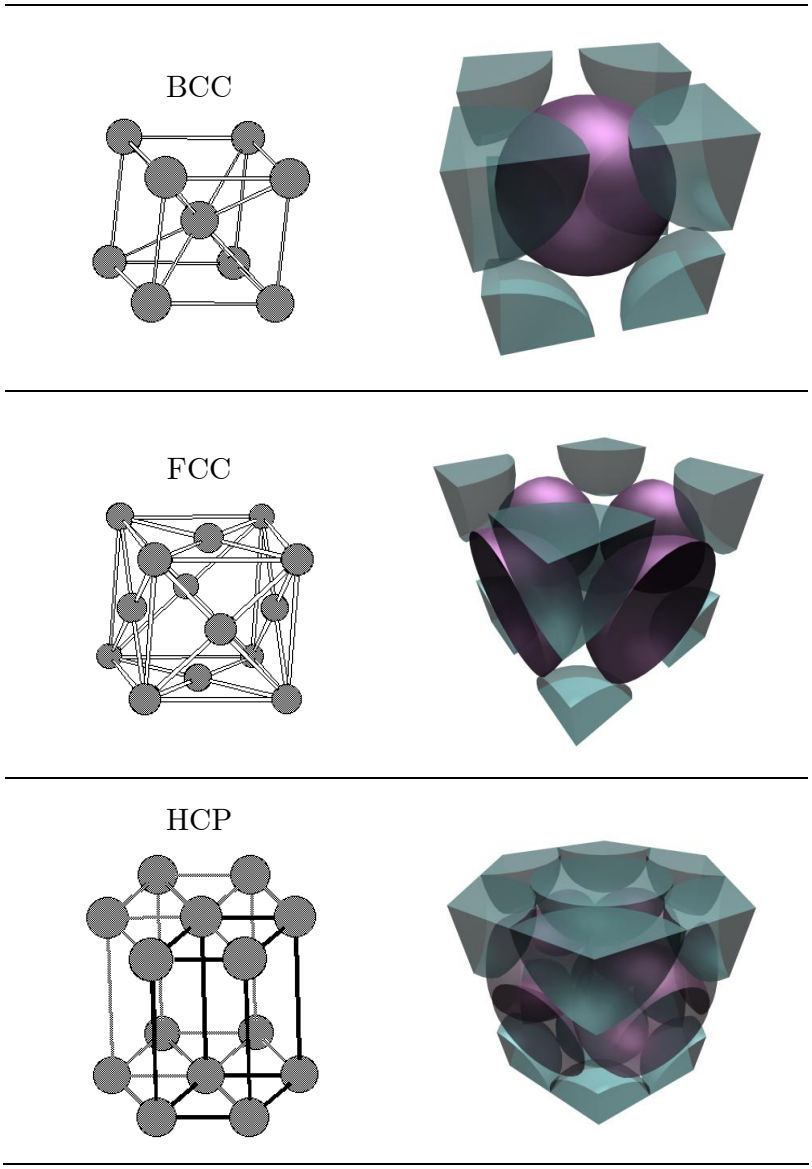

Figure 1-1: Main crystal structures for metals (Van Note, 2006).

Taylor and Elam (1923; 1925) provided the basis of the kinematics of plastic deformation in terms of crystallographic slip. It was given the notion of *slip system* as a pair composed by one slip plane and direction. Particularly for an aluminum crystal, they defined a criterion of plastic yielding as the Schmid Law, stating that plastic yielding takes place when the *Resolved Shear Stress* (RSS) on a given slip system reaches a critical value, the so-called *Critical Resolved Shear Stress* (CRSS).

The first approach for a polycrystal model was proposed by Sachs (1928). The main assumption of the lower-bound model of Sachs is to consider all grains subjected to the same stress state. Then, each grain can deform with no boundary restriction. It is also assumed that for each grain, only one slip system (the one with highest RSS) is active. However, by considering an unconstrained deformation for each single crystal, this model has a limited range of application, achieving reasonably accurate results only if applied for strain values below 10%.

In the same year, von Mises (1928) pointed out that, to cause a shape change in an incompressible body, at least five independent strain components must exist. Based on this assumption, Taylor (1938) proposed a more refined polycrystal model, possibly accounting for large plastic deformations, instead of Sachs model. In Taylor upper bound model, all grains of a polycrystal undergo the same amount of deformation. If the crystal is embedded in a polycrystalline aggregate, it cannot change its shape freely due to constraints from the surrounding polycrystal. In this case, slip from five independent slip systems is generally required to accommodate the five independent strain components for plastic deformation. Based on the principle of virtual work, Taylor hypothesized that, among all combinations of five slip systems which are capable of accommodating the imposed strain, the active combination is the one with the minimum accumulated slip. A variation of the classical Full-Constrained (FC) Taylor model is the so-called Relaxed Constraint (RC) Taylor model (Van-Houtte, 1988), where the strict assumption of imposing the same strain to all grains is dropped, i.e., the compatibility of well-chosen terms of the velocity gradient is relaxed. RC models sometimes produce better results than FC models for rolling texture predictions, but their justification is still under debate (Habraken, 2004).

Self consistent models provide solutions between lower and upper bound methods. Based on Eshelby's inclusion theory (Eshelby, 1957) the self-consistent scheme was introduced by Kröner (1962) and Budiansky and Wu (1962). In self-consistent models, the grains are regarded as inclusions in an infinite homogeneous matrix. Eshelby has shown that stress and strain states are uniform within the inclusion if it has an ellipsoidal shape. The properties of the matrix are determined as the

overall average properties of the single crystal agglomerate. In the Kröner and Budiansky-Wu models the coupling between a grain and the polycrystal (matrix) is determined by the elastic stiffness of the matrix and the constituents, which is a stiff coupling in the plastic regime. Also, the interaction between the grains and the pseudo polycrystal is incorporated in the model, but the direct grain-to-grain interaction is not taken into account. Supplementary, the self-consistent modeling schemes of Hill (1965a; 1965b; 1966) and Hutchinson (1970) introduced the elastic-plastic coupling between the grains and the matrix, which predicts more realistic deformation heterogeneities in the polycrystal. In these models, the interaction between the grain and the matrix is determined by the instantaneous grain and matrix modulus. This approach is not straightforward to adopt in nonlinear cases, because it demands a rather long iterative solution procedure. This is due to the fact that macroscopic values must coincide with the average of grain responses. In this sense, a considerable improvement should be carried out in order to handle non-academic realistic problems.

Among the cited polycrystal approaches, the FC Taylor upper-bound model is the most successful in dealing with FCC and BCC metals. Indeed, FCC and BCC crystals hold a sufficient number of slip systems to accommodate arbitrary deformations when surrounded by other crystals. However, this polycrystal plasticity framework carries some difficulties: as entirely based on Schmid law, the appearance of slip on a certain slip system depends only on the value of the RSS in that system. Thus, influence of stress states in other slip systems is not taken into account. The independence of slip systems leads to the ambiguity of crystal kinematics, i.e., several combinations of slip rates give the same strain rate of the crystal. As a consequence, the number of unknowns exceeds the number of formulated equations and the problem cannot be represented by a complete system of equations. Bishop and Hill (1951a; 1951b) and Bishop (1953) introduced the *principle of maximum work* to overcome this difficulty, but even so the task of choosing the set of five active slip systems (from a very high number of possibilities) continued to be a very lengthy process. Gambin (2000) pointed out deviations of the Schmid law due to slip systems' interactions, as observed experimentally. Finally, the resulting piece-wise linear yield surface according to

Schmid law, is a Tresca-type characterized by the presence of sharp corners. The plastic-corner effect is responsible for several errors and convergence problems in numerical analysis since it doesn't allow for a sole definition of the plastic flow vector on that point.

Despite the above difficulties, relevant works were carried out on constitutive relations between slip rates and shear stresses on Schmid law-based rate-independent models, as on Rice (1971), Hill and Rice (1972), Asaro and Rice (1977), Peirce et al. (1982), Asaro (1983) and Anand and Kothari (1996)

To avoid the referred difficulties related to rate-independent models, Pan and Rice (1983), Peirce et al. (1983) and Asaro and Needleman (1985) proposed a new way of describing the deformation of a crystal. A small deviation from pure plasticity to a visco-plastic behavior of the material is assumed. All slip systems are considered active, thus overcoming the issue about the choice of active slip systems. As a consequence, the problem can be formulated in terms of a complete system of equations. Nevertheless, the introduction of a pre-defined reference strain rate into formulations promotes a lack of generality and deteriorates accuracy. In addition, for low values of the rate-sensitivity parameter (also included in this kind of formulations) the constitutive equations are rather stiff demanding heavy calculations.

In view of that, grain level approaches, with no resort to viscoplastic rate-dependent slip system level approaches, continue to be a very attractive alternative to model realistic plastic anisotropy behaviour. Gambin (1991a; 1991b) and independently Arminjon (1991), found another solution to avoid the sharp corner effect problem by introducing the concept of interaction between slip systems. Also, it circumvents the issue of the uniqueness of the set of active slip systems to be chosen. In fact, the problem becomes governed by a highly nonlinear regularized Schmid law and the occurrence of slip in a certain slip system depends on the RSS of all slip systems. In these models, a dimensionless parameter governs the interaction of the slip systems and defines the roundness of corresponding yield surfaces and, in this way, the strain-rate vector uniquely. Gambin (1991) pointed

out a correlation between this parameter and the stacking fault energy (SFE) of FCC materials.

Apart from the considerations given on this section, there are other recent but not so representative polycrystal plasticity models. Thus, they are not contemplated here. For an extensive state of art review on phenomenological and polycrystal models, the interested reader should check Habraken (2004).

1.2 Thesis Objectives and Outline

The numerical simulation of anisotropic sheet forming processes employing the finite element method encompasses a complex set of instruments. The main goal of the present work is to develop two important parts of this set: a nonlinear solid-shell finite element and a constitutive model for plastic anisotropy.
Considering the advantages of solid-shell elements given in the previous section, it is proposed a new solid-shell element with eight physical nodes, but including multiple integration points through thickness direction within a single layer. The element is denoted as RESS (Reduced Enhanced Solid-Shell). The major and distinguishing guidelines for RESS element are:

- In-plane Reduced Integration formulation, but allowing for an arbitrary number of integration points in thickness direction. Actually, this number should be increased (and can be easily done) when the stress distribution needs high detail like for springback evaluation;
- Elimination of locking effects via the Semi-Reduced Integration scheme and the Enhanced Strain Method. In the latter, only one enhancing variable is used, ensuring high computational efficiency;
- Physical stabilization procedure to correct the rank deficiencies coming from the stiffness matrix and internal force vector. The computation time can be reduced to a minimum since all integrals involved are calculated analytically and no empirical parameters are employed.

On the constitutive model, both phenomenological and polycrystal approaches are studied. Regarding phenomenological plasticity, Barlat's three-dimensional yield functions Yld91 and Yld2004-18p are utilized. If phenomenological yield functions are relatively easy to implement in FEM codes, the same does not happen for polycrystal models. Here, the time efficient grain-level approach by Gambin is implemented to describe the single crystal behavior. The micro-macro transition is governed by the FC Taylor model. For polycrystal plasticity implementation into a FEM code, the following guidelines are considered:

- In polycrystal approaches, one of the main reasons to take huge computational time is the consideration of slip systems stretching while keeping orthogonality and also due to the use of Kirchhoff stress in time integration. In this work, the incremental deformation theory is applied to remove those drawbacks. In the incremental deformation theory (Yoon, 1997; Yoon, 1999a), the material deforms to follow the minimum plastic work path. Under this assumption, slip system orthogonality is kept without stretching. The rotation tensor dominates all lattice rotations and the Cauchy stress can be conveniently used for time integration. By doing so, the formulation is very simple and efficient;
- In the grain-level crystal plasticity model by Gambin, the equilibrium equation is only considered for grain level and the slip rate at slip system level is calculated by simple algebraic equations. Hence, it is possible to reduce tremendously computational time when compared to slip-system level rate-dependent crystal plasticity models.

In face of that, the scope and outline of this dissertation will be the following:

- In Chapter 2, a brief review is given on nonlinear continuum mechanics and implementation guidelines. Starting from the essentials like strain and stress measures, and passing through the nonlinear EAS method, the ground rules for the numerical simulation of forming processes are provided.
- In Chapter 3, it is presented the RESS Solid-Shell element. The theoretical aspects of the RESS formulation kinematics, the employed methods to

handle locking and the developed physical stabilization scheme are discussed.

- In Chapter 4, a physical insight into the plasticity of FCC (aluminum crystals) is given. Barlat's yield functions used in this work (Yld91 and Yld2004-18p) are reviewed. The description of the grain-level single crystal model of Gambin (interacting slip systems assumption) is given, along with the kinematics of the FC Taylor model providing the micro-macro transition. Validity and robustness of the polycrystal plasticity model are also assessed by means of iso-error maps;
- In Chapter 5, various examples are given. Initially, academic examples are showed to assess the accuracy and locking-free properties of the solid-shell element. Then, complex examples with contact, anisotropy and large deformations are presented.
- In Chapter 6, the closure is given along with conclusions and future lines of research.

Chapter 2

Topics in Nonlinear Formulations

In the following sections a brief summary of nonlinear continuum mechanics is provided. The objective is not to enter in full detail on the subjects, but to focus precisely on the points that have been employed and implemented throughout this work. Starting with basic topics, such as strain and stress measures, the theoretical background of the corotational approach is described. Computational plasticity aspects are also discussed. In the end, the extension of the Enhanced Assumed Strain method to account for nonlinearities is treated in detail, with the main advantages of the adopted approach being highlighted.

2.1 General Aspects

In nonlinear continuum mechanics a body experiences large deformations under applied external loads. Since such deformation isn't small enough so that the final configuration almost coincides with the initial, the deformed body's configuration can be substantially different from the initial one. In this case, the solution procedure is to divide the problem into small increments, being the evolution described by increasing time steps $(\ldots n-1,\ \ n,\ \ n+1\ldots)$ where equilibrium equations are satisfied for each configuration and the solution for the overall incremental problem is obtained.

In fact, the global solution of a nonlinear problem may be regarded as a sum of sub-step solutions where configurations and solution processes are known, which means that a Lagrangian or material formulation is adopted (Belytschko, 2000). Particularly, if the configuration is always updated and the reference configuration used for the equilibrium equations' integration is always the last converged

configuration at the time step (n), then it is convenient to use the updated Lagrangian approach[1].

In this work, the configuration is always updated. To obtain the solution for a given time step, the reference configuration is always the last converged configuration. In the classical total Lagrangian approach, all quantities are also updated but always referred to the very initial configuration. On the other hand, for the updated Lagrangian approach herein used, the reference configuration is always the last converged configuration at an updated time step (n) and the current or spatial configuration is the one at time step $(n+1)$.

For further application into the Finite Element Method for large displacements and strains, it is useful to establish a set of configurations related to which each particle in the deforming body can be referred to. Several coordinate systems can then be distinguished (Figure 2-1):

i. global coordinate system, described by global coordinates $\mathbf{x} = x_i = (x, y, z)$ at the reference $({}^{n}x_i)$ or current configuration $({}^{n+1}x_i)$;
ii. natural coordinate system described by parametric coordinates $\boldsymbol{\psi} = (\xi, \eta, \zeta)$ where $(\xi, \eta, \zeta) \in [-1,1],[-1,1],[-1,1]$ defining the so-called parametric cubic domain;
iii. convective coordinate system, defined by tangent vectors to ξ, η and ζ lines $(\mathbf{x}_{,\xi}, \mathbf{x}_{,\eta}$ and $\mathbf{x}_{,\zeta})$.

Due to the non-orthogonal character of the convective frame, a local orthonormal frame $\mathbf{r} = (\mathbf{r}^1, \mathbf{r}^2, \mathbf{r}^3)$, will be utilized to follow the motion of the body, serving as a corotational coordinate system. The initial configuration of this frame can be obtained, for instance, following the simple algorithm described in Box 1 (Fontes Valente, 2004):

---

[1] If the current configuration is used to integrate the equilibrium equations, the so-called Eulerian approach is utilized. Nevertheless, the Eulerian approach is generally more suitable for Fluid Mechanics analysis and will not be focused on this text.

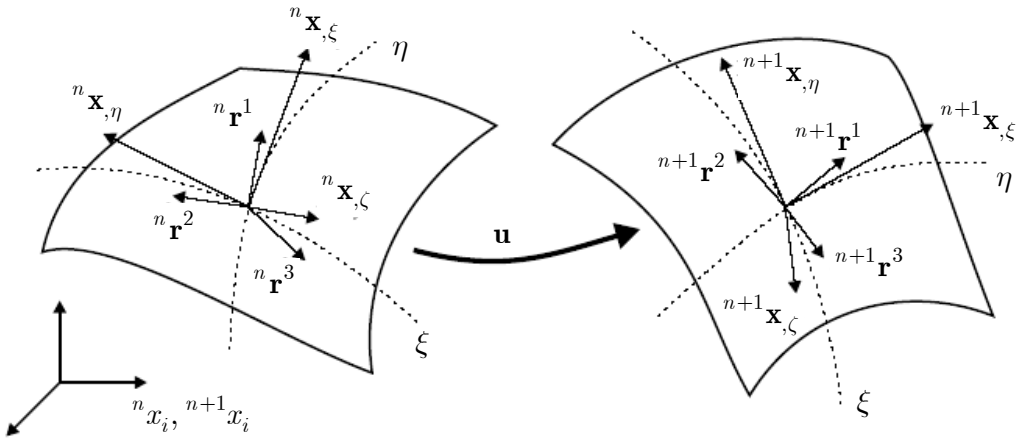

Figure 2-1: Coordinate systems; reference and current configurations.

1. Let $\mathbf{r}^3 = \left[\frac{\partial x}{\partial \xi} \; \frac{\partial y}{\partial \xi} \; \frac{\partial z}{\partial \xi}\right]^{\mathrm{T}} \times \left[\frac{\partial x}{\partial \eta} \; \frac{\partial y}{\partial \eta} \; \frac{\partial z}{\partial \eta}\right]^{\mathrm{T}}$
2. $\mathbf{r}^3 = \dfrac{\mathbf{r}^3}{\left\|\mathbf{r}^3\right\|}$
3. $\mathbf{r}^1 = \left[\frac{\partial x}{\partial \xi} \; \frac{\partial y}{\partial \xi} \; \frac{\partial z}{\partial \xi}\right]$
4. $\mathbf{r}^1 = \dfrac{\mathbf{r}^1}{\left\|\mathbf{r}^1\right\|}$
5. $\mathbf{r}^2 = \mathbf{r}^3 \times \mathbf{r}^1$

Box 2-1: Definition of orthonormal reference frame.

Besides the referred coordinate system, an additional crystal lattice coordinate system will be introduced to properly implement a crystal plasticity model in Chapter 4.

2.2 Body Motion and Strain Measures

Considering the set of unit base vectors of a rectangular Cartesian coordinate system ($\mathbf{e}_i$), any point in the initial reference configuration or in the current configuration can be uniquely defined as

$$\begin{aligned} {}^{n}\mathbf{x} &= {}^{n}x_i\mathbf{e}_i \\ {}^{n+1}\mathbf{x} &= {}^{n+1}x_i\mathbf{e}_i \end{aligned} \quad , \tag{2.1}$$

where ${}^{n}x_i$ and ${}^{n+1}x_i$ are the position vectors for both configurations.
The displacement field of a point in the converged state is obtained as usual by the difference between its position vectors in current and reference configurations,

$${}^{n+1}_{n}\mathbf{u} = {}^{n+1}\mathbf{x} - {}^{n}\mathbf{x}\,. \tag{2.2}$$

The partial derivatives of the position vector ($\mathbf{x}$) allows for the definition of the convective coordinate system, defined by the covariant basis vector, either in the current or reference configuration, in the form:

$$\begin{aligned} {}^{n+1}\mathbf{g}_a\left(\boldsymbol{\psi}\right) &= \frac{\partial\,{}^{n+1}\mathbf{x}}{\partial\psi_a} \\ {}^{n}\mathbf{g}_a\left(\boldsymbol{\psi}\right) &= \frac{\partial\,{}^{n}\mathbf{x}}{\partial\psi_a} \end{aligned} \quad . \tag{2.3}$$

Alternatively, contravariant base vectors could also be used. Such vectors are obtained from the following relation:

$$\mathbf{g}_a \cdot \mathbf{g}^b = \delta_a^b \quad , \tag{2.4}$$

where δ_a^b is the well-known Kronecker delta. Since contravariant basis vectors are orthogonal to covariant basis vectors, they also can be defined as:

$$\begin{aligned} {}^{n+1}\mathbf{g}^a\left(\boldsymbol{\psi}\right) &= \frac{\partial\psi_a}{\partial\,{}^{n+1}\mathbf{x}} \\ {}^{n}\mathbf{g}^a\left(\boldsymbol{\psi}\right) &= \frac{\partial\psi_a}{\partial\,{}^{n}\mathbf{x}} \end{aligned} \quad . \tag{2.5}$$

The preceding notions give the basis to define the deformation gradient ($\mathbf{F}$). The incremental deformation gradient between configurations (n) and (n+1) can be written as a function of the position vectors in these configurations:

$${}^{n+1}_{n}\mathbf{F} = \frac{\partial\,{}^{n+1}\mathbf{x}}{\partial\,{}^{n}\mathbf{x}}\,, \tag{2.6}$$

or alternatively through covariant and contravariant basis vectors:

$$ {}^{n+1}_{n}\mathbf{F} = {}^{n+1}\mathbf{g}_a \otimes {}^{n}\mathbf{g}^a \,. \tag{2.7} $$

The physical interpretation of the deformation gradient can be easily inferred by observing that it represents the length variation of a linear segment when the body deforms from the reference into the current configuration, that is,

$$ d\,{}^{n+1}\mathbf{x} = \mathbf{F} \cdot d\,{}^{n}\mathbf{x} \quad . \tag{2.8} $$

Similarly, the deformation gradient can also be used to map volume variations between the reference and current configurations (Doghri, 2000). Nevertheless, one of the most important features of the deformation gradient is its possibility to be decomposed into an unique product of two matrices, a symmetric right or left stretch matrices, **U** or **V**, respectively, and an orthogonal matrix **R** corresponding to a rigid-body rotation such that (dropping from now on indices for simplicity sake),

$$ \mathbf{F} = \mathbf{RU} = \mathbf{VR} \quad . \tag{2.9} $$

The relation expressed by (2.9) and represented in Figure 2-2 is well-known as the *Polar Decomposition Theorem*. The theoretical basis of the polar decomposition theorem is given for instance in the work of Yoon et al. (1999a). It is particularly useful in problems involving large deformations described by the use of corotational coordinate systems. In addition, it allows for a physical explanation of the 2$^{\text{nd}}$ Piola Kirchhoff stress tensor.

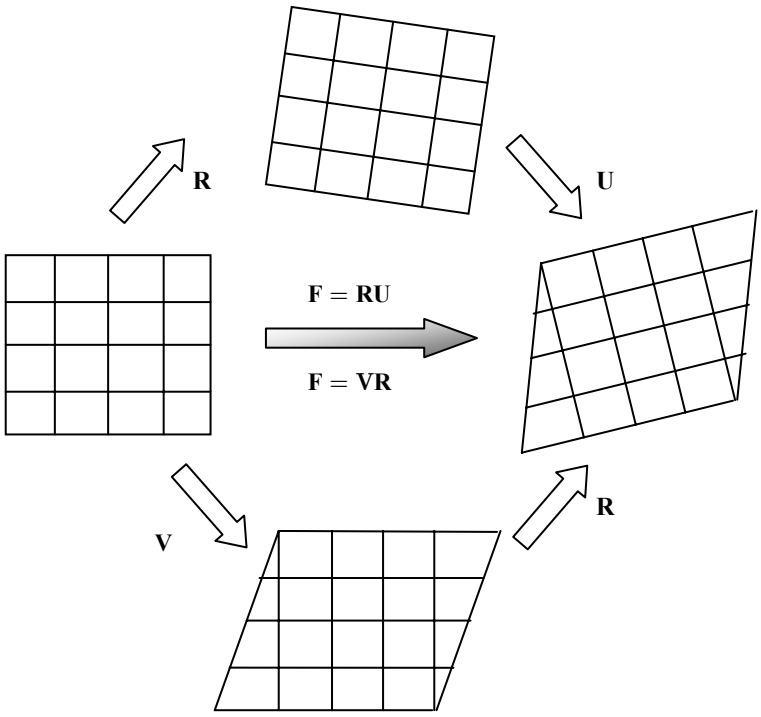

Figure 2-2: Schematic representation of the polar decomposition theorem

The polar decomposition theorem becomes also useful in the definition of some important strain measures. In fact, the left and right Cauchy-Green strain tensors ($\mathbf{C}^*$ and $\mathbf{b}^*$) are obtained decomposing the deformation gradient in the form:

$$\begin{aligned} \mathbf{F}^{\mathrm{T}} \cdot \mathbf{F} &= \mathbf{U}^{\mathrm{T}} \cdot \mathbf{R}^{\mathrm{T}} \cdot \mathbf{R} \cdot \mathbf{U} = \mathbf{U}^2 = \mathbf{C}^* \\ \mathbf{F} \cdot \mathbf{F}^{\mathrm{T}} &= \mathbf{V} \cdot \mathbf{R} \cdot \mathbf{R}^{\mathrm{T}} \cdot \mathbf{V}^{\mathrm{T}} = \mathbf{V}^2 = \mathbf{b}^* \end{aligned} \tag{2.10}$$

Nevertheless, regarding a Lagrangian approach, the most important strain measure is the Green-Lagrange strain tensor (Belytschko, 2000; Doghri, 2000). Using the deformation gradient, the Green-Lagrange strain tensor can be defined as:

$$\mathbf{E} = \frac{1}{2}\left(\mathbf{F}^{\mathrm{T}}\mathbf{F} - \mathbf{I}_2\right) = \frac{1}{2}\left(\mathbf{C}^* - \mathbf{I}_2\right) \quad , \tag{2.11}$$

where $\mathbf{I}_2$ stands for the second order identity matrix. In case of an Eulerian approach, not contemplated in this work, the Almansi strain tensor should be used. It can be defined like:

$$\mathbf{e} = \frac{1}{2}\left(\mathbf{I}_2 - \mathbf{F}^{\mathrm{T}}\mathbf{F}^{-1}\right) = \frac{1}{2}\left(\mathbf{I}_2 - \mathbf{b}^*\right) \quad . \tag{2.12}$$

As a final note, from relations posed in equations (2.3) to (2.7) it is possible to rewrite the incremental Green-Lagrange strain tensor expliciting its linear and nonlinear sub-terms (Doghri, 2000),

$$ {}^{n+1}_{n}E_{ab} = \frac{1}{2}\left(\underbrace{ {}^{n}\mathbf{g}_a \cdot \frac{\partial^{n+1}_{n}\mathbf{u}}{\partial^{n}\psi_b} + \frac{\partial^{n+1}_{n}\mathbf{u}}{\partial^{n}\psi_a} \cdot {}^{n}\mathbf{g}_b }_{\text{linear part}} + \underbrace{ \frac{\partial^{n+1}_{n}\mathbf{u}}{\partial^{n}\psi_a} \cdot \frac{\partial^{n+1}_{n}\mathbf{u}}{\partial^{n}\psi_b} }_{\text{non-linear part}} \right). \tag{2.13} $$

2.3 Stress Measures

In nonlinear continuum mechanics several stress measures can be used. Their definitions depend on the configurations where the forces are applied. Most used stress measures are Cauchy ($\boldsymbol{\sigma}$) and second Piola-Kirchhoff ($\mathbf{S}$). In physical terms, the Cauchy stress components are obtained dividing the external forces acting on the current configuration by the current areas. The second Piola-Kirchhoff stress components are defined in terms of forces, transformed by the local deformation, by a non-deformed unit area. In fact, the onset of the second Piola-Kirchhoff stress tensor comes from the derivation of equilibrium equation at a Lagrangian coordinate system, not allowing the utilization of the naturally physical Cauchy stress (Natal Jorge, 1997). Finally, it is worth mentioning the Kirchhoff stress ($\boldsymbol{\tau}$) with no physical meaning, and the 1st Piola-Kirchhoff stress ($\mathbf{P}$), coming from the forces, without any transformation, by unit area. In the next paragraphs, a brief description of these measures is given.

The natural starting point for any description of stress measures is the Cauchy stress tensor. To define the Cauchy stress vector, consider a body in the current configuration under external forces action, as illustrated in Figure 2-3. Also, let us define a plane by its normal ($\mathbf{n}$), which splits the body into two parts.

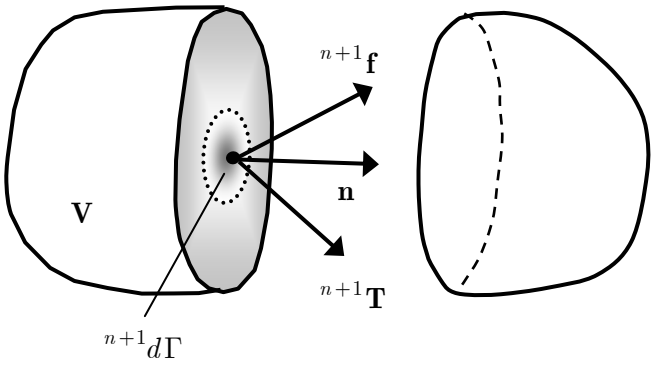

Figure 2-3: Stress vector definition

Considering the elemental surface area $^{n+1}d\Gamma$ defining the vicinity of a given point of the body's surface, the stress vector is defined as:

$$^{n+1}\mathbf{T} = \frac{^{n+1}\mathbf{f}}{^{n+1}d\Gamma} \quad . \tag{2.14}$$

Similarly, the stress vector could be defined at the reference configuration. After obtaining the stress vector, the Cauchy stress comes as a tensor $\boldsymbol{\sigma}$ transforming the unit normal vector $\mathbf{n}$ into the stress vector $^{n+1}\mathbf{T}$ acting upon $^{n+1}d\Gamma$ as follows,

$$^{n+1}\mathbf{T} = \boldsymbol{\sigma} \cdot \mathbf{n} \quad . \tag{2.15}$$

Although not having an immediate physical meaning the Kirchhoff stress tensor is directly related with the Cauchy stress in the form (Başar, 2000):

$$\boldsymbol{\tau} = \det(\mathbf{F})\boldsymbol{\sigma} \quad , \tag{2.16}$$

thus it is evident that for incompressible deformation states, where $\det(\mathbf{F})=1$, there is no numerical distinction between the Cauchy and Kirchhoff stress measures.

On the other hand, both 1st and 2nd Piola-Kirchhoff stress can be obtained from the stress vector and some mathematical manipulation. In the end, the expression for the 1st Piola-Kirchhoff stress tensor is given as function of the Kirchhoff stress (Cardoso, 2002):

$$\mathbf{P} = \mathbf{F}^{-\mathrm{T}} \cdot \boldsymbol{\tau} \quad , \tag{2.17}$$

and the 2nd Piola-Kirchhoff as function of the Cauchy stress,

$$\mathbf{S} = \det(\mathbf{F})\mathbf{F}^{-1} \cdot \boldsymbol{\sigma} \cdot \mathbf{F}^{\mathrm{T}} \quad . \tag{2.18}$$

In the scope of this work, where an updated Lagrangian solution procedure is used, particular attention must be given to the 2nd Piola-Kirchhoff stress. Given its complementarity's, the Green Lagrange strain tensor ($\mathbf{E}$) and the 2ndPiola-Kirchhoff stress tensor are conjugate measures[2].

Applying the polar decomposition theorem to equation (2.18) results in:

$$\mathbf{S} = \det(\mathbf{F})(\mathbf{R} \cdot \mathbf{U})^{-1} \cdot \boldsymbol{\sigma} \cdot \mathbf{R}^{\mathrm{T}} \cdot \mathbf{U}^{\mathrm{T}} \tag{2.19}$$

$$\boldsymbol{\sigma} = \det(\mathbf{F})^{-1}\mathbf{R} \cdot \mathbf{U} \cdot \mathbf{S} \cdot \mathbf{R}^{\mathrm{T}} \cdot \mathbf{U}^{\mathrm{T}} \quad . \tag{2.20}$$

Considering the case of small strains but arbitrary large displacements and rotations, an interesting and useful relation is obtained by considering that the stretch tensor $\mathbf{U} \approx \mathbf{I}_2$, the determinant of the deformation gradient det($\mathbf{F}$)=1 and, from the orthogonality property, $\mathbf{R}^{\mathrm{T}} \cdot \mathbf{R} = \mathbf{R} \cdot \mathbf{R}^{\mathrm{T}} = \mathbf{I}_2$:

$$\begin{aligned} \mathbf{S} &\approx \mathbf{R}^{\mathrm{T}} \cdot \boldsymbol{\sigma} \cdot \mathbf{R} \\ \boldsymbol{\sigma} &\approx \mathbf{R} \cdot \mathbf{S} \cdot \mathbf{R}^{\mathrm{T}} \end{aligned} \quad . \tag{2.21}$$

Hence, the second Piola-Kirchhoff can be viewed as the rotated Cauchy stress. In case of pure rotation, it remains unchanged relatively to the local corotational coordinate system. Thus, the second Piola-Kirchhoff stress tensor behaves as if it was frozen into the material coordinate system.

2.4 Strain and Stress Rates; Constitutive Update

Let us first consider the time derivative of the deformation gradient $\mathbf{F}$:

[2] In a Eulerian description the natural choice as work-conjugate measures are the Almansi strain and the Cauchy stress (Doghri, 2000).

$$\dot{\mathbf{F}} = \frac{\partial}{\partial t}\left(\frac{\partial^{n+1}\mathbf{x}}{\partial^{n}\mathbf{x}}\right) = \frac{\partial}{\partial^{n}\mathbf{x}}\underbrace{\left(\frac{\partial^{n+1}\mathbf{x}}{\partial t}\right)}_{=\mathbf{v}} = \frac{\partial \mathbf{v}}{\partial^{n}\mathbf{x}} = \frac{\partial \mathbf{v}}{\partial^{n+1}\mathbf{x}}\frac{\partial^{n+1}\mathbf{x}}{\partial^{n}\mathbf{x}} = \mathbf{L}\cdot\mathbf{F} \tag{2.22}$$

From the previous equation comes the definition of the velocity gradient tensor:

$$\mathbf{L} = \dot{\mathbf{F}}\cdot\mathbf{F}^{-1} \quad . \tag{2.23}$$

The polar decomposition theorem gives rise to the following relation:

$$\mathbf{L} = \dot{\mathbf{F}}\cdot\mathbf{F}^{-1} = \frac{d\mathbf{F}}{dt}\cdot\mathbf{F}^{-1} = \left(\mathbf{R}\frac{d\mathbf{U}}{dt} + \frac{d\mathbf{R}}{dt}\mathbf{U}\right)\cdot\mathbf{U}^{-1}\mathbf{R}^{-1} \tag{2.24}$$

$$\mathbf{L} = \underbrace{\frac{d\mathbf{R}}{dt}\mathbf{R}^{\mathrm{T}}}_{=\boldsymbol{\Omega}} + \mathbf{R}\frac{d\mathbf{U}}{dt}\mathbf{U}^{-1}\mathbf{R}^{\mathrm{T}} \quad , \tag{2.25}$$

where ($\boldsymbol{\Omega}$) is the rotation rate tensor which physically represents the rate of rigid-body rotation at a given material point. Its importance is related to the definition of the Green-Naghdi-McInnis objective stress rate of the Cauchy stress ($\boldsymbol{\sigma}$) in the form (Marsden and Hughes, 1994; Doghri, 2000):

$$\overset{\mathrm{G}}{\boldsymbol{\sigma}} = \dot{\boldsymbol{\sigma}} - \boldsymbol{\Omega}\boldsymbol{\sigma} + \boldsymbol{\sigma}\boldsymbol{\Omega} \quad . \tag{2.26}$$

The velocity gradient can be alternatively decomposed into symmetric and antisymmetric parts, defining the spatial rate of deformation tensor ($\mathbf{D}$) and the spin rate tensor ($\mathbf{W}$) respectively:

$$\begin{aligned} \mathbf{D} &= \frac{1}{2}(\mathbf{L} + \mathbf{L}^{\mathrm{T}}) = \frac{1}{2}\left(\frac{d\mathbf{U}}{dt}\mathbf{U}^{-1} + \mathbf{U}^{-1}\frac{d\mathbf{U}}{dt}\right) \\ \mathbf{W} &= \frac{1}{2}(\mathbf{L} - \mathbf{L}^{\mathrm{T}}) = \frac{1}{2}\left(\frac{d\mathbf{U}}{dt}\mathbf{U}^{-1} - \mathbf{U}^{-1}\frac{d\mathbf{U}}{dt}\right) \end{aligned} \quad . \tag{2.27}$$

The spin rate tensor ($\mathbf{W}$) represents the rate of deformation of the principal axes of the spatial rate of deformation ($\mathbf{D}$). This tensor is used in the definition of the Jaumann stress rate of the Cauchy stress tensor in the form (Marsden and Hughes, 1994; Doghri, 2000):

$$\overset{\mathrm{J}}{\boldsymbol{\sigma}} = \dot{\boldsymbol{\sigma}} - \mathbf{W}\boldsymbol{\sigma} + \boldsymbol{\sigma}\mathbf{W} \quad . \tag{2.28}$$

Compared to the objective stress rate of equation (2.26), the difference is on the definition of the spin rate tensor. However, if the rotation tensor coming from the polar decomposition of (**F**) is entirely used for the update of the local reference frame, the principal material lines of (**U**) are kept constant. As a consequence, the principal axes of (**D**) coincide to those of (**U**). At this point, the rate of deformation tensor and the spin rate tensor can be simplified like (Yoon et al., 1999a):

$$\begin{aligned} \mathbf{D} &= \mathbf{R}\frac{d\mathbf{U}}{dt}\mathbf{U}^{-1}\mathbf{R}^{\mathbf{T}} \\ \mathbf{W} &= \frac{d\mathbf{R}}{dt}\mathbf{R}^{-1} \end{aligned} \quad , \tag{2.29}$$

so that the Jaumann and the Green-Naghdi-McInnis stress rates turn to be formally the same ($\mathbf{W} = \mathbf{\Omega}$).

The symmetric part of the second term in the right-hand side of equation (2.25) points to the corotated deformation rate tensor (Doghri, 2000; Fontes Valente, 2004):

$$\hat{\mathbf{D}} = \frac{1}{2}(\dot{\mathbf{U}}\mathbf{U}^{-1} + \mathbf{U}^{-1}\dot{\mathbf{U}}) \quad , \tag{2.30}$$

which defines an instantaneous strain rate in the local (follower) reference frame. In equation (2.30), the superscript $\hat{\blacksquare}$ means materially embedded system rotated to reference configutation by **R**. Thus, the quantity is frame indifferent and objective. The same quantity can be defined by means of the orthogonal rotation tensor as

$$\hat{\mathbf{D}} = \mathbf{R}^{\mathrm{T}}\mathbf{D}\mathbf{R} \quad . \tag{2.31}$$

Once the spatial rate of deformation tensor is work-conjugated to the spatial Cauchy stress tensor, it is possible to define a rotation neutralized spatial stress tensor, related to the local co-rotational frame and expressed as:

$$\hat{\boldsymbol{\sigma}} = \mathbf{R}^{\mathrm{T}}\boldsymbol{\sigma}\mathbf{R} \, . \tag{2.32}$$

The now defined corotated Cauchy stress tensor serves as a basis to define a general equation for the constitutive update between (n) and (n + 1) configurations,

$$ {}^{n+1}\hat{\boldsymbol{\sigma}} = {}^{n}\hat{\boldsymbol{\sigma}} + \Delta t \frac{d\hat{\boldsymbol{\sigma}}}{dt} \quad . \tag{2.33} $$

Still retaining the hypothesis that elastic strains developed during deformation remain small when compared to its plastic counterparts (as is common in ductile metal plasticity), with elastic modulus orders of magnitude greater than the plastic yield stress value, it is possible to perform an additive decomposition of the velocity gradient like (Doghri, 2000; Fontes Valente, 2004):

$$ \mathbf{L} \approx \mathbf{L}^{e} + \mathbf{L}^{p} \quad , \tag{2.34} $$

and consequently,

$$ \mathbf{D} \approx \mathbf{D}^{e} + \mathbf{D}^{p} \tag{2.35} $$

$$ \hat{\mathbf{D}} \approx \hat{\mathbf{D}}^{e} + \hat{\mathbf{D}}^{p} \, , \tag{2.36} $$

where the superscripts (e) and (p) point to the elastic and plastic parts of deformation, respectively. Once this strain rate has an instantaneous definition, its computational treatment requires integration over the time step between configurations (n) and $(n+1)$. By doing so, the increment of rotated strain is calculated like (Yoon et al., 1999a;b):

$$ {}^{n+1}_{n}\hat{\mathbf{e}} = \int_{t_n}^{t_{n+1}} \hat{\mathbf{D}} \; dt \;\; \equiv {}^{n+\frac{1}{2}}_{n}\hat{\mathbf{D}} \; \Delta t \quad . \tag{2.37} $$

The use of the mid-point configuration $\left(n+\frac{1}{2}\right)$ to calculate strain increments is introduced in order to ensure an unconditionally stable and second-order accurate transition from the continuum to the discrete algorithm. According to Hughes (2000), the constitutive (discrete) analysis over point $\left(n+\frac{1}{2}\right)$ represents a second-order accurate approximation to the exact integration of the instantaneous rate of strain, between states (n) and $(n+1)$.

With a proper treatment of the incremental rotated strain, the constitutive update follows its usual framework, as an extension of linear cases:

$$ {}^{n+1}\hat{\boldsymbol{\sigma}} = {}^{n}\hat{\boldsymbol{\sigma}} + {}^{n+1}_{n}\hat{\boldsymbol{\sigma}} = {}^{n}\hat{\boldsymbol{\sigma}} + \hat{\mathbf{C}}_4 \left({}^{n+1}_{n}\hat{\mathbf{e}} - {}^{n+1}_{n}\hat{\mathbf{e}}^{p} \right) \quad , \tag{2.38} $$

with ($\mathbf{C}_4$) as the 4^{th} order general constitutive tensor. However, a more elegant update can be derived in view of the equivalence between the second Piola-Kirchhoff and the Cauchy stresses, equation (2.21). Therefore, the increment on the material stress tensor (${}^{n+1}_{n}\hat{\mathbf{S}}$) referred to the rotated local frame (and thus affected by the rigid-body rotation part of the deformation) can be directly summed up to the converged spatial-based Cauchy stress tensor (${}^{n}\hat{\boldsymbol{\sigma}}$), as used for small strain theories (Doghri, 2000),

$$ {}^{n+1}\hat{\boldsymbol{\sigma}} = {}^{n}\hat{\boldsymbol{\sigma}} + {}^{n+1}_{n}\hat{\mathbf{S}} = {}^{n}\hat{\boldsymbol{\sigma}} + \hat{\mathbf{C}}_4 \left({}^{n+1}_{n}\hat{\mathbf{E}} - {}^{n+1}_{n}\hat{\mathbf{E}}^{p} \right) \quad . \tag{2.39} $$

This approach is equivalent to the adoption of a hypoelastic constitutive model, representative of a Green-Naghdi objective stress rate, which will derive an additive constitutive update of the stress tensor also in the nonlinear material range.
Thus, on the scope of the Enhanced Assumed Strain method, the material Green-Lagrange strain tensor will be additively enhanced with incompatible (element-wise defined) strain terms, forming in conjunction with the stress tensor $\mathbf{S}$ the variational structure of the EAS element proposed in this work, as shown in the next section.

2.5 Nonlinear Implementation of the EAS Method

The key point of the Enhanced Assumed Strain method (Simo and Rifai, 1990) is the enrichment of the displacement-based (Green-Lagrange) strain field ($\mathbf{E}$) by means of the so-called enhancing strain field ($\mathbf{E}^{\alpha}$), generating the so-called enhanced strain field $\tilde{\mathbf{E}}$:

$$ \tilde{\mathbf{E}} = \mathbf{E} + \mathbf{E}^{\alpha} \tag{2.40} $$

$$ \delta\tilde{\mathbf{E}} = \delta\mathbf{E} + \delta\mathbf{E}^{\alpha} \quad . \tag{2.41} $$

The Veubeke-Hu-Washizu variational principle (Fraeijs de Veubeke, 1951) is the starting mark for the EAS method in its linear version as originally presented by

Simo and Rifai (1990). In the nonlinear version (Vu-Quoc and Tan, 2003), the displacement field ($\mathbf{u}$), the conjugated Green-Lagrange strain tensor ($\mathbf{E}$) and 2nd Piola-Kirchhoff stress tensor ($\mathbf{S}$) are treated as independent variables. Considering the volume (V) and control areas (Γ_σ) and (Γ_u), the functional takes the form:

$$\Pi^{\text{VHW}}\left(\mathbf{u},\tilde{\mathbf{E}},\mathbf{S}\right)=\int_V W\left(\tilde{\mathbf{E}}\right)dV+\int_V \mathbf{S}:\left[\frac{1}{2}\left(\mathbf{F}^{\text{T}}\mathbf{F}-\mathbf{I}_2\right)-\tilde{\mathbf{E}}\right]dV-\Pi^{\text{ext}} \tag{2.42}$$

$$\Pi^{\text{ext}}=\int_V \rho\breve{\mathbf{b}}\cdot\mathbf{u}dV+\int_{\Gamma_\sigma}\breve{\mathbf{t}}\cdot\mathbf{u}d\Gamma-\int_{\Gamma_u}\mathbf{t}\cdot\left(\breve{\mathbf{u}}-\mathbf{u}\right)d\Gamma \tag{2.43}$$

where W is the strain energy, $\mathbf{t}$ and $\mathbf{b}$ are traction and body forces and ρ is the density. The superscript ($\breve{\blacksquare}$) denotes prescribed values on boundaries Γ_σ and Γ_u. As stated in Fontes Valente et al. (2004) and Miehe and Apel (2004), this approach keeps the original advantage of the displacement-based Green-Lagrange strain tensor additive enhancement, even in case of nonlinearities. Also, it is computationally simpler than the multiplicative decomposition adopted by other authors (Simo and Armero, 1992), although leading to the same numerical results. It is important to note the imposition of the orthogonality condition between the stress field and the enhancing strain field ($\mathbf{E}^\alpha$):

$$\int_V \mathbf{S}:\mathbf{E}^\alpha\ dV=0\quad , \tag{2.44}$$

which reduces the number of independent variables in the original functional (2.42) to just two:

$$\Pi^{\text{VHW}}\left(\mathbf{u},\mathbf{E}^\alpha\right)=\int_V W\left(\mathbf{E}+\mathbf{E}^\alpha\right)dV+\cancelto{=0}{\int_V \mathbf{S}:\mathbf{E}^\alpha dV}-\Pi^{\text{ext}}\quad . \tag{2.45}$$

The weak form of the above modified (enhanced) functional is obtained from the Gateaux or directional derivative, leading to the total variation (Vu-Quoc and Tan, 2003),

$$\delta\Pi\left(\mathbf{u},\mathbf{E}^\alpha\right)=\delta\Pi^{\text{int}}-\delta\Pi^{\text{ext}} \tag{2.46}$$

$$\delta\Pi^{\text{int}} = \int_V (\delta\mathbf{E} + \delta\mathbf{E}^\alpha) : \frac{\delta W(\mathbf{E}+\mathbf{E}^\alpha)}{\delta(\mathbf{E}+\mathbf{E}^\alpha)} dV \tag{2.47}$$

$$\delta\Pi^{\text{ext}} = \int_V \rho\breve{\mathbf{b}}\cdot\delta\mathbf{u}dV + \int_{\Gamma_\sigma} \breve{\mathbf{t}}\cdot\delta\mathbf{u}d\Gamma \quad , \tag{2.48}$$

where boundary conditions for the displacement field are omitted without loss of generality. The weak form can now be expanded via a truncated Taylor series at the n^{th} state $\left(\mathbf{u}|_n, \mathbf{E}^\alpha\big|_n\right)$, as in Bischoff and Ramm (1997):

$$\delta\Pi\left(\mathbf{u}|_{n+1}, \mathbf{E}^\alpha\big|_{n+1}\right) \approx \delta\Pi\left(\mathbf{u}|_n, \mathbf{E}^\alpha\big|_n\right) + \mathfrak{D}[\delta\Pi]\left(\mathbf{u}|_n, \mathbf{E}^\alpha\big|_n\right)\cdot\left({}^{n+1}_{n}\mathbf{u}, {}^{n+1}_{n}\mathbf{E}^\alpha\right) . \tag{2.49}$$

The explicit form of the $\mathfrak{D}[\delta\Pi]$ operator will be described afterwards. The description of interpolation functions and variables for both displacement-based and enhanced strain fields for the solid-shell element will be carried out in detail in the next chapter. At this point, only necessary relations are given. Then, the displacement field of equation (2.2) can be interpolated at each finite element domain (with the corresponding variation and increment) in the form,

$$\mathbf{u} \approx \mathbf{u}^h = \mathbf{N}\cdot\mathbf{d} \tag{2.50}$$

$$\delta\mathbf{u} \approx \delta\mathbf{u}^h = \mathbf{N}\cdot\delta\mathbf{d} \tag{2.51}$$

$${}^{n+1}_{n}\mathbf{u} \approx {}^{n+1}_{n}\mathbf{u}^h = \mathbf{N}\cdot {}^{n+1}_{n}\mathbf{d} \quad , \tag{2.52}$$

where the superscript (h) stands for finite element approximations while matrix $(\mathbf{N})$ contains usual isoparametric compatible shape functions for a 3D element, relating the continuum displacement field $(\mathbf{u})$ and the corresponding vector of 24 translational degrees-of-freedom $(\mathbf{d})$ of an 8-node brick element.

The enhanced Green-Lagrange strain tensor can be interpolated all over the element's domain (as well as its variations) using the displacement vector $(\mathbf{d})$ and the enhancing parameters vector $(\boldsymbol{\alpha})$,

$$\tilde{\mathbf{E}} = \mathbf{E} + \mathbf{E}^\alpha = \begin{bmatrix}\mathbf{B}_u & \mathbf{B}_\alpha\end{bmatrix}\begin{bmatrix}\mathbf{d} \\ \boldsymbol{\alpha}\end{bmatrix}. \tag{2.53}$$

Both strain-displacement operators ($\mathbf{B}_u$ and $\mathbf{B}_\alpha$) will be further explicited. Within these FEM interpolation assumptions, the second member of the right-hand side of the linearized weak form (2.49) can be rewritten (dropping state indices) in the form (Bischoff and Ramm, 1997; Klinkel and Wagner, 1997; Klinkel et al., 1999 and Vu-Quoc and Tan, 2003):

$$\mathfrak{D}[\delta\Pi](\mathbf{d},\boldsymbol{\alpha})\cdot\left({}^{n+1}_{n}\mathbf{d},\,{}^{n+1}_{n}\boldsymbol{\alpha}\right)=\frac{\delta\left(\delta\Pi^{\text{int}}-\delta\Pi^{\text{ext}}\right)}{\delta\left(\mathbf{d},\boldsymbol{\alpha}\right)}\cdot\left({}^{n+1}_{n}\mathbf{d},\,{}^{n+1}_{n}\boldsymbol{\alpha}\right), \tag{2.54}$$

where the variations $\delta\Pi^{\text{int}}$ and $\delta\Pi^{\text{ext}}$ take the form:

$$\begin{aligned}\delta\Pi^{\text{int}}\left(\mathbf{d},\boldsymbol{\alpha}\right)&=\delta\mathbf{d}^{\text{T}}\int_{V}\left(\hat{\mathbf{B}}_u\right)^{\text{T}}\hat{\mathbf{S}}\,dV+\delta\boldsymbol{\alpha}^{\text{T}}\int_{V}\left(\hat{\mathbf{B}}_\alpha\right)^{\text{T}}\hat{\mathbf{S}}\,dV\\ \delta\Pi^{\text{ext}}\left(\mathbf{d}\right)&=\delta\mathbf{d}^{\text{T}}\int_{V}\mathbf{N}^{\text{T}}\rho\breve{\mathbf{b}}\,dV+\delta\mathbf{d}^{\text{T}}\int_{\Gamma_\sigma}\mathbf{N}^{\text{T}}\breve{\mathbf{t}}\;d\Gamma\end{aligned}\quad . \tag{2.55}$$

Attending to the variation of the internal part ($\delta\Pi^{\text{int}}$) of the whole potential, it is possible to state that:

$$\begin{aligned}&\mathfrak{D}\left[\delta\Pi^{\text{int}}\right]\cdot\left({}^{n+1}_{n}\mathbf{d},\,{}^{n+1}_{n}\boldsymbol{\alpha}\right)=\frac{\delta\left(\delta\Pi^{\text{int}}\right)}{\delta\mathbf{d}}\cdot\,{}^{n+1}_{n}\mathbf{d}+\frac{\delta\left(\delta\Pi^{\text{int}}\right)}{\delta\boldsymbol{\alpha}}\cdot\,{}^{n+1}_{n}\boldsymbol{\alpha}\\ &=\delta\mathbf{d}^{\text{T}}\left[\left(\hat{\mathbf{K}}^{uu}_{lg}+\hat{\mathbf{K}}^{uu}_{nlg}\right){}^{n+1}_{n}\mathbf{d}+\hat{\mathbf{K}}^{u\alpha}\left({}^{n+1}_{n}\boldsymbol{\alpha}\right)\right]+\delta\boldsymbol{\alpha}^{\text{T}}\left[\hat{\mathbf{K}}^{\alpha u}\left({}^{n+1}_{n}\mathbf{d}\right)+\hat{\mathbf{K}}^{\alpha\alpha}\left({}^{n+1}_{n}\boldsymbol{\alpha}\right)\right],\\ &(\forall\delta\mathbf{d},\delta\boldsymbol{\alpha}).\end{aligned} \tag{2.56}$$

Linear and nonlinear geometric (initial stress) stiffness matrices ($\mathbf{K}^{uu}_{lg}$ and $\mathbf{K}^{uu}_{nlg}$) are defined like in the fully displacement-based formulation (Hughes, 2000), with corresponding expressions discussed in Chapter 3. The main result of the inclusion of enhanced parameters into the variational formulation is the appearance of coupling stiffness matrices $\mathbf{K}^{\alpha u}$ and $\mathbf{K}^{u\alpha}$, as well as the enhanced stiffness operator $\mathbf{K}^{\alpha\alpha}$, all of them possessing the same structure as in the linear formulation of Simo and Rifai (1990).

In fact, the adopted additive approach (2.40) leads to a straightforward algorithmic extension from the linear case, with no inclusion of nonlinear geometric stiffness matrices associated with the enhanced variables, which happens in formulations based on the multiplicative enhancement of the deformation gradient, as in the works of Simo and Armero (1992) and Miehe (1998), among others. The final result

(Bischoff and Ramm, 1997; Klinkel and Wagner, 1997; Klinkel et al., 1999; Vu-Quoc and Tan, 2003) is an equivalent system of equations, on matrix form, presented as:

$$\begin{bmatrix} \hat{\mathbf{K}}^{uu}_{lg} + \hat{\mathbf{K}}^{uu}_{nlg} & \hat{\mathbf{K}}^{u\alpha} \\ \hat{\mathbf{K}}^{\alpha u} & \hat{\mathbf{K}}^{\alpha\alpha} \end{bmatrix} \begin{Bmatrix} {}^{n+1}_{n}\mathbf{d} \\ {}^{n+1}_{n}\boldsymbol{\alpha} \end{Bmatrix} = \underbrace{\begin{Bmatrix} \int_V \mathbf{N}^{\mathrm{T}} \rho \breve{\mathbf{b}} dV + \int_{\Gamma_\sigma} \mathbf{N}^{\mathrm{T}} \breve{\mathbf{t}} \; d\Gamma \\ 0 \end{Bmatrix}}_{\mathbf{f}^{ext}} - \underbrace{\begin{Bmatrix} \int_V \left(\hat{\mathbf{B}}_u\right)^{\mathrm{T}} \hat{\mathbf{S}} dV \\ \int_V \left(\hat{\mathbf{B}}_\alpha\right)^{\mathrm{T}} \hat{\mathbf{S}} dV \end{Bmatrix}}_{\mathbf{f}^{\mathrm{int}}}. \quad (2.57)$$

As a final remark, it is worth mentioning the absence of coupling between strain fields as shown in the equivalent expression (2.57). In the next chapter, a particular EAS formulation will be given with entire focus on a new eight node solid-shell finite element.

Chapter 3

Solid-Shell Finite Element Development

Accuracy and efficiency are the major features expected from numerical simulations using the finite element method. For three-dimensional analysis, the development of low-order eight-node finite elements to fulfill such objectives has been a continuous challenge. In the modeling of thin and thick walled applications, the well-known locking phenomena should be conveniently circumvented. In this chapter, the Enhanced Assumed Strain (EAS) method and a reduced integration scheme are combined to produce a new eight-node solid-shell element, accommodating the use of an arbitrary number of integration points along thickness direction. Furthermore, a physical stabilization procedure is employed in order to correct the element's rank deficiency. Several factors contribute to the high computational efficiency of the formulation, namely: i) the use of only one internal variable per element for the enhanced part of the strain field; ii) the reduced integration scheme; iii) the use of one element layer along thickness with multiple integration points,; iv) the evaluation of stabilization terms analytically instead of resorting to empirical parameters and numerical integration.

3.1 The Reduced Enhanced Solid-Shell element

In this chapter, a new concept of finite element, called as RESS (Reduced Enhanced Solid-Shell) element is presented. This solid-shell element is based on a one-point numerical quadrature scheme with eight physical nodes, but allowing for an arbitrary number of integration points through the thickness direction in a single element layer (Figure 3-1). This characteristic is distinctive within the class of solid-shell elements. In consequence, it avoids the use of several layers of elements in order to increase the number of thickness integration points in sheet metal forming problems. The capabilities of EAS and RI methods are combined together in order to eliminate locking problems. The computational efficiency is guaranteed

via the one-point quadrature integration scheme with just one enhancing parameter for the EAS method. The rank-deficiency caused by the in-plane reduced integration scheme demands an efficient and cost effective stabilization technique. In this work, the physical stabilization concept developed in the work of Cardoso et al. (2002) for one-point quadrature shell elements is extended for the RESS element, efficiently eliminating three-dimensional hourglass modes without resorting to empirical parameters.

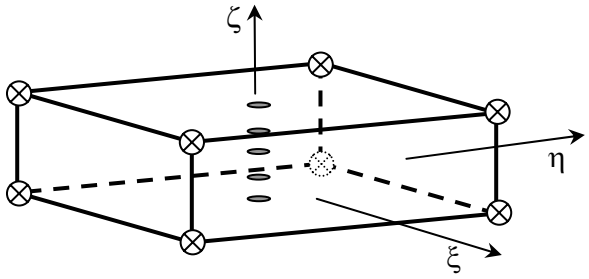

Figure 3-1: Solid-Shell element; integration scheme.

The main purpose of the RESS finite element is to simulate typical applications in sheet metal forming, including drawing, springback and hydroforming, which require multiple integration points through the thickness direction. It is well known that in these cases, shell elements have difficulties in deal with double-sided contact and conventional solid elements require several element layers to capture bending effects. Nevertheless, as presented in the numerical tests (Chapter 5), simulations are conducted by the RESS solid-shell element using *one element layer with multiple integration points through thickness*. To cover these kind of fully nonlinear problems, the adopted procedure (as shown in Chapter 2) is based on an additive split of the Green-Lagrange strain tensor for the enhanced strain part, which has proved to be as accurate as the deformation gradient multiplicative decomposition, although more simple and efficient as stated by Fontes Valente et al., (2004) or Miehe and Apel (2004). The physical stabilization procedure adopted corrects rank-deficiencies of the stiffness matrix and the internal force vector. Following Cardoso et al. (2002), the nonlinear hourglass forces are updated from the last converged configuration, being the incremental force vectors evaluated at the mid-configuration.

3.2 Kinematics

Consider the natural coordinates $\boldsymbol{\psi} = (\xi, \eta, \zeta)$ representing the isoparametric cubic domain $\square$ chosen in order that $\iiint_{\square} d\square = 8$. Without loss of generality, the reference configuration can be related to a converged state (n, the last increment), whereas the current configuration points to the unknown point (n+1), corresponding to the next increment. For the solid-shell topology treated in this work (Figure 3-1), a point in the reference configuration can be defined by the position vector ($\mathbf{x}$) as:

$$ {}^{n}\mathbf{x}(\boldsymbol{\psi}) = \frac{1}{2}(1+\zeta)\,{}^{n}\mathbf{x}_t(\xi,\eta) + \frac{1}{2}(1-\zeta)\,{}^{n}\mathbf{x}_b(\xi,\eta)\ , \tag{3.1} $$

where the subscripts (t) and (b) denote projections of the variable onto top ($\zeta = +1$) and bottom ($\zeta = -1$) surfaces, respectively. The corresponding position after incremental deformation (current configuration) can be defined by an analogous expression, referred to state (n+1).

The displacement field of a point in the converged state is obtained as usual by

$$ {}^{n+1}_{n}\mathbf{u}(\boldsymbol{\psi}) = {}^{n+1}\mathbf{x}(\boldsymbol{\psi}) - {}^{n}\mathbf{x}(\boldsymbol{\psi})\,, \tag{3.2} $$

being interpolated in each finite element's domain in the form,

$$ \mathbf{u} \approx \mathbf{u}^{h} = \mathbf{N}(\boldsymbol{\psi})\mathbf{d}\,. \tag{3.3} $$

The matrix ($\mathbf{N}$) contains the usual isoparametric compatible shape functions for a low order 3D element, relating the continuum displacement field ($\mathbf{u}$) and the corresponding vector of 24 translational degrees-of-freedom ($\mathbf{d}$) of the 8-node brick element,

$$ \mathbf{N}(\boldsymbol{\psi}) = \begin{bmatrix} N_i(\xi,\eta,\zeta) & 0 & 0 \\ 0 & N_i(\xi,\eta,\zeta) & 0 \\ 0 & 0 & N_i(\xi,\eta,\zeta) \end{bmatrix},\ i = 1, n_{\text{nodes}} \tag{3.4} $$

where

$$N_i(\xi,\eta,\zeta) = \frac{1}{8}(1+\xi_i\xi)(1+\eta_i\eta)(1+\zeta_i\zeta) \tag{3.5}$$

and

$$\begin{aligned}
\boldsymbol{\xi} &= \left\{-1\ 1\ 1\ -1\ -1\ 1\ 1\ -1\right\}^{\mathrm{T}} \\
\boldsymbol{\eta} &= \left\{-1\ -1\ 1\ 1\ -1\ -1\ 1\ 1\right\}^{\mathrm{T}} \\
\boldsymbol{\zeta} &= \left\{-1\ -1\ -1\ -1\ 1\ 1\ 1\ 1\right\}^{\mathrm{T}}
\end{aligned} \quad . \tag{3.6}$$

Recalling equation (3.1), it can be inferred a preferred thickness orientation of the finite element. Such starting point restricts this formulation to the class of problems usually solved by shell elements, although the number of nodes (8) and degrees-of-freedom (24) involved are still those coming from a three-dimensional continuous approach.

The convective frame is selected as the starting point for strain components and also for the enhancing strain field used in this element. Due to the non-orthogonal character of the convective frame, a local orthonormal frame $\mathbf{r} = (\mathbf{r}^1, \mathbf{r}^2, \mathbf{r}^3)$, is constructed at an element's center, being subsequently updated according to a deformation path. To do so, and after defined for the undeformed configuration (see Box 2-1), the local frame is subjected to the rigid-body rotation of the relative deformation gradient, evaluated between configurations (n) and (n+1) in the form:

$${}^{n+1}\mathbf{r} = {}^{n+1}_{n}\mathbf{R}\left({}^{n}\mathbf{r}\right) \ . \tag{3.7}$$

In this way, the local coordinate system for a given point is only affected by the rigid body component of the total deformation, characterizing this frame as a corotational one, with material strain (and stress) tensors being rotated as if they are frozen into the deformed continuum (Yoon, 1997; Yoon et al., 1999a;b; Belytschko, 2000). As discussed in the previous Chapter, the main advantage of the adoption of a corotational local frame is the simplified treatment of nonlinearities, either geometric or material, for solids subjected to finite rotations and displacements. A complete description of the constitutive behavior of a given body can be obtained resorting to stress and strain corotational tensors, continuously referred to the local frame and, consequently, following the deformation path from

the beginning. Doing so, in this work the rotated second Piola-Kirchhoff stress tensor and the rotated Green-Lagrange strain tensor are evaluated continuously at the rotated local reference system. This fact turns to be very useful, once the adopted Enhanced Assumed Strain procedure is entirely designed resorting to the material frame. Additionally, the use of material tensors grants objectivity within the formulation. A reference system rotating with the continuum body ensures objectivity requirements, for an observer situated at the body and affected by the rotation (but not the stretch) deformation part. To relate the convective frame and the local coordinate system, the orthonormal reference frame ($\mathbf{r}$) is used to obtain the matrix ($\mathbf{T}$):

$$\mathbf{T}(\boldsymbol{\psi}) = \left[\mathbf{r}^1 \;\; \mathbf{r}^2 \;\; \mathbf{r}^3\right]^{\mathrm{T}} (\mathbf{J})^{-1} \quad , \tag{3.8}$$

where ($\mathbf{J}$) is the conventional Jacobian matrix:

$$\mathbf{J} = \begin{Bmatrix} \mathbf{J}_1 \\ \mathbf{J}_2 \\ \mathbf{J}_3 \end{Bmatrix} = \begin{Bmatrix} \mathbf{x}_{,\xi} \\ \mathbf{x}_{,\eta} \\ \mathbf{x}_{,\zeta} \end{Bmatrix} \quad . \tag{3.9}$$

The convective frame and the local coordinate system can be related by the second order transformation tensor ${}^{l}_{c}\mathbf{T}$, by arranging the terms of matrix $\mathbf{T}$ in the following form (Bathe, 1996; Cardoso, 2002):

$${}^{l}_{c}\mathbf{T} = \begin{bmatrix} T_{11}T_{11} & T_{12}T_{12} & T_{13}T_{13} & T_{11}T_{12} & T_{11}T_{13} & T_{12}T_{13} \\ T_{21}T_{21} & T_{22}T_{22} & T_{23}T_{23} & T_{21}T_{22} & T_{21}T_{23} & T_{22}T_{23} \\ T_{31}T_{31} & T_{32}T_{32} & T_{33}T_{33} & T_{31}T_{32} & T_{31}T_{33} & T_{32}T_{33} \\ 2T_{11}T_{21} & 2T_{12}T_{22} & 2T_{13}T_{23} & (T_{11}T_{22})+(T_{12}T_{21}) & (T_{11}T_{23})+(T_{21}T_{13}) & (T_{12}T_{23})+(T_{22}T_{13}) \\ 2T_{11}T_{31} & 2T_{12}T_{32} & 2T_{13}T_{33} & (T_{11}T_{32})+(T_{12}T_{31}) & (T_{11}T_{33})+(T_{31}T_{13}) & (T_{12}T_{33})+(T_{32}T_{13}) \\ 2T_{21}T_{31} & 2T_{22}T_{32} & 2T_{23}T_{33} & (T_{21}T_{32})+(T_{22}T_{31}) & (T_{21}T_{33})+(T_{31}T_{23}) & (T_{22}T_{33})+(T_{32}T_{23}) \end{bmatrix}. \tag{3.10}$$

The strain field, like the strain-displacement operator, initially formulated in the convective frame, must be transformed onto the local (corotational) reference system. This can be achieved using the expression:

$${}^{n+1}_{n}\hat{\mathbf{E}} = {}^{l}_{c}\mathbf{T}\left({}^{n+1}_{n}\mathbf{E}\right) \quad . \tag{3.11}$$

3.2 Finite Element Equations for the EAS method

The kind of "Semi-reduced" integration scheme used in this formulation is not sufficient to overcome all pathologies related to locking phenomena. For this reason the EAS method is employed. As referred in Chapter 2, the Green-Lagrange strain and the second Piola-Kirchhoff stress tensor are chosen as work-conjugate measures in the updated Lagrangian approach:

$$ {}^{n+1}_{n}\mathbf{E} = \frac{1}{2}\left({}^{n+1}_{n}\mathbf{F}^{\mathrm{T}}\, {}^{n+1}_{n}\mathbf{F} - \mathbf{I}_2 \right) \tag{3.12} $$

$$ \mathbf{S} = S^{ab}\, {}^{n}\mathbf{g}_a \otimes {}^{n}\mathbf{g}_b \quad , \tag{3.13} $$

being its components posed in vector form as:

$$ \mathbf{E} = \left\{ E_{\xi\xi} \;\; E_{\eta\eta} \;\; E_{\zeta\zeta} \;\; E_{\xi\eta} \;\; E_{\xi\zeta} \;\; E_{\eta\zeta} \right\}^{\mathrm{T}} \tag{3.14} $$

$$ \mathbf{S} = \left\{ S_{\xi\xi} \;\; S_{\eta\eta} \;\; S_{\zeta\zeta} \;\; S_{\xi\eta} \;\; S_{\xi\zeta} \;\; S_{\eta\zeta} \right\}^{\mathrm{T}} \quad , \tag{3.15} $$

or in a 3×3 symmetric array form in case of stress as:

$$ \mathbf{S}_3 = \begin{bmatrix} S_{\xi\xi} & S_{\xi\eta} & S_{\xi\zeta} \\ S_{\xi\eta} & S_{\eta\eta} & S_{\eta\zeta} \\ S_{\xi\zeta} & S_{\eta\zeta} & S_{\zeta\zeta} \end{bmatrix} . \tag{3.16} $$

Now it is time to recall the key equation of the EAS method, that is, the enrichment of the displacement-based strain field ($\mathbf{E}$) by means of the so-called enhancing strain field ($\mathbf{E}^{\alpha}$), generating the enhanced strain field $\tilde{\mathbf{E}}$:

$$ \tilde{\mathbf{E}} = \mathbf{E} + \mathbf{E}^{\alpha} = \begin{bmatrix} \mathbf{B}_u & \mathbf{B}_{\alpha} \end{bmatrix} \begin{bmatrix} \mathbf{d} \\ \boldsymbol{\alpha} \end{bmatrix} . \tag{3.17} $$

The enhanced Green-Lagrange strain tensor can be interpolated all over the element's domain using the vector of nodal displacements ($\mathbf{d}$) and the vector of enhancing parameters ($\boldsymbol{\alpha}$). The matrix $\mathbf{B}_u$ is the standard [6×24] strain-

displacement operator, well-defined in the literature (see remark 1) and $\mathbf{B}_\alpha$ plays a similar role for the enhancing counterpart $\mathbf{E}^\alpha$. *A proper definition of* $\mathbf{B}_\alpha$ *dictates the ability of the formulation to alleviate locking phenomena.* For the sake of convenience, $\mathbf{B}_\alpha$ is normally defined in the convective frame, being transformed to the local cartesian frame as,

$$\hat{\mathbf{B}}_\alpha = {}^{l}_{c}\mathbf{T}_0 \mathbf{B}_\alpha \quad , \tag{3.18}$$

where ${}^{l}_{c}\mathbf{T}_0$ is the second order transformation tensor, equation (3.10), evaluated at the coordinates $(\xi = \eta = \zeta = 0)$. It is also worth mentioning that equation (3.18) appear as a simplification of the original expression proposed by Simo and Armero (1992),

$$\hat{\mathbf{B}}_\alpha = \underbrace{\frac{\det({}^{l}_{c}\mathbf{T}_0)}{\det({}^{l}_{c}\mathbf{T}_{\boldsymbol{\psi}})}}_{\approx 1} {}^{l}_{c}\mathbf{T}_0 \mathbf{B}_\alpha \quad , \tag{3.19}$$

which is only valid when modeling thin-walled geometries. Even with this simplification, the Taylor condition for arbitrary configurations is still fulfilled (Taylor et al., 1976).

Remark 1:

The definition of the classical strain-displacement matrix $\mathbf{B}_u$ can be found easily in the literature as:

$$\hat{\mathbf{B}}_u = \begin{bmatrix} N_{i,x} & 0 & 0 \\ & N_{i,y} & 0 \\ 0 & 0 & N_{i,z} \\ N_{i,y} & N_{i,x} & 0 \\ N_{i,z} & 0 & N_{i,x} \\ \underbrace{0 \quad N_{i,z} \quad N_{i,y}}_{\text{node } i} \end{bmatrix} . \tag{3.20}$$

Due to the in-plane integration scheme used for RESS element, the terms of matrix $\mathbf{B}_u$ depending on (ξ) and (η) are zero. For implementation convenience, $\mathbf{B}_u$ can

be calculated using the decomposition into constant (c) and zeta (ζ) dependent terms, i.e.,

$$\mathbf{B}_u = \mathbf{B}_u^c + \zeta \mathbf{B}_u^\zeta \,, \tag{3.21}$$

with $\mathbf{B}_u^c$ and $\mathbf{B}_u^\zeta$ detailed in Appendix. This simplified expression for $\mathbf{B}_u$ can also be used for a simpler evaluation of the stiffness and internal force vector associated with the displacement field.

Recalling Chapter 2, the adopted additive approach, equation (3.17), leads to a straightforward algorithmic extension from the linear case, with no inclusion of coupling nonlinear geometric stiffness matrices associated with the enhanced variables, generating the final system of equations,

$$\begin{bmatrix} \hat{\mathbf{K}}_{lg}^{uu} + \hat{\mathbf{K}}_{nlg}^{uu} & \hat{\mathbf{K}}^{u\alpha} \\ \hat{\mathbf{K}}^{\alpha u} & \hat{\mathbf{K}}^{\alpha\alpha} \end{bmatrix} \begin{Bmatrix} {}^{n+1}_{n}\mathbf{d} \\ {}^{n+1}_{n}\boldsymbol{\alpha} \end{Bmatrix} = \begin{Bmatrix} \mathbf{f}_u^{\text{ext}} \\ 0 \end{Bmatrix} - \begin{Bmatrix} \mathbf{f}_u^{\text{int}} \\ \mathbf{f}_\alpha^{\text{int}} \end{Bmatrix} \tag{3.22}$$

omitting some incremental indices for notation's convenience. The linear stiffness matrix ($\mathbf{K}_{lg}^{uu}$) is defined like in the fully displacement-based formulation as function of ($\mathbf{B}_u$). Coupling stiffness matrices ($\mathbf{K}^{\alpha u}$) and ($\mathbf{K}^{u\alpha}$) and the enhanced stiffness operator ($\mathbf{K}^{\alpha\alpha}$), possesses the same structure as in the linear formulation of Simo and Rifai (1990). However, three of the referred terms can be calculated more efficiently according to Remark 1.

$$\hat{\mathbf{K}}_{lg}^{uu} = \int_{V_e} \left(\hat{\mathbf{B}}_u\right)^{\mathrm{T}} \mathbf{C}^e \hat{\mathbf{B}}_u dV_e \tag{3.23}$$

$$\hat{\mathbf{K}}^{u\alpha} = \int_{V_e} \left(\hat{\mathbf{B}}_u\right)^{\mathrm{T}} \mathbf{C}^e \hat{\mathbf{B}}_\alpha dV_e \tag{3.24}$$

$$\hat{\mathbf{K}}^{\alpha u} = \int_{V_e} \left(\hat{\mathbf{B}}_\alpha\right)^{\mathrm{T}} \mathbf{C}^e \hat{\mathbf{B}}_u dV_e \tag{3.25}$$

$$\hat{\mathbf{K}}^{\alpha\alpha} = \int_{V_e} \left(\hat{\mathbf{B}}_\alpha\right)^{\mathrm{T}} \mathbf{C}^e \hat{\mathbf{B}}_\alpha dV_e \,, \tag{3.26}$$

where $\mathbf{C}^e$ stands for the second order elastic constitutive tensor:

$$\mathbf{C}^e = \frac{\mathrm{E}(1-\nu)}{(1+\nu)(1-2\nu)} \begin{bmatrix} 1 & \frac{\nu}{1-\nu} & \frac{\nu}{1-\nu} & 0 & 0 & 0 \\ \frac{\nu}{1-\nu} & 1 & \frac{\nu}{1-\nu} & 0 & 0 & 0 \\ \frac{\nu}{1-\nu} & \frac{\nu}{1-\nu} & 1 & 0 & 0 & 0 \\ 0 & 0 & 0 & \frac{1-2\nu}{2(1-\nu)} & 0 & 0 \\ 0 & 0 & 0 & 0 & \frac{1-2\nu}{2(1-\nu)} & 0 \\ 0 & 0 & 0 & 0 & 0 & \frac{1-2\nu}{2(1-\nu)} \end{bmatrix} . \tag{3.27}$$

The initial stress stiffness matrix $\hat{\mathbf{K}}^{uu}_{nlg}$ is defined in this very simple form (Fontes Valente, 2004):

$$\hat{\mathbf{K}}^{uu}_{nlg} = \int_{V_e} \left(\hat{\mathbf{B}}^{nlg}_u\right)^{\mathrm{T}} \hat{\mathbf{S}}_9 dV_e \ . \tag{3.28}$$

The strain-displacement operator $\mathbf{B}^{nlg}_u$ is described in the local frame as:

$$\hat{\mathbf{B}}^{nlg}_u = \begin{bmatrix} N_{\mathbf{r}^1} & 0 & 0 \\ N_{\mathbf{r}^2} & 0 & 0 \\ N_{\mathbf{r}^3} & 0 & 0 \\ 0 & N_{\mathbf{r}^1} & 0 \\ 0 & N_{\mathbf{r}^2} & 0 \\ 0 & N_{\mathbf{r}^3} & 0 \\ 0 & 0 & N_{\mathbf{r}^1} \\ 0 & 0 & N_{\mathbf{r}^2} \\ \underbrace{0 \quad 0 \quad N_{\mathbf{r}^3}}_{\text{node } k} \end{bmatrix} \text{, with } N_{\mathbf{r}^j} = \frac{\partial N}{\partial \psi_i} \frac{\partial \psi_i}{\partial \mathbf{r}^j} \ \text{(sum on } i\text{)} \tag{3.29}$$

for k=1,8. The 9×9 array $(\hat{\mathbf{S}}_9)$ is composed by sub-blocks of the stress tensor written in 3×3 array form and evaluated at each Gauss point,

$$\hat{\mathbf{S}}_9 = \begin{bmatrix} \hat{\mathbf{S}}_3 & \mathbf{0} & \mathbf{0} \\ \mathbf{0} & \hat{\mathbf{S}}_3 & \mathbf{0} \\ \mathbf{0} & \mathbf{0} & \hat{\mathbf{S}}_3 \end{bmatrix} \quad . \tag{3.30}$$

External and internal force vectors are calculated like:

$$\begin{aligned} \mathbf{f}_u^{ext} &= \int_{\Gamma_\sigma} \mathbf{N}^{\mathrm{T}} \breve{\mathbf{t}} \; d\Gamma + \int_{\Omega} \mathbf{N}^{\mathrm{T}} \rho \breve{\mathbf{b}} d\Omega \\ \mathbf{f}_u^{int} &= \int_{\Omega} \left(\hat{\mathbf{B}}_u \right)^{\mathrm{T}} \hat{\mathbf{S}} d\Omega \\ \mathbf{f}_\alpha^{int} &= \int_{\Omega} \left(\hat{\mathbf{B}}_\alpha \right)^{\mathrm{T}} \hat{\mathbf{S}} d\Omega \end{aligned} \quad . \tag{3.31}$$

From the discontinuity between finite element boundaries in the enhancing strain field, it is possible, like in the linear case, to condense out (${}^{n+1}_{n}\boldsymbol{\alpha}$) in (3.22) leading to a simpler expression for the stiffness calculation:

$$\left[\hat{\mathbf{K}}_{lg}^{uu} + \hat{\mathbf{K}}_{nlg}^{uu} - \hat{\mathbf{K}}^{u\alpha} \left(\hat{\mathbf{K}}^{\alpha\alpha} \right)^{-1} \hat{\mathbf{K}}^{\alpha u} \right] {}^{n+1}_{n}\mathbf{d} = \mathbf{f}_u^{ext} - \mathbf{f}_u^{int} + \hat{\mathbf{K}}^{u\alpha} \left(\hat{\mathbf{K}}^{\alpha\alpha} \right)^{-1} \mathbf{f}_\alpha^{int} \tag{3.32}$$

$$\hat{\mathbf{K}}^{u+\alpha} \left({}^{n+1}_{n}\mathbf{d} \right) = \mathbf{f}^{u+\alpha} \, . \tag{3.33}$$

Backing into the constitutive side of implementation, the calculation of the trial (supposed elastic) stress increment is performed at the intermediate configuration $\left(n + \frac{1}{2} \right)$ between the last (n) and the current configuration (n+1), at a given iteration (Box 3-1). To do so, the total incremental-iterative displacement and internal variables field (accumulated from the converged state) are considered.

1. ${}^{n+1}_{n}\boldsymbol{\alpha} = -\left(\hat{\mathbf{K}}^{\alpha\alpha} \right)^{-1} \hat{\mathbf{K}}^{\alpha u} \, {}^{n+1}_{n}\mathbf{d}$
2. ${}^{n+1}_{n}\hat{\tilde{\mathbf{E}}} = {}^{n+\frac{1}{2}}\hat{\mathbf{B}}_u \, {}^{n+1}_{n}\mathbf{d} + {}^{n+\frac{1}{2}}\hat{\mathbf{B}}_\alpha \, {}^{n+1}_{n}\boldsymbol{\alpha}$
3. ${}^{n+1}_{n}\boldsymbol{\sigma} = \hat{\mathbf{C}} \, {}^{n+1}_{n}\hat{\tilde{\mathbf{E}}}$
4. ${}^{n+1}\boldsymbol{\sigma} = {}^{n}\boldsymbol{\sigma} + {}^{n+1}_{n}\boldsymbol{\sigma}$

Box 3-1: Computation of trial elastic stress.

Finally, a multi-stage return mapping procedure is employed (Yoon, 1997; Yoon et al. 1999a;b) to determine numerically current stress states, respecting an anisotropic yield criterion, in a subject to be discussed in Chapter 4.

3.3 Locking Treatment

The class of low order finite elements is highly prone to the occurrence of locking phenomena (Hughes, 2000). Overestimation of the stiffness matrix, due to occurrence of locking, is a major source of poor results for this class of elements. Hauptmann et al. (2001) categorized several types of locking for solid-shell type elements. In case of sheet metal forming simulations involving plasticity and thin-walled geometries, distinct cases of locking can be expected and should be avoided, namely:

- Volumetric locking, appearing due to incompressible-type deformation in plasticity;
- Transverse shear locking, occurring as the thickness to length ratio tends to zero under bending;
- Thickness locking, related to an inefficient reproduction of the strain field along thickness direction.

In sections 3.3.1 and 3.3.2, it will be justified how the EAS method (by choosing a convenient $\mathbf{B}_{\alpha}$ operator) and the in-plane reduced numerical integration can work together in order to efficiently eliminate the several locking phenomena.

3.3.1 Subspace Analysis applied to Volumetric Locking

The framework of subspace analysis, successfully applied in 2D plane strain (César de Sá and Natal Jorge, 1999), shell (César de Sá et al., 2002) and solid elements (Alves de Sousa et al., 2003b) to eliminate volumetric and transverse shear locking problems, is described to determine the necessary conditions (or the necessary

subspace generated) such that any solid-shell element must fulfill to be free from volumetric locking pathologies.

Mathematically, the incompressibility problem can be formulated as a constrained minimization of a functional (César de Sá and Natal Jorge, 1999). In simple terms, the goal is to obtain, in the linear space of admissible solutions, denoted as (U), a displacement field ($\mathbf{u}$), that minimizes the total energy of the system, located in the subspace of the incompressible deformations, denoted as (I) and contained in the space of all the solutions ($I \subset U$). This statement can be posed by a simple condition:

$$I = \left\{ \mathbf{u} \in U : \ \mathrm{div}(\mathbf{u}) = 0 \right\} \ . \tag{3.34}$$

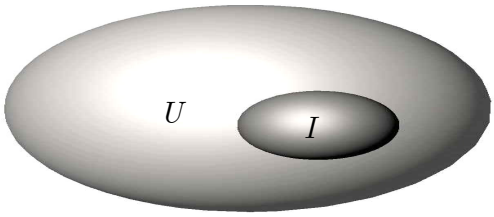

Figure 3-2: Linear space of admissible solutions (U) and subspace of the incompressible deformations (I).

In a general approach done with the FEM, the linear space of admissible solutions U, and the respective subspace I, previously defined, are approximated by U^h and I^h, respectively. In linear elasticity, a two field finite element solution can be expressed (César de Sá and Natal Jorge, 1999) by:

$$\begin{bmatrix} \mathbf{K} & \mathbf{Q} \\ -\mathbf{Q} & \mathbf{0} \end{bmatrix} \begin{bmatrix} \mathbf{u}^h \\ \mathbf{p}^h \end{bmatrix} = \begin{bmatrix} \mathbf{f}^{ext} \\ \mathbf{0} \end{bmatrix} \ , \tag{3.35}$$

where $\mathbf{p}$ is the hydrostatic pressure and $\mathbf{K}$ is the stiffness matrix. The incompressibility condition is then given by the second group of equations defined in (3.35) i.e.,

$$\mathbf{Q}\mathbf{u}^h = \mathbf{0} \ , \tag{3.36}$$

which will define the subspace of the incompressible deformations I^h as:

$$I^h = \left\{ \mathbf{u}^h \in U^h : \ \mathbf{Q}\mathbf{u}^h = \mathbf{0} \right\} \quad . \tag{3.37}$$

In order to avoid the trivial solution ($\mathbf{u}^h = \mathbf{0}$) in equation (3.36), the field of displacements $\mathbf{u}^h$ should belong to the null space of $\mathbf{Q}$, that is, to the subspace of incompressible deformations I^h. By doing so, any displacement $\mathbf{u}^h$ is contained in I^h being therefore, a linear combination of a given basis of I^h elements.

On the other hand, being (I^h) an approach to the original subspace (I), it is plausible to admit that it can not reproduce all possible solutions contained in (I). In fact, different finite element formulations lead to better or worse approximations of the (I) subspace. The volumetric locking phenomenon occurs when for a certain set of boundary conditions and external forces applied under a nearly incompressible deformation, the expected solution or some of its components do not appear properly represented in the approximated subspace (I^h).

To properly characterize I^h, let us consider a standard isoparametric eight-node hexahedral element with domain ($V_e = [-1,1]\times[-1,1]\times[-1,1]$). For small deformations, the incompressibility constraint ($e_{ii} = 0$) take the form:

$$\int_{V_e} \operatorname{div}(\mathbf{u}) \ dV_e = \int_{V_e} \left(\frac{\partial u}{\partial \xi} + \frac{\partial v}{\partial \eta} + \frac{\partial w}{\partial \zeta} \right) \ dV_e = 0 \quad . \tag{3.38}$$

One way to guarantee the incompressibility condition is to assure that the integrand function in (3.38) is zero. Substituting (3.3) in (3.38) results in

$$\frac{\partial u}{\partial \xi} + \frac{\partial v}{\partial \eta} + \frac{\partial w}{\partial \zeta} \ = \ \left[N_{i,\xi} \ \ N_{i,\eta} \ \ N_{i,\zeta} \right] \{\mathbf{d}\} = 0 \, , \tag{3.39}$$

for $i = 1, n^e_{nodes}$.

With the above definition, two opposite cases can be analyzed. The classical eight node hexahedral element, integrated using a complete quadrature rule (2×2×2, 8 Gauss points) highly sensitive to the locking phenomenon. In opposition, the pure reduced hexahedral element containing just one integration point at the element's

center $(\xi = \eta = \zeta = 0)$. The pure reduced integration is known to eliminate completely the volumetric locking phenomenon for eight node solid elements.

Making use of a complete integration, the application of equation (3.39) leads to,

$$\left[\begin{array}{cccccccccccccccccccccccc}
-a & -a & -a & a & -c & -c & c & c & -b & -c & a & -c & -c & -c & a & c & -b & c & b & b & b & -b & c & c \\
-a & -c & -c & a & -a & -a & c & a & -c & -c & c & -b & -c & -b & c & c & -c & a & b & c & c & -b & b & b \\
-c & -c & -b & c & -a & -c & a & a & -a & -a & c & -c & -b & -b & b & b & -c & c & c & c & a & -c & b & c \\
-c & -a & -c & c & -c & -b & a & c & -c & -a & a & -a & -b & -c & c & b & -b & b & c & b & c & -c & c & a \\
-c & -c & -a & c & -b & -c & b & b & -b & -b & c & -c & -a & -a & a & a & -c & c & c & c & b & -c & a & c \\
-c & -b & -c & c & -c & -a & b & c & -c & -b & b & -b & -a & -c & c & a & -a & a & c & a & c & -c & c & b \\
-b & -b & -b & b & -c & -c & c & c & -a & -c & b & -c & -c & -c & b & c & -a & c & a & a & a & -a & c & c \\
-b & -c & -c & b & -b & -b & c & b & -c & -c & c & -a & -c & -a & c & c & -c & b & a & c & c & -a & a & a
\end{array}\right] \{\mathbf{d}\} = \{0\} \tag{3.40}$$

where the results for each Gauss point are grouped by rows and

$$a = \frac{1}{8}(1+f)(1+f)\ ,\ b = \frac{1}{8}(1-f)(1-f)\ ,\ c = \frac{1}{8}(1+f)(1-f)\ \text{ and }\ f = \frac{\sqrt{3}}{3}\,. \tag{3.41}$$

The matrix $(\mathbf{Q})$ contained in equation (3.40) is rank 7. Being 24 the total number of degrees of freedom, i.e., the dimension of the subspace of admissible solutions (U^h), there will be a dimension 24-7=17 for the incompressible deformations subspace (I^h).

$$\text{rank}(\mathbf{Q})=7\ \wedge\ \text{nullity}(\mathbf{Q})=17 \tag{3.42}$$

For the pure reduced numerical integration scheme using only one Gauss point, the imposition of the condition (3.39) will lead to a subspace I^h of dimension 23, when the maximum dimension of the space U^h is 24. The matrix in (3.40) is rewritten as follows,

$$\frac{1}{8}\left[-1\ -1\ -1\ \ 1\ \ -1\ -1\ \ 1\ \ \ 1\ \ -1\ -1\ \ 1\ \ -1\ -1\ -1\ \ 1\ \ \ 1\ \ -1\ \ 1\ \ \ 1\ \ \ 1\ \ -1\ \ 1\ \ \ 1\right]\{\mathbf{d}\} = \{0\} \tag{3.43}$$

and

$$\text{rank}(\mathbf{Q})=1\ \wedge\ \text{nullity}(\mathbf{Q})=23\ . \tag{3.44}$$

Analyzing these two possible bases for the subspace of the incompressible deformations, it can be clearly inferred that the use of reduced integration allows

for the reproduction of six more incompressible displacement modes than the case of full integration. Since admissible incompressible solutions are a linear combination of a given (I^h) basis, there is now a reasonable explanation for the good performance of reduced integration techniques in volumetric locking problems, and why classical full numerical integration clearly locks.

For an unequivocal illustration of the last statements, it is shown in Figure 3-3 a graphical representation of the linearly independent elements which form the basis of the incompressible deformation subspace. Associated displacement fields are summarized in Table 3-1. Six rigid body motions can be obtained by linearly combining these elements. Modes 1 to 17 are reproduced both by complete and reduced integrations. Modes 18 to 23 are reproduced only by the reduced integration, being volumetric locking for the full integration. They can be divided into 3 main groups:

- Simple edges translations, in x, y and z directions, herein represented by modes 1 to 12;
- Expansion/Contraction of one element's face, modes 13 to 17;
- Hourglass modes, 18 to 20;
- Warping modes, 21 to 23.

1.º

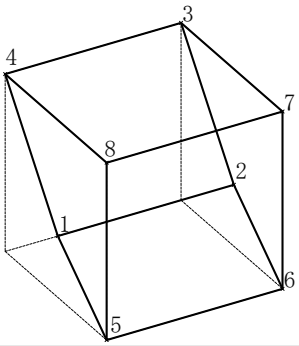

2.º

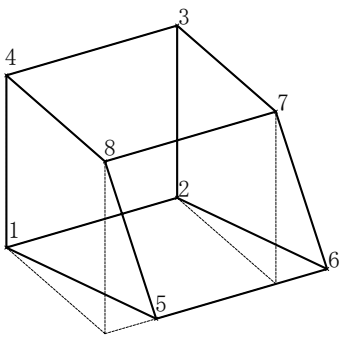

3.º

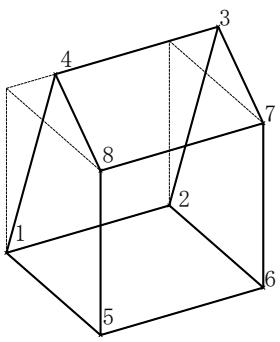

4.º

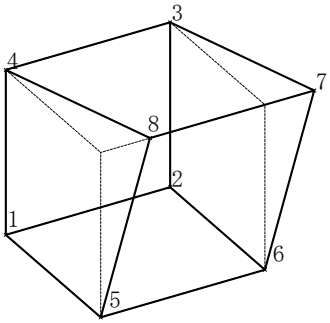

5.º

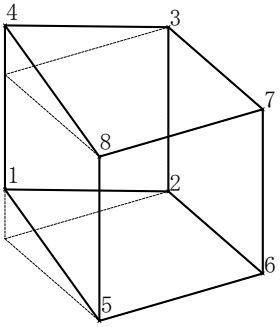

6.º

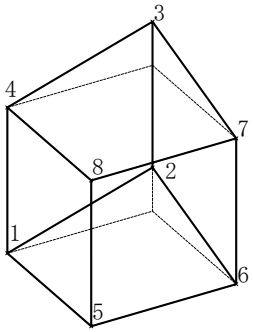

7.º

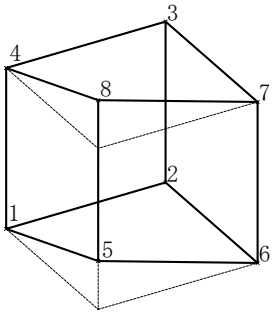

8.º

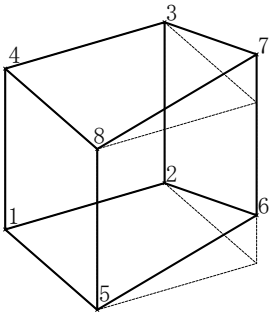

9.º

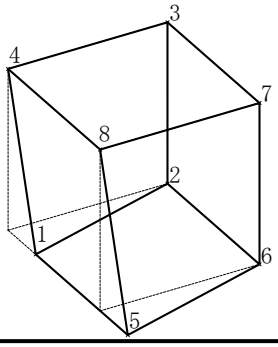

10.º

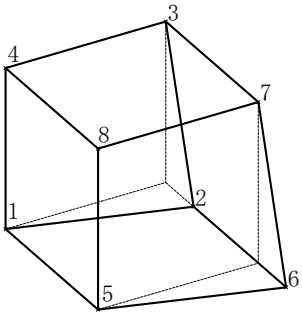

11.º

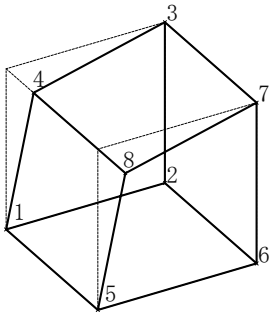

12.º

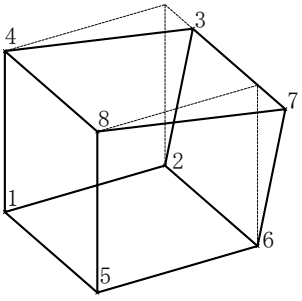

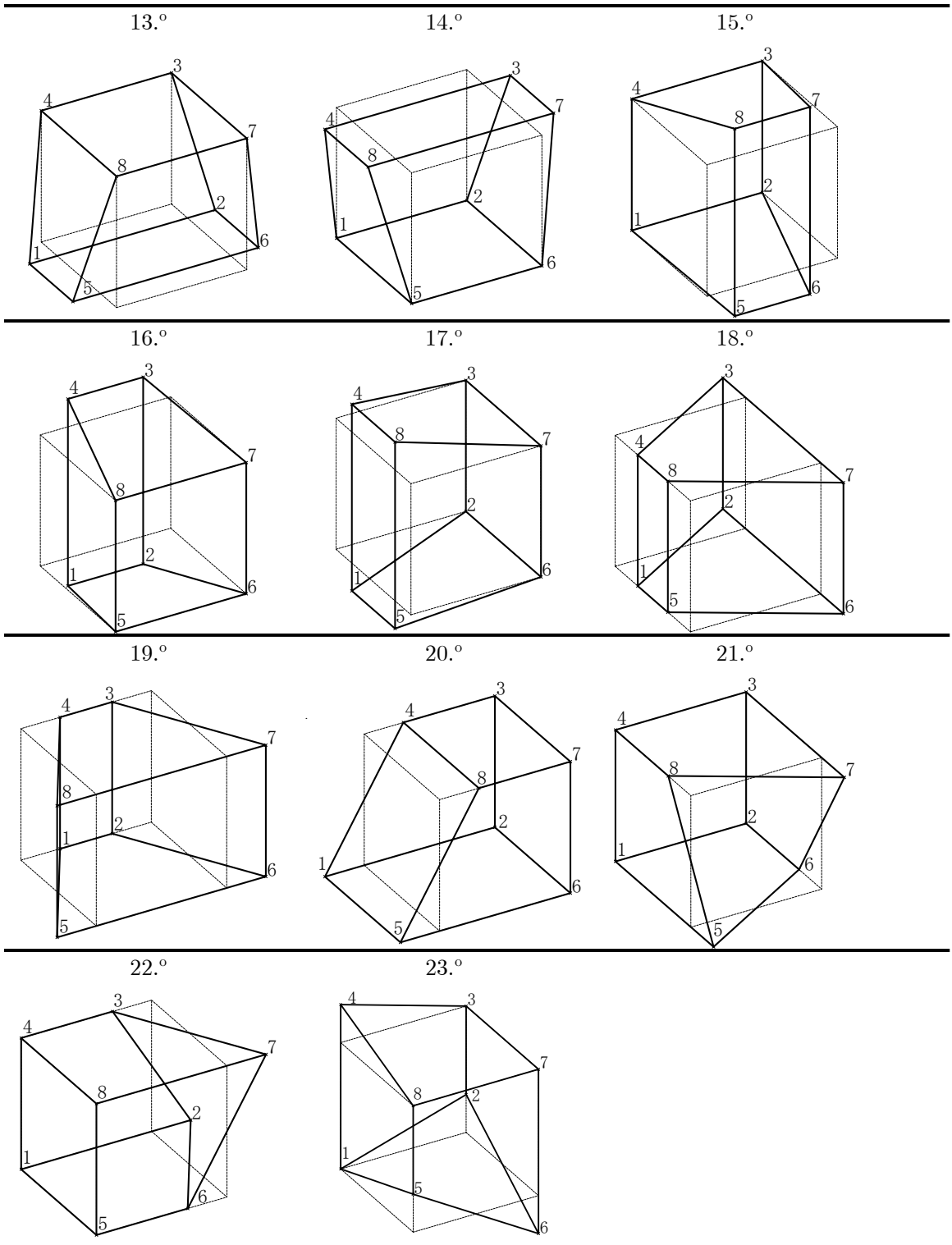

Figure 3-3: Deformation modes defining the basis of the incompressible deformations subspace.

$\mathbf{d}=$	{	u_1	v_1	w_1	u_2	v_2	w_2	u_3	v_3	w_3	u_4	v_4	w_4	u_5	v_5	w_5	u_6	v_6	w_6	u_7	v_7	w_7	u_8	v_8	w_8	}^{T}
$\mathbf{d}_1=$	{	1	0	0	1	0	0	0	0	0	0	0	0	0	0	0	0	0	0	0	0	0	0	0	0	}^{T}
$\mathbf{d}_2=$	{	0	0	0	0	0	0	0	0	0	0	0	0	1	0	0	1	0	0	0	0	0	0	0	0	}^{T}
$\mathbf{d}_3=$	{	0	0	0	0	0	0	1	0	0	1	0	0	0	0	0	0	0	0	0	0	0	0	0	0	}^{T}
$\mathbf{d}_4=$	{	0	0	0	0	0	0	0	0	0	0	0	0	0	0	0	0	0	0	1	0	0	1	0	0	}^{T}
$\mathbf{d}_5=$	{	0	1	0	0	0	0	0	0	0	0	1	0	0	0	0	0	0	0	0	0	0	0	0	0	}^{T}
$\mathbf{d}_6=$	{	0	0	0	0	1	0	0	1	0	0	0	0	0	0	0	0	0	0	0	0	0	0	0	0	}^{T}
$\mathbf{d}_7=$	{	0	0	0	0	0	0	0	0	0	0	0	0	0	1	0	0	0	0	0	0	0	0	1	0	}^{T}
$\mathbf{d}_8=$	{	0	0	0	0	0	0	0	0	0	0	0	0	0	0	0	0	1	0	0	1	0	0	0	0	}^{T}
$\mathbf{d}_9=$	{	0	0	1	0	0	0	0	0	0	0	0	0	0	0	1	0	0	0	0	0	0	0	0	0	}^{T}
$\mathbf{d}_{10}=$	{	0	0	0	0	0	1	0	0	0	0	0	0	0	0	0	0	0	1	0	0	0	0	0	0	}^{T}
$\mathbf{d}_{11}=$	{	0	0	0	0	0	0	0	0	0	0	0	1	0	0	0	0	0	0	0	0	0	0	0	1	}^{T}
$\mathbf{d}_{12}=$	{	0	0	0	0	0	0	0	0	1	0	0	0	0	0	0	0	0	0	0	1	0	0	0	0	}^{T}
$\mathbf{d}_{13}=$	{	-1	0	1	1	0	1	0	0	0	0	0	0	-1	0	-1	1	0	-1	0	0	0	0	0	0	}^{T}
$\mathbf{d}_{14}=$	{	0	0	0	0	0	0	1	0	1	-1	0	1	0	0	0	0	0	0	1	0	-1	-1	0	-1	}^{T}
$\mathbf{d}_{15}=$	{	0	0	0	0	0	0	0	0	0	0	0	0	1	-1	0	-1	-1	0	-1	1	0	1	1	0	}^{T}
$\mathbf{d}_{16}=$	{	1	-1	0	-1	-1	0	-1	1	0	1	1	0	0	0	0	0	0	0	0	0	0	0	0	0	}^{T}
$\mathbf{d}_{17}=$	{	0	-1	1	0	0	0	0	0	0	0	1	1	0	-1	-1	0	0	0	0	0	0	0	1	-1	}^{T}
$\mathbf{d}_{18}=$	{	0	0	1	0	0	-1	0	0	-1	0	0	1	0	0	-1	0	0	1	0	0	1	0	0	-1	}^{T}
$\mathbf{d}_{19}=$	{	1	0	0	-1	0	0	-1	0	0	1	0	0	-1	0	0	1	0	0	1	0	0	-1	0	0	}^{T}
$\mathbf{d}_{20}=$	{	-1	0	0	0	0	0	-1	0	0	0	0	0	-1	0	0	0	0	0	0	0	0	1	0	0	}^{T}
$\mathbf{d}_{21}=$	{	0	0	0	0	0	0	0	0	0	0	0	0	0	0	1	0	0	-1	0	0	1	0	0	-1	}^{T}
$\mathbf{d}_{22}=$	{	0	0	0	1	0	0	-1	0	0	0	0	0	0	0	0	-1	0	0	1	0	0	0	0	0	}^{T}
$\mathbf{d}_{23}=$	{	0	0	0	0	1	0	0	0	0	0	1	0	0	1	0	0	-1	0	0	0	0	0	0	0	}^{T}

Table 3-1: Displacement fields related to the incompressible deformation modes.

After inferring the ability of RESS element to reproduce all the 23 incompressible deformation modes without any aid of enhancing variables, it was concluded that 20 deformation modes were reproduced. To supply such lack of incompressible deformation modes (that would certainly induce volumetric locking) a one

parameter enhancing strain field was chosen with the following interpolation matrix defined in the convective frame:

$$\mathbf{B}_{\alpha}^{\mathrm{T}} = \begin{bmatrix} 0 & 0 & \zeta & 0 & 0 & 0 \end{bmatrix} . \tag{3.45}$$

It is also worth referring that the primary design condition stated by Simo and Rifai (1990) is satisfied, i.e., $\int_{\square} \mathbf{B}_{\alpha} d\square = 0$. Regardless of the number of integration points ($n \geq 3$ through the thickness direction), the number of enhanced strain parameters to cover the 23 incompressible deformation modes remains to be one. It is an extremely useful feature, particularly in plasticity-type problems, since it is normally necessary to have many integration points along thickness.

As far as the number of utilized enhancing parameters is concerned, RESS element utilizes the lowest possible number (one). Comparing with other well-established 3D formulations in the literature (where the number of enhancing parameters ranges from 9 to 54) it represents a tremendous advantage in terms of computational efficiency and stability.

Remark 2:

The inversion of $\mathbf{K}^{\alpha\alpha}$ matrix for each element is an important computational issue for conventional EAS elements, particularly for a large number of enhancing parameters. It is noticeable that for RESS element, since there is only one enhancing variable ($\boldsymbol{\alpha} \rightarrow \alpha$), $\mathbf{K}^{\alpha\alpha}$ in equation (3.26) becomes a scalar ($K^{\alpha\alpha}$). Therefore, equation (3.32) is simplified with no matrix inversion involved, saving a considerable amount of CPU work at this stage. This advantage retains a crucial contribution in the numerical simulation of demanding industrial processes.

$$\left[\hat{\mathbf{K}}_{lg}^{uu} + \hat{\mathbf{K}}_{nlg}^{uu} - \frac{1}{\hat{K}^{\alpha\alpha}} \hat{\mathbf{K}}^{u\alpha} \hat{\mathbf{K}}^{\alpha u} \right] {}_{n}^{n+1}\mathbf{d} = \mathbf{f}_{u}^{ext} - \mathbf{f}_{u}^{int} + \frac{f_{\alpha}^{int}}{\hat{K}^{\alpha\alpha}} \hat{\mathbf{K}}^{u\alpha} \tag{3.46}$$

$$\left(\hat{\mathbf{K}}^{u+\alpha} \right) {}_{n}^{n+1}\mathbf{d} = \mathbf{f}^{u+\alpha} \tag{3.47}$$

3.3.2 Other Locking Pathologies

The purpose of the enhancing parameter now included in the formulation, equation (3.45), is not only to solve volumetric locking but also *thickness locking*. In pure bending, thickness locking occurs when, due to the "ν-coupling" effect (Hauptmann et al., 2001), the stress component $\sigma_{\zeta\zeta}$ (that should be equal to zero) adopts a linear profile, Figure 3-4, leading to an overly stiff behavior. The added enhancing term plays an important role to generate an additional (enhancing) $E_{\zeta\zeta}$ linear variation in order to neutralize this effect. A similar remedy for thickness locking was also proposed by Büchter and Ramm (1994).

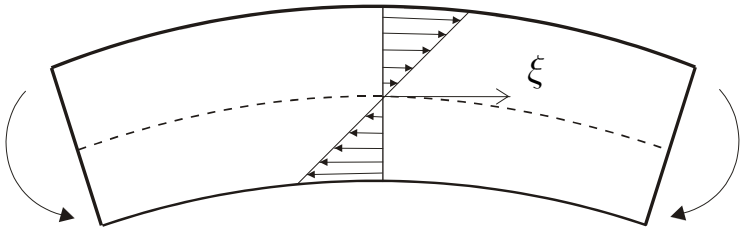

$$\sigma_{\zeta\zeta} = \frac{\mathrm{E}}{(1+\nu)(1\text{-}2\nu)}\left[(1\text{-}\nu)\varepsilon_{\zeta\zeta} + \left(\varepsilon_{\xi\xi} + \varepsilon_{\eta\eta}\right)\right]$$

Figure 3-4: Linear variation of strain component in bending situation.

Remark 3:

In pure bending, when the stress field along thickness must be zero, and although the enhancing parameter might be different from zero (since it has no physical meaning), there is no spurious strain energy generated, once the orthogonality condition ($\int_V \mathbf{S} : \mathbf{E}^{\alpha} \; dV = 0$) is satisfied.

The *transverse shear locking* phenomenon is associated to an overestimation of stiffness properties coming from the transverse strain energy, which does not automatically vanish in case of 2×2 in-plane integrated elements applied for thin-walled structures. However, in the works of César de Sá et al. (2002) and Fontes Valente et al. (2004), a subspace analysis applied for an enhanced strain shell

formulation proved that an in-plane reduced numerical integration scheme eliminates efficiently the transverse shear locking.

In this sense, regarding RESS element, the combination of a one-point quadrature integration scheme with the EAS method utilizing just one enhancing parameter is sufficient to overcome locking pathologies. However, the rank-deficiency generated by the reduced integration scheme employed demands a stabilization scheme, discussed section 3.4.

3.4 Stabilization Procedure

To avoid occurrence of hourglass problems, the physical stabilization procedure of Cardoso et al. (2002), originally suggested for a shell formulation, is extended to cover 3D solids. Both the equivalent stiffness matrix and the equivalent force vector of equation (3.47) are corrected at each time step, resulting in the modified expression for the nodal displacements' calculation:

$$\left(\hat{\mathbf{K}}^{u+\alpha} + {}^{stb}\hat{\mathbf{K}}\right) {}^{n+1}_{n}\mathbf{d} = \mathbf{f}^{u+\alpha} + {}^{stb}\mathbf{f} \quad . \tag{3.48}$$

To proceed with a computational affordable way of calculating ${}^{stb}\hat{\mathbf{K}}$ and ${}^{stb}\mathbf{f}$ terms, let us consider the linear components of the strain tensor, defined in the convective coordinate system:

$$E_{ab} = \frac{1}{2}\left(\mathbf{J}_a \frac{\partial \mathbf{u}}{\partial \psi_b} + \mathbf{J}_b \frac{\partial \mathbf{u}}{\partial \psi_a}\right) \quad . \tag{3.49}$$

The calculation of the Jacobian matrix, equation (3.9), is performed based on

$$\frac{\partial \mathbf{x}}{\partial \psi_a} = \frac{\partial N_i(\boldsymbol{\psi})}{\partial \psi_a}\mathbf{x}_i \quad , \tag{3.50}$$

involving derivatives of the standard shape functions.,

$$
\begin{aligned}
N_{i,\xi}(\xi,\eta,\zeta) &= \frac{1}{8}(\xi_i + h_{1i}\eta + h_{2i}\zeta + h_{4i}\eta\zeta) \\
N_{i,\eta}(\xi,\eta,\zeta) &= \frac{1}{8}(\eta_i + h_{1i}\xi + h_{3i}\zeta + h_{4i}\xi\zeta) \\
N_{i,\zeta}(\xi,\eta,\zeta) &= \frac{1}{8}(\zeta_i + h_{2i}\xi + +h_{3i}\eta + h_{4i}\xi\eta),
\end{aligned}
\tag{3.51}
$$

where

$$
\begin{aligned}
\mathbf{h}_1 &= \Big\{1\ -1\ 1\ -1\ 1\ -1\ 1\ -1\Big\}^{\mathrm{T}} \\
\mathbf{h}_2 &= \Big\{1\ -1\ -1\ 1\ -1\ 1\ 1\ -1\Big\}^{\mathrm{T}} \\
\mathbf{h}_3 &= \Big\{1\ 1\ -1\ -1\ -1\ -1\ 1\ 1\Big\}^{\mathrm{T}} \\
\mathbf{h}_4 &= \Big\{-1\ 1\ -1\ 1\ 1\ -1\ 1\ -1\Big\}^{\mathrm{T}}
\end{aligned}
\quad .
\tag{3.52}
$$

Combining equation (3.51) with equations (3.9) and (3.50), it is possible to write:

$$
\begin{aligned}
\mathbf{J}_1 &= \frac{1}{8}(\xi_j + h_{1j}\eta + h_{2j}\zeta + h_{4j}\eta\zeta)\mathbf{x}_j \\
\mathbf{J}_2 &= \frac{1}{8}(\eta_j + h_{1j}\xi + h_{3j}\zeta + h_{4j}\xi\zeta)\mathbf{x}_j \qquad (\text{sum on } j = 1, n^e_{nodes})\,. \\
\mathbf{J}_3 &= \frac{1}{8}(\zeta_j + h_{2j}\xi + +h_{3j}\eta + h_{4j}\xi\eta)\mathbf{x}_j
\end{aligned}
\tag{3.53}
$$

The expressions just derived can be decomposed into constant, linear and bilinear components depending on $\xi,\ \eta,\ \zeta,\ \xi\eta,\ \xi\zeta$ and $\eta\zeta$:

$$
\mathbf{J} = \mathbf{J}^c + \mathbf{J}^{\xi}\xi + \mathbf{J}^{\eta}\eta + \mathbf{J}^{\zeta}\zeta + \mathbf{J}^{\xi\eta}\xi\eta + \mathbf{J}^{\xi\zeta}\xi\zeta + \mathbf{J}^{\eta\zeta}\eta\zeta\,,
\tag{3.54}
$$

where each term is obtained after some algebra:

$$
\mathbf{J}^c = \frac{1}{8}\begin{bmatrix} \xi_j x_j & \xi_j y_j & \xi_j z_j \\ \eta_j x_j & \eta_j y_j & \eta_j z_j \\ \zeta_j x_j & \zeta_j y_j & \zeta_j z_j \end{bmatrix}
\tag{3.55}
$$

$$
\mathbf{J}^{\xi} = \frac{1}{8}\begin{bmatrix} 0 & 0 & 0 \\ h_{1j} x_j & h_{1j} y_j & h_{1j} z_j \\ h_{2j} x_j & h_{2j} y_j & h_{2j} z_j \end{bmatrix}
\tag{3.56}
$$

$$\mathbf{J}^{\eta} = \frac{1}{8}\begin{bmatrix} h_{1j}x_j & h_{1j}y_j & h_{1j}z_j \\ 0 & 0 & 0 \\ h_{3j}x_j & h_{3j}y_j & h_{3j}z_j \end{bmatrix} \tag{3.57}$$

$$\mathbf{J}^{\zeta} = \frac{1}{8}\begin{bmatrix} h_{2j}x_j & h_{2j}y_j & h_{2j}z_j \\ h_{3j}x_j & h_{3j}y_j & h_{3j}z_j \\ 0 & 0 & 0 \end{bmatrix} \tag{3.58}$$

$$\mathbf{J}^{\xi\eta} = \frac{1}{8}\begin{bmatrix} 0 & 0 & 0 \\ 0 & 0 & 0 \\ h_{4j}x_j & h_{4j}y_j & h_{4j}z_j \end{bmatrix} \tag{3.59}$$

$$\mathbf{J}^{\xi\zeta} = \frac{1}{8}\begin{bmatrix} 0 & 0 & 0 \\ h_{4j}x_j & h_{4j}y_j & h_{4j}z_j \\ 0 & 0 & 0 \end{bmatrix} \tag{3.60}$$

$$\mathbf{J}^{\eta\zeta} = \frac{1}{8}\begin{bmatrix} h_{4j}x_j & h_{4j}y_j & h_{4j}z_j \\ 0 & 0 & 0 \\ 0 & 0 & 0 \end{bmatrix}. \tag{3.61}$$

Using the set of equations (3.53) to (3.61) together with equation (3.50), the linear strain tensor in equation (3.49) can be redefined in a convenient way by the decomposed standard strain-displacement $\mathbf{B}_u$ matrix:

$$\mathbf{E} = \left(\mathbf{B}^{c} + \mathbf{B}^{\xi}\xi + \mathbf{B}^{\eta}\eta + \mathbf{B}^{\zeta}\zeta + \mathbf{B}^{\xi\eta}\xi\eta + \mathbf{B}^{\xi\zeta}\xi\zeta + \mathbf{B}^{\eta\zeta}\eta\zeta\right)\mathbf{u} \quad . \tag{3.62}$$

For the sake or clearness, the sub-terms of equation (3.62) are detailed in Appendix. Under the in-plane reduced integration scheme adopted in this formulation, stabilization must not be accounted for constant (c) and zeta (ζ) dependent terms since the used integration doesn't cancel them. For this reason, the strain-displacement sub-matrices that contribute to elements' stabilization are:

$${}^{stb}\mathbf{B} = {}^{stb}\mathbf{B}^{\xi}\xi + {}^{stb}\mathbf{B}^{\eta}\eta + {}^{stb}\mathbf{B}^{\xi\eta}\xi\eta + {}^{stb}\mathbf{B}^{\xi\zeta}\xi\zeta + {}^{stb}\mathbf{B}^{\eta\zeta}\eta\zeta \quad . \tag{3.63}$$

Also, it is useful to decompose ${}^{stb}\mathbf{B}$ matrix by lines:

$$\begin{aligned}
{}^{stb}\mathbf{B}_{\xi\xi} &= {}^{stb}\mathbf{B}^{\xi}_{\xi\xi}\xi + {}^{stb}\mathbf{B}^{\eta}_{\xi\xi}\eta + {}^{stb}\mathbf{B}^{\xi\eta}_{\xi\xi}\xi\eta + {}^{stb}\mathbf{B}^{\xi\zeta}_{\xi\xi}\xi\zeta + {}^{stb}\mathbf{B}^{\eta\zeta}_{\xi\xi}\eta\zeta \\
{}^{stb}\mathbf{B}_{\eta\eta} &= {}^{stb}\mathbf{B}^{\xi}_{\eta\eta}\xi + {}^{stb}\mathbf{B}^{\eta}_{\eta\eta}\eta + {}^{stb}\mathbf{B}^{\xi\eta}_{\eta\eta}\xi\eta + {}^{stb}\mathbf{B}^{\xi\zeta}_{\eta\eta}\xi\zeta + {}^{stb}\mathbf{B}^{\eta\zeta}_{\eta\eta}\eta\zeta \\
{}^{stb}\mathbf{B}_{\zeta\zeta} &= {}^{stb}\mathbf{B}^{\xi}_{\zeta\zeta}\xi + {}^{stb}\mathbf{B}^{\eta}_{\zeta\zeta}\eta + {}^{stb}\mathbf{B}^{\xi\eta}_{\zeta\zeta}\xi\eta + {}^{stb}\mathbf{B}^{\xi\zeta}_{\zeta\zeta}\xi\zeta + {}^{stb}\mathbf{B}^{\eta\zeta}_{\zeta\zeta}\eta\zeta \\
{}^{stb}\mathbf{B}_{\xi\eta} &= {}^{stb}\mathbf{B}^{\xi}_{\xi\eta}\xi + {}^{stb}\mathbf{B}^{\eta}_{\xi\eta}\eta + {}^{stb}\mathbf{B}^{\xi\eta}_{\xi\eta}\xi\eta + {}^{stb}\mathbf{B}^{\xi\zeta}_{\xi\eta}\xi\zeta + {}^{stb}\mathbf{B}^{\eta\zeta}_{\xi\eta}\eta\zeta \\
{}^{stb}\mathbf{B}_{\xi\zeta} &= \beta\Big({}^{stb}\mathbf{B}^{\xi}_{\xi\zeta}\xi + {}^{stb}\mathbf{B}^{\eta}_{\xi\zeta}\eta + {}^{stb}\mathbf{B}^{\xi\eta}_{\xi\zeta}\xi\eta + {}^{stb}\mathbf{B}^{\xi\zeta}_{\xi\zeta}\xi\zeta + {}^{stb}\mathbf{B}^{\eta\zeta}_{\xi\zeta}\eta\zeta\Big) \\
{}^{stb}\mathbf{B}_{\eta\zeta} &= \beta\Big({}^{stb}\mathbf{B}^{\xi}_{\eta\zeta}\xi + {}^{stb}\mathbf{B}^{\eta}_{\eta\zeta}\eta + {}^{stb}\mathbf{B}^{\xi\eta}_{\eta\zeta}\xi\eta + {}^{stb}\mathbf{B}^{\xi\zeta}_{\eta\zeta}\xi\zeta + {}^{stb}\mathbf{B}^{\eta\zeta}_{\eta\zeta}\eta\zeta\Big)
\end{aligned} \quad . \tag{3.64}$$

Once defined in the convective frame, the ${}^{stb}\mathbf{B}$ matrix is transposed to the local frame, utilizing the same methodology as in equation (3.18),

$${}^{stb}\hat{\mathbf{B}} = {}^{l}_{c}\mathbf{T}_{0}\,{}^{stb}\mathbf{B} \ . \tag{3.65}$$

Given that the stabilization procedure results in a stiffness matrix to be added to the standard counterpart, locking phenomena must also be accounted. When applying this formulation for thin-walled structures, the β parameter of equation (3.64) can be set to zero, not adding transverse shear energy and avoiding transverse shear locking, following a similar proposal from Li and Cescotto (2000).
To eliminate volumetric locking, the B-bar approach (Hughes, 1978) is adopted in the local frame. Accordingly, the hourglass counterpart of the strain-displacement operator is divided into its volumetric (dilatational) and deviatoric components, being the dilatational part integrated at the element's center,

$${}^{stb}\hat{\mathbf{B}}(\boldsymbol{\psi}) = {}^{stb}\hat{\mathbf{B}}(\boldsymbol{\psi})\big|_{dev} + {}^{stb}\hat{\mathbf{B}}(\mathbf{0})\big|_{dil} \ , \tag{3.66}$$

where ${}^{stb}\hat{\mathbf{B}}\big|_{dev}$ and ${}^{stb}\hat{\mathbf{B}}\big|_{dil}$ are further expanded according to equation (3.63). Since no constant terms are present in this expansion:

$${}^{stb}\hat{\mathbf{B}}(\mathbf{0})\big|_{dil} = \mathbf{0} \ , \tag{3.67}$$

and consequently:

$${}^{stb}\hat{\mathbf{B}}(\boldsymbol{\psi}) = {}^{stb}\hat{\mathbf{B}}(\boldsymbol{\psi})\big|_{dev} \ . \tag{3.68}$$

Back to equation (3.48), the hourglass stiffness (${}^{stb}\hat{\mathbf{K}}$) and the increment of hourglass forces (${}^{stb}\mathbf{f}$) are calculated like:

$$\begin{aligned} {}^{stb}\hat{\mathbf{K}} &= \hat{\mathbf{K}}^{\xi} + \hat{\mathbf{K}}^{\eta} + \hat{\mathbf{K}}^{\xi\eta} + \hat{\mathbf{K}}^{\xi\zeta} + \hat{\mathbf{K}}^{\eta\zeta} \\ {}^{stb}\left({}^{n+1}_{n}\mathbf{f}\right) &= {}^{n+1}_{n}\mathbf{f}^{\xi} + {}^{n+1}_{n}\mathbf{f}^{\eta} + {}^{n+1}_{n}\mathbf{f}^{\xi\eta} + {}^{n+1}_{n}\mathbf{f}^{\xi\zeta} + {}^{n+1}_{n}\mathbf{f}^{\eta\zeta} \end{aligned} \tag{3.69}$$

where the increment of hourglass forces is calculated at the mid-step configuration $\left(n+\frac{1}{2}\right)$. Each hourglass term in equation (3.69) is detailed below:

$$\hat{\mathbf{K}}^{\xi} = \iiint_{\square}\left[\left(\hat{\mathbf{B}}^{\xi}\right)^{\mathrm{T}}\mathbf{C}^{e}\hat{\mathbf{B}}^{\xi}\right]\xi^{2}\left|\mathbf{J}_{0}\right|d\square \tag{3.70}$$

$$\hat{\mathbf{K}}^{\eta} = \iiint_{\square}\left[\left(\hat{\mathbf{B}}^{\eta}\right)^{\mathrm{T}}\mathbf{C}^{e}\hat{\mathbf{B}}^{\eta}\right]\eta^{2}\left|\mathbf{J}_{0}\right|d\square \tag{3.71}$$

$$\hat{\mathbf{K}}^{\xi\eta} = \iiint_{\square}\left[\left(\hat{\mathbf{B}}^{\xi\eta}\right)^{\mathrm{T}}\mathbf{C}^{e}\hat{\mathbf{B}}^{\xi\eta}\right]\xi^{2}\eta^{2}\left|\mathbf{J}_{0}\right|d\square \tag{3.72}$$

$$\hat{\mathbf{K}}^{\xi\zeta} = \iiint_{\square}\left[\left(\hat{\mathbf{B}}^{\xi\zeta}\right)^{\mathrm{T}}\mathbf{C}^{e}\hat{\mathbf{B}}^{\xi\zeta}\right]\xi^{2}\zeta^{2}\left|\mathbf{J}_{0}\right|d\square \tag{3.73}$$

$$\hat{\mathbf{K}}^{\eta\zeta} = \iiint_{\square}\left[\left(\hat{\mathbf{B}}^{\eta\zeta}\right)^{\mathrm{T}}\mathbf{C}^{e}\hat{\mathbf{B}}^{\eta\zeta}\right]\eta^{2}\zeta^{2}\left|\mathbf{J}_{0}\right|d\square \ , \tag{3.74}$$

for the hourglass stiffness and

$${}^{n+1}_{n}\mathbf{f}^{\xi} = \iiint_{\square}\left[\left(\hat{\mathbf{B}}^{\xi}\right)^{\mathrm{T}}\,{}^{n+1}_{n}\boldsymbol{\sigma}^{\xi}\right]\xi\left|\mathbf{J}_{0}\right|d\square \tag{3.75}$$

$${}^{n+1}_{n}\mathbf{f}^{\eta} = \iiint_{\square}\left[\left(\hat{\mathbf{B}}^{\eta}\right)^{\mathrm{T}}\,{}^{n+1}_{n}\boldsymbol{\sigma}^{\eta}\right]\eta\left|\mathbf{J}_{0}\right|d\square \tag{3.76}$$

$${}^{n+1}_{n}\mathbf{f}^{\xi\eta} = \iiint_{\square}\left[\left(\hat{\mathbf{B}}^{\xi\eta}\right)^{\mathrm{T}}\,{}^{n+1}_{n}\boldsymbol{\sigma}^{\xi\eta}\right]\xi\eta\left|\mathbf{J}_{0}\right|d\square \tag{3.77}$$

$${}^{n+1}_{n}\mathbf{f}^{\xi\zeta} = \iiint_{\square}\left[\left(\hat{\mathbf{B}}^{\xi\zeta}\right)^{\mathrm{T}}\,{}^{n+1}_{n}\boldsymbol{\sigma}^{\xi\zeta}\right]\xi\zeta\left|\mathbf{J}_{0}\right|d\square \tag{3.78}$$

$${}^{n+1}_{n}\mathbf{f}^{\eta\zeta} = \iiint_{\square}\left[\left(\hat{\mathbf{B}}^{\eta\zeta}\right)^{\mathrm{T}}\,{}^{n+1}_{n}\boldsymbol{\sigma}^{\eta\zeta}\right]\eta\zeta\left|\mathbf{J}_{0}\right|d\square \ , \tag{3.79}$$

for the hourglass forces. The increment of the Cauchy stress (${}^{n+1}_{n}\boldsymbol{\sigma}$) is given as[1]:

$$ {}^{n+1}_{n}\boldsymbol{\sigma}^{\xi} = \xi \mathbf{C}^{e} \hat{\mathbf{B}}^{\xi} \mathbf{d} \tag{3.80} $$

$$ {}^{n+1}_{n}\boldsymbol{\sigma}^{\eta} = \eta \mathbf{C}^{e} \hat{\mathbf{B}}^{\eta} \mathbf{d} \tag{3.81} $$

$$ {}^{n+1}_{n}\boldsymbol{\sigma}^{\xi\eta} = \xi\eta \mathbf{C}^{e} \hat{\mathbf{B}}^{\xi\eta} \mathbf{d} \tag{3.82} $$

$$ {}^{n+1}_{n}\boldsymbol{\sigma}^{\xi\zeta} = \xi\zeta \mathbf{C}^{e} \hat{\mathbf{B}}^{\xi\zeta} \mathbf{d} \tag{3.83} $$

$$ {}^{n+1}_{n}\boldsymbol{\sigma}^{\eta\zeta} = \eta\zeta \mathbf{C}^{e} \hat{\mathbf{B}}^{\eta\zeta} \mathbf{d} \,. \tag{3.84} $$

In the set of equations (3.70) to (3.79), the non-constant terms can be calculated analytically:

$$ \begin{gathered} \iiint_{\square} \xi^2 d\square = \iiint_{\square} \eta^2 d\square = \frac{8}{3} \\ \iiint_{\square} \xi^2\eta^2 d\square = \iiint_{\square} \xi^2\zeta^2 d\square = \iiint_{\square} \eta^2\zeta^2 d\square = \frac{8}{9} \end{gathered} \,. \tag{3.85} $$

By doing so, no numerical integration is required at this stage, saving a considerable amount of computational time.

[1] The utilization of the Cauchy stresses to evaluate the hourglass forces is possible due to the equivalence between this stress measure and the second Piola-Kirchhoff stress, equation (2.21).

3.5 Summary of RESS Implementation

In this section, the most important steps concerning the non-linear implementation of the RESS solid-shell element are given.

Element level:

---

1. Update the orthonormal referential $\mathbf{r}$ using the polar decomposition theorem. For the first increment/iteration construct the local referential (Box 2-1).

Midpoint configuration

2. Perform the constitutive update (Box 3-1)
3. Perform the return-stress procedure
4. Compute the incremental hourglass forces ${}^{stb}\left({}^{n+1}_{n}\mathbf{f}\right)$

Stiffness computation:

Gauss point level:

---

1. Compute $\hat{\mathbf{B}}_u$
2. Compute $\mathbf{B}_\alpha$ in the convective frame
3. Transpose to the local frame using the local/convective operator (3.10)
4. Compute $\hat{\mathbf{K}}^{uu}_{lg}, \hat{\mathbf{K}}^{uu}_{nlg}, \hat{\mathbf{K}}^{u\alpha}$ and $\hat{\mathbf{K}}^{\alpha\alpha}$
5. Compute the internal force vectors $\hat{\mathbf{f}}^{int}_u$ and $\hat{\mathbf{f}}^{int}_\alpha$

Back to element level:

---

1. Obtain by static condensation $\hat{\mathbf{K}}^{u+\alpha}$ and $\hat{\mathbf{f}}^{u+\alpha}$, equation (3.46)
2. Compute the stabilization counterpart of stiffness ${}^{stb}\hat{\mathbf{K}}$
3. Update the stabilization counterpart of the internal force vector ${}^{stb}\hat{\mathbf{f}}$
4. Solve the final equation $\left(\hat{\mathbf{K}}^{u+\alpha} + {}^{stb}\hat{\mathbf{K}}\right) {}^{n+1}_{n}\mathbf{d} = \mathbf{f}^{u+\alpha} + {}^{stb}\mathbf{f}$

Chapter 4

Anisotropic Plasticity

Significant efforts are being made to replace steel sheets with aluminum alloy sheets, especially in the automotive industry. Aluminum is much lighter than steel, which improves for instance the vehicles fuel efficiency. However, besides higher material costs, there are several technical hurdles to overcome before a widespread usage of aluminum alloy sheets, namely lower formability and larger springback when compared to steel sheets. Anisotropy has an important effect on the strain distribution of aluminum alloys after sheet metal forming operations, and it is closely related to its thinning and formability. In this Chapter, the physics of aluminum deformation is reviewed at two different scales (macro and micro). Classical polycrystal models are described with corresponding single crystal constitutive models. Phenomenological yield functions accounting for anisotropy are also discussed. As closure, the validity and accuracy of an implemented polycrystal plasticity model is tested by means of iso-error maps.

4.1 Introduction and Motivation

The sheet metal anisotropy is a combination of the initial anisotropy due to its previous history of thermomechanical processing and the plastic deformation during stamping operation. The former generally leads to symmetry with orthotropic character while the latter, called deformation-induced anisotropy, possibly destroy this symmetry when the principal material symmetry and the deformation axes are not superimposed. Therefore, modeling of plastic anisotropy itself and its implementation into FEM codes can be complex. For practical purpose, the assumption that the change of anisotropic properties during sheet forming is small and negligible when compared to the anisotropy induced by rolling and heat treatment has been widely adopted in the analysis of sheet metal forming processes. This is particularly important for industrial applications, where user-friendliness

and computation time are important factors to consider. In this case, it is convenient to use the concepts of anisotropic mathematical yield functions and isotropic hardening.

For a more rigorous treatment, deformation-induced anisotropy, which is due to the evolution of the microstructure during forming, must be accounted for. Texture evolution, i.e., the rotation of individual grains, can be captured using polycrystal models, Figure 4-1. Dislocation accumulation and patterning in the material can be described by hardening rules that are based on the orientation distribution of slip elements. For instance, a sheet metal subjected to shear deformation loses its orthotropic character, Figure 4-1b. Therefore, the symmetry exhibited by the material during forming is an element that should be captured as well.

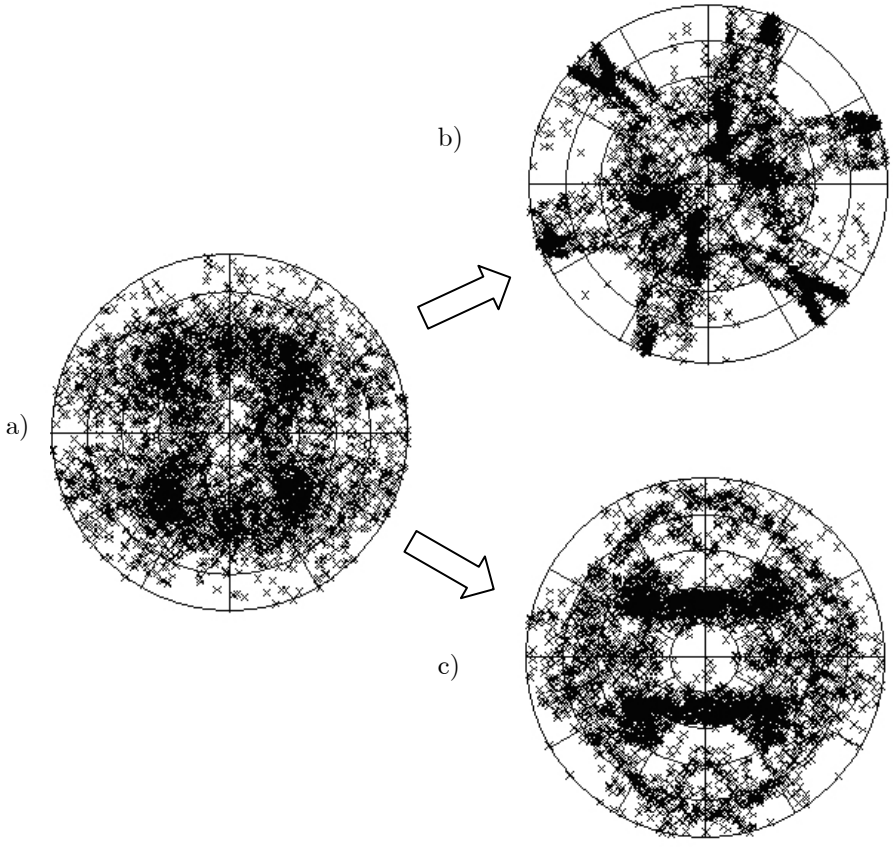

Figure 4-1: Texture evolution – {111} Pole Figures[1] of a 6022 Aluminum alloy captured by a polycrystal model: a) as rolled; b) after shear deformation; c) after uniaxial deformation.

[1] For a reader not familiarized with the concept of Pole Figures, an essential and succinct explanation is given in Appendix.

The methods describing deformation-induced anisotropy are more appealing in a theoretical point of view. As drawback, and despite the rapid evolution of computers' performance, the analysis of complex forming operations by means of polycrystal approaches still involves heavy calculations. The use of yield functions based on mechanical input parameters are for this reason much more popular, being well established in industry via commercial FEM codes. However, most recent and accurate yield functions demand a substantial number of mechanical tests for proper utilization. In addition, a complex nonlinear scheme may be needed in order to obtain the final input parameters. Hence, older and not so accurate yield functions like Hill'48 are still used nowadays given its simplicity. For polycrystal approaches, since only the initial texture is needed as input, a very accurate description can be obtained with a minimum input set. Thus, the development of time efficient polycrystal models in conjunction with FEM codes is a necessary requirement to disseminate this kind of approach.

In the following sections, the plasticity mechanisms of FCC crystals are described to introduce polycrystal models. A description of the single crystal constitutive behavior is made with emphasis on the grain level plasticity model using the notion of interacting slip systems. A brief description of chosen anisotropic yield functions is also given. At the end, guidelines to implement the described anisotropic plasticity model in a FEM code are provided and its accuracy and validity inferred by using iso-error maps.

4.1 Physical Approach – Background Considerations

Among the several crystalline structures found in the major part of metals, namely the Body Centered Cubic (BCC), the Hexagonal Close-Packed (HCP) or the Face-Centered Cubic (FCC), this work focus on the FCC system from which aluminum is made. Figure 4-2 shows the FCC atoms lattice and one unit cell. In the unit cell, there is one lattice point at each corner of the cube and one at the center of each cube face.

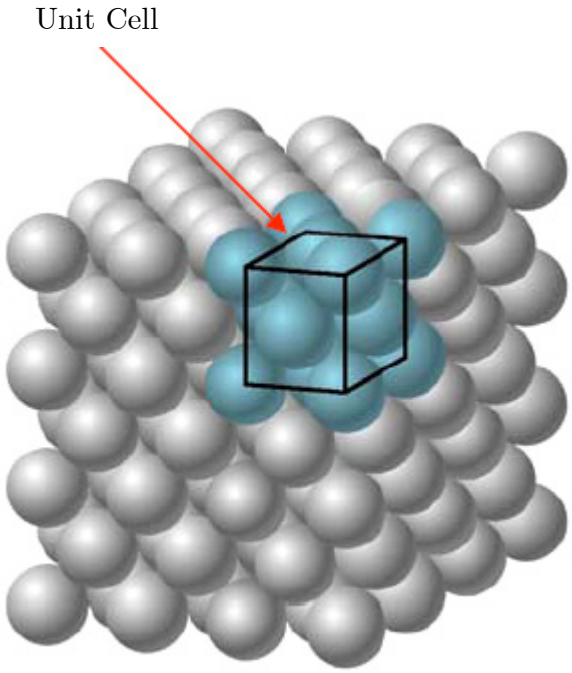

Figure 4-2: Face Centered Cubic lattice and unit cell.

For FCC crystals, plastic deformation appears only as a result of simple shears along the slip systems. Twinning plays no role on the plastic deformation of FCC crystals. Each slip system is composed by a slip plane, defined by its normal (**n**) and slip direction (**b**).

The definition of slip systems is based on an index system for crystal planes and directions called Miller indices (Bunge, 1982). The orientation of a crystal plane is determined by three non-collinear points contained in the plane. For convenience, these three points are chosen as the intersection points with the three crystal axes ([100],[010],[001]), defining the lattice constants a_1, a_2 and a_3. Directions can be obtained in a very similar way. Box 4-1 defines the basic rules to determine the Miller indices.

1.	Find the intercepts on the axes in terms of the lattice constants a_1, a_2 and a_3.
2.	Reduce the reciprocals of these numbers to three integers having the same ratio, usually the smallest three integers. The result, enclosed in parenthesis (hkl) for planes or brackets [hkl] for directions, is called the index.
3.	The set of indices {hkl} denote a set of parallel planes. A family of directions is defined by <hkl>.
4.	If a plane or direction cuts an axis on the negative side of the origin, the corresponding index is negative, indicated by the minus sign or bar above index: $(h\bar{k}l)$.

Box 4-1: Rules to define the Miller indices.

In Figure 4-3 it is exemplified a FCC crystal with the slip plane (111) and the corresponding slip directions. In fact, the 12 slip systems of a FCC crystal are defined by the family {111}<110>, Table 4-1.

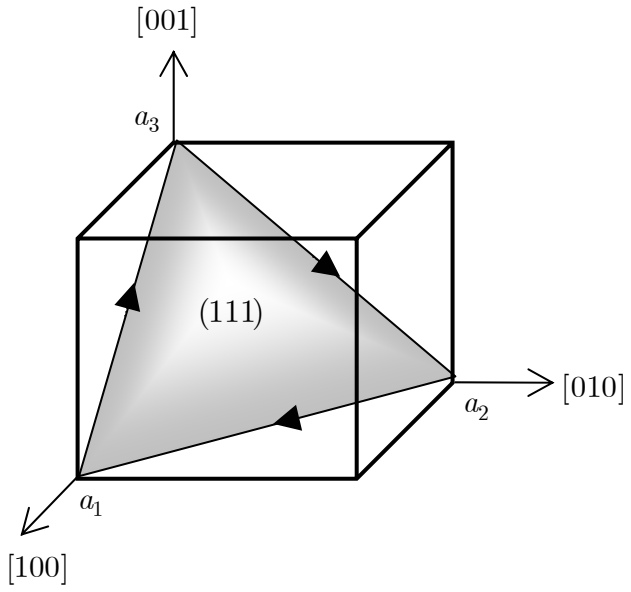

Figure 4-3: Slip plane and direction in FCC crystal; Miller indices.

Slip system (s)	**(Plane)[Direction]**
1	$\left(1\ 1\ 1\right)\left[0\ 1\ \overline{1}\right]$
2	$\left(1\ 1\ 1\right)\left[1\ 0\ \overline{1}\right]$
3	$\left(1\ 1\ 1\right)\left[1\ \overline{1}\ 0\right]$
4	$\left(1\ 1\ \overline{1}\right)\left[0\ 1\ 1\right]$
5	$\left(1\ 1\ \overline{1}\right)\left[1\ 0\ 1\right]$
6	$\left(1\ 1\ \overline{1}\right)\left[1\ \overline{1}\ 0\right]$
7	$\left(1\ \overline{1}\ \overline{1}\right)\left[0\ 1\ \overline{1}\right]$
8	$\left(1\ \overline{1}\ \overline{1}\right)\left[1\ 0\ 1\right]$
9	$\left(1\ \overline{1}\ \overline{1}\right)\left[1\ 1\ 0\right]$
10	$\left(1\ \overline{1}\ 1\right)\left[0\ 1\ 1\right]$
11	$\left(1\ \overline{1}\ 1\right)\left[1\ 0\ \overline{1}\right]$
12	$\left(1\ \overline{1}\ 1\right)\left[1\ 1\ 0\right]$

Table 4-1: The twelve slip systems of FCC crystals.

Once slip planes and directions are defined, it is possible to introduce the concept of Resolved Shear Stress (RSS) on a slip system (s),

$$\tau^{(s)} = b_i^{(s)} n_j^{(s)} \sigma_{ij} \ , \tag{4.1}$$

which is the projection of the stress tensor onto a specified slip system. According to the Schmid Law (Schmid, 1924) slip occurs in a given slip system when the RSS reaches the critical resolved shear stress (CRSS), τ_0:

$$\tau^{(s)} \geq \tau_0 \ . \tag{4.2}$$

The deformation of a single crystal is furthermore defined by the combination of simple shears on its slip systems. These simple shears are caused by dislocation motions that can easily reach, without constraints, the grain surface. Thus, a single crystal subjected to uniaxial tension is free to deform in a single slip system basis, with its lattice rotating as the deformation of the crystal takes place. However,

none of the above considerations are valid if the grain is embedded in an agglomerate of randomly oriented grains. In this case, individual grains may not be subjected to uniaxial stresses even if the polycrystalline specimen is deformed like that. In addition, boundaries between grains may cause obstacles to dislocations' movements, generating stress concentrations.

From the exposed, one can expect multiple slips in plastically deformed grains of a polycrystal subjected to an imposed deformation. In the next paragraphs, two classical polycrystal models are discussed: Sachs (1928) and Taylor (1938). First, let us consider a single crystal loaded by a uniaxial tensile stress as in Figure 4-4.

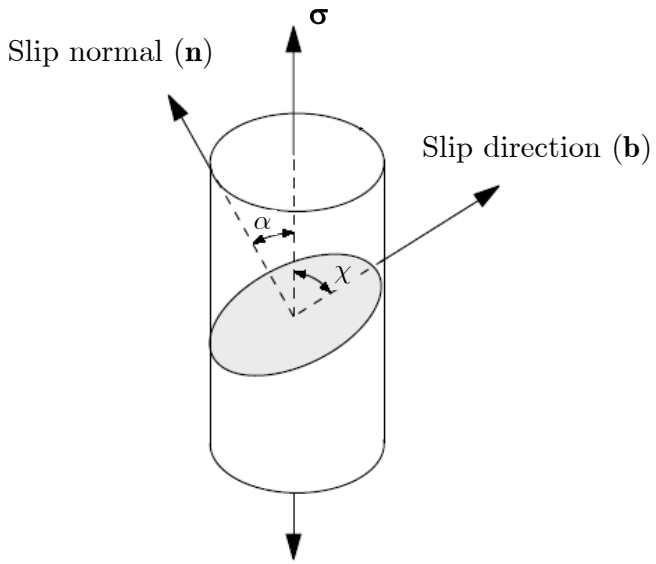

Figure 4-4: Slip system geometry.

Considering the Schmid law, equations (4.1) and (4.2), it is possible to conclude that the tensile yield stress (σ_c) depends on the orientation of a given slip system. This dependency can be rendered into the (m) parameter:

$$\sigma_c = m\tau_0 \,. \tag{4.3}$$

The resolved shear stress in this case can also be found as (Bunge, 1982)

$$\tau_0 = \cos(\alpha)\cos(\chi)\sigma_c \,, \tag{4.4}$$

where $\cos(\alpha)\cos(\chi)$ is known as the Schmid factor. Inversely, it is possible to define the Taylor factor:

$$m = \left[\cos(\alpha)\cos(\chi)\right]^{-1} = \frac{\sigma}{\tau} = \frac{\gamma}{\varepsilon}\,. \tag{4.5}$$

Then, the active slip system is the one with minimum m-factor. Considering a random aggregate of grains having the same CRSS (τ_0), the objective is to determine a mean value of $\bar{m}$ relating the polycrystal yield stress (σ_p) with (τ_0),

$$\sigma_p = \bar{m}\tau_0 \ . \tag{4.6}$$

Here appears the distinction between Sachs and Taylor models. Sachs (1928) assumed that a polycrystal is an aggregate of independently deforming single crystals, with the principal axes of stress being the same in all grains of the *homogeneously stressed* polycrystal. Under his assumption, Sachs calculated $\bar{m} = 2.24$. The Sachs model is quite satisfactory at the beginning of plastic strain. However, as plastic deformation increases, large interaction stresses between grains lead to material separation at the grain boundaries (Figure 4-5b), in an inadmissible physical solution.

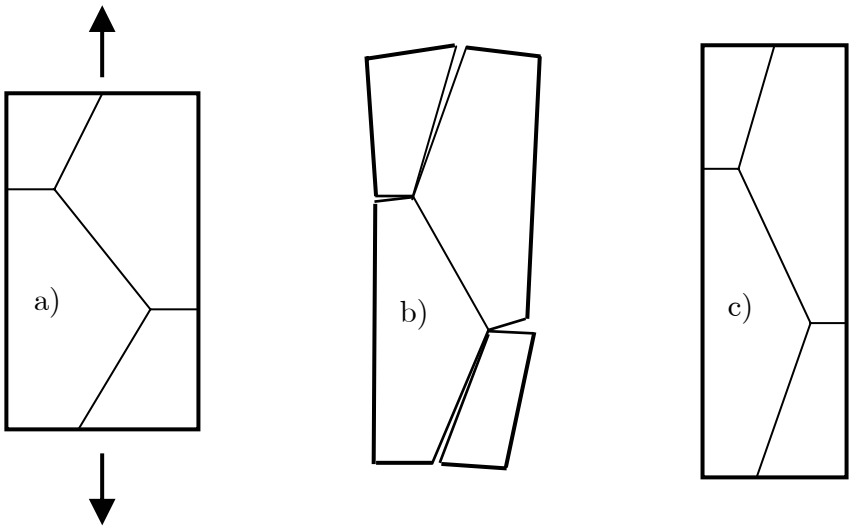

Figure 4-5: Large plastic deformation of a polycrystal: a) undeformed; b) according to Sachs model; c) according to Taylor model.

Taylor (1938) provided a better description based on physics. In opposition to Sachs, it is considered a *homogeneous strain* assumption for all polycrystal grains. Hence, all grains undergo the same imposed macroscopic strain. To fulfill such condition, and based on von Mises (1913) conclusions, Taylor stated that five active slip systems in each grain were necessary to accommodate the deformations. At the end, no boundaries between grains are violated (Figure 4-5c) but each grain adopts distinct stress values, generating a discontinuous stress field. The selected five active slip systems (from twelve possible choices) should be the ones where the sum of absolute values of the shear strain increments is minimal. The referred choice of active slip systems is a bulky task given the number of possibilities. At this point resides the weakness of Taylor model. Nevertheless, Taylor's calculation leaded to the value of $\overline{m} = 3.06$.

Bishop and Hill (1951a; 1951b) and Bishop (1953) developed another method for determining $\overline{m}$. Using the Schmid yield criterion, they constructed the yield locus of an FCC single crystal. In a five-dimensional deviatoric stress space (a section of the six-dimensional stress space) it is similar to a polyhedron with many facets and 56 vertices. The corresponding deviatoric stresses are called vertex stresses. Hill's *Maximum Work Principle* for rate-insensitive plasticity was then used to demonstrate that the stress which corresponds to a prescribed plastic strain vector will nearly always be a vertex stress. Mathematically, the activated vertex when a given grain rate of deformation ($\mathbf{D}^g$) is imposed is the vertex ($\vartheta^{(k)}$) that leads to maximum plastic work rate ($\dot{\mathbf{w}}$), i.e.,

$$\dot{\mathbf{w}} = \mathbf{D}^g_{ij} \vartheta^{(k)}_{ij} \quad . \tag{4.7}$$

There are 28 vertices and their 28 symmetric opposites in the FCC single crystal yield surface as listed by Bishop (1953). They are reproduced in Table 4-2 in terms of A, B, C, F, G and H parameters with the corresponding deviatoric stress states:

$$
\begin{aligned}
s_{xx} &= \frac{C-B}{3} \\
s_{yy} &= \frac{A-C}{3} \\
s_{zz} &= \frac{B-A}{3} \\
s_{yz} &= F \\
s_{xz} &= G \\
s_{xy} &= H
\end{aligned}
\tag{4.8}
$$

n.º	A	B	C	D	E	F
1	1	-1	0	0	0	0
2	0	1	-1	0	0	0
3	-1	0	1	0	0	0
4	0	0	0	1	0	0
5	0	0	0	0	1	0
6	0	0	0	0	0	1
7	½	-1	½	0	½	0
8	½	-1	½	0	- ½	0
9	-1	½	½	½	0	0
10	-1	½	½	- ½	0	0
11	½	½	-1	0	0	½
12	½	½	-1	0	0	- ½
13	½	0	- ½	½	0	½
14	½	0	- ½	- ½	0	½
15	½	0	- ½	½	0	- ½
16	½	0	- ½	- ½	0	- ½
17	0	- ½	½	0	½	½
18	0	- ½	½	0	- ½	½
19	0	- ½	½	0	½	- ½
20	0	- ½	½	0	- ½	- ½
21	- ½	½	0	½	½	0
22	- ½	½	0	- ½	½	0
23	- ½	½	0	½	- ½	0
24	- ½	½	0	- ½	- ½	0
25	0	0	0	½	½	- ½
26	0	0	0	½	- ½	½
27	0	0	0	- ½	½	½
28	0	0	0	½	½	½

Table 4-2: FCC single crystal vertices (Bishop, 1953)

The method of Bishop and Hill is strictly equivalent to Taylor's one leading to the value of $\bar{m} = 3.1$. From the exposed, it can be concluded that the assumption of Taylor is suitable for the analysis of forming processes, with moderately large strains.

4.2 Kinematics of Crystal Plasticity

To properly deal with a polycrystal model, one more coordinate system must be introduced in addition to the ones defined in Chapter 2. A lattice coordinate system is defined by the crystallographic directions [100], [010] and [001], Figure 4-6. Also, it is corotational with the crystalline lattice.

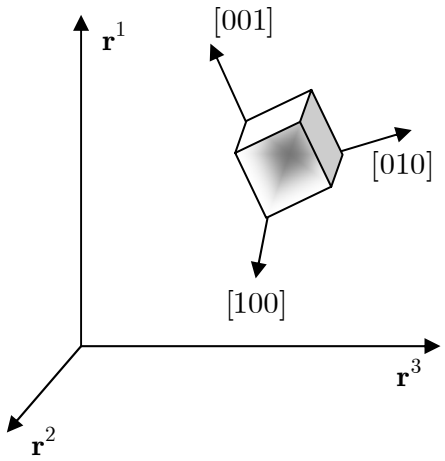

Figure 4-6: Lattice coordinate system.

At each Gauss point, the relationship between the lattice and the local ($\mathbf{r}$) coordinate systems can be derived by introducing Euler angles. In a FEM code, the displacement, the rate of deformation and nodal forces are calculated in the local system, but the single crystal constitutive equations are formulated in the lattice frame. Thus, the transformation between these two systems is necessary. For this purpose, let us define the matrix ($\mathbf{P}_3$), which transforms an entity from the lattice to the local frame (Bunge, 1982). Among many ways to represent an orientation, the Euler angles are well accepted.

Roe's Euler angles (Roe, 1965) define the orientation of a grain, whose crystal axes ([100],[010],[001]) are initially superimposed on the reference frame (x, y, z). The grain is then subjected to a succession of three rotations, ψ, θ and β resulting in a new frame (X, Y, Z) as detailed in Box 4-2 and Figure 4-7:

1. Rotate x and y axes about z through an angle ψ to form a new set of axes x', y' and $z' = z$
2. Rotate y' and z' about x' through an angle θ to form a set of axes $x' = x'', y''$ and $z'' = Z$
3. Rotate x'' and y'' about z'' through an angle β to form the final (X, Y, Z) axes

Box 4-2: Construction of Roe's Euler Angles.

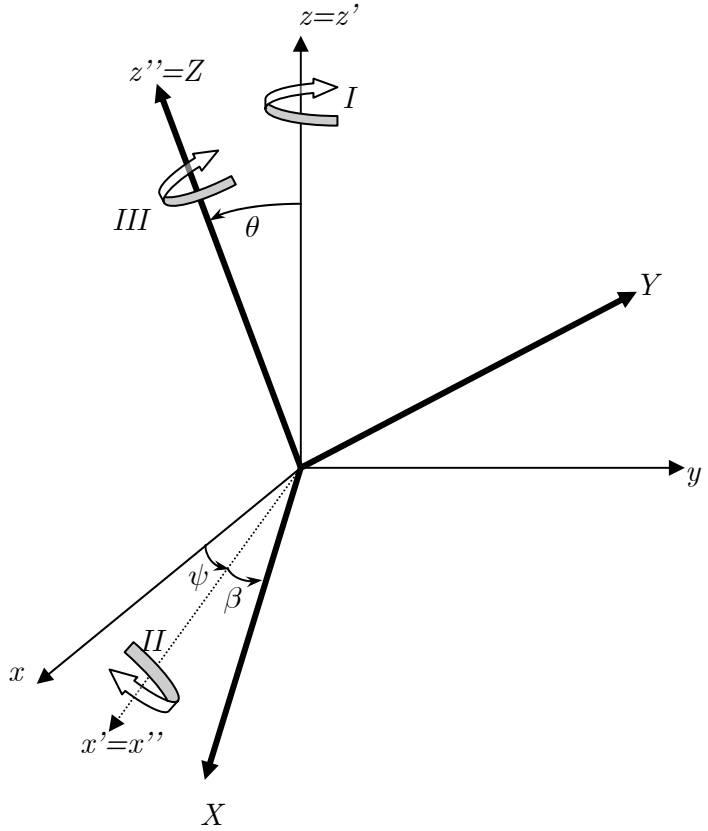

Figure 4-7: Roe's Euler Angles.

At the end, the corresponding transformation matrix $\mathbf{P}_3$ is defined as,

$$\mathbf{P}_3 = \begin{bmatrix} \cos\psi\cos\theta\cos\beta - \sin\theta\sin\beta & -\cos\psi\cos\theta\sin\beta - \sin\theta\cos\beta & \cos\psi\sin\theta \\ \sin\psi\cos\theta\cos\beta + \cos\theta\sin\beta & -\sin\psi\cos\theta\sin\beta + \cos\theta\cos\beta & \sin\psi\sin\theta \\ -\sin\psi\cos\beta & \sin\psi\cos\beta & \cos\psi \end{bmatrix}. \quad (4.9)$$

Using ($\mathbf{P}_3$), the components of a vector ($\mathbf{v}$) and a second order tensor ($\mathbf{S}$) can be transformed from the lattice (*lat*) coordinate to the local (*loc*) coordinate system as follows,

$$\begin{aligned} \mathbf{v}^{loc} &= \mathbf{P}_3 \cdot \mathbf{v}^{lat} \\ \mathbf{S}^{loc} &= \mathbf{P}_3 \cdot \mathbf{S}^{lat} \cdot \mathbf{P}_3 \end{aligned} . \quad (4.10)$$

In sections 4.2.1 and 4.2.2, two ways of dealing with the kinematics of crystal plasticity are given. The traditional framework, as described in the work of Peirce et al. (1982; 1983) or Asaro (1983a; 1983b), resorting to the multiplicative decomposition of the deformation gradient and a more convenient one, based on the incremental deformation theory (Yoon, 1997; Yoon et al. 1999a; 1999b).

4.2.1 Multiplicative decomposition of the deformation gradient

Following Lee (1969), the deformation gradient ($\mathbf{F}$) can be decomposed into a plastic counterpart ($\mathbf{F}^p$), which is in this scope the summation of the shear strain in each slip system, and a combination of elastic deformation and rigid body motion of the crystal lattice ($\mathbf{F}^e$) as shown in Figure 4-8,

$$\mathbf{F} = \mathbf{F}^e\mathbf{F}^p . \quad (4.11)$$

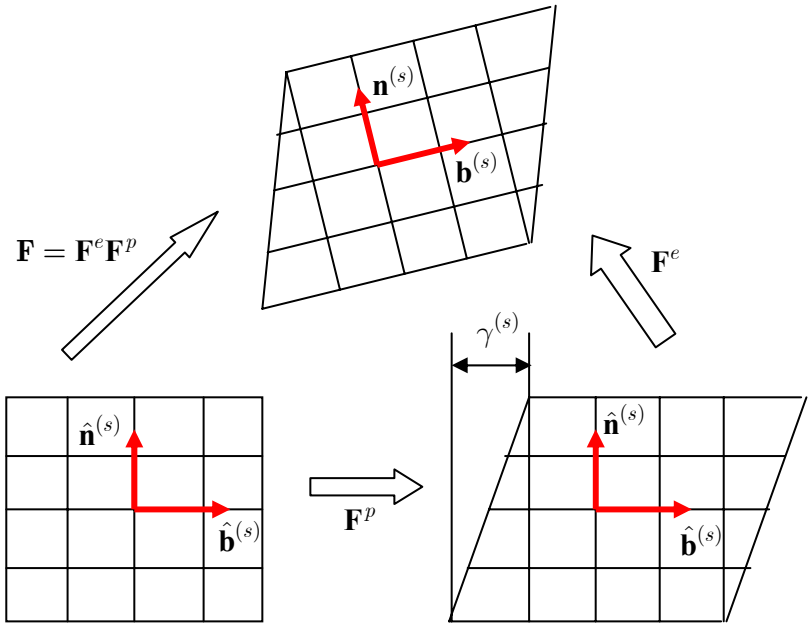

Figure 4-8: Multiplicative decomposition of deformation gradient

Recalling the expressions given in Chapter 2, the velocity gradient ($\mathbf{L}$) in the current configuration can be additively decomposed as,

$$\mathbf{L} = \mathbf{L}^e + \mathbf{L}^p = \dot{\mathbf{F}} \cdot \mathbf{F}^{-1} = \mathbf{D} + \mathbf{W} \quad . \tag{4.12}$$

The deformation rate ($\mathbf{D}$) and the spin ($\mathbf{W}$) can be rewritten as,

$$\begin{aligned} \mathbf{D} &= \mathbf{D}^e + \mathbf{D}^p \\ \mathbf{W} &= \mathbf{W}^e + \mathbf{W}^p \end{aligned} \quad , \tag{4.13}$$

where $\mathbf{D}^p$ and $\mathbf{W}^p$ are the plastic deformation rate and the plastic spin due to dislocation slip, and $\mathbf{D}^e$ and $\mathbf{W}^e$ are the elastic deformation rate and the elastic spin due to the crystal lattice deformation and rotation.
Considering an intermediate configuration in which only plastic deformation occurs, $\mathbf{L}^p$, $\mathbf{D}^p$ and $\mathbf{W}^p$ can be defined as follows:

$$\hat{\mathbf{L}}^p = \dot{\mathbf{F}}^p \cdot \left(\mathbf{F}^p\right)^{-1} = \hat{\mathbf{D}}^p + \hat{\mathbf{W}}^p = \frac{1}{2}(\hat{\mathbf{L}}^p + \hat{\mathbf{L}}^{p\mathrm{T}}) + \frac{1}{2}(\hat{\mathbf{L}}^p - \hat{\mathbf{L}}^{p\mathrm{T}}) \quad . \tag{4.14}$$

Since plastic deformation is considered to be caused by dislocation slip, $\hat{\mathbf{L}}^p$ is determined by the summation of shear strain ($\dot{\gamma}$) contributions of all slip systems:

$$\hat{\mathbf{L}}^p = \sum_{(s)} \dot{\gamma}^{(s)} \hat{\mathbf{b}}^{(s)} \hat{\mathbf{n}}^{(s)} \ . \tag{4.15}$$

After the lattice rotation, they can be conveniently transformed into

$$\begin{aligned} \mathbf{b}^{(s)} &= \mathbf{F}^e \hat{\mathbf{b}}^{(s)} \\ \mathbf{n}^{(s)} &= \mathbf{F}^e \hat{\mathbf{n}}^{(s)} \end{aligned} \ , \tag{4.16}$$

where

$$\begin{aligned} \mathbf{F}^e &= \mathbf{F} \left(\mathbf{F}^p \right)^{-1} \\ \left(\mathbf{F}^p \right)^{-1} &= \mathbf{I}_2 - \hat{\mathbf{b}}^{(s)} \hat{\mathbf{n}}^{(s)} \gamma^{(s)} \end{aligned} \ . \tag{4.17}$$

Since $\mathbf{n}^{(s)}$ and $\mathbf{b}^{(s)}$ are unit vectors and perpendicular to each other, the following relationship is valid,

$$\mathbf{n}^{(s)} \cdot \mathbf{b}^{(s)} = \mathbf{b}^{(s)} \cdot \mathbf{n}^{(s)} = 0 \, . \tag{4.18}$$

Therefore, the symmetric and skew symmetric part of $\mathbf{L}^p$, $\mathbf{D}^p$ and $\mathbf{W}^p$ can be written as

$$\begin{aligned} \hat{\mathbf{D}}^p &= \sum_{(s)} \dot{\gamma}^{(s)} \frac{1}{2} (\hat{\mathbf{b}}^{(s)} \hat{\mathbf{n}}^{(s)} + \hat{\mathbf{n}}^{(s)} \hat{\mathbf{b}}^{(s)}) \\ \hat{\mathbf{W}}^p &= \sum_{(s)} \dot{\gamma}^{(s)} \frac{1}{2} (\hat{\mathbf{b}}^{(s)} \hat{\mathbf{n}}^{(s)} - \hat{\mathbf{n}}^{(s)} \hat{\mathbf{b}}^{(s)}) \end{aligned} \ . \tag{4.19}$$

4.2.2 Incremental Deformation Theory

In this approach, the starting point is the polar decomposition of the deformation gradient, where the deformation is contained in the stretch tensor $\mathbf{U}$ and the rotation is dominated by the rotation tensor $\mathbf{R}$, as described in Figure 4-9:

$$\mathbf{F} = \mathbf{R}\mathbf{U} \ . \tag{4.20}$$

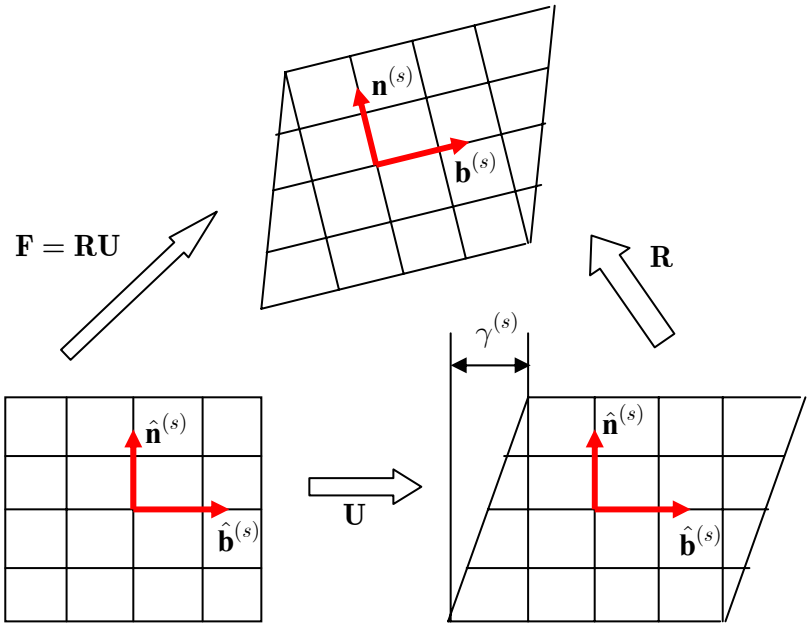

Figure 4-9: Polar decomposition of deformation gradient

Considering the relationship (4.12) together with equation (4.20), the following decomposition is obtained (Yoon et. al, 1999a;b),

$$\begin{aligned} \mathbf{W} &= \dot{\mathbf{R}} \cdot \mathbf{R}^{-1} + \mathbf{R}\left(\dot{\mathbf{U}}\mathbf{U}^{-1}\right)_{\text{asy}} \mathbf{R}^{\mathrm{T}} \\ \mathbf{D} &= \mathbf{R}\left(\dot{\mathbf{U}}\mathbf{U}^{-1}\right)_{\text{sym}} \mathbf{R}^{\mathrm{T}} \end{aligned} \quad , \tag{4.21}$$

where the subscripts (asy) and (sym) denote anti-symmetric and symmetric parts of the tensor, respectively. Moreover, when the same principal material lines are kept constant during deformation, the principal material lines of $\dot{\mathbf{U}}$ and $\mathbf{U}$ coincide and $(\dot{\mathbf{U}}\mathbf{U}^{-1})$ is symmetric. Therefore,

$$\begin{aligned} \mathbf{W} &= \dot{\mathbf{R}} \cdot \mathbf{R}^{-1} \\ \mathbf{D} &= \mathbf{R}\left(\dot{\mathbf{U}}\mathbf{U}^{-1}\right)_{\text{sym}} \mathbf{R}^{\mathrm{T}} \end{aligned} \quad . \tag{4.22}$$

Consequently, rotation is described entirely by $(\mathbf{R})$, i.e., rotation and deformation are completely decoupled by the polar decomposition. If the principal material directions vary continuously, rotation is affected by the term $\mathbf{R}\left(\dot{\mathbf{U}}\mathbf{U}^{-1}\right)_{\text{asy}} \mathbf{R}^{\mathrm{T}}$. Consequently, the condition of constant principal material lines is essential to

describe the effect of rotation in terms of ($\mathbf{R}$) only. A "rotationless" strain rate ($\hat{\mathbf{D}}$) can now be defined as

$$\hat{\mathbf{D}} = \hat{\mathbf{D}}^e + \hat{\mathbf{D}}^p = \mathbf{R}^{\mathrm{T}}\mathbf{D}\mathbf{R} = \left(\dot{\mathbf{U}}\mathbf{U}^{-1}\right)_{\mathrm{sym}} \ , \tag{4.23}$$

where

$$\hat{\mathbf{D}}^p = \sum_{(s)} \dot{\gamma}^{(s)} \frac{1}{2}(\hat{\mathbf{b}}^{(s)}\hat{\mathbf{n}}^{(s)} + \hat{\mathbf{n}}^{(s)}\hat{\mathbf{b}}^{(s)}) \ . \tag{4.24}$$

The quantity ($\hat{\mathbf{D}}$) is considered to be the values ($\mathbf{D}$) measured with respect to the coordinate system that rotates by ($\mathbf{R}$), so that the values are invariant when submitted to rigid body rotations. In this scope, ($\hat{\mathbf{D}}$) also becomes a Lagrangian quantity. The minimum plastic work condition is satisfied when the incremental deformation satisfies the following relation:

$${}^{n+1}_{n}\boldsymbol{\varepsilon} = \int_{t_n}^{t_{n+1}} \hat{\mathbf{D}}\, dt = \int_{t_n}^{t_{n+1}} \left(\dot{\mathbf{U}}\mathbf{U}^{-1}\right) dt = \ln(\mathbf{U}) \ . \tag{4.25}$$

Finally, the following relationship is obtained for logarithmic strain paths:

$$\hat{\mathbf{D}} = \hat{\mathbf{D}}^{\mathrm{e}} + \hat{\mathbf{D}}^{\mathrm{p}} \approx {}^{n+1}_{n}\hat{\boldsymbol{\varepsilon}} = {}^{n+1}_{n}\hat{\boldsymbol{\varepsilon}}^{e} + {}^{n+1}_{n}\hat{\boldsymbol{\varepsilon}}^{p} \ , \tag{4.26}$$

where

$${}^{n+1}_{n}\hat{\boldsymbol{\varepsilon}}^{p} = \sum_{(s)} \Delta\gamma^{(s)} \frac{1}{2}(\hat{\mathbf{b}}^{(s)}\hat{\mathbf{n}}^{(s)} + \hat{\mathbf{n}}^{(s)}\hat{\mathbf{b}}^{(s)}) \ . \tag{4.27}$$

As advantage, in each step $\hat{\mathbf{n}}^{(s)}$ and $\hat{\mathbf{b}}^{(s)}$ can be updated by applying only the rotation tensor ($\mathbf{R}$) and keeping its orthogonality, i.e.,

$$\begin{aligned} \mathbf{b}^{(s)} &= \mathbf{R}\cdot\hat{\mathbf{b}}^{(s)} \\ \mathbf{n}^{(s)} &= \hat{\mathbf{n}}^{(s)}\mathbf{R}^{\mathrm{T}} \end{aligned} \ . \tag{4.28}$$

4.3 Constitutive Relations for Polycrystals

4.3.1 Classical Rate-Independent Approach (Schmid Law)

One of the earliest attempts to model the crystalline constitutive behavior of FCC crystals (Hill and Rice, 1972) was based on the Schmid Law, equation (4.2). Using the Schmid law, the stress state of each slip system is absolutely independent of the remaining ones. In this case, the corresponding piece-wise linear plastic potential is an analogue of the classical Tresca yield condition (Figure 4-10). This model raises a serious disadvantage: the strain-rate vector at the corner of the yield surface is undefined, or at least can change abruptly, originating erroneous results. In addition, since several combinations of slip rates give the same strain rate of the crystal, the number of unknowns exceeds the number of formulated equations and the problem cannot be represented by a complete system of equations (Gambin, 2000).

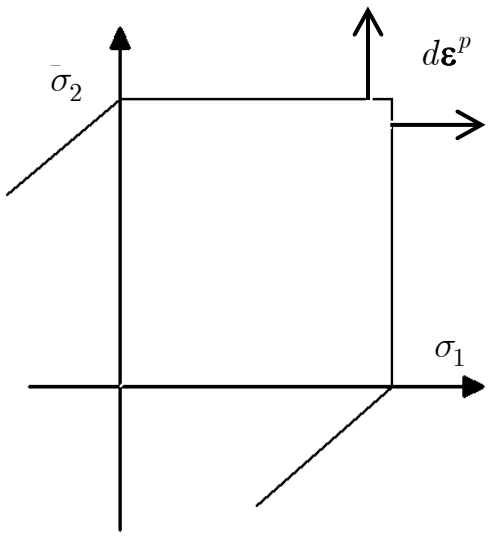

Figure 4-10: Schmid yield surfaces and plastic corner effect.

4.3.2 Rate Dependent Approach

The class of rate-dependent crystal models appeared to overcome the difficulties concerning the definition of the strain-rate vector. Pan and Rice (1983), Peirce et al. (1983), Asaro and Needleman (1985) and Molinari et al., (1987), among many others, proposed a new form to describe the deformation of a crystal. A viscoplastic behavior is assumed as a small deviation from pure plasticity. All slip systems are considered active overcoming the issue about the choice of active slip systems. As a consequence, the problem can be formulated in terms of a complete system of equations. A power law form used by Hutchinson (1970) or Pan and Rice (1983) is suggested:

$$\dot{\gamma}^{(s)} = \dot{\kappa}^{(s)} \left(\frac{\tau^{(s)}}{g^{(s)}} \right) \left(\left| \frac{\tau^{(s)}}{g^{(s)}} \right| \right)^{\frac{1}{a}-1} , \tag{4.29}$$

where $\tau^{(s)}$ is the resolved shear stress for each slip system. The set of functions $g^{(s)}$ characterize the current hardening of the crystal and $(\dot{\kappa})$ is the reference shearing strain rate. The exponent $(1/a)$ reflects the material rate sensitivity.

Although eliminating the issues related to the choice of active slip systems and defining uniquely the strain-rate vector, this type of model still depends on an arbitrary factor. Also, rate sensitivity is sometimes critical for numerical convergence than for accuracy in the physical description like aluminum alloys which are usually not rate-sensitive under cold forming.

4.3.3 Interacting Slip Systems (Regularized Schmid Law)

Experimental observations carried out by Diehl (1956) for BCC and FCC crystals showed deviations from the Schmid law, due to the interaction of slip systems. In this sense, the necessity of describing crystals with interacting slip systems was raised. Gambin (1991) and, independently, Arminjon (1991) derived an interaction rule between two slip systems (r) and (s):

$$\frac{\dot{\gamma}^{(s)}}{\dot{\gamma}^{(r)}} = \left(\frac{\tau_c^{(r)}}{\tau_c^{(s)}}\right)^{2a} \left(\frac{\tau^{(s)}}{\tau^{(r)}}\right)^{2a-1} . \tag{4.30}$$

In the above formula, and for a slip system (s), $\tau_c^{(s)}$ is the CRSS, $\tau^{(s)}$ is the RSS and $\dot{\gamma}^{(s)}$ is the slip strain rate. The (a) parameter possesses physical meaning according to Gambin and Barlat (1997), where it was correlated to the stacking fault energy of the material[2]. Under the assumption of interacting slip systems, the slip rate for each slip system is defined as (Gambin, 1991):

$$\dot{\gamma}^{(s)} = \frac{\lambda}{\tau_c^{(s)}} \left(\frac{\tau^{(s)}}{\tau_c^{(s)}}\right)^{2a-1} , \tag{4.31}$$

where (λ) is a non-negative scalar function, with the same value for all slip systems. Therefore, all slip systems are assumed to be active from the beginning of plastic yielding. The distribution of slip rates between slip systems is governed by the (a) parameter. When (a) is large enough, and from equation (4.30), $(\dot{\gamma}^{(r)})$ is negligible in comparison with $(\dot{\gamma}^{(s)})$, and an approximation to the classical Schmid law is obtained. Nevertheless, although describing the interaction degree of slip systems, the (a) parameter is considered as a phenomenological assumption (Gambin, 2000).

Like in the classical plasticity of anisotropic materials, it is possible to introduce a plastic potential to further define the strain rate and the plastic spin

$$\Phi\left(\sigma_{ij}\right) = \frac{1}{2a}\left[\sum_{(s)} \left(\frac{b_i^{(s)} n_j^{(s)} \sigma_{ij}}{\tau_c^{(s)}}\right)^{2a} b_i^{(s)} n_j^{(s)} - \phi^*\right], \tag{4.32}$$

which makes possible the definition of a smooth yield condition (Gambin, 2000):

$$\varphi\left(\sigma_{ij}\right) = \Phi\left(\frac{\sigma_{ij} + \sigma_{ji}}{2}\right) , \tag{4.33}$$

or in the following explicit form:

[2] Aluminum alloys possesses high stacking fault energies.

$$\varphi = \sum_{(s)} \left(\frac{\tau^{(s)}}{\tau_c^{(s)}} \right)^{2a} - \phi^* \,. \tag{4.34}$$

The (ϕ^*) parameter may be regarded as a material constant. But since the yield condition (4.34) is a smooth approximation of the Schmid Law, it is possible to simply set $\phi^* = 1$, as stated by Gambin (1991) or Arminjon (1991). For numerical convenience, let us introduce the following homogeneous function of degree one as yield function:

$$\phi = (\varphi)^{\frac{1}{2a}} = 1 \text{ (at yield)} \,. \tag{4.35}$$

The rate of deformation tensor and the plastic spin tensor are given by the associated flow rule:

$$\begin{aligned} \mathbf{D}^p &= \frac{\dot{\lambda}}{2} \left(\frac{\partial \phi}{\partial \sigma_{ij}} + \frac{\partial \phi}{\partial \sigma_{ji}} \right) \\ \mathbf{W}^p &= \frac{\dot{\lambda}}{2} \left(\frac{\partial \phi}{\partial \sigma_{ij}} - \frac{\partial \phi}{\partial \sigma_{ji}} \right) \end{aligned} \,. \tag{4.36}$$

As already referred, besides eliminating the issue about the choice of active slip systems (all of them are considered active), this model also overcome the plastic corner effect (see Figure 4-10), since the yield locus' corners are smooth until moderately large (a) values. In Figure 4-11, the yield function defined according to equation (4.35) is plotted for several values of the (a) parameter. When $a = 1$, the model reduces to a representation of the von Mises yield locus (inner curve). Maintaining all parameters, but increasing (a), the locus expands and its corners tighten. For $a = 12$, which is considered a reasonable approximation for aluminum alloys (Gambin, 2000), the resulting locus is represented by the outer curve. For the limit of ($a \to \infty$), the Schmid Tresca-type yield locus is obtained.

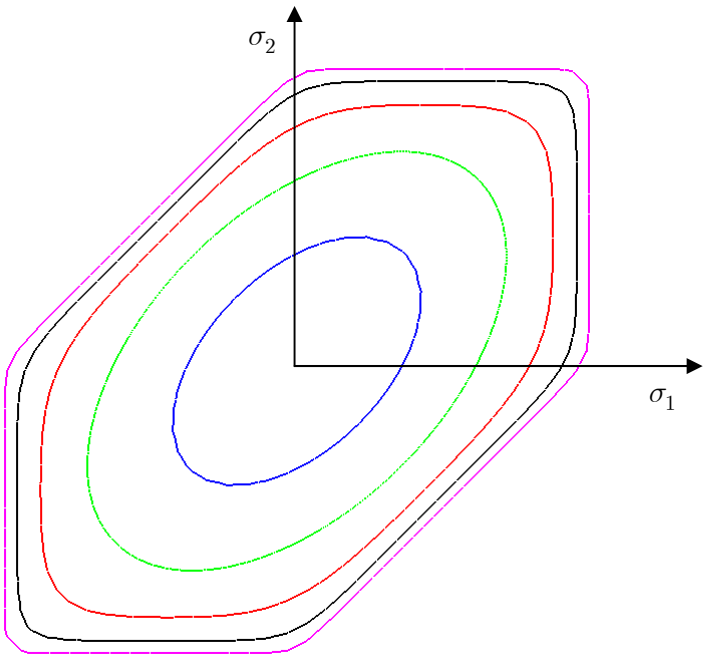

Figure 4-11: Yield locus deriving from the interacting slip systems assumption. Inner curve (a=1); Outer curve (a=12).

In sections 4.5.2 and 4.6, the implementation of the described model into a FEM code is given and its validity assessed. In the next section, attention will be paid to phenomenological yield functions.

4.4 Phenomenological Approaches

From the extensive set of works of Barlat and co-workers on phenomenological yield functions (Barlat and Richmond, 1987; Barlat and Lian, 1989, Barlat et al., 1991, 1997; 2002; 2003; 2005) two full 3D yield functions are chosen, being appropriate to use with the solid-shell element proposed in this work: Yld91 and Yld2004-18p. Thirteen years connect the two works, resulting in a significant difference in terms of complexity and accuracy. The solution accuracy between the two yield functions will be discussed in the numerical tests carried out in Chapter 5.

4.4.1 Barlat's Yld91 Yield Function

The starting point in the definition of this yield criterion is represented adequately by the following function, as suggested by Hosford (1972),

$$\phi = \left|\theta_1 - \theta_2\right|^a + \left|\theta_2 - \theta_3\right|^a + \left|\theta_3 - \theta_1\right|^a = 2\overline{\sigma}^a \quad , \tag{4.37}$$

where (θ_k) are principal values of the symmetric matrix θ_{ij},

$$\theta_{ij} = \begin{bmatrix} \theta_{xx} & \theta_{xy} & \theta_{xz} \\ \theta_{xy} & \theta_{yy} & \theta_{yz} \\ \theta_{xz} & \theta_{yz} & \theta_{zz} \end{bmatrix} \tag{4.38}$$

and $\overline{\sigma}$ is the yield stress. The exponent (a) is connected to the crystal structure of the material, i.e., 6 for BCC and 8 for FCC crystal structure. This was established as a result of many polycrystal simulations (Barlat et al., 2003). Therefore, although macroscopic, this model implicitly contains information pertaining to the structure of the material. In the Yld91 function, the values (θ_{ij}) are defined as function of the Cauchy stress components in the form:

$$\begin{aligned}
\theta_{xx} &= \frac{C_3\left(\sigma_{xx} - \sigma_{yy}\right) - C_2\left(\sigma_{zz} - \sigma_{xx}\right)}{3} \\
\theta_{yy} &= \frac{C_1\left(\sigma_{yy} - \sigma_{zz}\right) - C_3\left(\sigma_{xx} - \sigma_{yy}\right)}{3} \\
\theta_{zz} &= \frac{C_2\left(\sigma_{zz} - \sigma_{xx}\right) - C_1\left(\sigma_{yy} - \sigma_{zz}\right)}{3} \quad , \\
\theta_{yz} &= C_4\sigma_{yz} \\
\theta_{zx} &= C_5\sigma_{xz} \\
\theta_{xy} &= C_6\sigma_{xy}
\end{aligned} \tag{4.39}$$

where $C_{i=1\ldots6}$ are the anisotropic coefficients obtained from uniaxial mechanical tests. If the coefficients $C_{i=1\ldots6}$ reduce to one, the deviatoric stress components are obtained, that is, the material is isotropic.

4.4.2 Barlat's Yld2004-18p Yield Function

Because Yld91 is not able to capture the anisotropic behavior of aluminum sheet to a desirable degree of accuracy, Barlat et al. (2003) introduced two linear transformations operating on the sum of two yield functions for plane stress. This recently proposed yield function includes more anisotropy coefficients and therefore gives a better description of the anisotropic properties of a material. The extension of equation (4.37) for a general stress state is based on two linear transformations of the stress deviator (**s**). These two linear transformations can be expressed as:

$$\begin{aligned} \tilde{\mathbf{s}}' &= \mathbf{C}'\mathbf{s} = \mathbf{C}'\mathbf{Z}\boldsymbol{\sigma} = \mathbf{L}'\boldsymbol{\sigma} \\ \tilde{\mathbf{s}}'' &= \mathbf{C}''\mathbf{s} = \mathbf{C}''\mathbf{Z}\boldsymbol{\sigma} = \mathbf{L}''\boldsymbol{\sigma} \end{aligned} \quad , \tag{4.40}$$

where $\mathbf{Z}$ is a matrix that transforms the Cauchy stress tensor ($\boldsymbol{\sigma}$) to its deviator (**s**). Thus, $\tilde{\mathbf{s}}'$ and $\tilde{\mathbf{s}}''$ are linearly transformed stress deviators and $\mathbf{C}'$ and $\mathbf{C}''$ (or $\mathbf{L}'$ and $\mathbf{L}''$) are matrices containing the anisotropy coefficients.

The linear transformations can be expressed in the most general form with the following matrices:

$$\mathbf{C}' = \begin{bmatrix} 0 & -c'_{12} & -c'_{13} & 0 & 0 & 0 \\ -c'_{21} & 0 & -c'_{23} & 0 & 0 & 0 \\ -c'_{31} & -c'_{32} & 0 & 0 & 0 & 0 \\ 0 & 0 & 0 & c'_{44} & 0 & 0 \\ 0 & 0 & 0 & 0 & c'_{55} & 0 \\ 0 & 0 & 0 & 0 & 0 & c'_{66} \end{bmatrix} \tag{4.41}$$

$$\mathbf{C}'' = \begin{bmatrix} 0 & -c''_{12} & -c''_{13} & 0 & 0 & 0 \\ -c''_{21} & 0 & -c''_{23} & 0 & 0 & 0 \\ -c''_{31} & -c''_{32} & 0 & 0 & 0 & 0 \\ 0 & 0 & 0 & c''_{44} & 0 & 0 \\ 0 & 0 & 0 & 0 & c''_{55} & 0 \\ 0 & 0 & 0 & 0 & 0 & c''_{66} \end{bmatrix} . \tag{4.42}$$

Finally, the anisotropic yield function Yld2004-18p is defined as function of the principal values of $\tilde{\mathbf{s}}'$ and $\tilde{\mathbf{s}}''$ matrices:

$$\begin{aligned}\phi = \phi(\tilde{\mathbf{s}}', \tilde{\mathbf{s}}'') = \phi\left(\tilde{s}_i', \tilde{s}_j''\right) = \left|\tilde{s}_1' - \tilde{s}_1''\right|^a + \left|\tilde{s}_1' - \tilde{s}_2''\right|^a + \left|\tilde{s}_1' - \tilde{s}_3''\right|^a + \left|\tilde{s}_2' - \tilde{s}_1''\right|^a + \\ + \left|\tilde{s}_2' - \tilde{s}_2''\right|^a + \left|\tilde{s}_2' - \tilde{s}_3''\right|^a + \left|\tilde{s}_3' - \tilde{s}_1''\right|^a + \left|\tilde{s}_3' - \tilde{s}_2''\right|^a + \left|\tilde{s}_3' - \tilde{s}_3''\right|^a = 4\overline{\sigma}^a\end{aligned} . \quad (4.43)$$

For sheet metal forming applications, the experimental data to derive the anisotropy coefficients consists of flow stresses and strain ratios (r-values) for tension along seven directions in the plane of the sheet (RD to TD in 15^o increments), the biaxial flow stress from the bulge test and the biaxial (r) value from the disk compression test. Such amount of input information may be difficult to obtain in some cases. Note that when $\mathbf{C}' = \mathbf{C}''$ the formulation accounts for only one linear transformation and Yld2004-18p reduce to Yld91 provided that the number of independent coefficients is imposed to be 6. Additionally, this criterion is isotropic if all the coefficients c_{ij}' and c_{ij}'' reduce to one. The reader is referred to Barlat et al. (2005) and Yoon et al. (2005; 2006) for additional information about this model.

4.5 Guidelines for FEM Implementation

In this section, attention is given to the implementation of the anisotropic elastic-plastic constitutive models utilized in this work. First, basic equations for the implementation of Yld91 and Yld2004-18p models are depicted. Then, particular emphasis is given on the implementation of the polycrystal Taylor model with interacting slip systems.

4.5.1 Basic Equations of the Classical Plasticity Theory

The constitutive description of a material at the (macroscopic) continuum level is fully defined using the following set of equations:

$$\phi\left(\boldsymbol{\sigma}\right) = \phi\left(\sigma_{ij}\right) = \overline{\sigma} \text{ (yield condition)} \quad (4.44)$$

$$\dot{\varepsilon}_{ij}=\dot{\lambda}\frac{\partial\phi}{\partial\sigma_{ij}} \text{ (associated flow rule)} \tag{4.45}$$

$$\overline{\sigma}=\overline{\sigma}(\overline{\varepsilon}) \text{ with } \overline{\sigma}\,\dot{\overline{\varepsilon}}=\sigma_{ij}\dot{\varepsilon}_{ij} \text{ (hardening function)}. \tag{4.46}$$

It is assumed that the effects of temperature and strain rate can be included in the formulation through $\overline{\sigma}$ (the effective stress), for instance using $\overline{\sigma}=\overline{\sigma}\left(\overline{\varepsilon},\dot{\overline{\varepsilon}},T\right)$. Thus, the problem reduces to define the functions $\overline{\sigma}$ and ϕ. Macroscopically, the strain hardening behavior can be well characterized with the aid of Voce or Power laws:

$$\overline{\sigma}=A-B\exp(-C\overline{\varepsilon}) \tag{4.47}$$

$$\overline{\sigma}=K(\varepsilon_o+\overline{\varepsilon})^{n'}\ , \tag{4.48}$$

with *A,B,C,K* and *n'* as material parameters. Nevertheless, equation (4.47) is preferred to represent the hardening behavior of aluminum alloys.

Utilizing the normality rule, the associated plastic strain increment ($^{n+1}_{n}\varepsilon^{p}_{\alpha\beta}$) is obtained from the effective stress ($\overline{\sigma}$) as:

$$^{n+1}_{n}\varepsilon^{p}_{\alpha\beta}=\ ^{n+1}_{n}\overline{\varepsilon}^{p}\,\frac{\partial\overline{\sigma}}{\partial\sigma_{\alpha\beta}}, \tag{4.49}$$

where $^{n+1}_{n}\overline{\varepsilon}^{p}$ is the equivalent plastic strain increment. In order to obtain $^{n+1}_{n}\overline{\varepsilon}^{p}$, the calculation of $\overline{\sigma}$, $\dfrac{\partial\overline{\sigma}}{\partial\boldsymbol{\sigma}}$ and $\dfrac{\partial^2\overline{\sigma}}{\partial\boldsymbol{\sigma}\partial\boldsymbol{\sigma}}$ are generally required. These calculations are generally lengthy but straightforward. It can be found in detailed form in a number of works, like in Barlat et al. (2005) and Yoon et al. (2006) regarding the Yld2004-18p yield function, and in Barlat et al. (1991) and Yoon et al. (1999a;b) for the Yld91 yield function.

As discussed previously, to derive $^{n+1}_{n}\varepsilon^{p}_{\alpha\beta}$ the incremental deformation theory (Yoon et al., 1999a;b) is applied to the elastoplastic formulation based on the materially embedded coordinate system. Under this scheme, strain increments in the flow formulation are discrete true (or logarithmic) strain increments, and the material rotates according to the polar decomposition at each discrete step. Alternatively, the multiplicative decomposition theory can be also utilized with success.

In simple terms, the numerical procedure to obtain ${}^{n+1}_{n}\varepsilon^{p}_{\alpha\beta}$ is to find the unknown ${}^{n+1}_{n}\overline{\varepsilon}^{p}$ from nonlinear equations. Using ${}^{n+1}_{n}\overline{\varepsilon}^{p}$, all kinematics variables and stresses are updated at the end of every step. The nonlinear equations to solve for ${}^{n+1}_{n}\overline{\varepsilon}^{p}$ and which enable the resulting stresses to stay on the hardening curve $\rho = \rho(\overline{\varepsilon}^{p})$ are:

$$\overline{\sigma}({}^{n}\boldsymbol{\sigma} + {}^{n+1}_{n}\boldsymbol{\sigma}) = \rho({}^{n}\overline{\varepsilon} + {}^{n+1}_{n}\overline{\varepsilon}^{p}) \ , \tag{4.50}$$

where

$${}^{n+1}_{n}\boldsymbol{\sigma} = \mathbf{C}^{e}({}^{n+1}_{n}\boldsymbol{\varepsilon} - {}^{n+1}_{n}\boldsymbol{\varepsilon}^{p}) \tag{4.51}$$

and

$${}^{n+1}_{n}\boldsymbol{\varepsilon}^{p} = {}^{n+1}_{n}\overline{\varepsilon}^{p}\,\frac{\partial\overline{\sigma}}{\partial\boldsymbol{\sigma}}. \tag{4.52}$$

The incremental relationship of equation (4.51) is expressed in a materially embedded coordinate system. Therefore, this equation is objective with respect to the material rotation. Note that, in the incremental deformation theory, from the equivalence between plastic work and proportional loading, ${}^{n+1}_{n}\overline{\varepsilon}^{p} = \lambda$, i.e.,

$${}^{n+1}_{n}\overline{\varepsilon}^{p} = \frac{\boldsymbol{\sigma} : {}^{n+1}_{n}\boldsymbol{\varepsilon}^{p}}{\overline{\sigma}(\boldsymbol{\sigma})} = \frac{\boldsymbol{\sigma} : \gamma\dfrac{\partial\overline{\sigma}}{\partial\boldsymbol{\sigma}}}{\overline{\sigma}(\boldsymbol{\sigma})} = \frac{\gamma\overline{\sigma}(\boldsymbol{\sigma})}{\overline{\sigma}(\boldsymbol{\sigma})} = \lambda \ , \tag{4.53}$$

where $\overline{\sigma}$ is a first order homogenous function, $\overline{\sigma}(\boldsymbol{\sigma}) = \boldsymbol{\sigma}\dfrac{\partial\overline{\sigma}}{\partial\boldsymbol{\sigma}}$. The condition stipulating that the updated stress stays on the work-hardening curve provides the following equation:

$$F(\lambda) = \overline{\sigma}(\boldsymbol{\sigma}^{\mathrm{TR}} - \lambda\mathbf{C}^{e}\mathbf{m}) - h({}^{n}\overline{\varepsilon}^{p} + \lambda) = 0 \ , \tag{4.54}$$

where

$$\boldsymbol{\sigma}^{\mathrm{TR}} = {}^{n}\boldsymbol{\sigma} + \mathbf{C}^{e}\,{}^{n+1}_{n}\boldsymbol{\varepsilon} \tag{4.55}$$

and $\mathbf{m} = \dfrac{\partial\overline{\sigma}}{\partial\boldsymbol{\sigma}}$.

Indeed, the stress return algorithms are usually divided into two main steps, Figure 4-12:

1. the *elastic predictor step* in which a trial elastic stress ($\boldsymbol{\sigma}^{\mathrm{TR}}$) is defined from the previous converged stress state ${}^{n}\boldsymbol{\sigma}$, equation (4.55),
2. the *plastic corrector step* where, considering the associative flow rule, the final state is obtained from the trial state using equation (4.51), i.e.,

$$ {}^{n+1}_{n}\boldsymbol{\sigma} = \mathbf{C}^{e}\left({}^{n+1}_{n}\boldsymbol{\varepsilon} - \lambda \mathbf{m}\right). \tag{4.56}$$

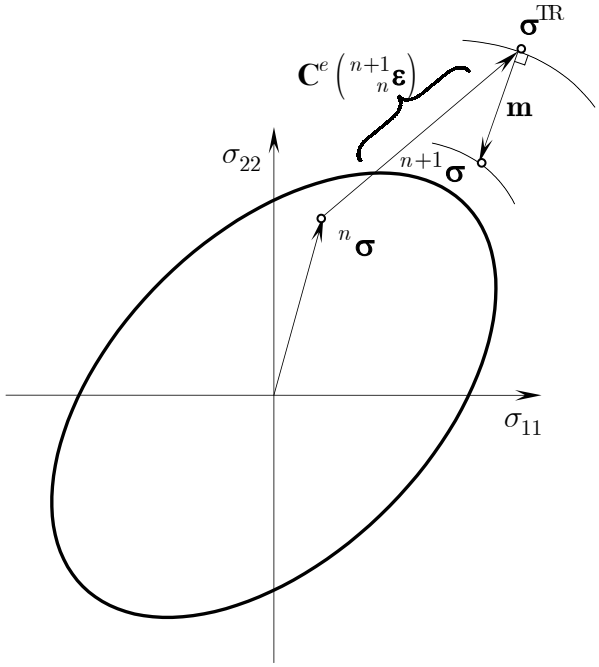

Figure 4-12: Stress return procedure.

Equation (4.54) is a nonlinear equation to solve for $\lambda = {}^{n+1}_{n}\bar{\varepsilon}^{p}$. Then, all kinematic variables and stresses are updated at the end of every step. The predictor-corrector scheme based on the Newton-Raphson method is generally used to solve the equation. However, while this equation has a mathematical solution, it can be difficult to obtain numerically if the strain increment is not small enough. In this work, a multi-stage return mapping procedure based on the control of the potential residual suggested by Yoon et al. (1999a; 1999b) is employed. The proposed method

is applicable to any non-quadratic yield function and a general strain hardening law with no need for a line search algorithm, even for a relatively large strain increment. When a semi-implicit algorithm is used, it also can be avoided the calculation of second order derivatives. Details about the multistage return mapping algorithm are given in appendix.

4.5.2 Crystal Plasticity FEM Implementation

At grain level, the nonlinear equation governing the stress return procedure can be expressed in terms of the RSS and CRSS of each slip system,

$$F(\lambda) = \phi(\tau^{(s)}, \tau_c^{(s)}) - \phi^* = 0\,, \tag{4.57}$$

where ϕ is the yield condition defined in equation (4.35) and ϕ^*=1. The hardening behavior of each slip system is given by a well accepted relation (Peirce et al., 1982; 1983),

$$\Delta\tau_c^{(s)} = \sum_{(b)} \frac{\partial \tau_c^{(s)}}{\partial \gamma^{(b)}} \Delta\gamma^{(b)} = \sum_{(b)} H_{sb} \Delta\gamma^{(b)} \ . \tag{4.58}$$

Using the relationship $\Delta\gamma^{(b)} = \lambda \dfrac{\partial \phi}{\partial \tau^{(b)}}$, equation (4.58) can be rewritten as follows:

$$\Delta\tau_c^{(s)} = \lambda \sum_{(b)} H_{sb} \frac{\partial \phi}{\partial \tau^{(b)}} \tag{4.59}$$

where H_{ab} are hardening moduli, with diagonal terms related to self hardening and the remaining (off-diagonal) to latent hardening, i.e., hardening influenced by other slip systems. One of the basic difficulties in crystalline plasticity is how to define a proper hardening evolution law for a certain crystal. In this work, the hardening law proposed by Peirce et al. (1982; 1983) is introduced,

$$H_{ab} = \kappa h + (1-\kappa) h \delta_{ab} \ , \tag{4.60}$$

where κ is the latent to self hardening ratio. According to experimental observations, κ can be taken between 1 and 1.4 (Peirce et al. 1983).

In equation (4.60), the (h) parameter appears as a function of the total shear strain (Γ). If Voce-hardening is employed,

$$h(\Gamma) = \frac{B}{m}\frac{C}{m}\exp(-\frac{C}{m}\Gamma), \quad \Gamma = \sum_{(s)}\left|\gamma^{(s)}\right| \tag{4.61}$$

where (m) is approximately the Taylor factor.
Focusing back on equation (4.57), it is necessary to define a solution procedure using an iterative scheme. To do so, the following set of equations is given:

$$\begin{aligned} &i) \quad \phi(\tau^{(s)}, \tau_c^{(s)}) - \phi^* = 0 \\ &ii) \quad \tau_c^{(s)} = \tau_{c(t=t_n)}^{(s)} + \lambda \sum_{(b)} H_{sb} \frac{\partial \phi}{\partial \tau^{(b)}} \quad , \\ &iii) \ \hat{\boldsymbol{\sigma}} = \hat{\boldsymbol{\sigma}}^{\mathrm{TR}} - \lambda \hat{\mathbf{C}}^e \frac{\partial \phi}{\partial \hat{\boldsymbol{\sigma}}} \end{aligned} \tag{4.62}$$

which can define the following functions:

$$g_1(\lambda) = \phi(\tau^{(s)}, \tau_c^{(s)}) - \phi^* = 0 \tag{4.63}$$

$$g_2^{(s)}(\lambda) = \tau_c^{(s)} - \tau_{c(t=t_n)}^{(s)} - \lambda \sum_{(b)} H_{sb} \frac{\partial \phi}{\partial \tau^{(b)}} = 0 \tag{4.64}$$

$$\mathbf{g}_3(\lambda) = \left(\hat{\mathbf{C}}^e\right)^{-1} (\hat{\boldsymbol{\sigma}} - \hat{\boldsymbol{\sigma}}^{\mathrm{TR}}) + \lambda \frac{\partial \phi}{\partial \hat{\boldsymbol{\sigma}}} = 0 \ . \tag{4.65}$$

At this stage, and for each iteration, equation (4.63) can be linearized around the current values of state variables. Thus, the equilibrium at grain level is obtained as

$$g_1(\lambda) + \frac{\partial \phi}{\partial \tau^{(s)}} \frac{\partial \tau^{(s)}}{\partial \hat{\boldsymbol{\sigma}}} \Delta \hat{\boldsymbol{\sigma}} + \frac{\partial \phi}{\partial \tau_c^{(s)}} \Delta \tau_c^{(s)} = 0 \ , \tag{4.66}$$

where the increment and iteration indices are dropped for the sake of clearness. In addition, let us consider summation over repeated symbols. The equilibrium at slip system level (micro-scale) is obtained deriving equation (4.64), i.e.,

$$g_2^{(s)}(\lambda) + \Delta\tau_c^{(s)} - \lambda\left(\sum_{(b)} H_{sb}\,\frac{\partial^2\phi}{\partial\tau^{(b)}\partial\tau^{(a)}}\,\frac{\partial\tau^{(a)}}{\partial\hat{\boldsymbol{\sigma}}}\right)\Delta\hat{\boldsymbol{\sigma}} \;-\; \Delta\lambda\sum_{(b)} H_{sb}\,\frac{\partial\phi}{\partial\tau^{(b)}} = 0\,. \quad (4.67)$$

Similarly, the derivation of equation (4.65) conducts to the equilibrium equation at macro-scale level,

$$\mathbf{g}_3(\lambda) + \left(\hat{\mathbf{C}}^e\right)^{-1}\Delta\hat{\boldsymbol{\sigma}} + \lambda\,\frac{\partial^2\phi}{\partial\hat{\boldsymbol{\sigma}}\partial\hat{\boldsymbol{\sigma}}}\Delta\hat{\boldsymbol{\sigma}} + \Delta\lambda\,\frac{\partial\phi}{\partial\hat{\boldsymbol{\sigma}}} = 0 \;\;. \quad (4.68)$$

Even if Yoon et al. (1999a;b) used a "fully-implicit" multi-stage return mapping method, the "semi-implicit" procedure is utilized in this work by keeping the multi-stage return strategy. In the semi-implicit method the return direction is fixed and the magnitude is the only unknown. For this reason, it requires a small time step to maintain the accuracy. But, there is no need to calculate second order derivatives (Cardoso, 2002). This simplification turns to be efficient since the yield function of equation (4.35) requires lengthy calculations to attain its second order derivatives. As proved in Yoon et al. (1999a;b), the proper usage of the multistage return mapping algorithm is time efficient and accurate.

Doing so, and neglecting second order derivatives, we arrive in the so-called semi-implicit return mapping algorithm. In this algorithm, there is no (λ) dependency. Therefore, equations (4.67) and (4.68) can be rewritten as:

$$g_2(\lambda) + \Delta\tau_c^{(s)} \;-\; \Delta\lambda\sum_{(b)} H_{sb}\,\frac{\partial\phi}{\partial\tau^{(b)}} = 0 \quad (4.69)$$

$$\mathbf{g}_3(\lambda) + \left(\hat{\mathbf{C}}^e\right)^{-1}\Delta\hat{\boldsymbol{\sigma}} + \Delta\lambda\,\frac{\partial\phi}{\partial\hat{\boldsymbol{\sigma}}} = 0 \;\;. \quad (4.70)$$

By taking $\lambda = 0$ (no λ dependency only for first derivative), it is possible to use the following:

$$g_1(\lambda = 0) = \phi - \phi^* \quad (4.71)$$

$$g_2(\lambda = 0) = \tau_c^{(s)} - \tau_{c(t=t_n)}^{(s)} = 0 \quad (4.72)$$

$$\mathbf{g}_3(\lambda = 0) = \left(\hat{\mathbf{C}}^e\right)^{-1}(\hat{\boldsymbol{\sigma}} - \hat{\boldsymbol{\sigma}}^{\mathrm{T}}) = 0 \;\;. \quad (4.73)$$

Substitution of equations (4.71), (4.72) and (4.73) into equations (4.66), (4.69) and (4.70) respectively yields,

$$\phi - \phi^* + \sum_{(s)} \left(\frac{\partial \phi}{\partial \tau^{(s)}} \frac{\partial \tau^{(s)}}{\partial \hat{\boldsymbol{\sigma}}} \Delta \hat{\boldsymbol{\sigma}} + \frac{\partial \phi}{\partial \tau_c^{(s)}} \Delta \tau_c^{(s)} \right) = 0 \tag{4.74}$$

$$\Delta \tau_c^{(s)} - \Delta \lambda \sum_{(b)} H_{sb} \frac{\partial \phi}{\partial \tau^{(b)}} = 0 \tag{4.75}$$

$$\Delta \hat{\boldsymbol{\sigma}} + \Delta \lambda \hat{\mathbf{C}}^e \frac{\partial \phi}{\partial \hat{\boldsymbol{\sigma}}} = 0 \tag{4.76}$$

By inserting (4.75) and (4.76) into (4.74) the expression to calculate $\Delta\lambda$ is obtained, i.e.,

$$\Delta \lambda = \frac{\phi - \phi^*}{\left(\frac{\partial \phi}{\partial \tau^{(s)}} \frac{\partial \tau^{(s)}}{\partial \hat{\boldsymbol{\sigma}}} \right) \left(\mathbf{C}^e \right)^{-1} \frac{\partial \phi}{\partial \hat{\boldsymbol{\sigma}}} + \sum_{(b)} H_{sb} \frac{\partial \phi}{\partial \tau_c^{(s)}} \frac{\partial \phi}{\partial \tau^{(b)}}} . \tag{4.77}$$

4.5.3 Implementation Algorithm

At each Gauss point, a summary of the FE implementation is given.

Gauss point level:

Input parameters:

- Number and orientation of grains in Roe's Euler angles form ($\mathbf{P}_3$);
- Macroscopic velocity gradient, to be imposed to all grains under Taylor assumption.

Grain Level:

1) Rotate the imposed strain and spin into crystal axis;
2) Calculate the trial stress based on the last converged stress value (zero for the first step): $\hat{\boldsymbol{\sigma}}^{\mathrm{T}} = {}^{n}\hat{\boldsymbol{\sigma}} + \hat{\mathbf{C}}^e ({}^{n+1}_{n}\hat{\boldsymbol{\varepsilon}})$
3) Check the yield condition: $\phi = \left(\sum_{(s)} \left| \frac{\tau^{(s)}}{\tau_c^{(s)}} \right|^a \right)^{1/a}$

i. if $\phi \leq 1$, elastic, $\begin{cases} {}^{n+1}\boldsymbol{\sigma} \leftarrow \boldsymbol{\sigma}^{\mathrm{TR}} \\ \lambda = 0 \end{cases}$

ii. if $\phi > 1$, plastic, go to iterative procedure

4) Iterative procedure:

i. Initialization $\begin{cases} \hat{\boldsymbol{\sigma}}_i \leftarrow \hat{\boldsymbol{\sigma}}^{\mathrm{T}} \\ \lambda = 0 \end{cases}$

ii. Recover CRSS ($\tau_c^{(s)}$) values from the last step. For the first step, $\tau_c^{(s)} = \dfrac{A}{m} - \dfrac{B}{m}$ is a plausible starting value;

iii. For every sub-step of the multistage return mapping algorithm (Appendix B),

Do while $\phi - \phi^* > Tol$

a. Calculate $\Delta\lambda$, equation (4.77);

b. $\lambda = \lambda + \Delta\lambda$

c. $\hat{\boldsymbol{\sigma}}_{i+1} = \hat{\boldsymbol{\sigma}}_i - \Delta\lambda \hat{\mathbf{C}}^e \dfrac{\partial \phi}{\partial \hat{\boldsymbol{\sigma}}}$

d. $\tau_c^{(s)}\big|_{i+1} = \tau_c^{(s)}\big|_i + \Delta\lambda \sum_{(b)} H_{sb} \dfrac{\partial \phi}{\partial \tau^{(b)}}$

e. $\phi = \left(\sum_{(s)} \left| \dfrac{\tau^{(s)}}{\tau_c^{(s)}} \right|^a \right)^{1/a}$

5) Grain convergence

i. Update new (hardened) values of CRSS ($\tau_c^{(s)}$) for the next step;

ii. Texture evolution – update $\mathbf{P}_3$ matrix for the current grain;

iii. Rotate the converged stress value from lattice to local frame, using equation (4.10).

Back to Gauss point (macro) level

6) Update the averaged macroscopic stress: $\boldsymbol{\Xi} = \dfrac{1}{n_{grains}} \sum_{g=1}^{n_{grains}} \boldsymbol{\sigma}^g$

4.6 Iso-Error Maps for Polycrystal Plasticity

In order to estimate the accuracy and stability of stress integration algorithms, iso-error maps are frequently utilized as in Simo and Taylor (1986) or Yoon et al. (1999a). In this work, they are utilized to infer about the accuracy of the stress return algorithm used in the polycrystal model herein presented.

Consider the three representation stress points: A (uniaxial), B (biaxial) and C (pure shear), as shown in Figure 4-13. Without loss of generality, it is assumed that $\varepsilon_{12} = 0$ and consequently $\sigma_{12} = 0$. Additionally, no hardening is considered so the yield surface does not expand. According to these assumptions $\boldsymbol{\sigma}$ can be represented by a position vector in the principal stress plane.

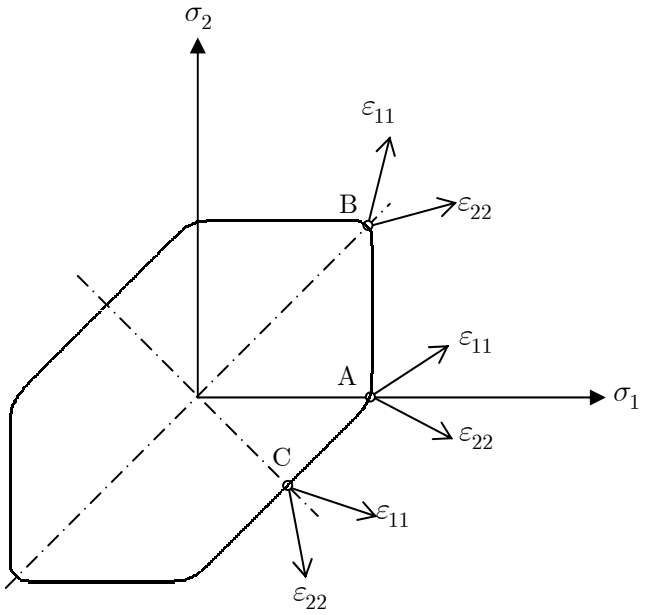

Figure 4-13: Points for iso-error maps (a=12).

Strain increments ($\boldsymbol{\varepsilon}$) ranging up to six times the yield strain ε_Y are applied to the three stress points, respectively. The iso-error maps are drawn based on $ERR(\%)$, equation (4.78), meaning the percentage of the relative root mean square of errors, between a computed stress $\boldsymbol{\sigma}$ and an exact stress $\boldsymbol{\sigma}^*$. The exact stress, due to the lack of an analytic solution, is obtained using 1000 sub-increments.

$$ERR(\%) = \frac{\sqrt{(\boldsymbol{\sigma} - \boldsymbol{\sigma}^*) : (\boldsymbol{\sigma} - \boldsymbol{\sigma}^*)}}{\sqrt{(\boldsymbol{\sigma}^*) : (\boldsymbol{\sigma}^*)}} \times 100 \tag{4.78}$$

Computations are carried out using the grain-level plasticity model of equation (4.35) with the (a) paramater chosen as 12, generating the yield surface for an aluminum alloy (Gambin and Barlat, 1997) drawn in Figure 4-13.

Figure 4-14 to Figure 4-16 show the iso-error maps for the three distinct cases. Even though a non-quadratic and highly nonlinear yield function is tested, the level of error observed is roughly equivalent to that previously reported in literature for other return mapping algorithms for continuum level quadratic yield functions. The error at the biaxial stress state (B point) is smaller than the uniaxial or shear stress state. Such fact agrees with earlier results (Simo and Taylor, 1986). However, the proposed algorithm shows a stable convergence for the entire test region. The magnitude of error is found to be within an acceptable range.

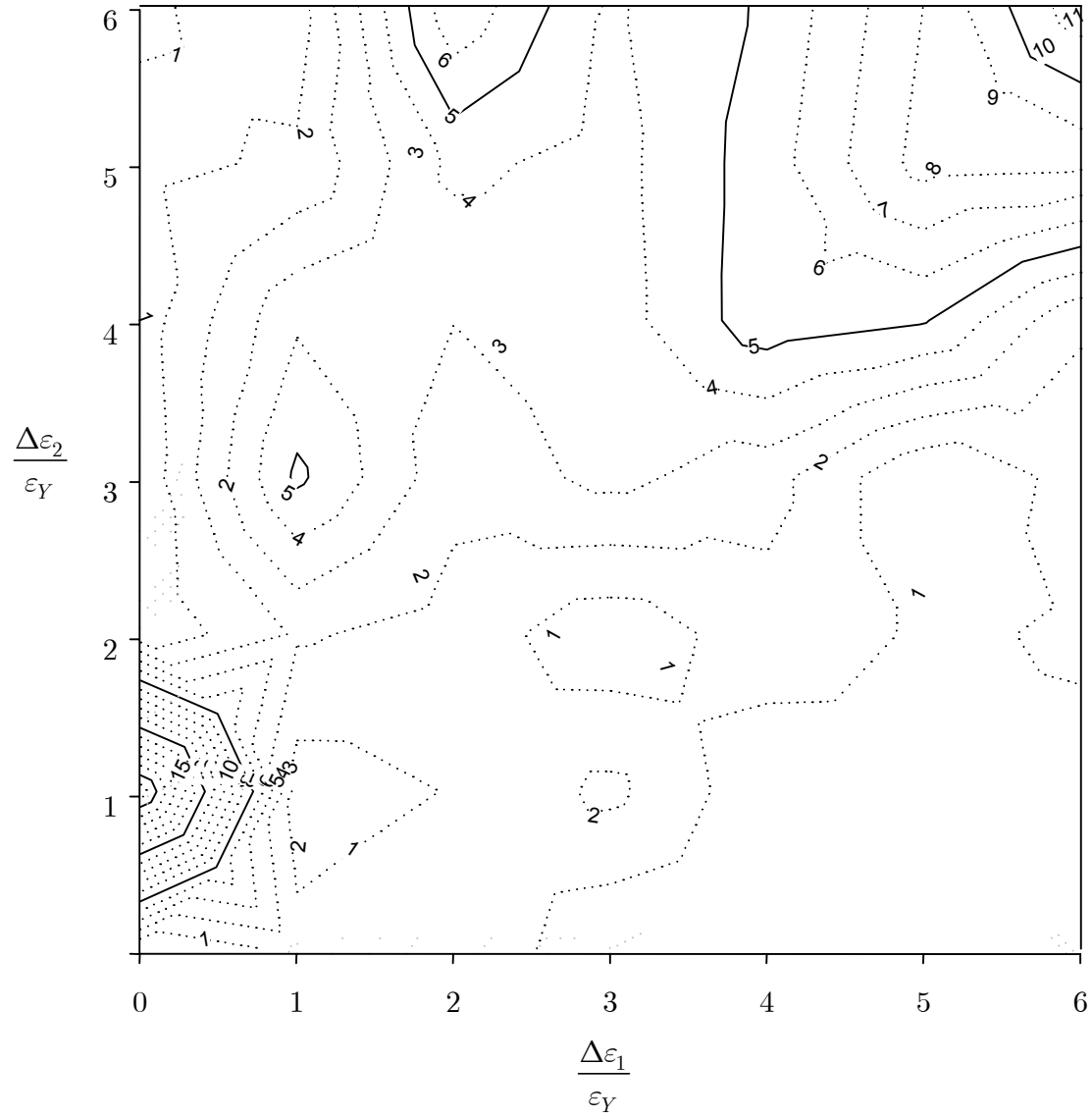

Figure 4-14: Iso-error map corresponding to point A (uniaxial stress).

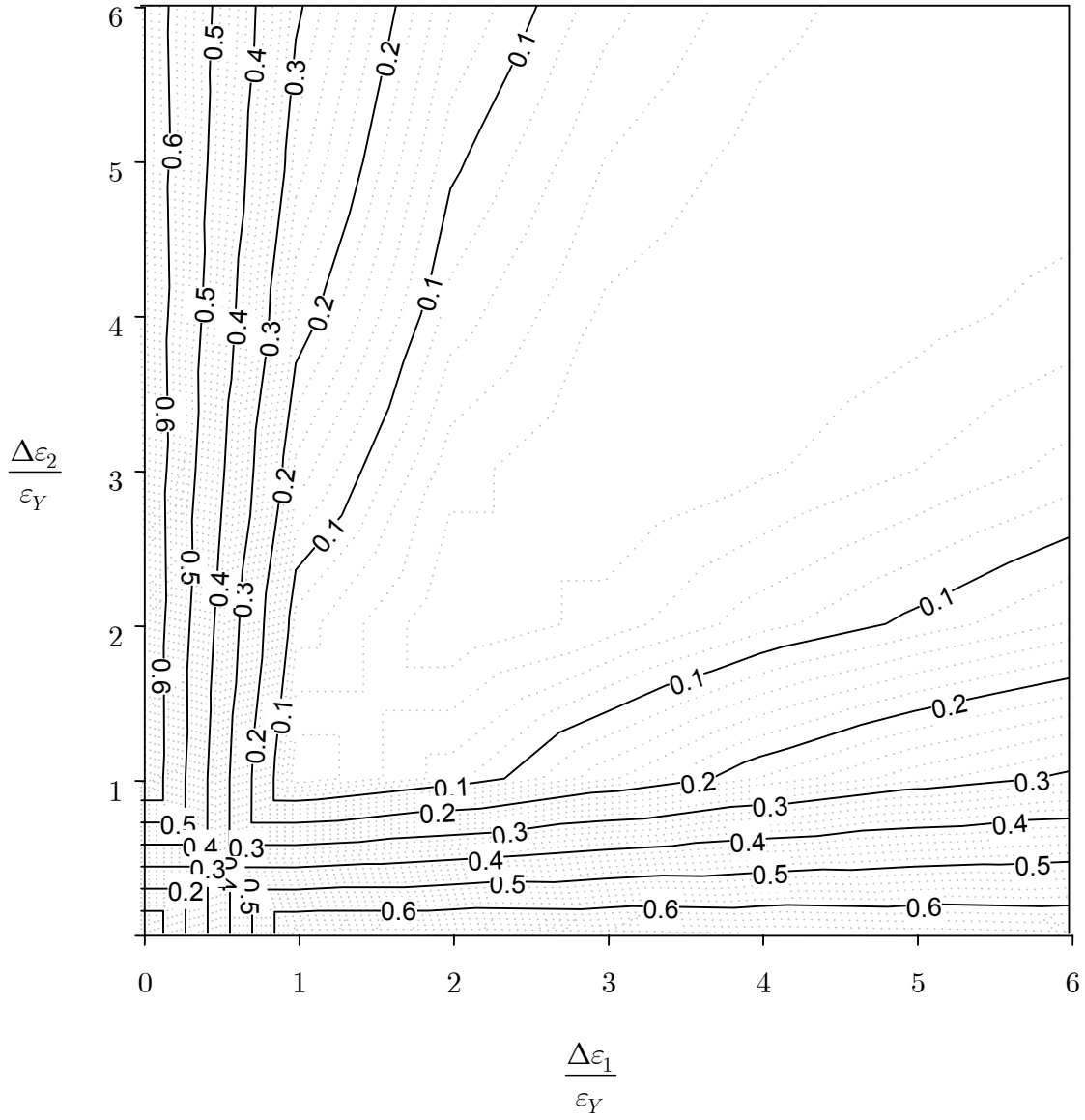

Figure 4-15: Iso-error map corresponding to point B (biaxial stress).

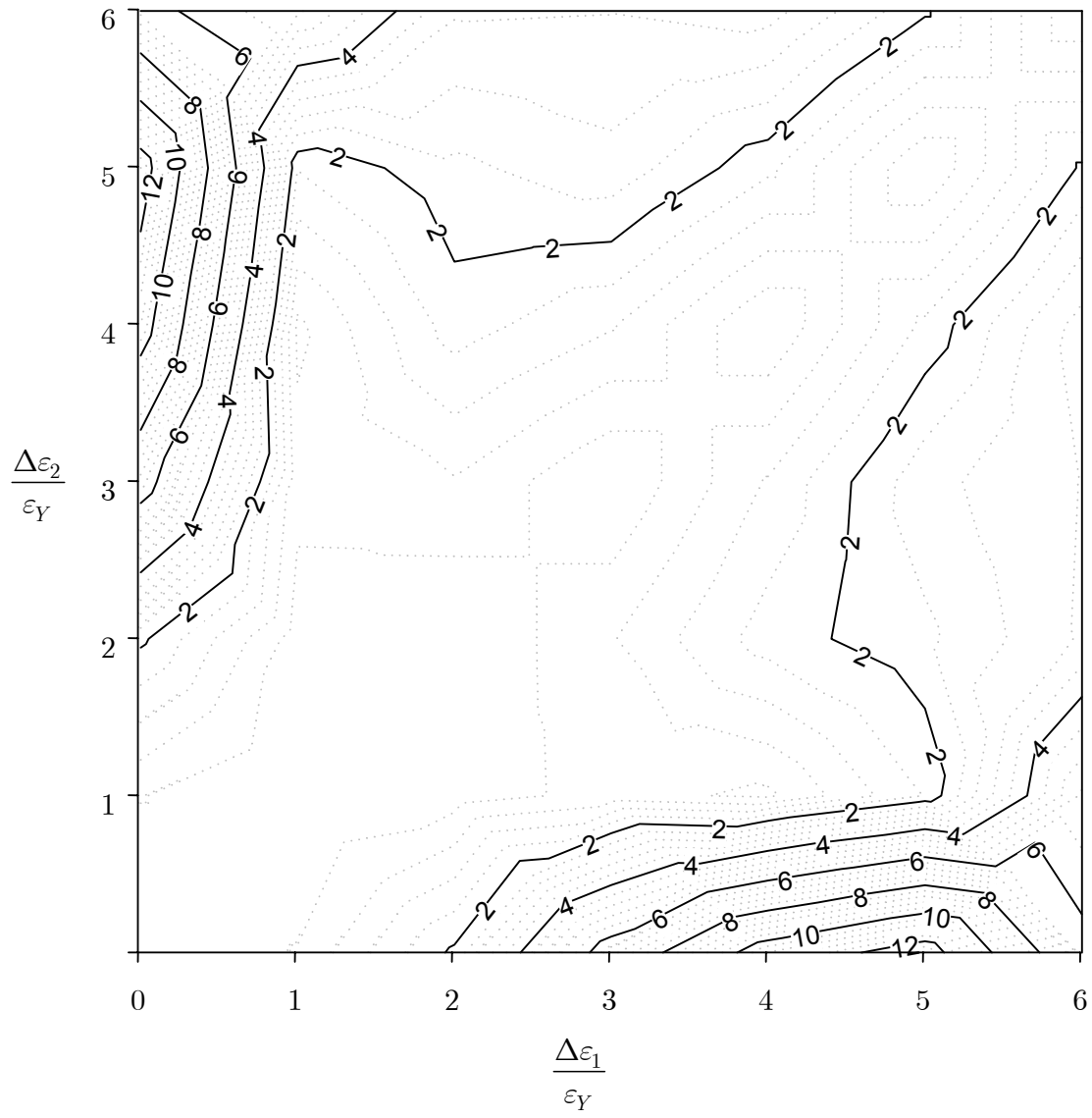

Figure 4-16: Iso-error map corresponding to point C (shear stress).

Chapter 5

Numerical Tests

Numerical tests are carried out in order to evaluate the performance and accuracy of the proposed RESS solid-shell finite element. A wide-range of benchmark studies are conducted including classical linear examples, geometrically nonlinear problems involving large displacements and rotations and finally complex applications involving plastic anisotropy and contact. Intrinsically, the adopted (and implemented) nonlinear material and geometric procedures are tested. Solutions taken from the literature are used for comparison purposes, and a complete characterization of the capabilities of the proposed solid-shell element is achieved.

5.1 Introductory Remarks

The RESS solid-shell element is currently implemented under the platform of a general implicit in-house research code called CEREBRO, developed by Cardoso (2004). For comparison purposes, the following conventions are defined. Otherwise, authors' names are specified.

Solid Elements:

- Disp – Standard eight-node brick element with 2×2×2 numerical integration scheme as detailed for instance in Hughes (2000);
- HCiS12 –Fully integrated EAS solid-shell element with 12 internal variables proposed in Alves de Sousa et al. (2003b);
- QS(N)/E9 and QS/E12 – Eight-node fully integrated EAS elements with 9 and 12 internal variables respectively proposed by Korelc (1996);

- H1/ME9 – Mixed-Enhanced fully integrated eight-node element with 9 enhanced modes, proposed by Kasper and Taylor (2000).

Shell elements:

- S4E6P7 – Fully integrated EAS element, proposed by César de Sá *et al.* (2002);
- MITC4 – Fully integrated and mixed interpolated bilinear element proposed by Dvorkin and Bathe (1984);
- EAS7-ANS – Bilinear in-plane enhanced shell element proposed by Andelfinger and Ramm (1993);
- CYSE – One point quadrature shell element with physical hourglass control proposed by Cardoso et al. (2002) and Cardoso and Yoon (2005a).
- 7PCYSE – An improvement of CYSE element accounting for through-thickness stretch (Cardoso and Yoon, 2005b)

Some examples do not have dimensional units, however the units used are consistent and any unit system can be accommodated. The number of integrations points for RESS element will vary to show solution differences, except in linear elastic cases where it has no influence on results. In some examples, to obtain simple support boundary conditions, and since the solid element have only translational degrees of freedom, only the bottom nodes are restrained, allowing in this form the rotation of upper nodes.

5.2 Linear Elasticity

Although involving simple geometries, loading and boundary conditions, the following linear problems can give a deep insight into the accuracy and robustness of the proposed element formulation. To do so, problems enforcing locking situations are studied as well as mesh distortion effects. Also, the solution convergence from coarse meshes to refined ones is compared with well-established approaches.

5.2.1 Morley's 30° skew plate

Originally proposed by Morley (1963), this plate example is conducted in order to analyze the sensitivity to mesh distortions, as well the ability to avoid membrane and transverse shear locking phenomena. The geometry possesses a low thickness to length ratio (L/t=1/100) and the elements are uniformly distorted (Figure 5-1). The plate is simply supported and subjected to a uniform pressure (Q). The data of the problem is based on the work of Andelfinger and Ramm (1993).

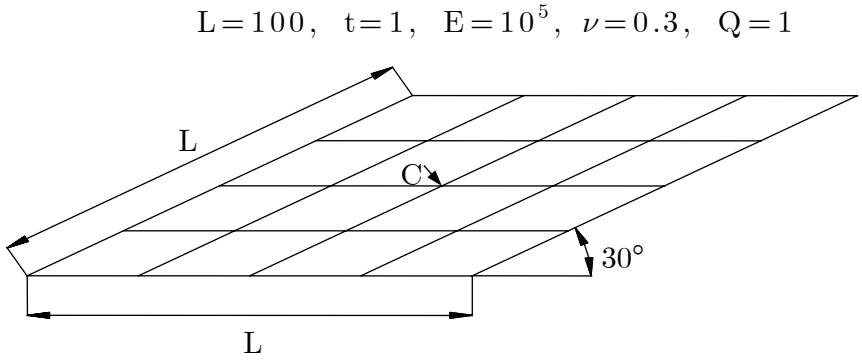

Figure 5-1: Morley's 30° skew plate (4 elements per side).

The Kirchhoff reference solution of 4.455 for the deflection at the plate's center (point C) presented by Morley, is replaced by the value of 4.640 (Andelfinger and Ramm, 1993) since for this thickness to length ratio (1/100), shear deformation effects should not be neglected. The normalized results are summarized in Table 5-1.

Elements per side	**4**	**8**	**16**	**32**
Disp	0.021	0.069	0.176	0.340
HCiS12	0.971	0.953	0.964	0.986
RESS	**0.978**	**0.960**	**0.970**	**0.987**
S4P6E7	0.972	0.956	0.966	0.983
CYSE	0.944	0.908	0.922	0.959
MITC4	0.844	0.840	0.902	0.950
EAS7-ANS	0.908	0.910	0.943	0.966

Table 5-1: Morley's skew plate: Normalized values for the central vertical deflection.

The presented formulation leads to excellent results, even for coarse meshes. Mesh convergence to the reference solution is achieved.

5.2.2 Clamped square plate with concentrated load

In the following example, several factors inducing locking problems are put together in analysis. In Figure 5-2, a clamped square plate loaded by a concentrated load (F) is represented. For the sake of simplicity, one quarter of the geometry is analyzed, using meshes of 2×2 and 4×4 elements. The results are normalized against the analytical solution (Table 5-2) of the Kirchhoff plate theory. Firstly, results using regular meshes and Poisson values for compressible and near-incompressible behaviors are studied, as well thickness to length ratios (1/100 and 1/1000).

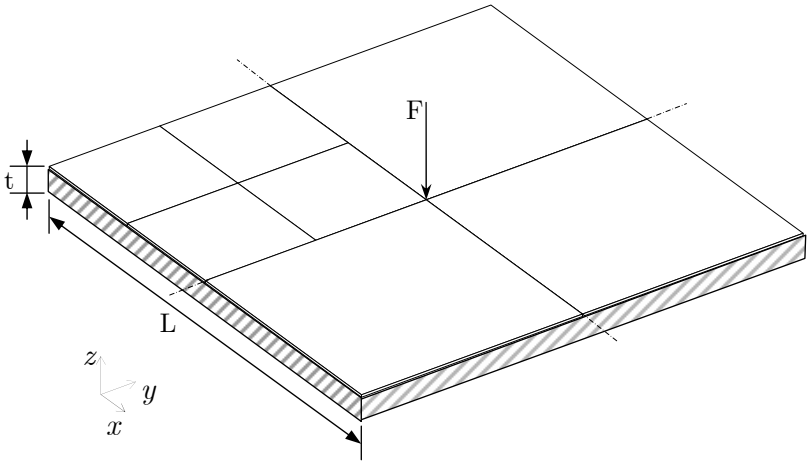

Figure 5-2: Clamped square plate under concentrated load (2×2 mesh).

Normalized results ($\nu = 0.3$)

t/L	Mesh	Theory	**RESS**	HCiS12	S4E6P7	MITC4	CYSE
1/100	2×2	1.000	**0.893**	0.869	0.869	0.868	0.884
	4×4	1.000	**0.978**	0.970	0.971	0.969	0.975
1/1000	2×2	1000	**0.886**	0.866	0.866	0.814	0.828
	4×4	1000	**0.975**	0.966	0.966	0.966	0.971

Normalized results ($\nu = 0.499$)

t/L	Mesh	Theory	**RESS**	HCiS12	S4E6P7	MITC4	CYSE
1/100	2×2	0.827	**0.906**	0.875	0.875	0.819	0.829
	4×4	0.827	**0.984**	0.973	0.974	0.970	0.973
1/1000	2×2	827.0	**0.896**	0.868	0.870	0.816	0.827
	4×4	827.0	**0.976**	0.968	0.968	0.965	0.970

Table 5-2: Normalized displacements for the clamped square plate.

The proposed formulation provides the best solution both in situations of near incompressibility and/or involving very small thickness, where volumetric and transverse shear locking would be expected.

In a second phase, a study of mesh distortion effects is performed. Accordingly, the central node of the 2×2 mesh is translated by the quantity Δ, as shown in Figure 5-3. Material properties are maintained (E=10000; ν=0.3) and geometry is selected such as t/L=1/100.

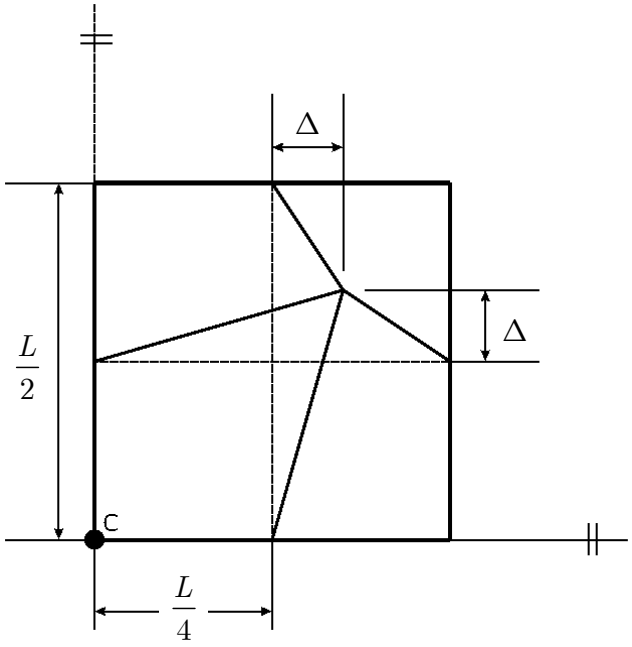

Figure 5-3: Mesh distortion analysis for the clamped square plate.

The normalized results from Table 5-3 show the reduced mesh distortion sensitivity of RESS, even with critical shape changes ($\Delta = 12.5$).

Δ	**0**	**2.5**	**5**	**7.5**	**10**	**12.5**
RESS	**0.893**	**0.888**	**0.871**	**0.846**	**0.814**	**0.777**
HCiS12	0.869	0.825	0.771	0.712	0.655	0.606
CYSE	0.884	0.879	0.862	0.830	0.780	0.703
MITC4	0.867	0.863	0.847	0.816	0.760	0.681
S4E6P7	0.869	0.827	0.774	0.717	0.663	0.616
QS/E9	0.073	0.066	*	*	*	*
QS/E12	0.874	0.514	*	*	*	*

Table 5-3: Evolution of results with increasing distortion level Δ.

5.2.3 Scordelis-Lo roof problem

The original problem from Scordelis and Lo (1969) reports to a cylindrical shell with radius R, length L and thickness t, supported by rigid diaphragms at the curved edges. The structure is subjected to dead (self-weighted) load (Figure 5-4). Due to its symmetry, only one quarter of the model is studied.

The midpoint free edge's (point D) vertical displacement is assessed. Table 5-4 presents values normalized by the reference solution of 0.3024 (Belytschko and Leviathan, 1994).

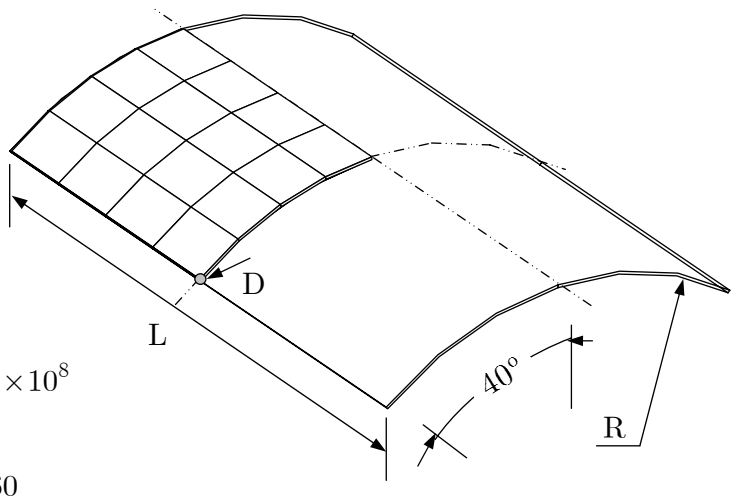

L=50 E=4.32×10^8
R=25 ν=0.0
t=0.25 ρg = 360

Figure 5-4: Scordelis-Lo roof geometry.

Elements per side	**4**	**8**	**16**	**32**
HCiS12	0.937	0.974	0.990	0.995
RESS	**0.995**	**0.986**	**0.993**	**0.996**
S4E6P7	1.001	1.002	0.992	0.993
MITC4	0.937	0.973	0.993	*
EAS7-ANS	1.041	1.006	1.002	*
CYSE	0.942	1.008	1.005	1.006

Table 5-4: Scordelis-Lo roof normalized deflection at free edge's midpoint (D).

It can be concluded that all elements perform well, even for coarse meshes. Nevertheless, is worth to remark that the RESS element shows compatible accuracy with shell elements.

5.2.4 Pinched cylinder with end diaphragms

This recognized shell benchmark is illustrated in Figure 5-5. For analysis purposes, one eighth of a cylindrical shell with radius R, length L, thickness t and containing rigid diaphragms at the end edges is studied. The elastic material data is also shown in Figure 5-5. The whole structure is subjected to a pair of concentrated loads F=1. Poor mesh convergence, for a considerable range of finite elements in the literature is associated to this example. Table 5-5 presents normalized results for the vertical displacement in the loaded point (reference solution:1.82488×10^{-5}),

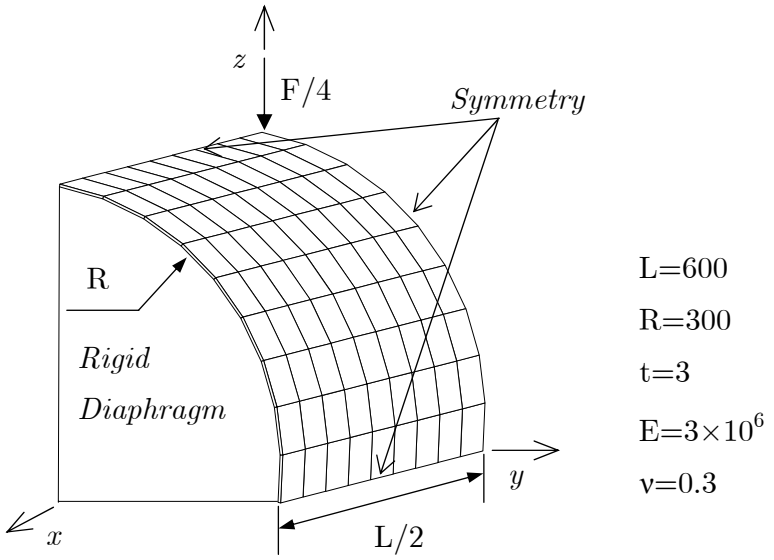

Figure 5-5: Pinched cylinder with end diaphragms.

Mesh	**RESS**	HCiS12	H1/ME9	S4E6P7	CYSE	MITC4
4×4	**0.112**	0.104	0.107	0.392	0.406	0.370
8×8	**0.590**	0.494	0.496	0.746	0.862	0.728
16×16	**0.933**	0.912	0.914	0.923	1.080	0.930
32×32	**0.998**	0.995	0.992	0.982	1.080	0.971

Table 5-5: Normalized values for central vertical displacement for the pinched cylinder.

The RESS element attains the reference solutions using a moderately refined mesh, and shows good mesh convergence properties.

Additionally, mesh distortion effects in curved shells are also studied in this example. Accordingly, regular meshes of 8×8, 16×16 and 32×32 elements are distorted utilizing a bias factor of 10, as illustrated in Figure 5-6. Corresponding results are listed in Table 5-6.

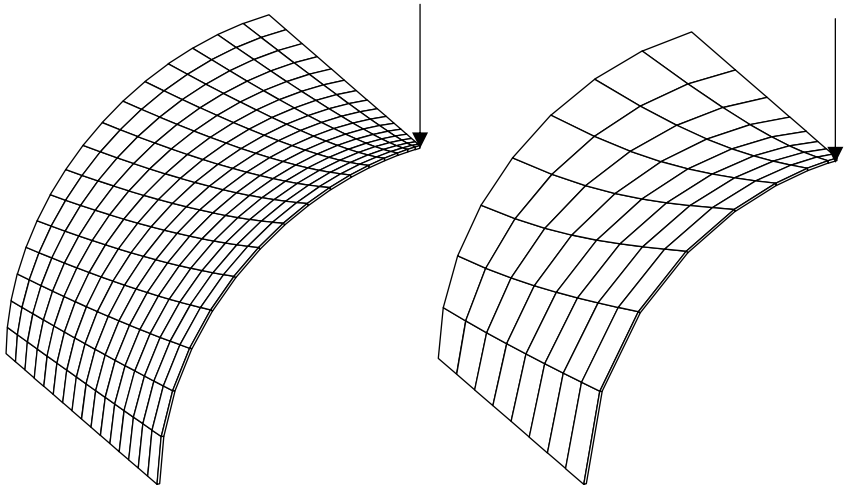

Figure 5-6: Distorted meshes for pinched cylinder example (Bias=10).

Mesh	**RESS**	HCiS12	CYSE	S4E6P7	MITC4
8×8	**0.735**	0.686	0.807	0.768	0.787
16×16	**0.957**	0.943	0.949	0.938	0.943
32×32	**1.002**	*	*	*	*

Table 5-6: Normalized values for central vertical displacement for the pinched cylinder (Bias=10).

5.2.5 Partly clamped hyperbolic paraboloid

This interesting bending-dominated test was introduced in the work of Chapelle and Bathe (2000) and further developed in Bathe et al. (2000). Briefly, this case study is a self-weighted hyperbolic paraboloid shell structure, clamped at one edge, and free at the others, as represented in Figure 5-7. By symmetry reasons, only one half of the geometry is considered. Additional details on this problem can be found for instance in the work of Chapelle and Bathe (2000).

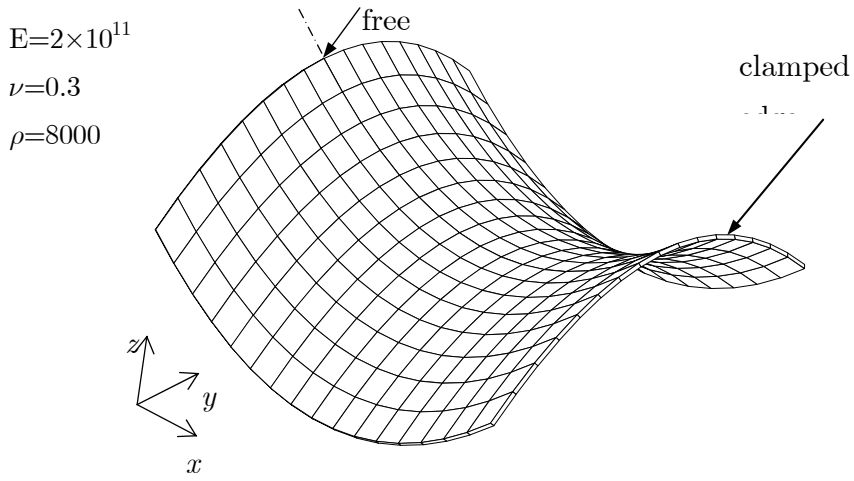

Figure 5-7: Hyperbolic paraboloid shell structure.

For modeling purposes, mesh sequences of $N \times N/2$ elements (N=8,16,32,64) are considered. Thickness to length ratios of 1/100, 1/1000 and 1/10000 are employed, following the suggestion of Bathe et al. (2000). Given that there is no analytical solution for this problem, reference values for the total strain energy are those

obtained from the same author, using a high order shell element and a refined mesh. In Figure 5-8 to Figure 5-10, strain energy error values (E_r) from other formulations' results (E_h) are put against the reference solution (E), for thickness to length ratios of 1/100, 1/1000 and 1/10000, respectively.

$$E_r = 1 - \frac{E_h}{E} \tag{5.1}$$

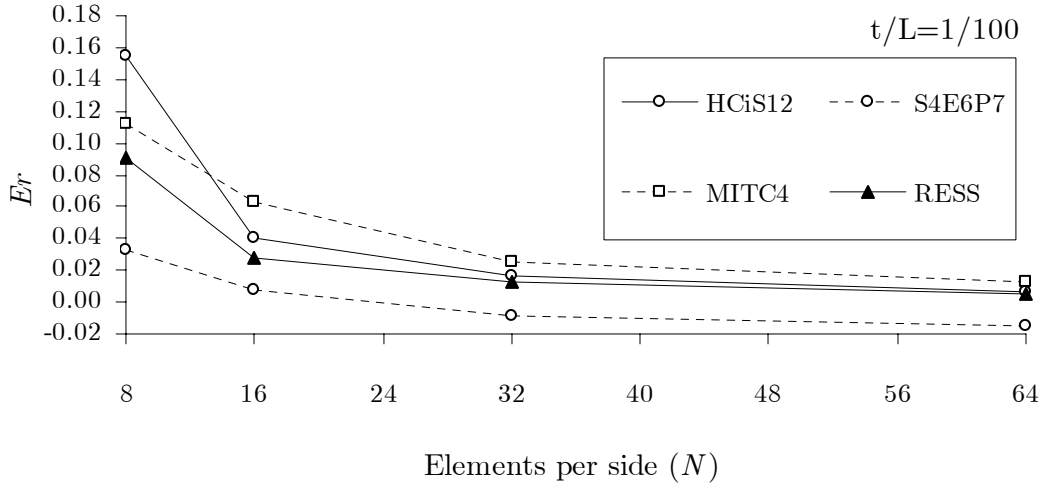

Figure 5-8: Energy error for hyperbolic paraboloid structure (t/L=1/100).

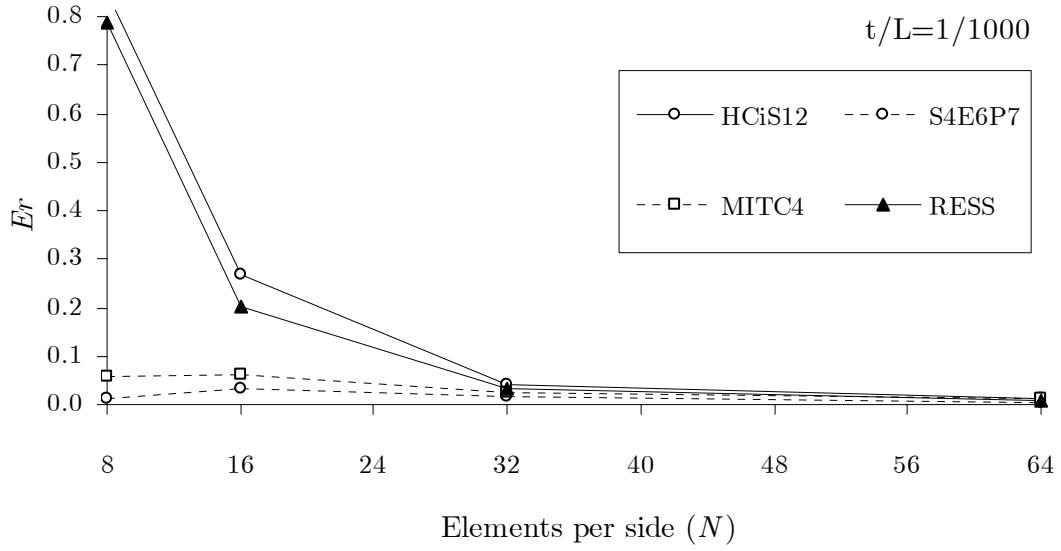

Figure 5-9: Energy error for hyperbolic paraboloid structure (t/L=1/1000).

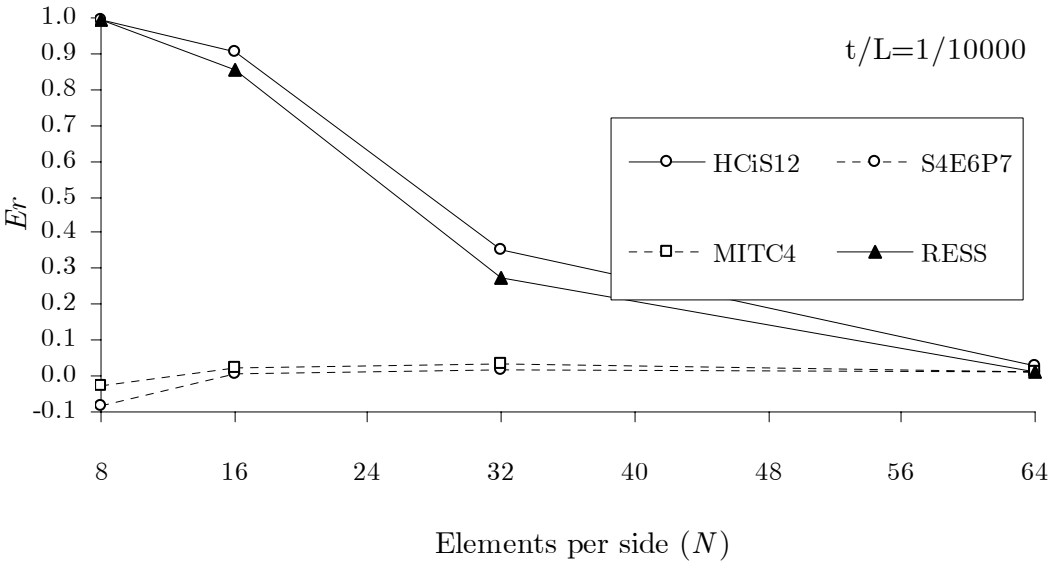

Figure 5-10: Energy error for hyperbolic paraboloid structure (t/L=1/10000).

The reference solution is attained by RESS element in all cases. However, for the last 2 situations (1/1000 and 1/10000), the reference solution is achieved only employing more refined meshes when compared to shell elements.

5.3 Materially nonlinear examples

5.3.1 Simply Supported Square Plate under Pressure

This example includes plasticity in small deformation range. It was chosen to illustrate solution differences of RESS element when the number of integration points through the thickness is changed in a single element layer. Consider the square plate illustrated in Figure 5-2. Dimensions are altered (L=508, t=2.54) and loading is set to a pressure in the entire domain. The plate is simply supported all over its border. The material properties are elected considering a coherent system of units,

$$\begin{aligned} &\text{E}=6.9\times10^4 \\ &\nu=0.3 \\ &\sigma_Y = 248 \\ &\text{H}=0 \end{aligned} \tag{5.2}$$

By considering symmetry, only one quarter of the model is analyzed, using a mesh of 5×5 elements with only one layer according to Ramm and Matzenmiller (1988). Simulation is performed with RESS element using two different integration schemes (3 and 7 points through thickness) in a single element layer, in order to show the importance of the number of integration points. In Figure 5-11, the central vertical displacement of the plate is plotted against the uniform pressure value. As a reference solution for shell, the result obtained from Ramm and Matzenmiller (1988) with seven integration points through the thickness direction is used. Fully integrated EAS element (Alves de Sousa et al., 2003a) with a single element layer (eight integration points: 2×2×2) is also plotted together for comparison purposes.

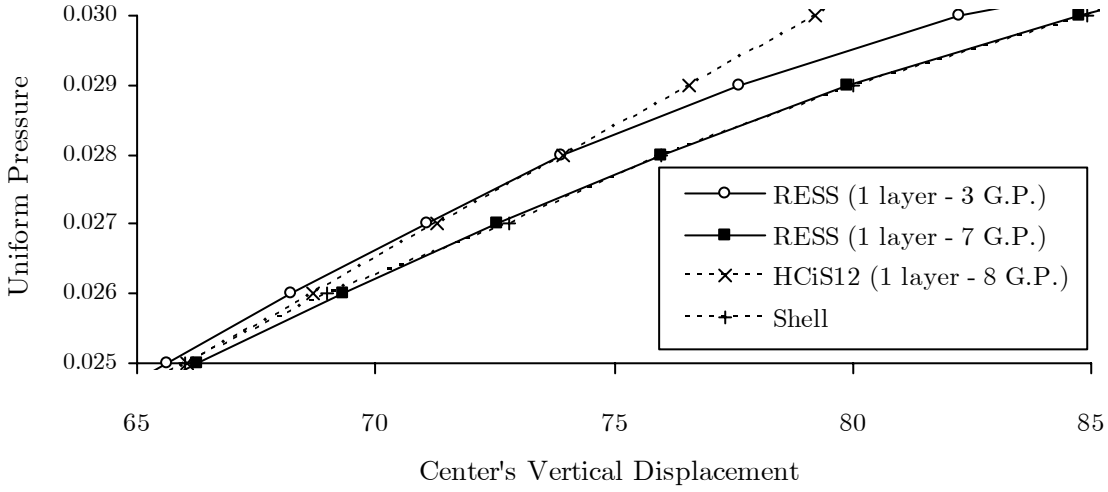

Figure 5-11: Square plate analysis (5×5 elements and 1 layer).

As can be seen in the figure, an excellent agreement with the shell solution is achieved when the same number of integration points is incorporated along thickness direction. However, the result based on three integration points shows deviation from the reference solution. Concerning the solid-shell HCiS12 element, since only two integration points through the thickness direction are allowed within a single layer, results are not accurate. In short, the total integration points used in the proposed element are seven (1×1×7) in order to accomplish the same solution than the shell.

5.3.2 Plate under transversal normal stress

The purpose of this test is to show the ability of the formulation evaluating the influence of a transversal normal stress on the thickness distribution, which is a simple analogy for the double sided contact which occurs on the blank holder in sheet metal forming processes. The model is composed by a square element with dimensions 1×1 and thickness 0.1, consistent units. Boundary conditions are expressed in Figure 5-12. The load set for this example is a prescribed displacement on top nodes of 0.5 and a uniform transverse normal stress (applied as pressure). The material data is: Young's modulus $\mathrm{E} = 2\times10^5$, Poisson's ratio $\nu = 0.3$, initial

yield stress $\sigma_0 = 3\times10^2$ and hardening modulus $\mathrm{H} = 1.2\times10^3$. In Figure 5-13, it is compared the thickness variation as function of the transverse normal stress. The transverse normal stress should affect the results. The proposed one point quadrature solid-shell element presents good behavior, compatible with the Abaqus 3D continuum element or with the shell element accounting for thickness deformation (7P-CYSE).

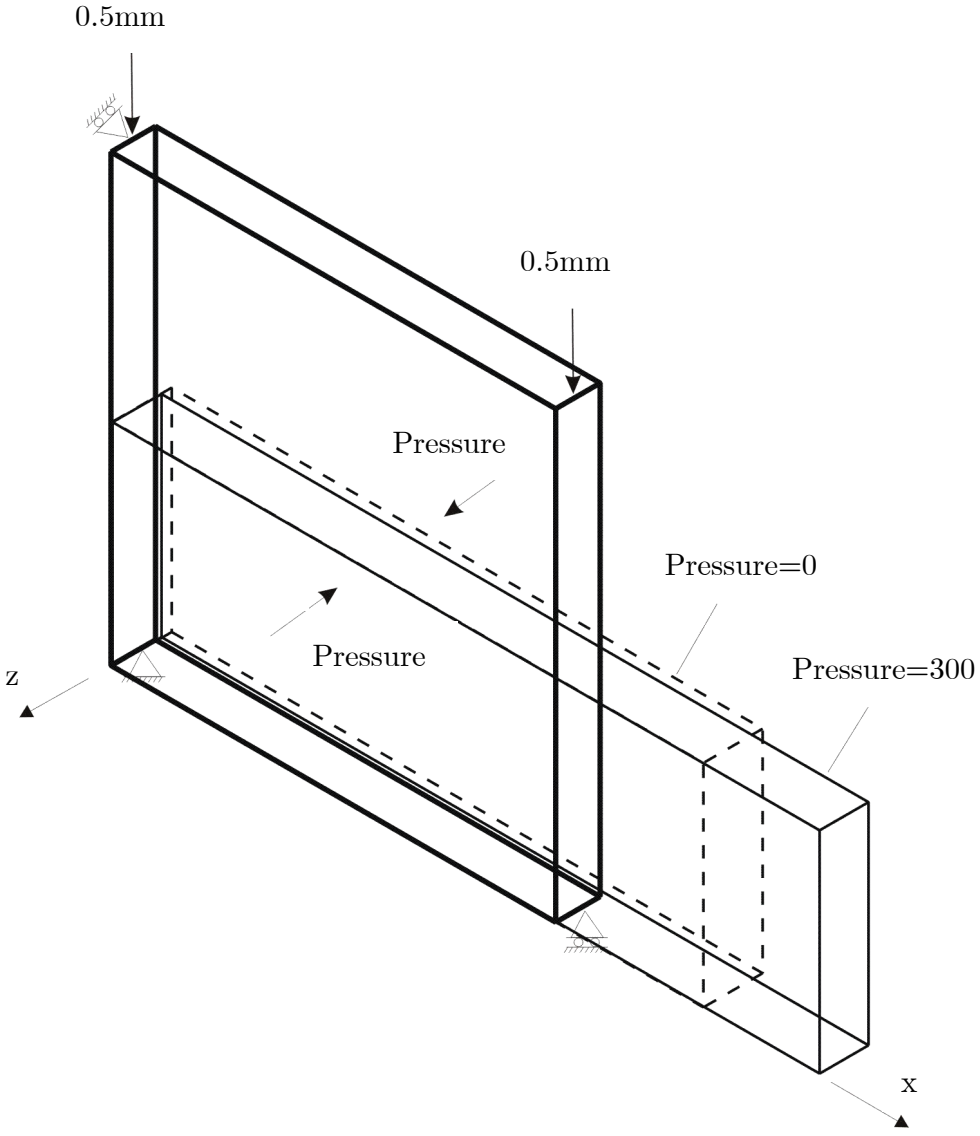

Figure 5-12: Plate under transversal normal stress – problem set up.

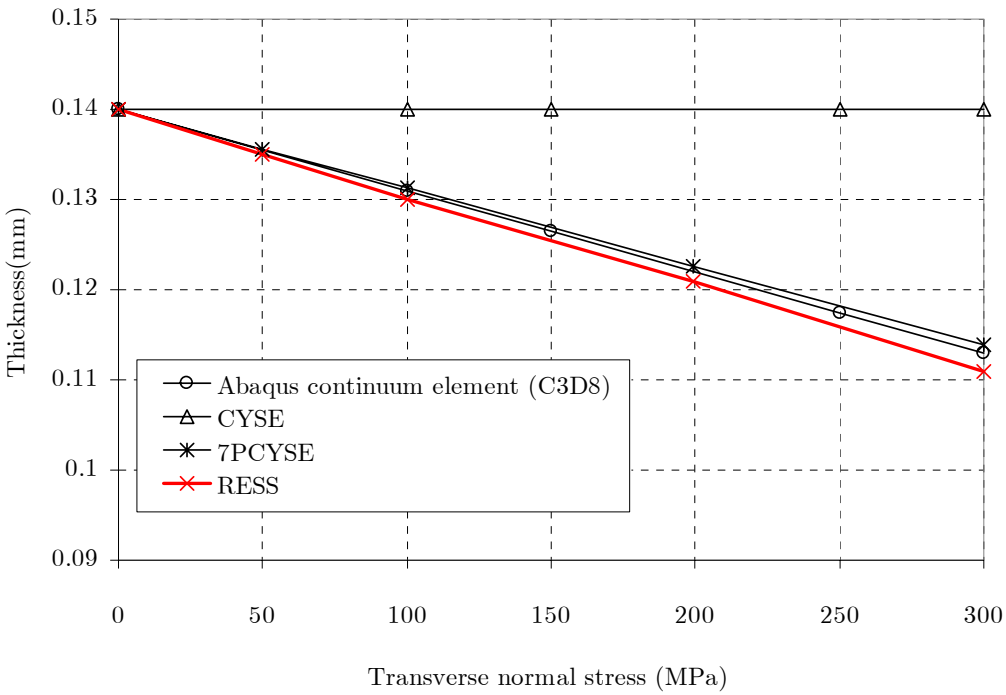

Figure 5-13: Plate under transversal normal stress – thickness variation.

5.4 Geometrically nonlinear but materially linear problems

5.4.1 Pinching of a clamped cylinder

In this test problem an elastic cylindrical shell, fully clamped at one end, is subjected to a pair of concentrated loads at its free end. Following references using shell and solid-shell elements (Brank et al., 1995; Fontes Valente et al. 2004), a regular mesh of 16×16 elements is employed as shown in Figure 5-14. Elastic constitutive parameters consists of Young modulus E=2.0685×10^{7} and Poisson's ratio $\nu = 0.3$. The length of the cylinder is L=3.048, mean radius R=1.016 and thickness a=0.03. The maximum nominal load is $F_{tot} = 1600.0$. Due to symmetry, only a quarter of the structure is analyzed. Results obtained from RESS element for

the deflection at the point under concentrated load (point A) are represented in Figure 5-15, and compared to those of Brank et al. (1995). It is clear that the presented results are in good agreement with those obtained from the reference. The deformed shape under the maximum load level is depicted in Figure 5-16.

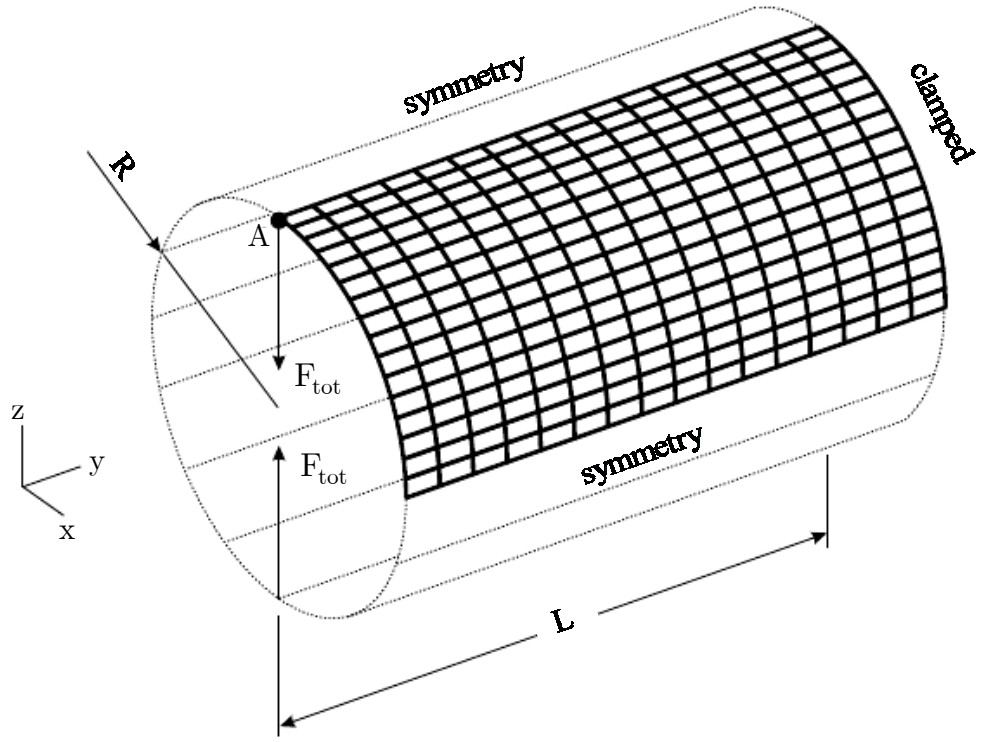

Figure 5-14: Clamped cylinder – Problem setup.

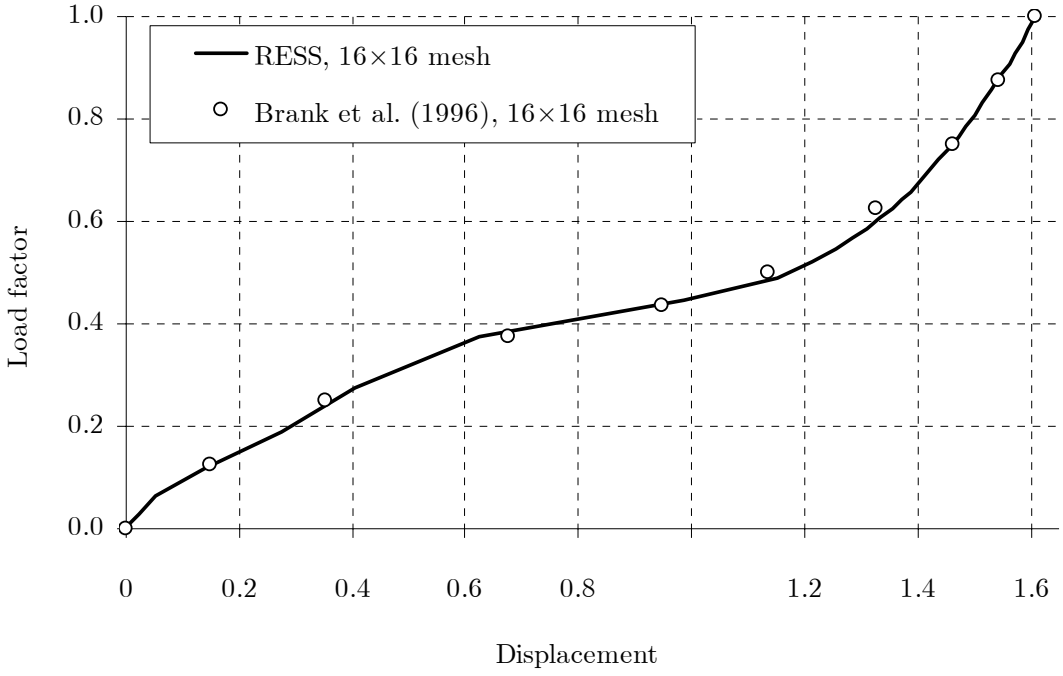

Figure 5-15: Clamped cylinder - Vertical displacement of point A.

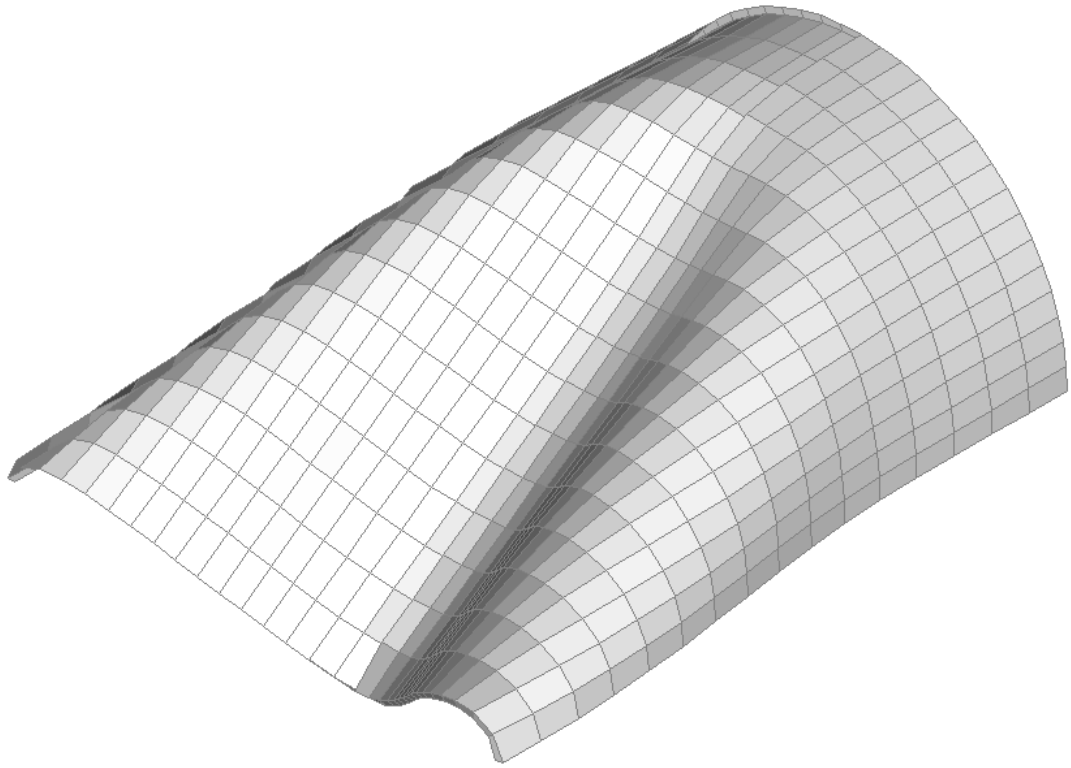

Figure 5-16: Clamped cylinder - Deformed configuration at maximum load level.

5.4.2 Snap through behavior of a shallow roof structure

As a classical buckling shell example, a snap-through and snap-back load-displacement path of a cylindrical shell is analyzed. The structure, schematically represented in Figure 5-17, is mapped with 5×5 RESS elements on a quarter of its surface, along with 2 elements over the thickness direction. The imposition of these two elements is only related to the proper reproduction of the hinged support at the straight edges. The input data for this problem is linear dimensions $L_1 = 508.0$ and $L_2 = 507.15$, nominal radius R=2540.0 and thickness a=6.35. Material parameters are taken as E=3102.75 and $\nu = 0.3$. The maximum load level attained is equal to $F_{tot} = 1000.0$. Vertical displacements at the points A and B are reproduced in Figure 5-18, plotted against the load level and compared to the solution of

Horrigmoe and Bergan (1978) based on a shell formulation. It is noticeable a very good agreement between the two solutions, along the entire unstable load-displacement path.

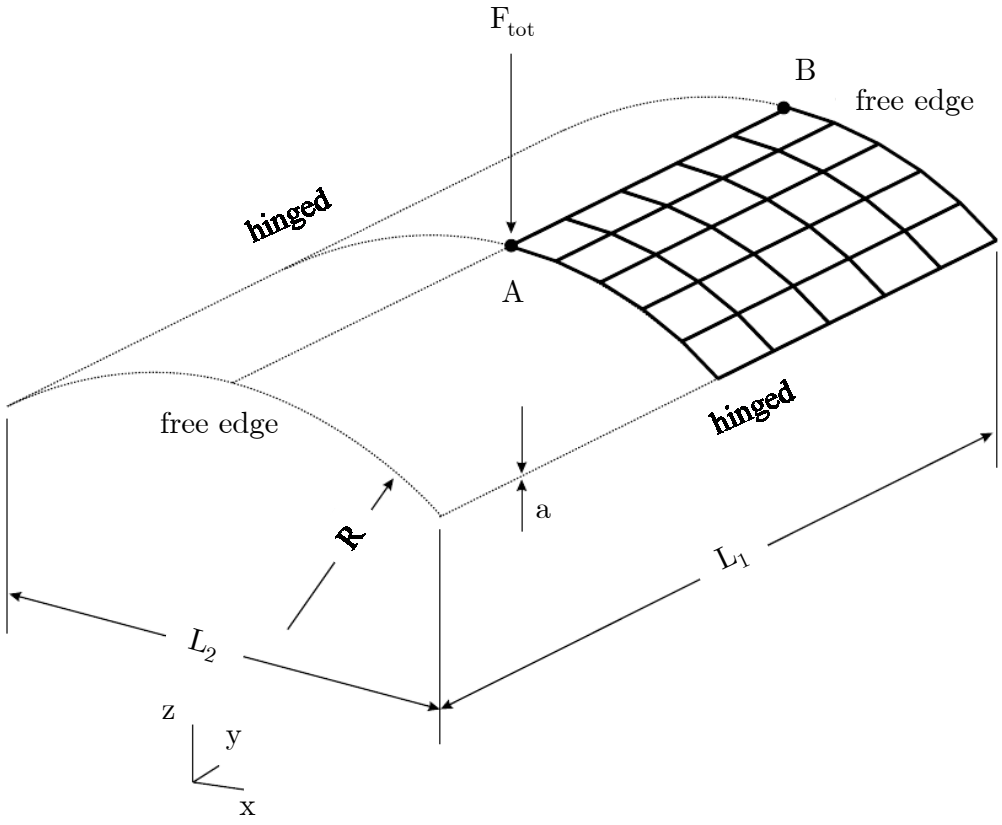

Figure 5-17: Roof structure - Problem setup

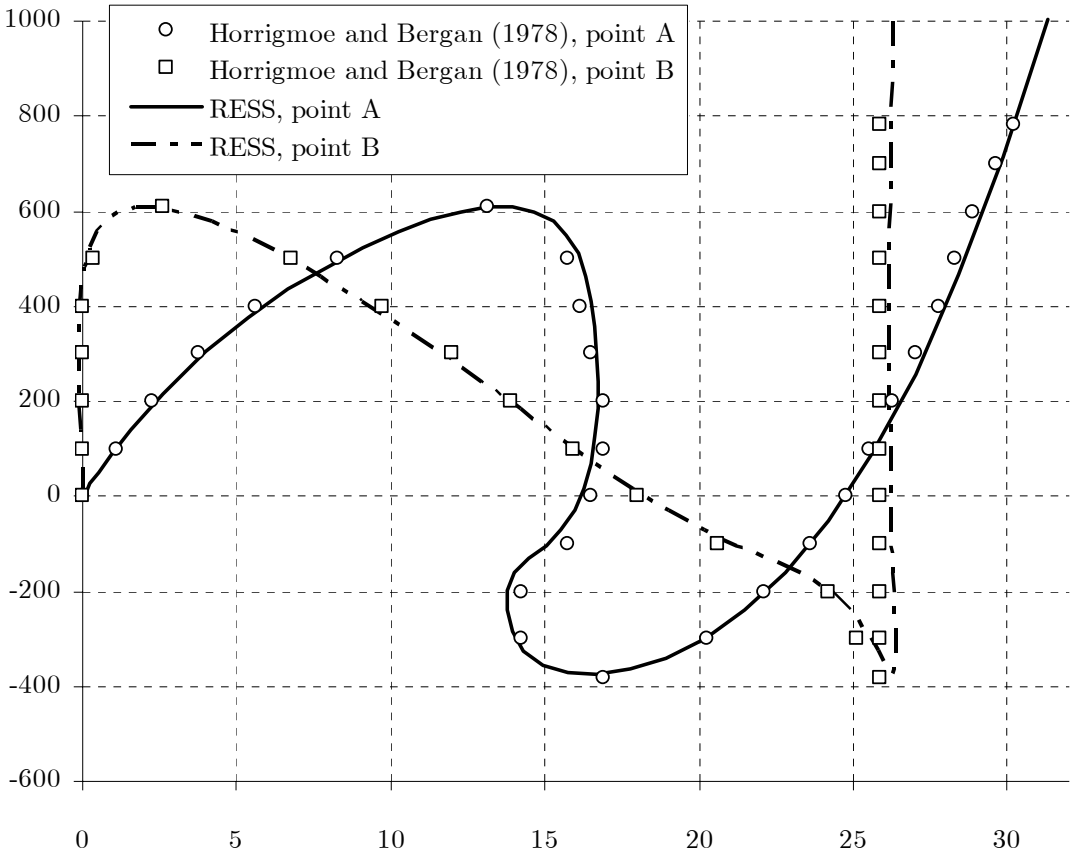

Figure 5-18: Roof structure - Vertical displacement at points A and B.

5.4.3 Torsion of a flat strip

The torsion of a flat strip is a typical example to test element warping, rotation and at the same time to illustrate robustness. A torsional moment is applied to the end of the initially flat strip, whereas the other end is clamped, leading to a large rotation of 180° at the tip of the deformed part. Contrary to shells, the applied torsional moment is here replaced by a couple of deformation-following concentrated loads. The material standard input data consists of Young modulus $\mathrm{E} = 12 \times 10^6$ and Poisson's ratio $\nu = 0.3$. For geometry, length L=1.0 and width w=0.25. In this work, two different ratios thickness/length are used: 1/10, as proposed originally by Simo et al. (1990), and 1/100, here introduced to increase the difficult level of the test. Initial, intermediate (90°) and deformed mesh

configurations are shown in Figure 5-19. This example clearly indicates the excellent performance of RESS element regarding the warping behavior even for a thin-walled structure.

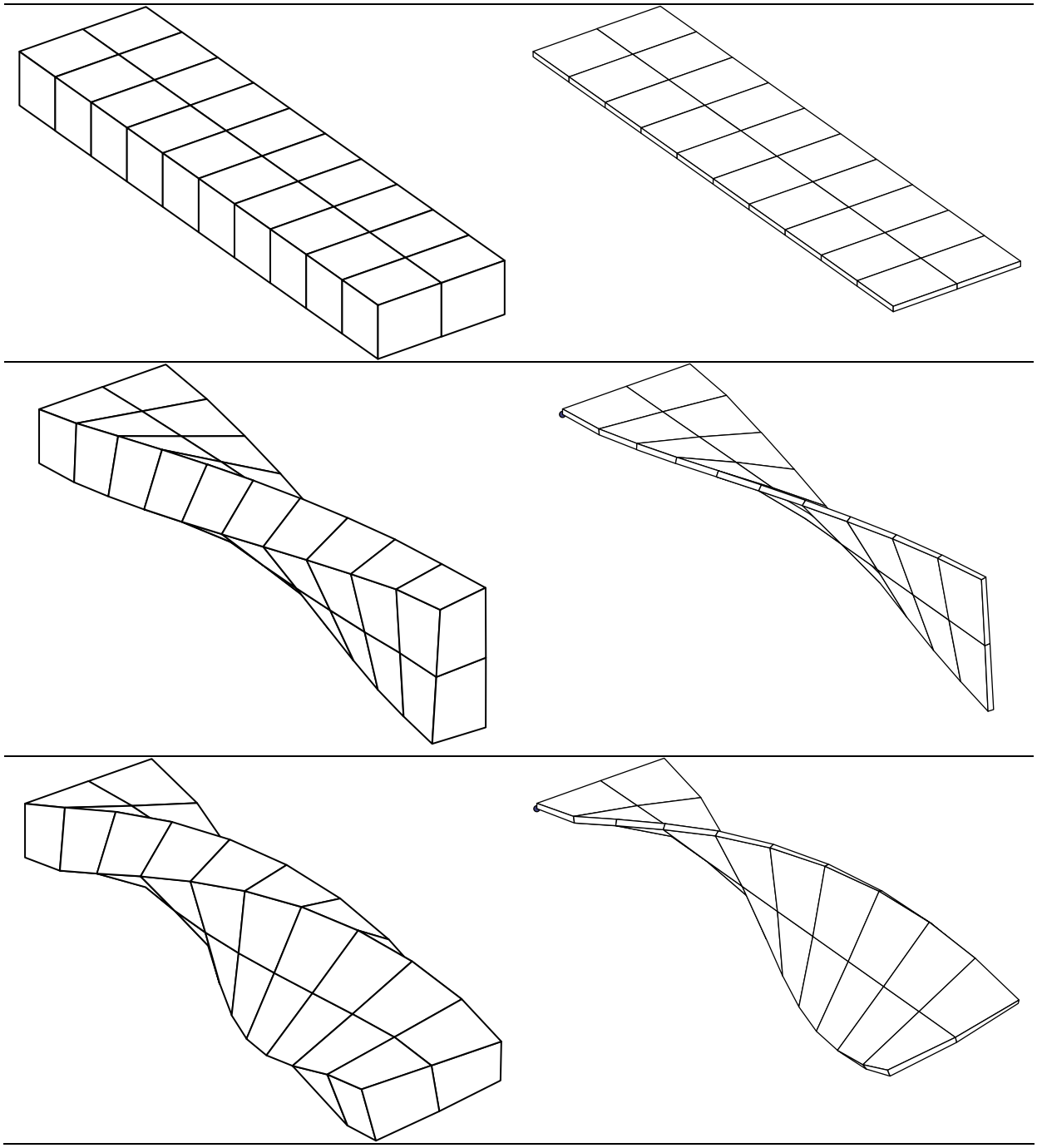

Figure 5-19: Torsion of a flat strip - Undeformed, 90° deformed and 180° deformed configurations.

5.5 Geometric and material nonlinear examples

5.5.1 Pinched hemispherical shell

This well-known nonlinear geometric hemispherical shell test, introduced by Simo et al. (1989), is now considered with the inclusion of elastoplastic effect. This combined nonlinear behavior has been previously investigated by Masud et al. (2000), based on reduced integrated solid elements and a corotational framework. Geometric and elastic parameters, as well as restraint conditions, follow the work of Simo et al. (1989), while a new set of plastic properties in coherent units (initial yield stress $\sigma_0 = 6.825 \times 10^5$; isotropic linear hardening $H_{iso} = 6.825 \times 10^6$) is introduced. The maximum load level is set to F=400.0, in opposition to the value of 200.0 in the original example. For the sake of comparison, results of Masud et al. (2000) using a mapped mesh of 18×18×2 are included in this work. In the present simulation, RESS is used with a coarser mesh of 16×16×1 elements.

Results of the absolute displacement along the OX and OY directions (traction and compression external loads, respectively) are represented in Figure 5-20. It is noticeable the good agreement between present and reference results, even resorting to a lower number of elements and integration points. The deformed configuration for the maximum load level is shown in Figure 5-21.

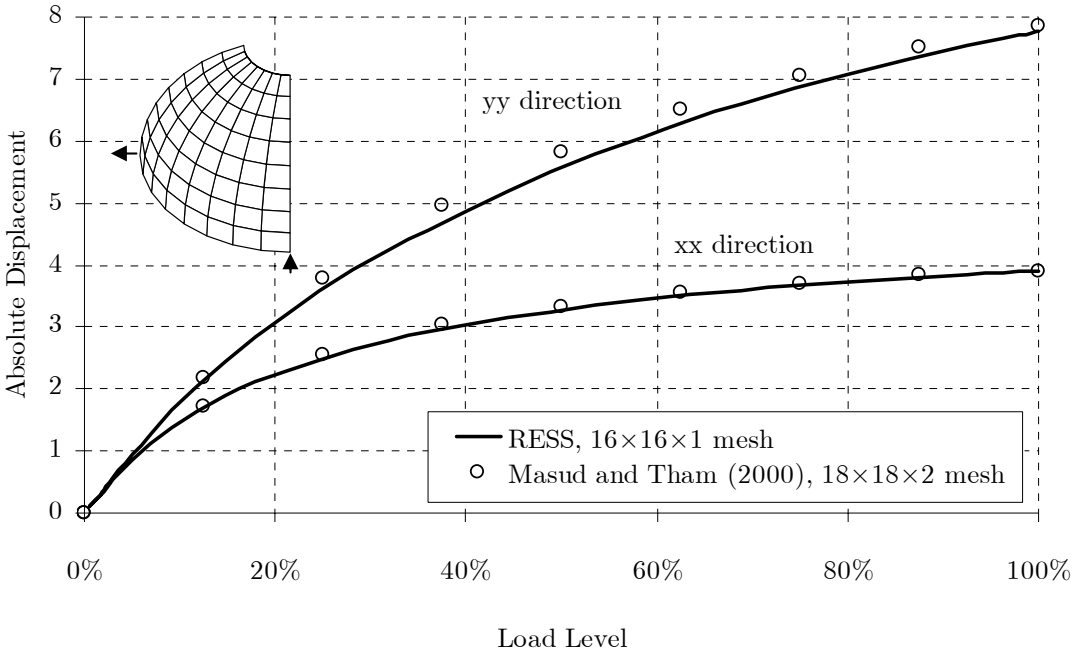

Figure 5-20: Pinched hemispherical shell - Inward and outward absolute displacements.

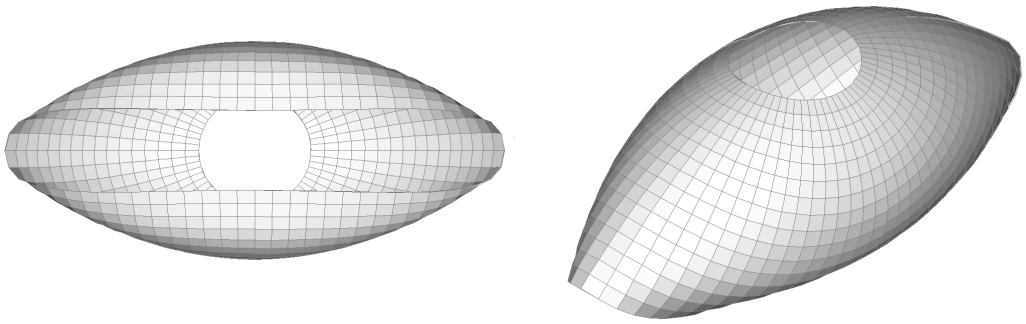

Figure 5-21: Pinched hemispherical shell - Bottom and isometric views (load level=100%).

5.5.2 Simply supported plate with pressure loads

In this test the inflation of a square plate is analyzed. This example has been treated before by many references, for instance Fontes Valente et al. (2004), Eberlein and Wriggers (1999), Betsch and Stein (1999) or Hauptmann et al. (2000). Geometric properties are defined by relations length/width/thickness of 508/508/2.54. The plate is submitted to a uniformly pressure load of $p_0 = 60 \times 10^{-2}$. Material properties are given as E=6.9×10^4 and $\nu = 0.3$, with a perfectly plastic hardening law characterized by an initial yield stress of $\sigma_0 = 248$. Boundary conditions only restrain displacements in the plate's normal direction, being applied just to the mesh bottom surface nodes (defined over one quarter of the plate). Due to this fact, it is valid the occurrence of a sort of ''edge-rotations'' and, as the pressure value increases, the plate assumes a ''pillow-type'' deformation, changing from a bending dominated deformation (in the beginning) to a membrane dominated one.

Two different meshes are considered for comparison, a 15×15×1 topology (coming from Eberlein and Wriggers, 1999), refined around corners and using 5 integration points through the thickness direction and a second one with 24×24×1 mapped elements, following Betsch and Stein (1999), with 6 integration points through the thickness direction. The so-called ''6-parameter'' formulation from Eberlein and Wriggers (1999) is selected for comparison purposes. Concerning RESS element, the mesh was designed in order to achieve an approximated number of Gauss points as used in the compared references. Thus, it was chosen a mesh of 35×35 elements, refined around the corners (bias factor=20), as represented in Figure 5-22. Resulting out-of-plane displacement curves are shown in Figure 5-23, where the central node of the plate is monitored. It can be seen that the present results are in good agreement with reference solutions, although the number of integration points used are only about half comparing to Betsch and Stein (1999). The deformed configuration at the full load is represented in Figure 5-24.

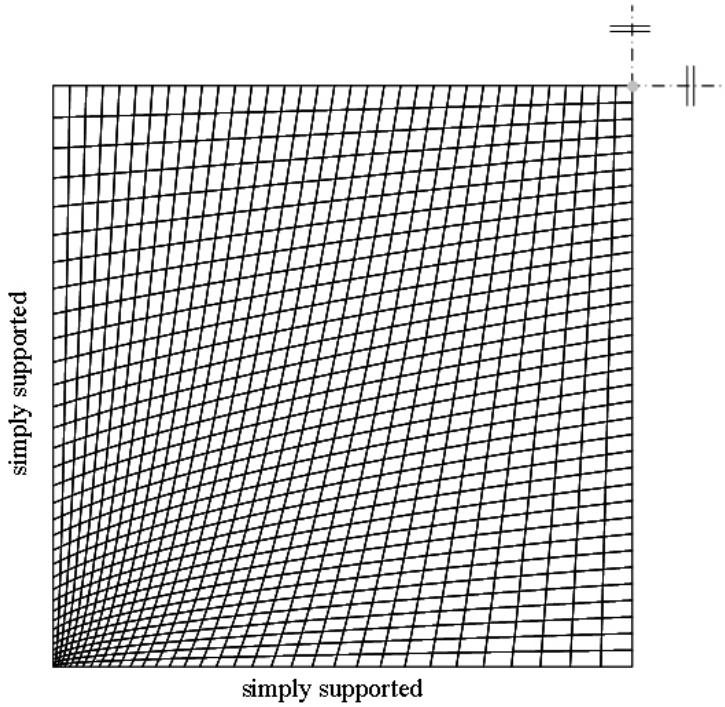

Figure 5-22: Simply supported plate - Mesh of 35×35×1 elements (bias factor=20).

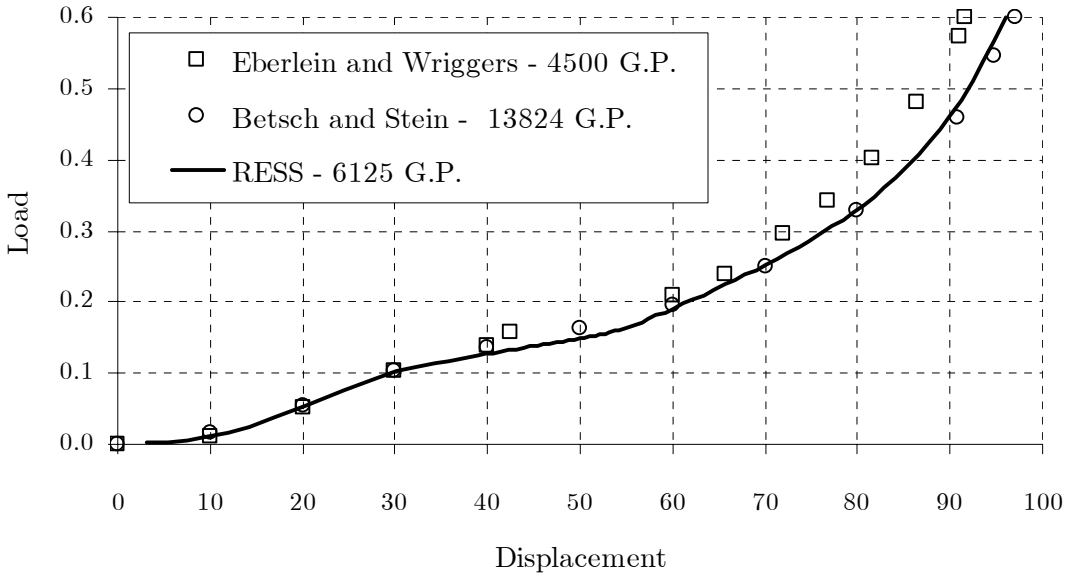

Figure 5-23: Simply supported plate – Central vertical displacement (G.P. – Gauss Points).

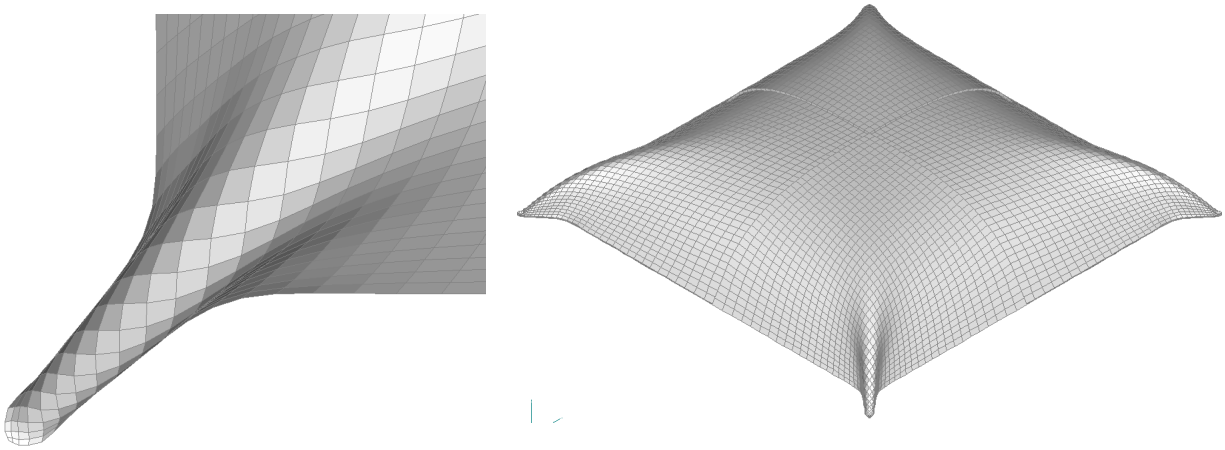

Figure 5-24: Simply supported plate – Deformation for $p_0 = 60 \times 10^{-2}$.

Recently, Fontes Valente et al. (2005) performed more investigation into the structural behavior of this example. To do so, the load was further increased until values of $p_1 = 600 \times 10^{-2}$. Carrying out this analysis with RESS, besides the relevant amount of out-of-plane displacement observed, it can be verified the onset of wrinkles at the mid-side of the plate's edge (Figure 5-25b).

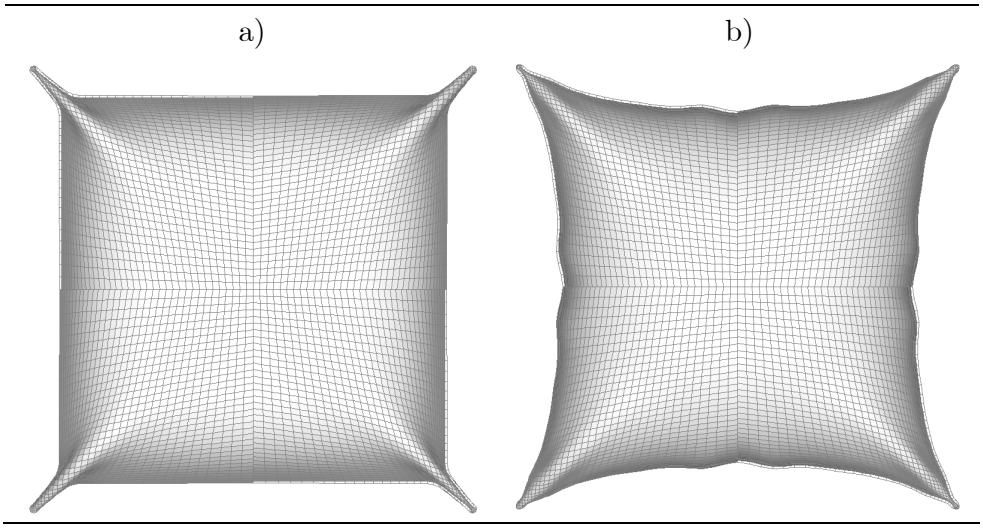

Figure 5-25 : Simply supported plate - top view's deformation: a) p=100×10^{-2} ; b) p=400×10^{-2}

Further raising the load factor, the plate is only able to accommodate extra deformation by adopting a spherical shape. The corner zones of the plate tend,

therefore, to assume a rounded shape, losing their sharp aspect as shown in Figure 5-26.

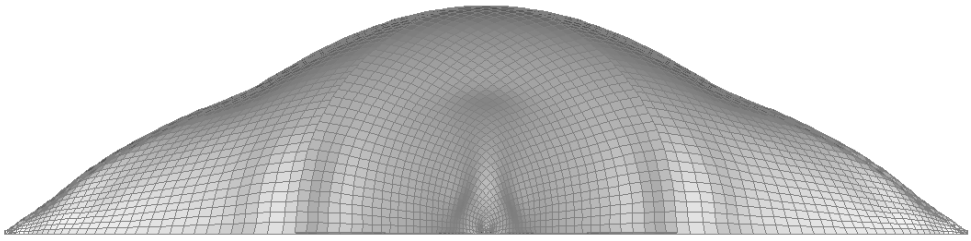

Figure 5-26: Simply supported plate - Corner's view.

5.5.3 Bending and stretching of a sheet

This simulation aims to illustrate the capability of RESS element to evaluate the thickness variation of a sheet subjected to double-sided contact together with bending and stretching. A blank with dimensions length L = 100 mm, width w = 10 mm and thickness a = 1 mm, is positioned as shown in Figure 5-27. Both ends of the sheet metal are fixed. The displacements along the width of the blank are restrained for all nodes so that material only deforms along the length and thickness of the blank. The sheet metal is bent and stretched with the movement of the middle punch, equally spaced from the other two dies. The total movement of the middle punch is 15 mm and the radius of all tools is 5 mm. The material data for the analysis is Young's modulus E = 200 GPa and Poisson's ratio $\nu = 0.3$. The stress–strain curve for isotropic hardening is $\overline{\sigma} = 508.79 + (0.000903 + \overline{\varepsilon})^{0.247}$ [MPa].

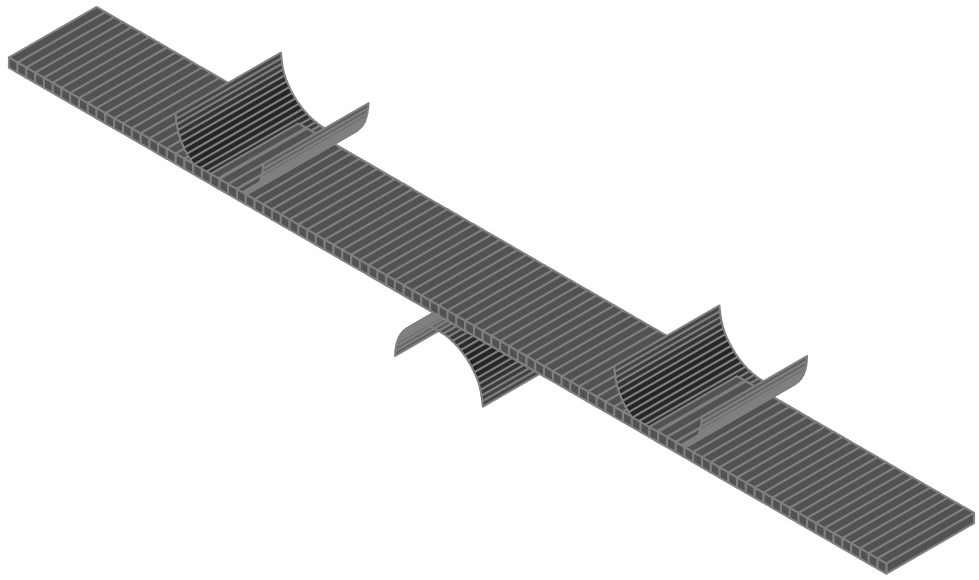

Figure 5-27: Bending and stretching of a sheet: problem setup

RESS simulation is compared with the following elements: MSC.Marc 3D Reduced Integrated solid element (element library n.º 117); a traditional shell element (Bathe, 1996); a full quadrature shell element based on Abbasi and Meguid (2000) and 7P-CYSE. For the MSC.Marc element, 5 layers along thickness are used with a total of 1000 elements. For RESS, 7P-CYSE and Abbasi and Meguid elements, a total of 200 elements with 5 integration points along thickness are used. The deformed shape of the sheet using RESS solid-shell element is represented in Figure 5-28. In Figure 5-29, it is shown the thickness distribution of the sheet at the punch stroke of 15 mm. As can be concluded from the results, traditional shell naturally is not able to capture the nominal stress effect along thickness direction. Results of RESS element are in good conformity with those obtained from 3D solid elements and the fully integrated shell of Abbasi and Meguid, showing that the present one point quadrature solid-shell can be successfully applied to simulations involving plasticity and double-sided contact, without deterioration of accuracy.

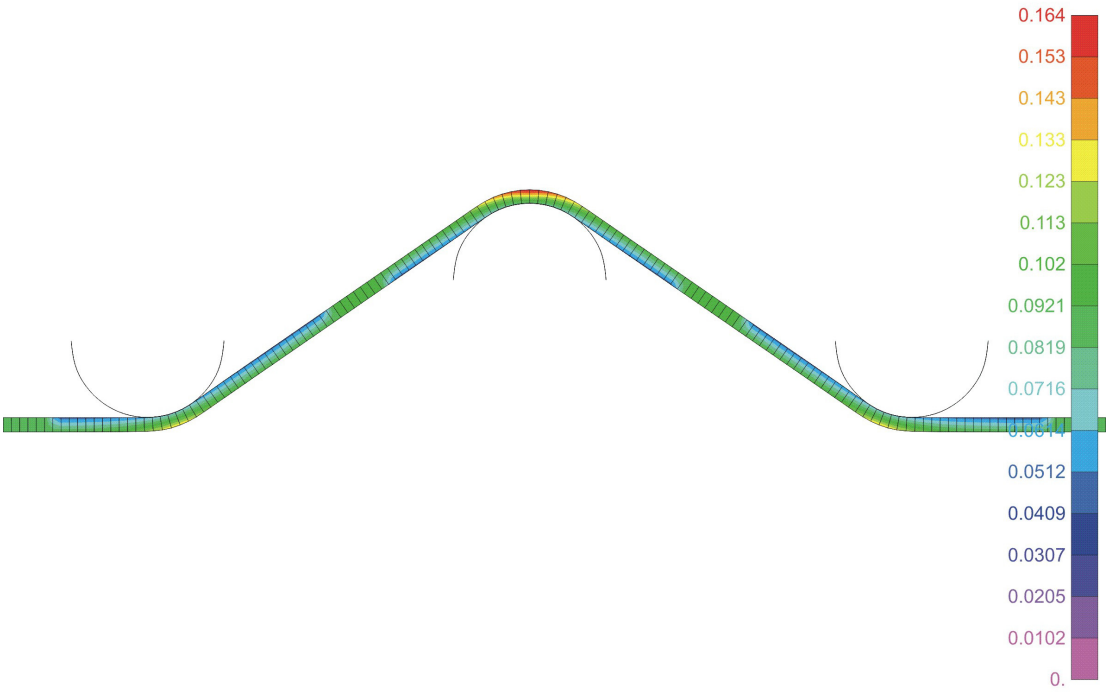

Figure 5-28: Bending and stretching of a sheet – deformed shape and effective plastic strain countour.

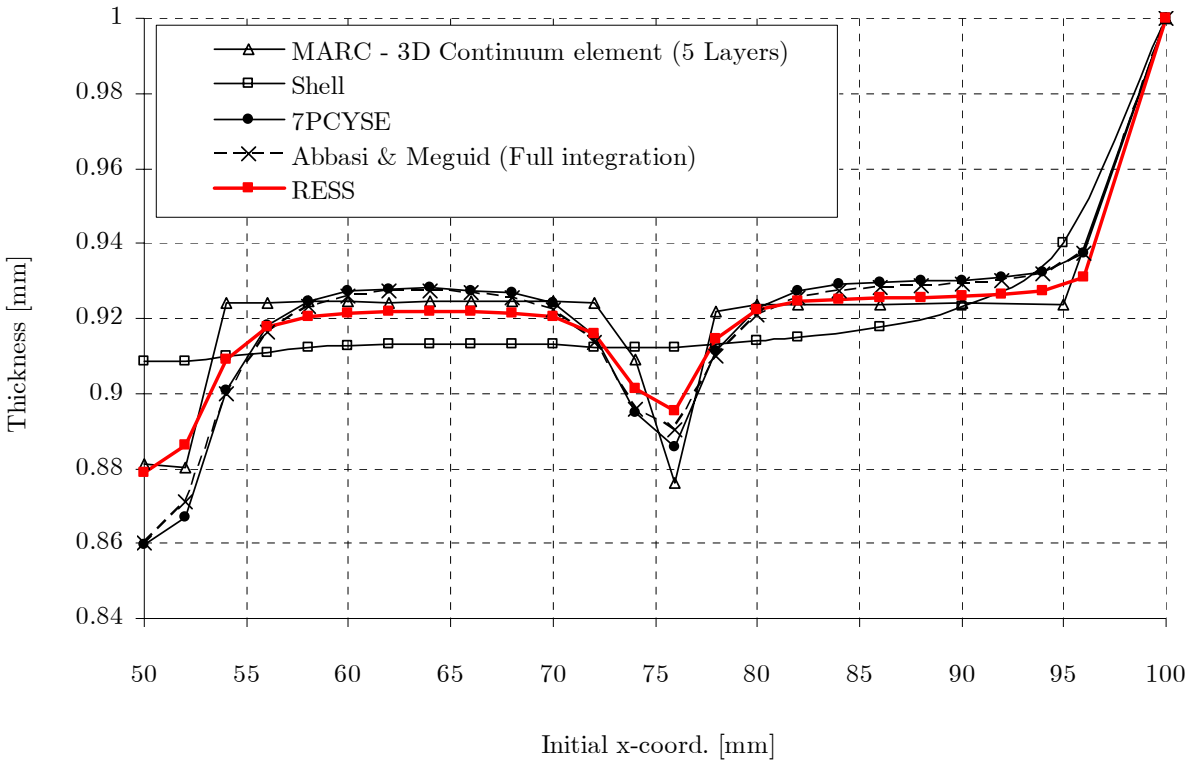

Figure 5-29: Bending and stretching of a sheet – thickness distribution.

5.5.4 Tube hydroforming with a square cross-sectional die

The following example is based on the work of Hwang and Chen (2005), where a circular tube of initial thickness $t_0 = 2\text{mm}$ and internal radius $R = 28\text{mm}$ is subjected to an increasingly internal pressure and formed against a square die, Figure 5-30. The purpose of the model is to predict the necessary internal hydroforming pressure, as well the thickness distribution after the forming operation.

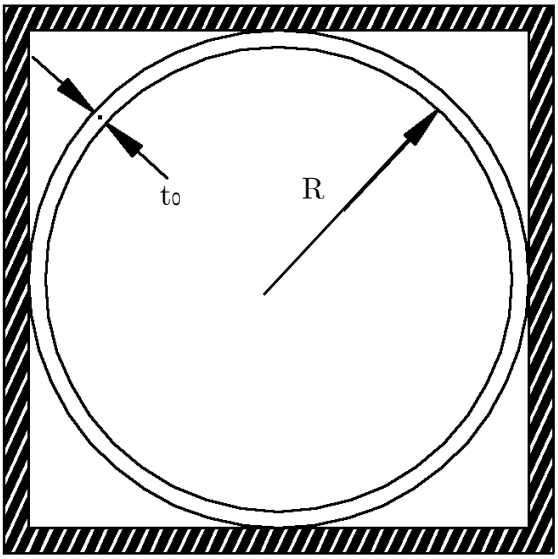

Figure 5-30: Tube hydroforming: problem set up.

Benefiting from symmetry conditions, only a quarter of the model is analyzed. In the work of Hwang and Chen (2005), finite element simulations were conducted using 1200 four-node elements along 7 layers through the thickness direction. These results were compared with experimental data, provided for a given range of friction coefficient values.

Concerning the numerical simulation using RESS element, 40 finite elements are employed. However, 15 integration points through the thickness direction are used in order to accurately describe the plastic behavior and thickness variation. Friction is not considered. Finally, constitutive aspects of the AISI 1008 carbon steel are described by means of von Mises plasticity and a hardening behaviour modeled by the power law curve:

$$\bar{\sigma} = 657.2\bar{\varepsilon}^{0.24} \text{ [MPa]} \tag{5.3}$$

The analyzed results are summarized in Figure 5-31 and Figure 5-32. For the sake of comparison, results chosen from the reference are the ones with the lowest friction coefficient: $(\mu = 0.01)$ for experimental data and no friction for the FEM simulations.

Figure 5-31 depicts the evolution of the tube corner radius as the internal pressure is raised. The radius value tends to a minimum as the internal pressure increases to very high values. The reference results, both experimental and numerical, are in accordance with RESS simulation results.

Figure 5-32 shows the thickness distributions along the tube's perimeter. The FEM simulations from the reference and RESS are in good agreement: the lowest values of thickness occur in the transition between the contacted part and the free expansion part (q=25). In this region, a complex stress state is expected with normal and tangential components coming from the contacted segments and free expansion segments, respectively. Experimental data deviates from both FEM simulations, with thickness values diminishing uniformly until a minimum value at the corner of the tube (q=30).

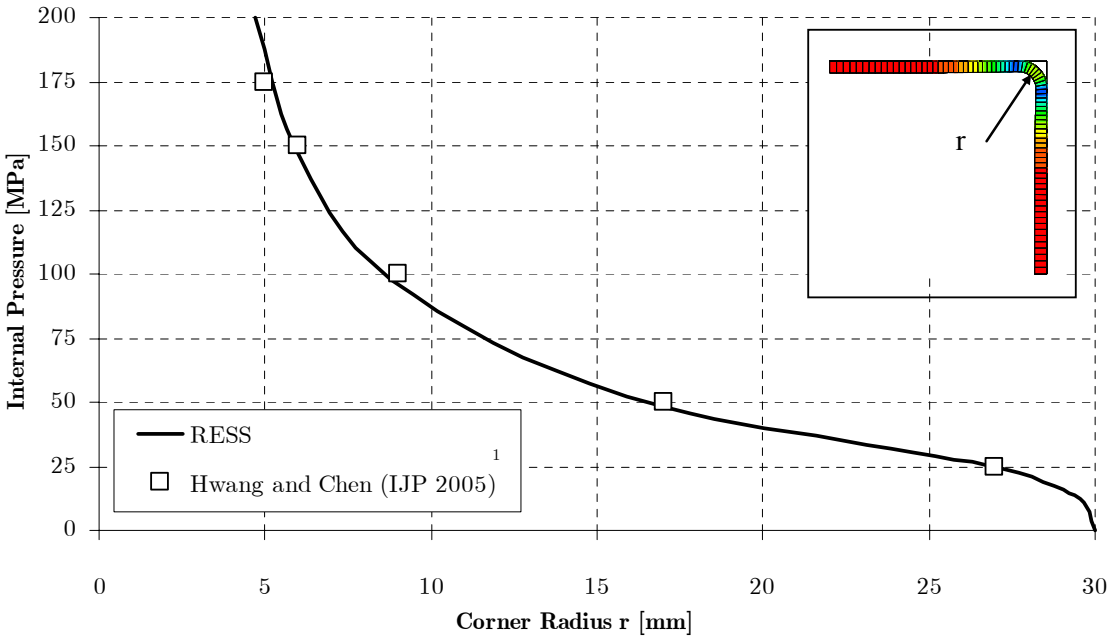

[1] Deviation between experimental and simulation data is negligible

Figure 5-31: Influence of forming pressure around corner's radius.

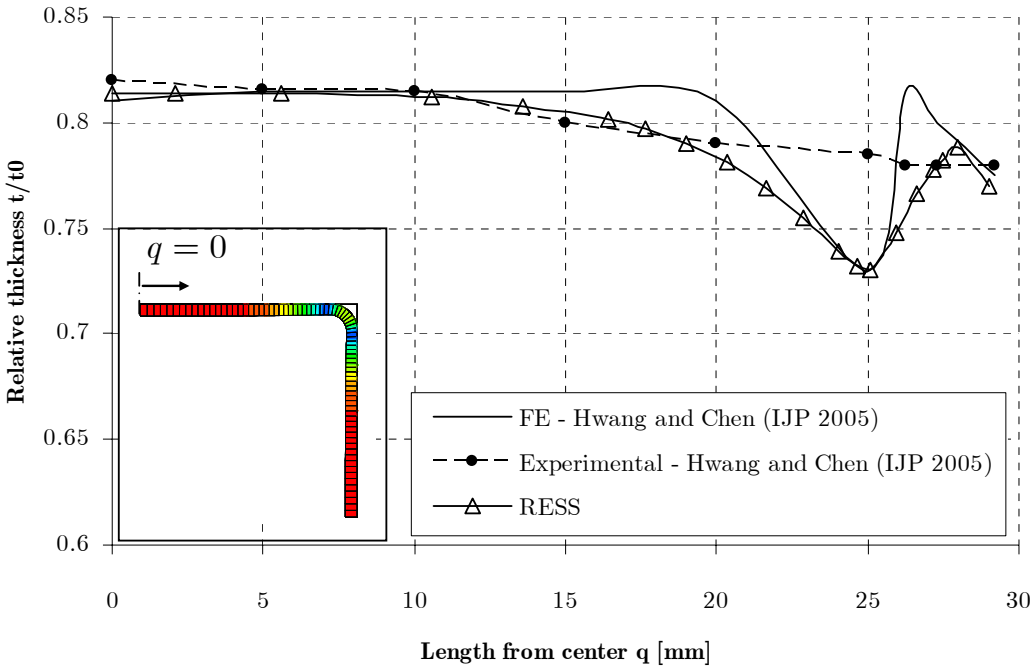

Figure 5-32: Tube's thickness distribution after expansion process.

5.6 Spring back analysis

5.6.1 Unconstrained cylindrical bending

One of the NUMISHEET (2002) benchmark examples was simulated to test spring-back analysis and efficiency of the contact algorithm using RESS element. The deformation is bending dominant since there is no blank holder. Nevertheless, the example has complex contact boundary conditions during forming operation and the springback after forming is severe. Following the reference, the sheet's geometry (Figure 5-33) for this problem has length L = 120 mm, width w = 30 mm and thickness a = 1.0 mm. Material data is given for high-strength steel: Young's modulus E = 215.98 GPa and Poisson's ratio $\nu = 0.3$, following the experimental hardening curve: $\bar{\sigma} = 620.19(0.005128 + \bar{\varepsilon})^{0.24557}$ [MPa].

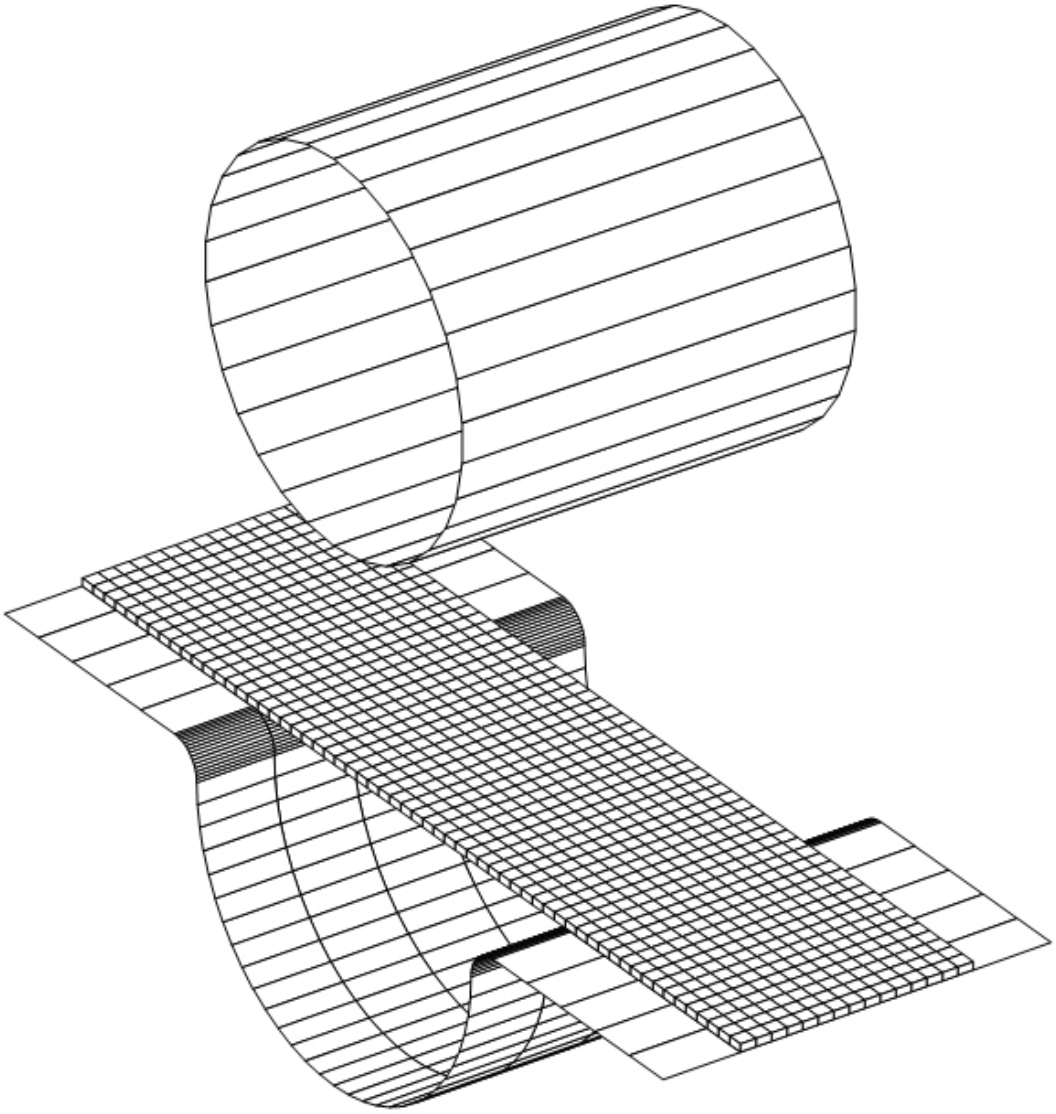

Figure 5-33: Unconstrained cylindrical bending – problem setup.

In order to obtain a reasonable distribution of the stress field along the thickness direction, seven integration points are used in this simulation. Results of RESS element are compared to the experimental values published at NUMISHEET (2002) proceedings. Table 5-7 compares the angular distance of the farthest points of contact at punch strokes of 7, 14, 21 and 28.5mm (Φ angle, Figure 5-34); Table 5-8 shows values of the angle Θ at the punch stroke of 28.5mm (before and after spring

back phenomenon), along with values for the punch stroke at which the contact region changes from one to two points ("bifurcation stroke").

Φ angle	Minimum experimental value	Maximum experimental value	**RESS**
Punch Stroke=7mm	20°	47°	**36°**
Punch Stroke=14mm	61°	90°	**74°**
Punch Stroke=21mm	110°	135°	**126°**
Punch Stroke=28.5mm	150°	180°	**164°**

Table 5-7: Unconstrained cylindrical bending – comparison between RESS and experimental values.

	Minimum experimental value	Maximum experimental value	**RESS**
Θ angle before spring back	21°	23°	**23°**
Θ angle after spring back	31°	37°	**37°**
Bifurcation punch stroke	3mm	8.4mm	**4.7mm**

Table 5-8: Unconstrained cylindrical bending – comparison between RESS and experimental values.

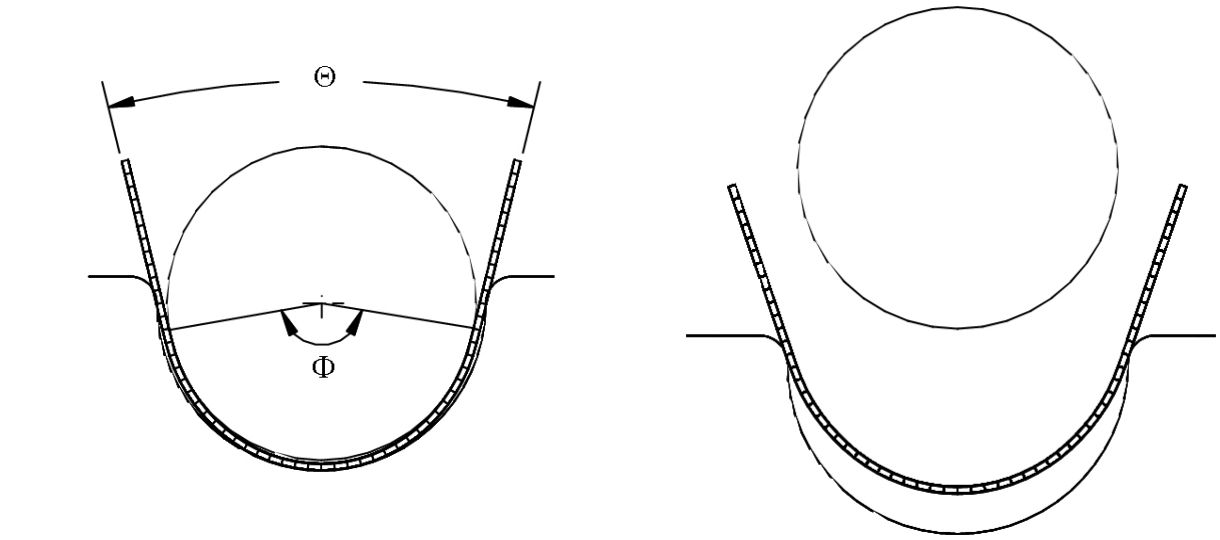

Figure 5-34: Unconstrained cylindrical bending – definition of comparison angles; deformed sheet after spring-back.

From the above results it's observed the excellent agreement between simulation and experimental values. The results also attest the accuracy and stability of RESS element.

5.6.2 Unconstrained cylindrical bending (modified version)

The example of a sheet undergoing unconstrained cylindrical bending and springback was also studied in the work of Yoon et al. (2002). The die geometry and dimensions are similar to the benchmark example of NUMISHEET (2002) proceedings with a minor difference in the die cavity radius R_2 as shown in Figure 5-35. The design by Yoon et al. (2002) makes the deformed sheet come out from die after spring-back naturally. The example is here included also for the sake of direct comparison with the experimental results, Figure 5-36.

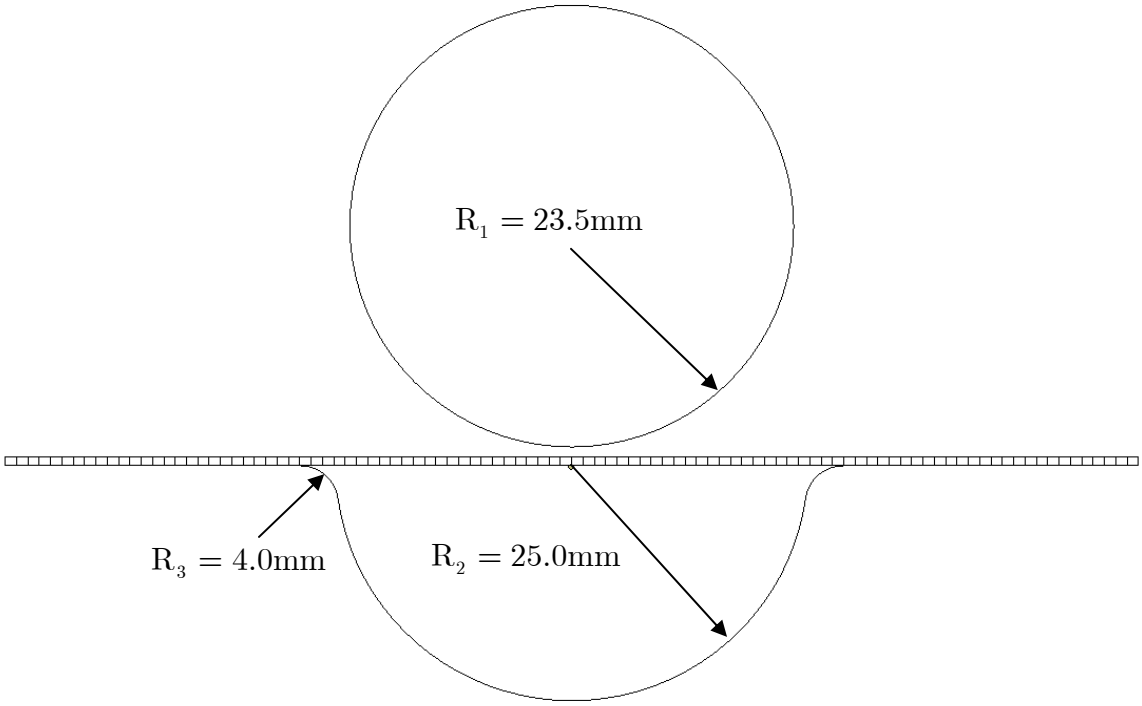

Figure 5-35: Unconstrained cylindrical bending and springback: modified version dimensions.

The sheet dimensions are: length/width/thickness = 120/30/1 [mm]. The material used is the 6111-T4 aluminum alloy obeying the hardening curve $\bar{\sigma} = 429.8 - 237.7\exp(-8.504\bar{\varepsilon})$ [MPa].

Numerical simulation is carried out using RESS element with 7 integration points along the thickness direction and compared with experimental data from Yoon et al. (2002). The entire process (deformation and springback) is carried out implicitly. The results of Figure 5-36 show an excellent agreement between experiment and simulation. In Table 5-9, measured and simulated values of the reference angle (θ) before and after springback phenomenon are quite close. Once again, it is remarkable the possibility to analyze springback using a single element layer through the thickness direction.

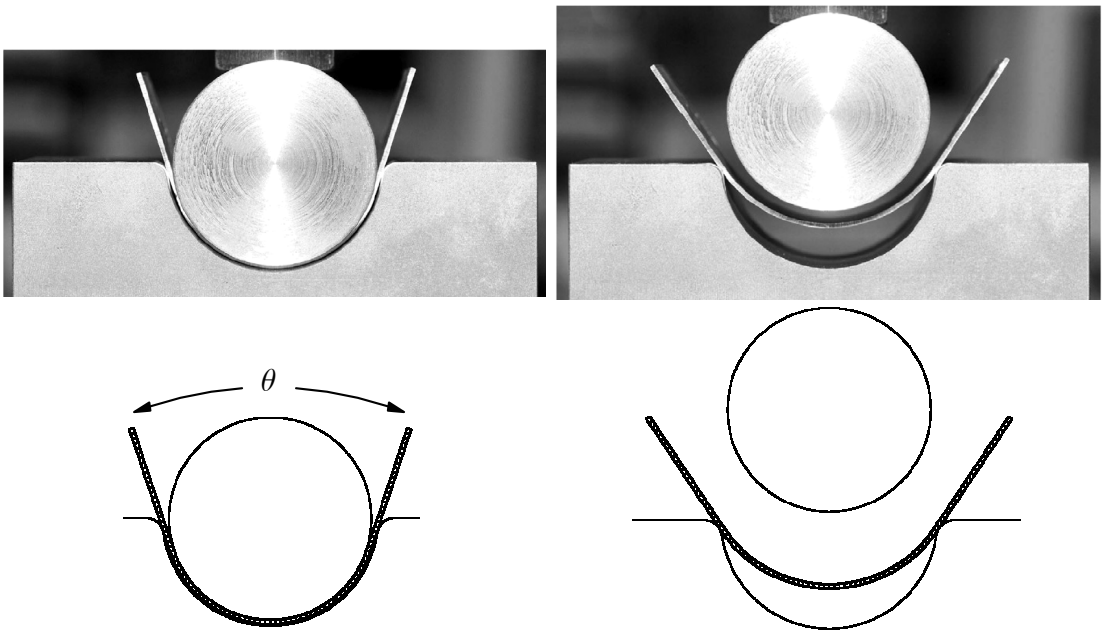

Figure 5-36: Unconstrained cylindrical bending and springback: left – before springback; right – after springback.

Reference angle (θ)	**Before spring back**	**After spring back**
Experimental	35°	68°
RESS	37°	67°

Table 5-9: Measured and simulated springback angles.

5.7 Plastic Anisotropy of Aluminum

5.7.1 Hydraulic Bulge Test with Al2008-T4

The hydraulic bulge test example is schematically represented in Figure 5-37. This test is commonly employed to evaluate biaxial stress-strain curves for sheet metal forming. Although the test geometry is axisymmetric, non-axisymmetric deformation is induced by the planar anisotropic material properties of the 2008-T4 aluminum alloy sheet.

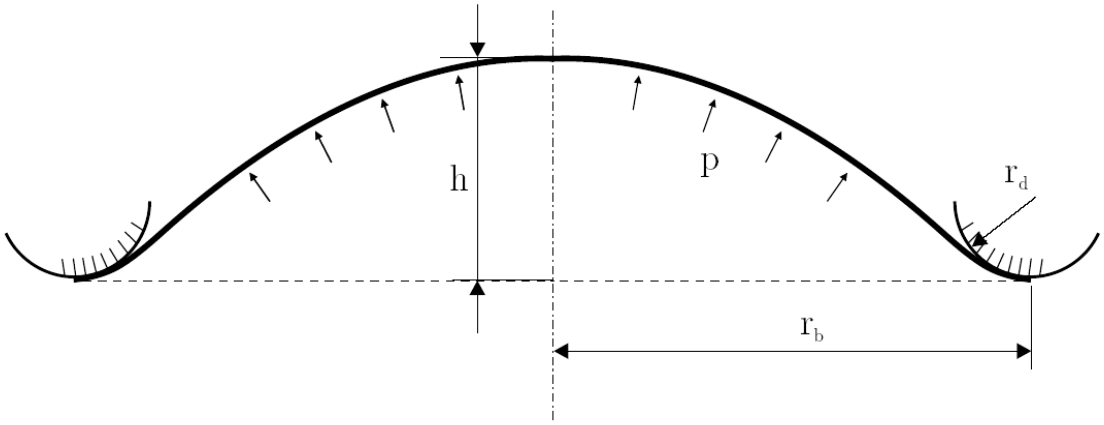

Figure 5-37: Hydraulic bulge test: problem setup.

FEM simulations are performed using RESS element with 7 Gauss points through the thickness direction and Yld91 (Barlat et al., 1991) yield function (coefficients listed in Table 5-10). Remaining material parameters are given as follows: Young's modulus E = 69.0 GPa; Poisson's ratio $\nu = 0.33$; initial yield stress $\sigma_{Y0} = 185\,\text{MPa}$; Voce-law hardening curve $\bar{\sigma} = 408.0 - 223.0\exp(-6.14\bar{\varepsilon})$ [MPa]. Geometry dimensions are given in Table 5-11. Only a quarter section of the specimen is analyzed due to the orthotropic material symmetry.

Yld91 coefficients

C_1	C_2	C_3	C_4	C_5	C_6	a
1.223	1.014	0.986	1.000	1.000	1.000	11

Table 5-10: Material data for Al2008-T4.

Blank radius	$r_b = 81.0$mm
Die profile radius	$r_d = 12.70$mm
Initial sheet thickness	1.24mm

Table 5-11: Geometry data for bulge test example.

The deformed configuration for the final internal pressure value (p=7 MPa), along with the thickness distribution contour is shown in Figure 5-38.

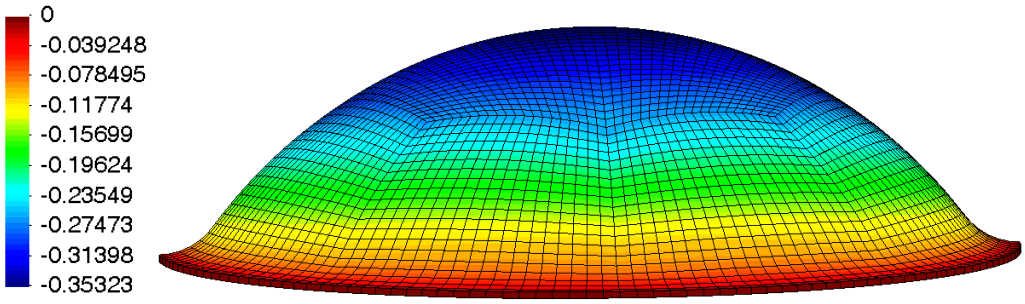

Figure 5-38: Bulge test: final deformed configuration and thickness contour.

Figure 5-39 plots the measured and predicted pressure-displacement relations at the pole (h). In order to show the importance of accounting for planar anisotropic effects in this example, simulation is also performed using von Mises isotropic yield function.

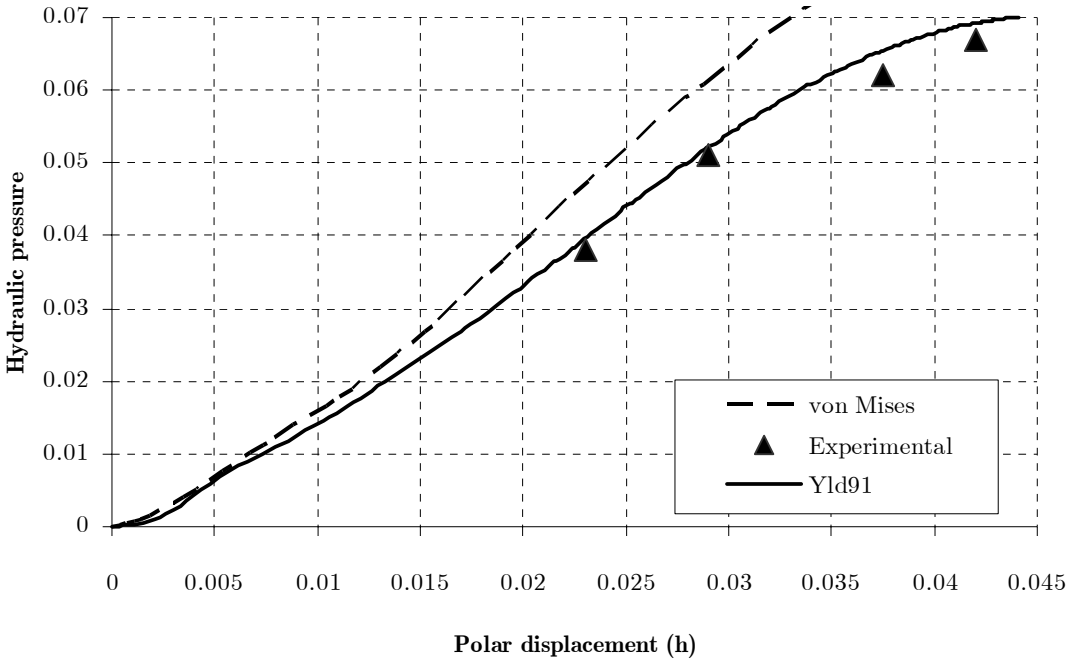

Figure 5-39: Bulge test: polar displacement (h) against hydraulic pressure.

The results are in agreement with experimental results as well as with the numerical results from Chung and Shah (1992), based on continuum elements and with Yoon (1997) or Cardoso (2002) regarding shell elements. The agreement between numerical simulation and experiments in the hydraulic bulge test is attained when the anisotropic yield criterion is used. Also, it is a good indicator about the accuracy of RESS element to account for thickness change and planar anisotropic effects.

5.7.2 Earing prediction for the AA2090-T3 aluminum alloy sheet

In this example, a cylindrical cup drawing test is carried out using RESS element with 5 integration points through the thickness direction. Since the constant blank holding force is applied during the cup forming, it is a typical double sided contact problem, which is difficult to be described with conventional shell elements. Due to the material orthotropy, only a quarter of the cup is analyzed resorting to a total of

1125 solid-shell elements. No friction is considered. Material and geometrical data (Table 5-12, Figure 5-40) is obtained after the work of Yoon et al. (2006).

Punch Diameter	$D_p = 97.46\text{mm}$
Punch profile radius	$r_p = 12.70\text{mm}$
Die opening diameter	$D_d = 101.48\text{mm}$
Die profile radius	$r_d = 12.70\text{mm}$
Blank diameter	$D_b = 158.76\text{mm}$
Initial sheet thickness	$t_0 = 1.6\text{mm}$
Hardening curve	$\overline{\sigma} = 646(0.025 + \overline{\varepsilon})^{0.227}\,[\text{MPa}]$
Blank holding force	22.2 KN

Table 5-12: Material and geometrical data for the cup drawing example.

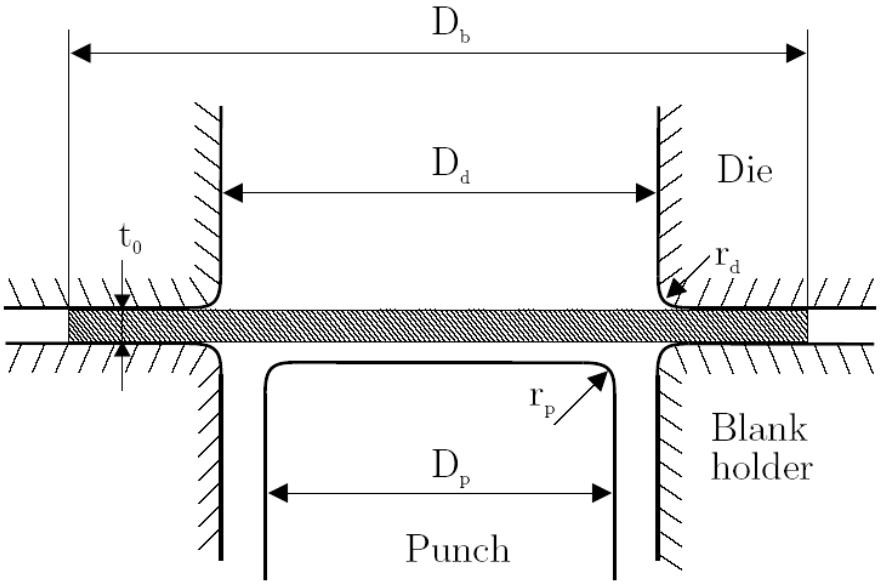

Figure 5-40: Cup drawing setup.

Two phenomenological yield functions accommodating three-dimensional stress states are used for comparison purposes: Yld91 and Yld2004-18p (Barlat et al, 2005). It can be shown that only Yld2004-18p is able to predict the experimental cup height profiles ("earing" profiles) with six ears successfully. In Table 5-13, the coefficients used for both yield functions, taken from references Yoon et al. (2000; 2006), are summarized.

Yld91

C_1	C_2	C_3	C_4	C_5	C_6
1.0674	0.8559	1.1296	1.0000	1.0000	1.297

Yld2004-18p

c'_{12}	c'_{13}	c'_{21}	c'_{23}	c'_{31}	c'_{32}	c'_{55}	c'_{66}	c'_{44}
-0.0698	0.9364	0.0791	1.003	0.5247	1.3631	1.0237	1.069	0.9543
c''_{12}	c''_{13}	c''_{21}	c''_{23}	c''_{31}	c''_{32}	c''_{55}	c''_{66}	c''_{44}
0.9811	0.4767	0.5753	0.8668	1.145	-0.0792	1.0516	1.1471	1.4046

Table 5-13: Yield function coefficients for Al2090-T3 (a=8).

Figure 5-41 shows deformed configurations of completely drawn cups. In Figure 5-42, experimental cup height profiles are compared with RESS simulations based on Yld91 and Yld2004-18p. For an orthotropic material, the cup height profile between 0° and 90° should be a mirror image of the cup height profile between 90° and 180°. However, the measured experimental earing profile slightly deviates from this condition. This deviation can be due to an inexact alignment between the center of the blank and the centers of die and punch during the drawing experiment (Yoon et al., 2000).

Analyzing the plot, it can be concluded that the earing profile obtained with RESS simulations is in accordance with the works of Yoon et al. (2000) based on a shell element and Yld91, and Yoon et al. (2006) based on a solid element and Yld2004-18p, i.e., four ears obtained with Yld91 and six ears with Yld2004-18p. The latter shows a very good agreement with the experimental measured profile.

Yld91 (a)	**Yld2004-18p (b)**

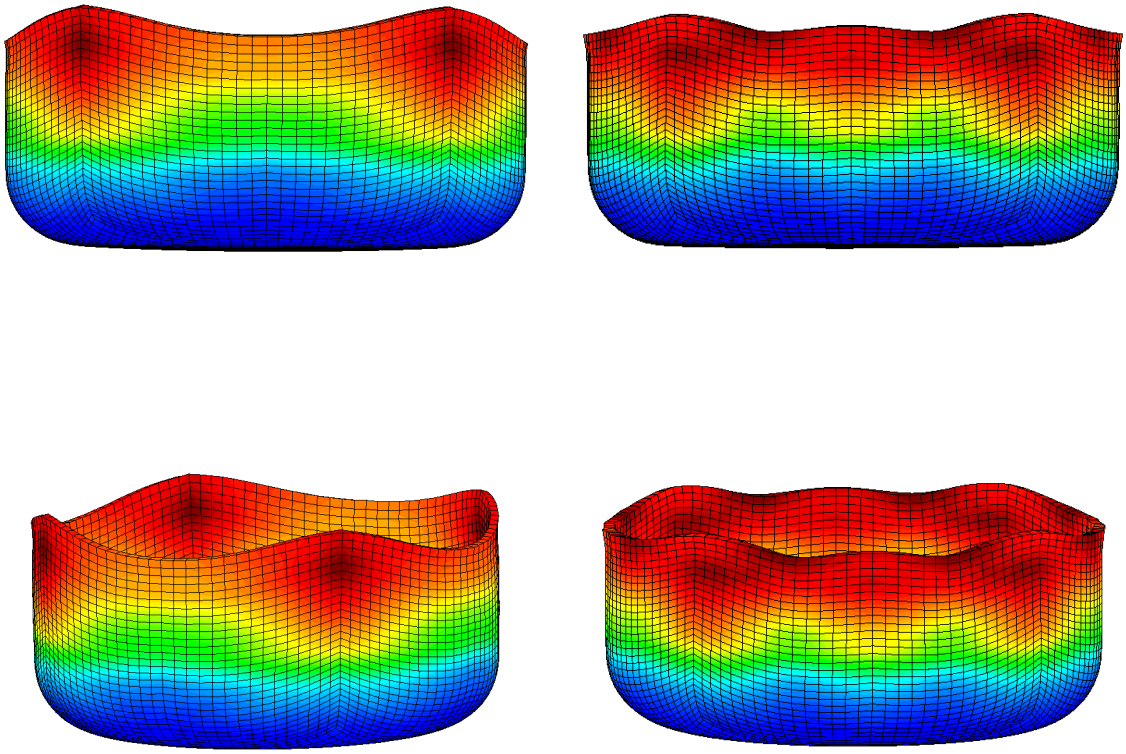

Figure 5-41: Deformed shapes obtained using (a) Yld91 yield function; (b) Yld2004-18p yield function.

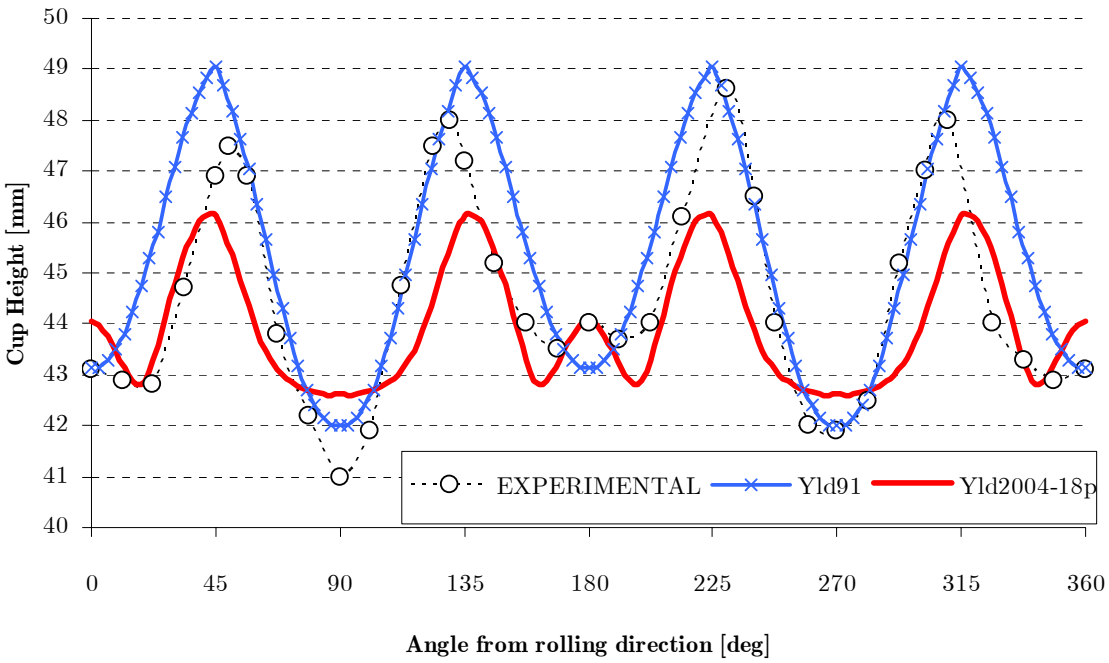

Figure 5-42: Cup height profiles: experimental data with RESS simulation.

Chapter 6

Closure

The primary goal of this thesis was to design a new solid-shell element appropriate for the numerical simulation of anisotropic sheet metal forming processes. The result was a new formulation encompassing very useful features in terms of accuracy and computational efficiency. Among them, the most distinctive attribute is the possibility to model geometries by using only a single element layer with an arbitrary number of integration points in the thickness direction. Because of that, the proposed finite element becomes particularly useful in the simulation of metal forming and spring-back.

6.1 Conclusions

To achieve the thesis' main objectives, the research focused mainly on the RESS finite element development. The formulation is based on a one-point quadrature numerical integration scheme (conferring computational efficiency) combined with the EAS (Enhanced Assumed Strain) method using a minimum number of extra degrees of freedom (one). Both methods are applied for locking treatment of the solid-type element.

In **Chapter 1,** a start-of-art review about finite element technology for sheet metal forming simulation and modeling of anisotropic plasticity was given. In **Chapter 2** the guidelines of nonlinear continuum mechanics, as used and implemented throughout this work were discussed, including the framework of the updated Lagrangian solution procedure using a corotational coordinate system, the non-linear version of the EAS method resorting to the additive decomposition of Green-Lagrange strain tensor and computational plasticity aspects. In **Chapter 3**, the

RESS formulation was detailed. The treatment of locking phenomena using the EAS method and the reduced integration scheme was justified by means of a suitable subspace analysis. The time-efficient physical stabilization scheme was also depicted and implementation guidelines were provided. As stated in the numerical tests documented in **Chapter 5**, the marriage of the Enhanced Strain Method with the technology of one point quadrature shell elements created a formulation simultaneously accurate and computationally efficient. The formulation's potential is enormous:

- Linear benchmarks attested the ability to deal with volumetric, transverse shear and thickness locking. Low sensitivity to mesh distortions was detected;
- In material and geometrical nonlinear tests, the importance of the arbitrary number of integration points along thickness the direction was highlighted. In a single element layer, such number can be increased to capture (with high detail) the stress distribution. On the other hand, it can be decreased in order to improve CPU speeds. The effectiveness of the nonlinear algorithms to deal with large displacements and rotations was at the same time verified;
- Proper evaluation of plastic anisotropy was also inferred. In the bulge test example, the importance of accounting for planar anisotropy was attested by comparing the results with the ones obtained using von Mises plasticity. In the earing example, it was possible to show the solution accuracy difference between Yld91 and Yld2004-18p yield functions concerning the number of ears predicted;
- Challenging examples with double sided contact were successfully conducted. In all of them, the quality of the results is comparable to refined shell formulations. The highlight of this work was to conduct spring-back examples based on single layer finite elements with one-point quadrature numerical integration scheme, by accommodating multiple integration points through the thickness, being in this way the original scientific contribution of the thesis.

In short, the potential application range of RESS element is wide and general. Once possessing eight physical nodes, the consideration of double-sided contact and normal stress is remarkable. The variable number of integration points through the thickness direction in a single layer is a powerful feature in plasticity based problems or demanding spring-back analysis. Application into real complex examples is possible due to its computational efficiency, ensured by the one-point quadrature numerical integration scheme, one EAS parameter and physical stabilization scheme, the latter involving only analytical integration.

In polycrystal plasticity studies, a time efficient grain-level plasticity model was introduced, possibly covering either rate-dependent or rate-independent approaches. An efficient stress-integration method was proposed based on the semi-implicit multi-stage return mapping. All guidelines for proper implementation of the continuum and grain-level plasticity approaches were given in **Chapter 4**. For each Gauss point the model was tested with success, and texture evolution was successfully evaluated. The integration of the grain-level approach into a FEM code is under development.

6.2 Future Work

The following topics are considered as potentially future works:

- Consideration of shear components in the stabilization part: in this work all shear components in the stabilization part were neglected for the formulation's simplicity by following the work of Li and Cescotto (2000). In order to prevent any possible flexible behaviors or potential hourglass modes, mathematical treatments for these components (like the ANS method for transverse shear components and the mixed formulation for the membrane shear term in the stabilization part) may be utilized for a more rigorous theoretical basis;
- Consideration of a linear distribution for the normal stress component: As discussed in Chapter 3, the formulation handle with the linearity of the

normal stress component using the EAS method, which shows linearity, but the normal component is not completely set to zero on the free surface. This is due to the use of the low-order (first order) shape functions. Higher order shape functions may be needed to complete the linear distribution of the component;

- Implementation of the grain-level plasticity into a FEM code: the implementation of the grain-level crystal plasticity will be a powerful tool for multi-scale plasticity approaches based on the solid-shell element;
- Other attractive possibilities in terms of application areas may be the utilization of RESS to model composite materials or in biomechanics field, like shape memory alloys.

7. References and Further Reading

ABAQUS (2002), "Theory Manual, Version 6.3", *Hibbitt, Karlsson & Sorensen, Inc.*, Rhode Island, USA.

Ahmad S., Irons, B.M. & Zienkiewicz, O.C., (1970), "Analysis of thick and thin shells structures by curved finite elements", *International Journal for Numerical Methods in Engineering*, Vol. 2, pp. 419-451.

Alves de Sousa, R.J., Natal Jorge, R.M., Areias, P.M.A., Fontes Valente, R.A. and César de Sá, J.M.A., (2002), "Low Order Elements for 3D Analysis", *Proceedings of the Fifth World Congress on Computational Mechanics* (WCCM V), Wien, Austria.

Alves de Sousa, R.J., Natal Jorge, R.M., Fontes Valente, R.A. and César Sá, J.M.A. (2003a), "Formulation of EAS solid elements for incompressibility and thin shell applications in non-linear range" *Proceedings of COMPLAS VII – Seventh World Congress in Computational Plasticity*, Barcelona, Spain.

Alves de Sousa, R.J., Natal Jorge, R.M., Fontes Valente, R.A., César Sá, J.M.A. (2003b), "A new volumetric and shear locking-free EAS element", *Engineering Computations*, Vol. 20, pp. 896-925.

Alves de Sousa, R.J., Cardoso, R.P.R., Fontes Valente, R.A., Yoon, J.W., Grácio, J.J. and Natal Jorge, R.M. (2004), "A new one-point quadrature Enhanced Assumed Strain (EAS) solid-shell element with multiple integration points along thickness: Part I – Geometrically Linear Applications", *International Journal for Numerical Methods in Engineering,* Vol. 62, pp. 952-977.

Alves de Sousa, R.J., Cardoso, R.P.R., Fontes Valente, R.A., Yoon, J.W., Grácio, J.J. and Natal Jorge, R.M. (2006), "A new one-point quadrature Enhanced Assumed Strain (EAS) solid-shell element with multiple integration points along thickness: Part II –Nonlinear Applications", *International Journal for Numerical Methods in Engineering,* Vol. 67, pp. 160–188

Anand, L. and Kothari, M. (1996), "A computational procedure for rate-independent crystal plasticity", *Journal of Mechanics and Physics of Solids,* Vol. 44, pp. 525-558.

Andelfinger, U. and Ramm, E., (1992), 2D and 3D enhanced assumed strain elements and their application in plasticity, *Proceedings of the 3rd International Conference on Computational Plasticity* (COMPLAS III), 17-21 August, Barcelona.

Andelfinger, U. and Ramm, E. (1993), "EAS-Elements for 2D, 3D, plate and shell structures and their equivalence to HR-elements", *International Journal for Numerical Methods in Engineering*, Vol. 36, pp. 1311-1337.

Armero, F. and Dvorkin, E.N. (2000), "On finite elements for nonlinear solid mechanics", *Computers and Structures*, Vol. 75, Issue 3.

Arminjon, M. (1991), "A regular form of the Schmid law. Application to the ambiguity problem", *Textures and Microstructures,* Vol. 14, pp. 1121-1128.

Asaro, R.J. and Rice, J.R. (1977), "Strain localization in ductile single crystals", *Journal of the Mechanics and Physics of Solids*, Vol. 25, pp. 309-338.

Asaro, R. J. (1983a), "Crystal Plasticity". *Journal of Applied Mechanics*, Vol. 50, pp. 921-934.

Asaro, R. J. (1983b), "Micromechanics of Crystal and Polycrystals". *Advances in Applied Mechanics*, Vol. 23, pp. 2-111.

Asaro, R.J. and Needleman, A. (1985), "Texture development and strain hardening in rate dependent polycrystals", *Acta Metallurgica*, Vol. 33, pp. 923-953.

Banabic, D., (2000), "Anisotropy of sheet metals. In: Banabic, D. (Ed.), Formability of Metallic Materials", Springer, Berlin, pp. 119-172.

Banabic, D., Cazacu, O., Barlat, F., Comsa, D.S., Wagner, S., Siegert, K., (2000), "Recent anisotropic yield criteria for sheet metals", *Proceedings of the Romanian Academy* Vol. 3, pp. 91-98.

Barlat, F. and Richmond, O. (1987), "Prediction of tricomponent plane stress yield surfaces and associated flow and failure behaviour of strongly textured FCC polycrystalline sheets", *Materials Science and Engineering*, Vol. 91, pp. 15–29.

7. References

Barlat, F. and Lian, J., (1989), "Plastic behavior and stretchability of sheet metals. Part I: yield function for orthotropic sheets under plane stress conditions", *International Journal of Plasticity*, Vol. **5**, pp. 51.

Barlat, F., Lege, D.J., Brem, J.C. (1991), "A six-component yield function for anisotropic metals", *International Journal of Plasticity*, Vol. 7, pp. 693.

Barlat, F., Becker, R.C., Hayashida, Y., Maeda, Y., Yanagawa, M., Chung, K., Brem, J.C., Lege, D.J., Matsui, K., Murtha, S.J. and Hattori, S. (1997), "Yielding description for solution strengthened aluminium alloys", *International Journal of Plasticity*, Vol. 13, pp. 385–401.

Barlat, F., Banabic, D. and Cazacu, O. (2002), "Anisotropy in sheet metals", *Proceedings of the NUMISHEET 2002 Conference*, Jeju Island, Korea. pp. 515–524.

Barlat F., Brem J.C., Yoon J.W., Chung K., Dick R.E., Lege D.J., Pourboghrat F., Choi S.H. and Chu E. (2003), "Plane stress yield function for aluminum alloy sheets — part 1: theory", *International Journal of Plasticity*, Vol. 19, pp. 1297-1319

Barlat, F., Aretz, H., Yoon, J.W., Karabin, M.E., Brem, J.C., Dick, R.E. (2005). "Linear transformation based anisotropic yield function", *International Journal of Plasticity*, Vol. 21, pp. 1009.

Bassani, J.L. (1977), "Yield characterisation of metals with transversally isotropic plastic properties", *International Journal of Mechanical Sciences*, Vol. 19 pp. 651–6544.

Bathe, K.J. and Dvorkin, E. (1986), "A formulation of general shell elements – the use of mixed interpolation of tensorial components", *International Journal for Numerical Methods in Engineering*, Vol. 22, pp. 697-722.

Bathe, K.J., (1996), *Finite Element Procedures,* 2nd Edn., Prentice-Hall, New Jersey.

Bathe, K.J., Iosilevich, A. and Chapelle, D. (2000), "An evaluation of the MITC shell elements", *Computers and Structures*, Vol. 75, pp. 1-30.

Başar Y. and Weicher, D. (2000), "Nonlinear Continuum Mechanics of Solids", *Springer-Verlag*, Berlin, Heidelberg, New York.

Beaudouin, A.J., Mathur, K.K., Dawson, P.R. and Johnson, G.C. (1993), "Three-dimensional deformation process simulation with explicit use of polycrystalline plasticity model", *International Journal of Plasticity*, Vol. 9, pp. 833-860.

Becker, R., (1991), "Analysis of texture evolution in channel-die compression – 1. Effects of grain interaction", *Acta Metallurgica et Materialia,* Vol. 39, pp. 1211-1230.

Belytschko T. and Tsay, C. (1983), "A stabilization procedure for the quadrilateral plate element with one-point quadrature", *International Journal for Numerical Methods in Engineering,* Vol. 19, pp. 405–419

Belytschko, T., Stolarski, H., Liu, W.K., Carpenter, N. and Ong, J.S.J. (1985), "Stress projection for membrane and shear locking in shell finite elements", *Computer Methods in Applied Mechanics and Engineering*, Vol. 51, pp. 221-258.

Belytschko, T. and Bindeman, L.P. (1991), "Assumed strain stabilization of the 4-node quadrilateral with 1-point quadrature for non-linear problems", *Computer Methods in Applied Mechanics and Engineering*, Vol. 88, pp. 311-340.

Belytschko, T., Wong, B.L. and Chiang, H.Y. (1992), "Advances in one-point quadrature shell elements", *Computer Methods in Applied Mechanics and Engineering*, Vol. 96, pp. 93-108.

Belytschko, T. and Bindeman, L.P. (1993), "Assumed strain stabilization of the eight node hexahedral element", *Computer Methods in Applied Mechanics and Engineering,* Vol. 105, pp. 225–260.

Belytschko, T. and Leviathan, I. (1994), "Physical stabilization of the 4-node shell element with one point quadrature", *Computer Methods in Applied Mechanics and Engineering*, Vol. 113, pp. 321-350.

Belytschko, T., Liu, W.K., Moran, B. (2000), *Nonlinear Finite Elements for Continua and Structure*", John Wiley & Sons, West Sussex, England

Betsch, P. and Stein, E. (1999), "Numerical implementation of multiplicative elasto-plasticity into assumed strain elements with application to shells at large

strains", *Computer Methods in Applied Mechanics and Engineering*, Vol. 179, pp. 215-245.

Bischoff, M. and Ramm, E. (1997), "Shear deformable shell elements for large strains and rotations", *International Journal for Numerical Methods in Engineering*, Vol. 40, pp. 4427-4449.

Bishop, J.F.W. and Hill, R. (1951a), "A theory of the plastic distortion of a polycrystalline aggregate under combined stresses", *Philosophical Magazine* Vol. 42, pp. 414.

Bishop, J.F.W. and Hill, R. (1951b), "A theoretical derivation of the plastic properties of a polycrystalline face-centered metal", *Philosophical Magazine* Vol. 42, pp. 1298.

Bishop, J.F.W., (1953), "A theoretical examination of the plastic deformation of crystals by glide", *Philosophical Magazine* Vol. 44, pp. 51-64.

Brank, B., Peric, D. and Damjanic, F.B. (1995), "On implementation of a nonlinear four node shell finite element for thin multilayered elastic shells", *Computational Mechanics*, Vol. 16, pp. 341–359.

Brank, B., Peric, D. and Damjanic, F.B., (1997), "On Large Deformations of Thin Elasto-Plastic Shells: Implementation of a Finite Rotation Model for Quadrilateral Shell Element", *International Journal for Numerical Methods in Engineering,* Vol. 40, pp. 689-726.

Bridgman, P.W. (1923), "The compressibility of thirty metal as a function of pressure and temperature", *Proceedings of the American Academy of Sciences*, Vol. 58, pp. 165.

Bron F. and Besson J. (2004), "A yield function for anisotropic materials: Application to aluminum alloys", *International Journal of Plasticity*, Vol. 20, pp. 937-963.

Büchter, N. and Ramm, E. (1994), "Three-dimensional extension of a non-linear shell formulation based on the Enhanced Assumed Strain concept", *International Journal for Numerical Methods in Engineering*, Vol. 37, pp. 2551-2568.

Budiansky, B. and Wu, T.T. (1962), "Theoretical Prediction of Plastic Strains of Polycrystals, *Proccedings of the 4th Congress in Applied Mechanics*, pp. 1175.

Budiansky B. (1984), "Anisotropic plasticity of plane-isotropic sheets" *Dvorak GJ, Shield RT, (eds). Mechanics of materials behaviour*, Elsevier, The Netherlands.

Cardoso, R.P.R, Yoon, J.-W., Grácio, J.J., Barlat, F. and César Sá, J.M.A. (2002), "Development of a one point quadrature shell element for nonlinear application with contact and anisotropy", *Computer Methods in Applied Mechanics and Engineering*, Vol. 191, pp. 5177-5206.

Cardoso, R.P.R. (2002), "Development of one point quadrature shell elements with anisotropic material models for sheet metal forming analysis", *PhD. Thesis*, University of Aveiro, Portugal.

Cardoso, R.P.R. (2004), *CEREBRO – Finite Element Analysis Software.* license ASSOFT n.º 1169/d/04.

Cardoso, R.P.R. and Yoon, J.W. (2005a), "One point quadrature shell elements for sheet metal forming analysis", *Archives of Computational Methods in Engineering,* Vol. 12, pp. 3-66.

Cardoso, R.P.R. and Yoon, J.W. (2005b), "One point quadrature shell element with through-thickness stretch", *Computer Methods in Applied Mechanics and Engineering*, Vol. 194, pp. 1161-1199.

Cazacu, O., Barlat, F. (2001), "Generalization of Druker's yield criterion to orthotropy", *Mathematics and Mechanics of Solids*, Vol. 6, pp. 613-630.

Cazacu, O., Barlat, F. (2003), "Application of the theory of representation to describe yielding of anisotropic aluminum alloys", *International Journal of Engineering Science*, Vol. 41, pp. 1367-1385

Cazacu, O., Barlat, F. (2004), "A criterion for description of anisotropy and yield differential effects in pressure-insensitive metals", *International Journal of Plasticity*, Vol. 20, pp. 2027-2045

César de Sá, J.M.A. and Natal Jorge, R.M. (1999), "New enhanced strain elements for incompressible problems", *International Journal for Numerical Methods in Engineering*, Vol. 44, pp. 229-248.

César de Sá, J.M.A. and Owen, D.R.J., (1986), "The imposition of the incompressibility constraint in finite elements - A review of methods with a new insight to the locking phenomena", in Taylor, C. *et al.* (eds.), *Proceedings of the III International Conference on Numerical Methods for Non-Linear Problems*, Dubrovnik, Pineridge Press, Swansea, U.K.

César de Sá, J.M.A., (1986), "*Numerical Modeling of Incompressible Problems in Glass Forming and Rubber Technology*," PhD. Thesis, University College of Swansea, Wales, C/Ph/91/86, U.K.

César de Sá, J.M.A., Areias, P.M.A. and Natal Jorge, R.M., (2001), "Quadrilateral elements for the solution of elasto-plastic finite strain problems", *International Journal for Numerical Methods in Engineering*, Vol. 51, pp. 883-917.

César de Sá, J.M.A., Natal Jorge, R.M, Fontes Valente, R.A. and Areias, P.M.A. (2002), "Development of shear locking-free shell elements using an enhanced assumed strain formulation", *International Journal for Numerical Methods in Engineering*, Vol. 53, pp. 1721-1750.

Chakrabarty, J., (1987), *Theory of Plasticity*, McGraw-Hill, Singapore.

Chapelle, D. and Bathe, K.J. (2000), "The mathematical shell model underlying general shell elements", *International Journal for Numerical Methods in Engineering*, Vol. 48, pp. 289-313.

Chung, K. and Richmond, O. (1993), "A deformation theory of plasticity based on minimum work paths", *International Journal of Plasticity,* Vol. 9, pp. 907-920.

Chung, K. and Shah, K. (1992), "Finite element simulation of sheet metal forming for planar anisotropic metals", *International Journal of Plasticity,* Vol. **8**, pp. 453.

Crisfield, M.A., (1994), *Non-linear Finite Element Analysis of Solids and Structures*; Vol.1, John Wiley & Sons, Chichester, U.K.

Dao, M. and Asaro, R.J., (1996), "Localized deformation modes and non-schmid effects in crystalline solids. Part I. Crytical conditions of localization", *Mechanics of Materials.*, Vol. 23, pp. 71-102.

Dao, M. and Li, M. (2000), "A micromechanics study on strain localization induced fracture initiation in bending/hemming using crystal plasticity models", *Report No. 00-038, Alcoa Technical center*, 2000-04-25.

Dawson, P.R. and Beaudoin, A.J. (1998), "Finite element simulations of metal forming", *Kocks, U.F., Tomé, C.N. and Wenk, H.-R. (Eds.), Cambridge University Press*, pp. 533-558.

de Borst, R. and Groen, A.E. (1999), "Towards efficient and robust elements for 3D-soil plasticity", *Computers and Structures*, Vol. 70, pp. 23-34.

de Souza Neto, E.A., Peric, D., Dutko, M. & Owen, D.R.J., (1996), "Design of simple low order finite elements for large strain analysis of nearly incompressible solids", *International Journal of Solids and Structures*, Vol. 33, pp. 3277-3296.

Diehl, J. (1956), "Zugverformung von Kupfer-Einkristalen", *Z. Metallk.,* Vol. 47, pp. 351.

Doghri, I. (2000), *Mechanics of Deformable Solids - Linear, Nonlinear, Analytical and Computational Aspects,* Springer-Verlag, Berlin.

Doherty, W.P., Wilson, E.L. & Taylor, R.L., (1969), *Stress analysis of axisymmetric solids utilizing higher order quadrilateral finite elements*, SESM Report N° 69-3, University of California, Berkeley.

Doll, S., Schweizerhof, K., Hauptmann, R. and Freischlager, C. (2000), "On volumetric locking of low-order solid and solid-shell elements for finite elastoviscoplastic deformations and selective reduced integration", *Engineering Computations*, Vol. 17, pp. 874-902.

Drucker, D. C., (1951), "A more fundamental approach to plastic stress-strain solutions," *Proceedings of the 1st US national Congress in Applied Mechanics*, pp.487-491

Dvorkin, E.N. and Bathe, K.J. (1984), "A continuum mechanics based four-node shell element for general nonlinear analysis", *Engineering Computations*, Vol. 1, pp. 77-88.

Eberlein, R. and Wriggers, P. (1999), "Finite element concepts for finite elastoplastic strains and isotropic stress response in shells: theoretical and

computational analysis", *Computer Methods in Applied Mechanics and Engineering*, Vol. 171, pp. 243-279.

Ekmark, B., (1983), On *Large Strain Theories in Sheet Metal Forming*, PhD. Thesis, Luleå University, Sweden.

El-Abbasi, N. and Meguid, S.A. (2000), "A new shell element accounting for through-thickness deformation", *Computer Methods in Applied Mechanics and Engineering*, Vol. 189, pp. 841-862.

Eshelby, J.D. (1957), "The Determination of the Elastic Field of an Ellipsoidal Inclusion, and Related Problems", *Proceedings of the Royal Society London*, Vol. 241, pp.376.

Ewing, J.A. and Rosenhein, W. (1899), "Experiments in micro-metallurgy: effects of strain, preliminary notice", *Proceedings of the Royal Society London*, Vol. 65, pp. 85-90.

Fontes Valente, R.A., Natal Jorge, R.M., César de Sá, J.M.A. & Areias, P.M.A., (2002), Application of the Enhanced Assumed Strain Concept Towards the Development of Shear Locking-Free Shell Elements, *Proceedings of the Fifth World Congress on Computational Mechanics* (WCCM V), Vienna, Austria.

Fontes Valente, R.A., Natal Jorge, R.M., Cardoso, R.P.R., César de Sá, J.M.A., Grácio, J.J.A. (2003), "On the use of an enhanced transverse shear strain shell element for problems involving large rotations", *Computational Mechanics*, Vol. 30, pp. 286-296

Fontes Valente, R.A., Alves de Sousa, R.J., Natal Jorge, R.M. (2004), "An enhanced strain 3D element for large deformation elastoplastic problems in thin-shell applications", *Computational Mechanics*, Vol. 34, pp. 38-52.

Fontes Valente, R.A. (2004), *Developments on Shell and Solid-Shell Finite Elements Technology in Nonlinear Continuum Mechanics,* PhD. Thesis, University of Porto, Portugal.

Fontes Valente, R.A., Natal Jorge, R.M., César Sá, J.M.A. and Gracio, J.J. (2005), "Enhanced transverse shear strain shell formulation applied to large elasto-

plastic deformation problems", *International Journal for Numerical Methods in Engineering*, Vol. 62, pp. 1360-1398.

Fraeijs de Veubeke, B. M. (1951), "Diffusion des inconnues hyperstatiques dans les voilures à longeron couples", *Bull. Serv. Technique de L'Aéronautique n.º 24*, Imprimeríe Marcel Hayez, Bruxelles.

Freischlager, C. and Schweizerhof, K. (1996), "On a systematic development of trilinear three dimensional solid elements based on Simo's enhanced strain formulation", *International Journal of Solids and Structures,* Vol. 33, pp. 2993–3017.

Gambin, W. and Barlat, F. (1997), "Modeling of deformation texture based on rate independent crystal plasticity", *International Journal of Plasticity*, Vol.13, pp.75-85.

Gambin, W., (1991), "Plasticity of crystals with interacting slip systems", *Engineering Transactions,* Vol. 39, pp. 303.

Gambin, W. (1992), "Refined analysis of elastic-plastic crystals", *International Journal of Solids and Structures*, Vol. 29, pp. 2013.

Gambin, W. (2000), "Plasticity and Textures", Kluwer Academic Press.

Glaser, S. and Armero, F. (1997), "On the formulation of enhanced strain finite elements in finite deformations", *Engineering Computations*, Vol. 14, pp. 759-791.

Gotoh, M. (1977), "A theory of plastic anisotropy used on a yield function of fourth order", *International Journal of Mechanical Sciences* Vol. 19, pp. 505–520.

Gotoh, M. and Ishise, F., (1978), "A finite element analysis of rigid-plastic deformation of the flange in a deep-drawing process based on a fourth-degree yield function", *International Journal of Mechanical Sciences*, Vol. 20, pp. 423.

Habraken, A.M. (2004), "Modeling the plastic anisotropy of Metals", *Archives of Computational Methods in Engineering,* Vol. 11, pp. 3-96.

Han, C.S., Chung, K., Wagoner, R.H., Oh, S.I. (2003), "A multiplicative finite elasto-plastic formulation with anisotropic yield functions", *International Journal of Plasticity,* Vol. 19, pp. 197.

Harnau, M. and Schweizerhof, K. (2002), "About linear and quadratic 'solid-shell' elements at large deformations", *Computers and Structures*, Vol. 80, pp. 805-817.

Hauptmann, R. and Schweizerhof, K. (1998), "A systematic development of solid-shell element formulations for linear and non-linear analyses employing only displacement degrees of freedom", *International Journal for Numerical Methods in Engineering*, Vol. 42, pp. 49-69.

Hauptmann, R., Schweizerhof, K. and Doll, S. (2000), "Extension of the 'solid-shell' concept for application to large elastic and large elastoplastic deformations", *International Journal for Numerical Methods in Engineering*, Vol. 49, pp. 1121-1131.

Hauptmann, R., Doll, S., Harnau, M. and Schweizerhof, K. (2001), "Solid-shell elements with linear and quadratic shape functions at large deformations with nearly incompressible materials", *Computers and Structures*, Vol. 79, pp. 1671-1685.

Hecker, S.S. (1976), "Experimental Studies of Yield Phenomena in Biaxially Loaded Metals" *Constitutive Equations in Viscoplasticity: Computational and Engineering Aspects. ASME*, New York, pp. 1-33.

Hill, R. (1948), "A theory of the yielding and plastic flow of anisotropic materials", *Royal Society London Proceedings,* Vol. 19A, pp. 281-297.

Hill, R., (1950), *The Mathematical Theory of Plasticity*, Oxford University Press. England.

Hill, R. (1965a), "Continuum Micro-mechanics of Elastoplastic Polycrystals", *Journal of Mechanics and Physics of Solids*, Vol. 13, pp. 89.

Hill, R. (1965b), "A Self-consistent Mechanics of Composite Materials", *Journal of Mechanics and Physics of Solids*, Vol. 13, pp.231

Hill, R. (1966), "Generalized Constitutive Relations for Incremental Deformation of Metal Crystals by Multislip", *Journal of Mechanics and Physics of Solids*, Vol. 14, pp. 95.

Hill, R. and Rice, J.R. (1972), "Constitutive analysis of Elastic-Plastic Crystals at Arbitrary Strain", *Journal of Mechanics and Physics of Solids*, Vol. 20, pp. 401-413.

Hill, R. (1979), "Theoretical plasticity of textured aggregates", *Mathematical Proceedings of the Cambridge Philosophical Society,* Vol. 85, pp. 179–91.

Hill R., (1990), "Constitutive modelling of orthotropic plasticity in sheet metals", *Journal of the Mechanics and Physics of Solids*, Vol. 38, pp. 405–17.

Hill R., (1993), "A user-friendly theory of orthotropic plasticity in sheet metals", *International Journal of Mechanical Sciences,* Vol. 15, pp. 19–25.

Hodge, P.G., (1959), *Plastic Analysis of Structures*, McGraw-Hill.

Horrigmoe, G., Bergan, P.G. (1978), "Nonlinear analysis of freeform shells by flat finite elements", *Computer Methods in Applied Mechanics and Engineering*, Vol. 16, pp. 11-35.

Hosford, W.F. (1972), "A generalized isotropic yield criterion". *Journal of Applied Mechanics,* Vol. 39, pp. 607–609.

Hosford W.F. (1979), "On yield loci of anisotropic cubic metals", *Proceedings of the Seventh North American Metalworking Conference. Dearborn: SME* , pp. 191–197.

Hosford, W.F. (1993), *The Mechanics of Crystals and Textured Polycrystals*, Oxford University Press.

Hughes, T.J.R., (1977), "Equivalence of finite elements for nearly incompressible elasticity", *Journal of Applied Mechanics*, Vol. 44, pp. 181-183.

Hughes, T.J.R., Cohen, M. and Haroun, M. (1978), "Reduced and selective integration techniques in finite element analysis of plates", *Nuclear Engineering Design*, Vol. 46, pp. 203-222.

Hughes, T.J.R. (1980a), "Generalization of selective integration procedures to anisotropic and nonlinear media", *International Journal for Numerical Methods in Engineering*, Vol. 15, pp. 1413-1418.

Hughes, T.J.R., (1980b), Recent developments in computer methods for structural analysis, *Nuclear Engineering Design*, Vol. 57, pp. 427-439.

Hughes, T.J.R. (2000), *The Finite Element Method: Linear Static and Dynamic Finite Element Analysis*, Dover Editions, New Jersey.

Hutchinson, J.W. (1970), "Elastic-Plastic Behavior of Polycrystalline Metals and Composites", *Proccedings of the Royal Society London,* Vol. 319, pp. 247-272.

Hwang, Y.M. and Chen, W.C. (2005), "Analysis of tube hydroforming in a square cross-sectional die", *International Journal of Plasticity*, Vol. 21, pp. 1815-1833.

Kachanov, L.M., (1974), *Fundamentals of the Theory of Plasticity*, MIR Publishers, Moscow.

Kalindi, S.R., Bronkhorst, C.A. and Anand, L. (1992), "Crystallographic texture in bulk deformation processing of FCC metals", *Journal of Mechanics and Physics of Solids*, Vol. 40, pp. 537-569.

Karafillis, A.P. and Boyce, M.C. (1993), "A general anisotropic yield criterion using bounds and a transformation weighting tensor", *Journal of the Mechanics and Physics of Solids*, Vol. **41**, pp. 1859.

Kasper, E.P. and Taylor, R.L. (2000), "A mixed-enhanced strain method: Part I - linear problems", *Computer and Structures,* Vol. 75, pp. 237-250.

Kelly, E.W., Hosford, W.F. (1968), "The deformation characteristics of textured magnesium", *AIME Trans. Metall. Doc.*, Vo.l. 242, pp. 654-661.

Klinkel, S. and Wagner, W. (1997), "A geometrical non-linear brick element based on the EAS method", *International Journal for Numerical Methods in Engineering*, Vol. 40, pp. 4529-4545.

Klinkel, S., Gruttman, F. and Wagner, W. (1999), "A continuum based 3D-shell element for laminated structures", *Computers and Structures,* Vol. 71, pp. 43-62.

Kocks, U.F., Tomes, C.N., Wenk, H.R., (1998), *Texture and Anisotropy*, Cambridge University Press.

Korelc, J. (1996), "Symbolic approach in computational mechanics and its application to the Enhanced Strain method", *PhD. Thesis,* University of Darmstadt, Germany.

Korelc, J. and Wriggers, P. (1996), "An efficient 3D enhanced strain element with taylor expansion of the shape functions", *Computational Mechanics*, Vol. 19, pp. 30-40.

Krieg, R. D. and Krieg, D. B. (1977), "Accuracies of Numerical Solution Methods for the Elastic-Perfectly Plastic Model", *Journal of Pressure Vessel Technology*, ASME, Vol. 99, pp. 510-515.

Kröner, E. (1961), "Zur Plastischen Verformung des Vielkristalls", *Acta Metallurgica*, Vol. 9, pp. 155.

Kurtyka, T., Zyczkowski, M., (1996) "Evolution equations for distortional plastic hardening", *International Journal of Plasticity,* Vol. 23, pp. 191-213.

Lebensohn, R.A and Tomé, C.N. (1993), "A self-consistent anisotropic approach for the simulation of plastic deformation and texture development in polycrystals – Application to zirconium alloys", *Acta Metallurgica et Materialia,* Vol. 41, pp. 2611-2624.

Lee, E.H. (1969), "Elastic-plastic deformations at finite strain", *Journal of Applied Mechanics,* Vol. 36, pp. 1-6.

Lee, P.S. and Bathe, K.J. (2002), "On the asymptotic behaviour of shell structures and the evaluation of finite element solutions", *Computers and Structures*, Vol. 80, pp. 235-255.

Legay, A. and Combescure, A. (2003), "Elastoplastic stability analysis of shells using the physically stabilized finite element SHB8PS", *International Journal for Numerical Methods in Engineering*, Vol. 57, pp. 1299-1322.

Li, K.P., and Cescotto, S., (1997), "An 8-node brick element with mixed formulation for large deformation analyses", *Computer Methods in Applied Mechanics and Engineering*, Vol. 141, pp. 157-204.

Lindberg, G., Olson, M.M.D. and Cowper, G.R., (1969), New Developments in the Finite Element Analysis of Shells, *Quartely Bulletin of the Division of*

Mechanical Engineering and the National Aeronautical Establishment, National Research Council of Canada, Vol. 4.

Liu, W.K., Hu, Y.K., and Belytschko, T. (1994), "Multiple-quadrature underintegrated finite elements", *International Journal for Numerical Methods in Engineering*, Vol. 37, pp. 3263-3289.

Liu, W.K., Guo, Y., Tang, S. and Belytschko, T. (1998), "A multiple-quadrature eight-node hexahedral finite element for large deformation elastoplastic analysis", *Computer Methods in Applied Mechanics and Engineering*, Vol. 154, pp. 69-132.

Lubliner, J., (1990), *Plasticity Theory,* McMillan, New York.

MacMeecking, R.M. and Rice, J.R. (1975), "Finite formulation for problems of large elastic-plastic deformations", *International Journal of Solids and Structures*, Vol. 11, pp. 601-616.

Macneal, R.H. and Harder, R.L., (1985), "A proposed set of problems to test finite element accuracy", *Finite Elements in Analysis and Design*, Vol. 1, pp. 3-20.

Malkus, D.S. and Hughes, T.J.R., (1978), "Mixed finite element methods-reduced and selective integration techniques: a unification of concepts", *Computer Methods in Applied Mechanical Engineering*, Vol. 15, pp. 63-81.

Marques, J.M.M.C., (1984), "Stress computation in elastoplasticity, *Engineering Computations"*, Vol. 1, pp. 42-51.

Marsden, J.E. and Hughes, T.J.R. (1994), "Mathematical Foundations of Elasticity", *Dover Publications*, New York.

Masud, A., Tham, C.L., Liu, W.K. (2000), "A stabilized 3D co-rotational formulation for geometrically nonlinear analysis of multi-layered composite shells", *Computational Mechanics*, Vol. 26, pp. 1-12.

Mendelson, A., (1968), *Plasticity: Theory and Application*, McMillan, New York.

Miehe, C. and Apel, N. (2004), "Anisotropic elastic-plastic analysis of shells at large strains. A comparison of multiplicative and additive approaches to enhanced

finite element design and constitutive modeling". *International Journal for Numerical Methods in Engineering*, Vol. 61, pp. 1977-2181

Miehe, C., (1998), "A theoretical and computational model for isotropic elastoplastic stress analysis in shells at large strains", *Computer Methods in Applied Mechanics and Engineering,* Vol. 155, pp. 193-233.

Molinari, A., Canova, G.R. and Ahzi, S. (1987), "A self-consistent approach of the large deformation polycrystal viscoplasticity", *Acta Metallurgica*, Vol. 35, pp. 2983-2994.

Mori, K., (ed.) (2001), *Proceedings of the 7th International Conference on Numerical Methods in Industrial Forming Processes* (Numiform'01), Toyohashi, Japan, A.A. Balkema, Rotterdam.

Morley, L.S.D. (1963), *Skew Plates and Structures*, Pergamon Press, Oxford.

Nagtegaal, J.C., Parks, D.M. and Rice, J.R., (1974), "On Numerical accurate finite element solutions in the fully plastic range", *Computer Methods in Applied Mechanical Engineering*, Vol. 4, pp. 153-177.

Natal Jorge, R.M., (1997), *Modelação de Problemas Incompressíveis pelo Método das Deformações Acrescentadas baseado em Modos Compatíveis*, Phd. Thesis, University of Porto.

Nina Lautersztajn, S. and Samuelsson, A., (2000), Further discussion on four-node isoparametric quadrilateral elements in plane bending, *International Journal for Numerical Methods in Engineering*, Vol. 47, pp. 129-140.

NUMISHEET2002 organizing committee (2002), "Proceedings of the 5th International Conference and Workshop on Numerical Simulation of 3D Sheet Forming Processes", Jeju Island, Korea.

Oden, J.T. and Kikuchi, N., (1982), "Finite element methods for constrained problems in elasticity", *International Journal for Numerical Methods in Engineering*, Vol. 18, pp. 701-725.

Ortiz, M. and Popov, E.P., (1985), "Accuracy and stability of integration algorithms for elastoplastic constitutive equations", *International Journal for Numerical Methods in Engineering*, Vol. 21, pp. 1561-1576.

Owen, D.R.J. and Hinton, E., (1980), *Finite Elements in Plasticity: Theory and Practice*, Pineridge Press, Swansea, U.K.

Pan, J. and Rice J.R. (1983), "Rate Sensitivity of Plastic Flow and Implications for Yield Surface Vertices", *International Journal of Solids and Structures*, Vol. 19, pp. 973-987

Park, K.C. (1986), "Improved strain interpolation for curved C0 elements", *International Journal for Numerical Methods in Engineering*, Vol. 22, pp. 281-288.

Park, K.C. and Stanley, G. (1986), "A curved C0 shell element based on assumed natural coordinate strains", *Journal of Applied Mechanics*, Vol. 53, pp. 278-290.

Pastor, M., Quecedo, M. and Zienkiewicz, O.C., (1997), "A mixed displacement-pressure formulation for numerical analysis of plastic failure", *Computers and Struct*ures, Vol.62, pp.13-23.

Peirce, D., Asaro, R. J., and Needleman, A. (1982), "An analysis of Nonuniform and Localized deformation in ductile single crystals" *Acta Mettalurgica*, Vol. 30, pp. 1087-1119.

Peirce, D., Asaro, R. J., and Needleman, A. (1983), "Material rate dependence and localized deformation in crystalline solids", *Acta Mettalurgica*, Vol. 31, pp. 1951-1976.

Piltner, R. (2000), "An implementation of mixed enhanced finite elements with assumed strains in Cartesian and natural element coordinates using sparse B-matrices", *Engineering Computations*, Vol. 17, pp. 933-949.

Prager, W., (1959), *An Introduction to Plasticity*, Addison-Wesley.

Puso, M.A., (2000), "A highly efficient enhanced assumed strain physically stabilized hexahedral element", *International Journal for Numerical Methods in Engineering*, Vol. 49, pp. 1029-1064.

Ramm, E. and Matzenmiller, A. (1988), "Consistent linearization in elasto-plastic shell analysis", *Engineering Computations*, Vol. 5, pp. 289-299.

Reese S., Kussner, M., and Reddy B.D. (1999), "A new stabilization technique for finite elements in non-linear elasticity", *International Journal for Numerical Methods in Engineering*, Vol. 44, pp. 1617 – 1652.

Reese S., Wriggers, P., and Reddy B.D. (2000), "A new locking-free brick element technique for large deformation problems in finite elasticity", *Computers and Structures,* Vol. 75, pp. 291-304.

Reese, S. (2002), "On the equivalence of mixed element formulations and the concept of reduced integration in large deformation problems", *International Journal of Nonlinear Sciences and Numerical Simulation,* Vol. 3, pp. 1-33.

Reese, S. (2005), "On a physically stabilized one point finite element formulation for three-dimensional finite elasto-plasticity", *Computer Methods in Applied Mechanics and Engineering,* Vol. 194, pp. 4685-4715.

Reese, S. (2006), "A large deformation solid-shell concept based on reduced integration with hourglass stabilization", *International Journal for Numerical Methods in Engineering,* available online.

Reese, S. and Wriggers, P. (2000), "A stabilization technique to avoid hourglassing in finite elasticity", *International Journal for Numerical Methods in Engineering*, Vol. 48, pp. 79-109.

Rice, J.R. (1971), "Inelastic Constitutive Relations for Solids: An Internal Variable Theory and Its Application to Metal Plasticity", *Journal of the Mechanics and Physics of Solids*, Vol. 19, pp. 433-455

Roe, R.J. (1965), Journal of Applied Physics, Vol. 36, pp. 2024-2031

Rohel, D. and Ramm, E. (1996), "Large elasto-plastic finite element analysis of solids and shells with the enhanced assumed strain concept", *International Journal of Solids and Structures*, Vol. 33, pp. 3215-3237.

Runesson, K., Samuelsson, A. and Bernspang, L., (1986), "Numerical techniques in plasticity including solution advancement control", *International Journal for Numerical Methods in Engineering*, Vol. 22, pp. 769-788.

Sachs, G. (1928), "Zur Ableitung einer Fliessebedingung", *Zeichschrift der Verein deutscher Ingenieur,* Vol. 72, pp. 734.

Schmid. E. (1924), "Yield point of crystals – Critical Shear stress law", *Proceedings of the International Congress in Applied Mechanics,* Delft, pp. 324

Schönauer, M., (1993), *Unified numerical analysis of cold and hot metal forming processes*, PhD. Thesis, University College of Swansea, Wales, U.K.

Scordelis, A.C. and Lo, K.S. (1969), "Computer analysis of cylindrical shells", *Journal of American Concrete Institute*, Vol. 61, pp. 539-561.

Simo, J.C. and Taylor, R.L., (1985), "Consistent tangent operators for rate-independent elastoplasticity", *Computer Methods in Applied Mechanical Engineering*, Vol. 48, pp. 101-118.

Simo, J.C. and Hughes, T.J.R., (1986), "On the variational foundations of assumed strain methods", *Journal of Applied Mechanics*, ASME, Vol. 53, pp. 51-54.

Simo, J.C. and Taylor, R.L., (1986), "A return mapping algorithm for plane stress elastoplasticity", *International Journal for Numerical Methods in Engineering*, Vol. 22, pp. 649-670.

Simo, J.C., Fox, D.D. and Rifai, M.S., (1989), "On a stress resultant geometrically exact shell model. Part II: The linear theory – computational aspects", *Computer Methods in Applied Mechanics and Engineering*, Vol. 73, pp. 53-92.

Simo, J.C., Fox, D.D. and Rifai, M.S., (1990), "On a stress resultant geometrically exact shell model. Part III: Computational aspects of the nonlinear theory", *Computer Methods in Applied Mechanics and Engineering*, Vol. 79, pp. 21-70.

Simo, J.C. and Rifai, M.S. (1990), "A class of mixed assumed strain methods and the method of incompatible modes", *International Journal for Numerical Methods in Engineering*, Vol. 29, pp. 1595-1638.

Simo, J.C. and Armero, F. (1992), "Geometrically non-linear enhanced strain mixed methods and the method of incompatible modes", *International Journal for Numerical Methods in Engineering*, Vol. 33, pp. 1413-1449.

Simo, J.C., Armero, F. and Taylor, R.L. (1993), "Improved versions of assumed enhanced strain tri-linear elements for 3D finite deformation problems", *Computer Methods in Applied Mechanics and Engineering*, Vol. 110, pp. 359-386.

Simo, J.C. and Hughes, T.J.R., (1998), *Computational Inelasticity*, Interdisciplinary Applied Mathematics, Springer, New York.

Simões, F.J.P. (2006), "Asymmetric Rolling of Aluminum Alloys", *PhD Thesis,* University of Aveiro, Portugal.

Stoughton, T.B. and Yoon, J.W. (2006) "Review of Drucker's Postulate and the Issue of Plastic Stability", *International Journal of Plasticity*, Vol. 22, pp. 391-433.

Taylor, G.I. and Elam, C.F. (1923), "The distortion of an aluminum crystal during a tensile test", *Proceedings of the Royal Society London*, Vol. 102 pp. 643-667.

Taylor, G.I. and Elam, C.F. (1925), "The plastic extension and fracture of aluminum crystals", *Proceedings of the Royal Society London*, Vol. 108, pp. 25-51.

Taylor, G.I. (1938), "Plastic strain in metals", *Journal Institute of Metals*, Vol. 62 pp. 307-324

Taylor, R.L., (1998), *FEAP (A Finite Element Analysis Program) Theory Manual - Version 7.4*, University of California, Berkeley.

Taylor, R.L., Beresford, P.J. and Wilson, E.L. (1976), "A non-conforming element for stress analysis", *International Journal for Numerical Methods in Engineering*, Vol. 10, pp. 1211-1219.

Teodosiu, C. and Hu, Z. (1998), "Microstructure in the continuum modeling of plastic anisotropy", "*Proceedings of the Riso International Symposium on Material Science: Modelling of Structure and Mechanics of Materials from Microscale to products*", Riso National Lab, Roskilde, Denmark, pp. 149-168.

TexSEM Laboratories (2006), "Introduction to OIM analysis", TSL / EDAX, Utah, USA.

Timoshenko, S.P. and Goodier, J.N., (1951), *Theory of Elasticity*, McGraw-Hill, New York.

Tomé, C.N. and Canova, G.R. (1998), "Self-Consistent Modeling of Heterogenous Plasticity, in Texture and Anisotropy", *Kocks, U.F., Tomé, C.N. and Wenk, H.-R. (Eds), Cambridge University Press*, pp. 467-531.

Van Houtte, P. (1988), "A comprehensive mathematical formulation of an extended Taylor–Bishop–Hill model featuring relaxed constraints, the Renouard-Winterberger theory and a strain rate sensitive model", *Textures and Microstructures,* Vol. 8, pp. 313–350.

Van Note, S. (2006), Web Page, www.public.asu.edu/~scottv/index.html

Vegter, D., Drent, P. and Huetink, J. (1995), "A planar isotropic yield criterion based on mechanical testing at multiaxial stress states", *Proceedings of the NUMIFORM 1995 Conference,* Ithaca, USA, pp. 354–360.

von Mises, R., (1913), Mechanik der festen Körper im Plastisch deformablen Zustand, *Götting. Nachr. Math. Phys. Kl.,* pp. 582-592.

Vu-Quoc, L. (1990), "A perturbation method for dynamic analysis of under-integrated shell elements", *Computer Methods in Applied Mechanics and Engineering,* Vol. 79, pp. 129-172,.

Vu-Quoc, L. and Tan, X.G. (2003), "Optimal solid-shells for non-linear analysis of multilayer composites. Part I: Statics", *Computer Methods in Applied Mechanics and Engineering*, Vol. 192, pp. 975-1016.

Vu-Quoc, L. and Tan, X.G. (2003), "Optimal solid-shells for non-linear analysis of multilayer composites. Part II: Dynamics", *Computer Methods in Applied Mechanics and Engineering*, Vol. 192, pp. 1017-1059.

Vu-Quoc, L., and Hoff, C. (1992), "On a highly robust spurious-mode filtering method for uniformly reduced-integrated shell elements", *International Journal for Numerical Methods in Engineering*, Vol. 34, pp. 209-220.

Vu-Quoc, L., and Mora, J.A. (1989), "A class of simple and efficient degenerated shell elements - Analysis of global spurious-mode filtering", *Computer Methods in Applied Mechanics and Engineering*, Vol. 74, pp. 117-175.

Wagner, W., Klinkel, S., Gruttmann, F. (2002), "Elastic and plastic analysis of thin-walled structures using improved hexahedral elements", *Computers and Structures*, Vol. 80, pp.857–869

Wagoner, R.H. and Chenot, J.-L., (2001), *Metal forming analysis*, Cambridge University Press, U.K.

Washizu, K., (1982), *Variational Methods in Elasticity and Plasticity,* 3rd Edition, Pergamon Press, Oxford.

Wilkins, M.L., (1964), Calculation of elastic-plastic flow, *Methods of Computational Physics*, B. Alder *et al.* (Eds.), Vol. 3, Academic Press, New York.

Wilson, E.L., Taylor, R.L., Doherty, W.P. and Ghaboussi, J. (1973), Incompatible displacement models, in S.J. Fenves et al. (Eds.): *Numerical Computational Models in Structural Mechanics*, Academic Press, New York.

Wriggers, P., Eberlein, R. and Reese, S. (1996), "A comparison of three-dimensional continuum and shell elements for finite plasticity", *International Journal for Solids and Structures*, Vol. 33, pp. 3309-3326.

Yoon, J.W. (1997), "Finite element formulation based on incremental deformation theory for sheet metal forming of planar anisotropic materials", Ph.D. Dissertation, Department of Mechanical Engineering, Korea Advanced Institute of Science and Technology

Yoon, J. W., Yang, D. Y. and Chung, K. (1999a), "Elasto-plastic finite element method based on incremental deformation theory and continuum based shell elements for planar anisotropic sheet materials", *Computer Methods in Applied Mechanics and Engineering*, Vol. 174, pp. 23-56.

Yoon, J.W., Yang, D.Y., Chung, K. and Barlat, F. (1999b), "A general elasto-plastic finite element formulation based on incremental deformation theory for planar anisotropy and its application to sheet metal forming", *International Journal of Plasticity*, Vol. 15, pp. 35-67.

Yoon, J.W., Barlat, F. and Dick, R.E. (2000a) "Sheet metal forming simulation for aluminum alloy sheet", *SAE 2000*, Michigan, USA pp. 67-72.

Yoon, J.W., Barlat, F., Chung, K., Pourboghrat, F. and Yang, D.Y. (2000b), "Earing predictions based on asymmetric non-quadratic yield function", *International Journal of Plasticity*, Vol. 16, pp. 1075-1104.

Yoon, J.W., Pourboghrat, F., Chung, K. and Yang, D.Y. (2002), "Springback prediction for sheet metal forming process using a 3D hybrid membrane/shell method", *International Journal of Mechanical Sciences*, Vol. 44, pp. 2133–2153.

Yoon, J.W., Barlat, F., Gracio, J.J., Rauch, E. (2005), "Anisotropic strain hardening behavior in simple shear for cube textured aluminum alloy sheets" *International Journal of Plasticity,* Vol. 21, pp. 2426-2447.

Yoon, J.W., Barlat, F., Dick, R.E. and Karabin, M.E. (2006), "Prediction of six or eight ears in a drawn cup based on a new anisotropic yield function", *International Journal of Plasticity*, Vol. 22, pp. 174-193.

Zienkiewicz, O.C. and Taylor, R.L., (2000), *The Finite Element Method*, 5th ed., Vol. 1&2, McGraw-Hill, New York.

Zienkiewicz, O.C., Taylor, R.L. & Baynham, J.M., (1983), "Mixed and irreducible formulations in finite element analysis", *Hybrid and Mixed Finite Element Methods,* S.N. Atluri *et al.* (Eds.), John Wiley & Sons, London, pp.405-431.

Zienkiewicz, O.C., Taylor, R.L. and Too, J.M. (1971), "Reduced integration technique in general analysis of plates and shells"*, International Journal for Numerical Methods in Engineering*, Vol. 3, pp. 275-290.

Appendix A

Decomposition of Strain-Displacement operator B

Let us recall the following decomposition of the classical strain-displacement operator $\mathbf{B}_u$, as utilized in Chapter 3.

$$\mathbf{B}_u = \mathbf{B}^c + \mathbf{B}^\xi \xi + \mathbf{B}^\eta \eta + \mathbf{B}^\zeta \zeta + \mathbf{B}^{\xi\eta} \xi\eta + \mathbf{B}^{\xi\zeta} \xi\zeta + \mathbf{B}^{\eta\zeta} \eta\zeta \,. \qquad (A.1)$$

In the following pages, the expressions for each term in equation (A.1) are given.

Appendix A: Decomposition of Strain-Displacement operator B

$$\mathbf{B}^{c} = \frac{1}{64}\begin{bmatrix} \xi_j x_j \xi_i & \xi_j y_j \xi_i & \xi_j z_j \xi_i \\ \eta_j x_j \eta_i & \eta_j y_j \eta_i & \eta_j z_j \eta_i \\ \zeta_j x_j \zeta_i & \zeta_j y_j \zeta_i & \zeta_j z_j \zeta_i \\ \xi_j x_j \eta_i + \eta_j x_j \xi_i & \xi_j y_j \eta_i + \eta_j y_j \xi_i & \xi_j z_j \eta_i + \eta_j z_j \xi_i \\ \xi_j x_j \zeta_i + \zeta_j x_j \xi_i & \xi_j y_j \zeta_i + \zeta_j y_j \xi_i & \xi_j z_j \zeta_i + \zeta_j z_j \xi_i \\ \eta_j x_j \zeta_i + \zeta_j x_j \eta_i & \eta_j y_j \zeta_i + \zeta_j y_j \eta_i & \eta_j z_j \zeta_i + \zeta_j z_j \eta_i \end{bmatrix} \tag{A.2}$$

$$\mathbf{B}^{\xi} = \frac{1}{64}\begin{bmatrix} 0 & 0 & 0 \\ \eta_j x_j h_{1i} + h_{1j} x_j \eta_i & \eta_j y_j h_{1i} + h_{1j} y_j \eta_i & \eta_j z_j h_{1i} + h_{1j} z_j \eta_i \\ \zeta_j x_j h_{2i} + h_{2j} x_j \zeta_i & \zeta_j y_j h_{2i} + h_{2j} y_j \zeta_i & \zeta_j z_j h_{2i} + h_{2j} z_j \zeta_i \\ \xi_j x_j h_{1i} + h_{1j} x_j \xi_i & \xi_j y_j h_{1i} + h_{1j} y_j \xi_i & \xi_j z_j h_{1i} + h_{1j} z_j \xi_i \\ \xi_j x_j h_{2i} + h_{2j} x_j \xi_i & \xi_j y_j h_{2i} + h_{2j} y_j \xi_i & \xi_j z_j h_{2i} + h_{2j} z_j \xi_i \\ \eta_j x_j h_{2i} + \zeta_j x_j h_{1i} + h_{1j} x_j \zeta_i + h_{2j} x_j \eta_i & \eta_j y_j h_{2i} + \zeta_j y_j h_{1i} + h_{1j} y_j \zeta_i + h_{2j} y_j \eta_i & \eta_j z_j h_{2i} + \zeta_j z_j h_{1i} + h_{1j} z_j \zeta_i + h_{2j} z_j \eta_i \end{bmatrix} \tag{A.3}$$

$$\mathbf{B}^{\eta} = \frac{1}{64}\begin{bmatrix} \xi_j x_j h_{1i} + h_{1j} x_j \xi_i & \xi_j y_j h_{1i} + h_{1j} y_j \xi_i & \xi_j z_j h_{1i} + h_{1j} z_j \xi_i \\ 0 & 0 & 0 \\ \zeta_j x_j h_{3i} + h_{3j} x_j \zeta_i & \zeta_j y_j h_{3i} + h_{3j} y_j \zeta_i & \zeta_j z_j h_{3i} + h_{3j} z_j \zeta_i \\ \eta_j x_j h_{1i} + h_{1j} x_j \eta_i & \eta_j y_j h_{1i} + h_{1j} y_j \eta_i & \eta_j z_j h_{1i} + h_{1j} z_j \eta_i \\ \xi_j x_j h_{3i} + \zeta_j x_j h_{1i} + h_{1j} x_j \zeta_i + h_{3j} x_j \xi_i & \xi_j y_j h_{3i} + \zeta_j y_j h_{1i} + h_{1j} y_j \zeta_i + h_{3j} y_j \xi_i & \xi_j z_j h_{3i} + \zeta_j z_j h_{1i} + h_{1j} z_j \zeta_i + h_{3j} z_j \xi_i \\ \eta_j x_j h_{3i} + h_{3j} x_j \eta_i & \eta_j y_j h_{3i} + h_{3j} y_j \eta_i & \eta_j z_j h_{3i} + h_{3j} z_j \eta_i \end{bmatrix} \tag{A.4}$$

$$\mathbf{B}^{\zeta} = \frac{1}{64}\begin{bmatrix} \xi_j x_j h_{2i} + h_{2j} x_j \xi_i & \xi_j y_j h_{2i} + h_{2j} y_j \xi_i & \xi_j z_j h_{2i} + h_{2j} z_j \xi_i \\ \eta_j x_j h_{3i} + h_{3j} x_j \eta_i & \eta_j y_j h_{3i} + h_{3j} y_j \eta_i & \eta_j z_j h_{3i} + h_{3j} z_j \eta_i \\ 0 & 0 & 0 \\ \xi_j x_j h_{3i} + \eta_j x_j h_{2i} + h_{2j} x_j \eta_i + h_{3j} x_j \xi_i & \xi_j y_j h_{3i} + \eta_j y_j h_{2i} + h_{2j} y_j \eta_i + h_{3j} y_j \xi_i & \xi_j z_j h_{3i} + \eta_j z_j h_{2i} + h_{2j} z_j \eta_i + h_{3j} z_j \xi_i \\ \zeta_j x_j h_{2i} + h_{2j} x_j \zeta_i & \zeta_j y_j h_{2i} + h_{2j} y_j \zeta_i & \zeta_j z_j h_{2i} + h_{2j} z_j \zeta_i \\ \zeta_j x_j h_{3i} + h_{3j} x_j \zeta_i & \zeta_j y_j h_{3i} + h_{3j} y_j \zeta_i & \zeta_j z_j h_{3i} + h_{3j} z_j \zeta_i \end{bmatrix} \tag{A.5}$$

Appendix A: Decomposition of Strain-Displacement operator B

$$\mathbf{B}^{\xi\eta} = \frac{1}{64}\begin{bmatrix} 0 & 0 & 0 \\ 0 & 0 & 0 \\ \zeta_j x_j h_{4i} + h_{4j} x_j \zeta_i + h_{2j} x_j h_{3i} + h_{3j} x_j h_{2i} & \zeta_j y_j h_{4i} + h_{4j} y_j \zeta_i + h_{2j} y_j h_{3i} + h_{3j} y_j h_{2i} & \zeta_j z_j h_{4i} + h_{4j} z_j \zeta_i + h_{2j} z_j h_{3i} + h_{3j} z_j h_{2i} \\ 2h_{1j} x_j h_{1i} & 2h_{1j} y_j h_{1i} & 2h_{1j} z_j h_{1i} \\ \xi_j x_j h_{4i} + h_{4j} x_j \xi_i + h_{1j} x_j h_{2i} + h_{2j} x_j h_{1i} & \xi_j y_j h_{4i} + h_{4j} y_j \xi_i + h_{1j} y_j h_{2i} + h_{2j} y_j h_{1i} & \xi_j z_j h_{4i} + h_{4j} z_j \xi_i + h_{1j} z_j h_{2i} + h_{2j} z_j h_{1i} \\ \eta_j x_j h_{4i} + h_{4j} x_j \eta_i + h_{1j} x_j h_{3i} + h_{3j} x_j h_{1i} & \eta_j y_j h_{4i} + h_{4j} y_j \eta_i + h_{1j} y_j h_{3i} + h_{3j} y_j h_{1i} & \eta_j z_j h_{4i} + h_{4j} z_j \eta_i + h_{1j} z_j h_{3i} + h_{3j} z_j h_{1i} \end{bmatrix} \quad (\text{A.6})$$

$$\mathbf{B}^{\xi\zeta} = \frac{1}{64}\begin{bmatrix} 0 & 0 & 0 \\ \eta_j x_j h_{4i} + h_{4j} x_j \eta_i + h_{1j} x_j h_{3i} + h_{3j} x_j h_{1i} & \eta_j y_j h_{4i} + h_{4j} y_j \eta_i + h_{1j} y_j h_{3i} + h_{3j} y_j h_{1i} & \eta_j z_j h_{4i} + h_{4j} z_j \eta_i + h_{1j} z_j h_{3i} + h_{3j} z_j h_{1i} \\ 0 & 0 & 0 \\ \xi_j x_j h_{4i} + h_{4j} x_j \xi_i + h_{1j} x_j h_{2i} + h_{2j} x_j h_{1i} & \xi_j y_j h_{4i} + h_{4j} y_j \xi_i + h_{1j} y_j h_{2i} + h_{2j} y_j h_{1i} & \xi_j z_j h_{4i} + h_{4j} z_j \xi_i + h_{1j} z_j h_{2i} + h_{2j} z_j h_{1i} \\ 2h_{2j} x_j h_{2i} & 2h_{2j} y_j h_{2i} & 2h_{2j} z_j h_{2i} \\ \zeta_j x_j h_{4i} + h_{4j} x_j \zeta_i + h_{2j} x_j h_{3i} + h_{3j} x_j h_{2i} & \zeta_j y_j h_{4i} + h_{4j} y_j \zeta_i + h_{2j} y_j h_{3i} + h_{3j} y_j h_{2i} & \zeta_j z_j h_{4i} + h_{4j} z_j \zeta_i + h_{2j} z_j h_{3i} + h_{3j} z_j h_{2i} \end{bmatrix} \quad (\text{A.7})$$

$$\mathbf{B}^{\eta\zeta} = \frac{1}{64}\begin{bmatrix} \xi_j x_j h_{4i} + h_{4j} x_j \xi_i + h_{1j} x_j h_{2i} + h_{2j} x_j h_{1i} & \xi_j y_j h_{4i} + h_{4j} y_j \xi_i + h_{1j} y_j h_{2i} + h_{2j} y_j h_{1i} & \xi_j z_j h_{4i} + h_{4j} z_j \xi_i + h_{1j} z_j h_{2i} + h_{2j} z_j h_{1i} \\ 0 & 0 & 0 \\ 0 & 0 & 0 \\ \eta_j x_j h_{4i} + h_{4j} x_j \eta_i + h_{1j} x_j h_{3i} + h_{3j} x_j h_{1i} & \eta_j y_j h_{4i} + h_{4j} y_j \eta_i + h_{1j} y_j h_{3i} + h_{3j} y_j h_{1i} & \eta_j z_j h_{4i} + h_{4j} z_j \eta_i + h_{1j} z_j h_{3i} + h_{3j} z_j h_{1i} \\ \zeta_j x_j h_{4i} + h_{4j} x_j \zeta_i + h_{2j} x_j h_{3i} + h_{3j} x_j h_{2i} & \zeta_j y_j h_{4i} + h_{4j} y_j \zeta_i + h_{2j} y_j h_{3i} + h_{3j} y_j h_{2i} & \zeta_j z_j h_{4i} + h_{4j} z_j \zeta_i + h_{2j} z_j h_{3i} + h_{3j} z_j h_{2i} \\ 2h_{3j} x_j h_{3i} & 2h_{3j} y_j h_{3i} & 2h_{3j} z_j h_{3i} \end{bmatrix} \quad (\text{A.8})$$

Appendix B

Multi-Stage Return Mapping

The multi-stage return mapping algorithm was firstly introduced by Yoon (1997) and further employed by Yoon et al. (1999a; 1999b) and Cardoso et al. (2002) in the context of anisotropic yield functions for aluminum. In this work, the procedure is utilized both for phenomenological and physically based yield functions. The core idea of the multi-stage return mapping algorithm, in a stress-return procedure, is to divide the total residual into several sub-steps, Figure B-1. In cases where second order derivatives are not calculated (which may be a cumbersome task in case of highly nonlinear yield functions), the multi-stage return mapping helps the normal vector to follow a more correct path until convergence in the final yield locus.
Let us consider a modified equation stipulating that the updated stress stays on the work-hardening curve, equation (4.54). For a given sub-step (k), the equation is modified with the given residual as follows:

$$F(\lambda_{(k)}) = \overline{\sigma}(\boldsymbol{\sigma}^{\mathrm{TR}} - \lambda_{(k)}\mathbf{C}^{e}\mathbf{m}_{(k)}) - h(\overline{\varepsilon}_{n}^{p} + \lambda_{(k)}) = F_{(k)}\,. \tag{B.1}$$

Based on the incremental deformation theory ($\lambda = \overline{\varepsilon}^{p}$), equation (B.1) can be interpreted like this for a given number of substeps (n_{step}):

$$\begin{aligned}
&F(\lambda_{(0)}) = \overline{\sigma}(\boldsymbol{\sigma}^{\mathrm{TR}}) - h({}^{n}\overline{\varepsilon}^{p}) = F_{(0)} \\
&F(\lambda_{(1)}) = \overline{\sigma}({}^{n+1}\boldsymbol{\sigma}_{(0)} - \lambda_{(1)}\mathbf{C}^{e}\mathbf{m}_{(0)}) - h({}^{n}\overline{\varepsilon}^{p} + \lambda_{(1)}) = F_{(1)} \\
&F(\lambda_{(2)}) = \overline{\sigma}({}^{n+1}\boldsymbol{\sigma}_{(1)} - \lambda_{(2)}\mathbf{C}^{e}\mathbf{m}_{(1)}) - h({}^{n}\overline{\varepsilon}^{p} + \lambda_{(2)}) = F_{(2)} \\
&\vdots \\
&F(\lambda_{(n_{step})}) = \overline{\sigma}({}^{n+1}\boldsymbol{\sigma}_{(n_{step}-1)} - \lambda_{(n_{step})}\mathbf{C}^{e}\mathbf{m}_{(n_{step}-1)}) - h({}^{n}\overline{\varepsilon}^{p} + \lambda_{(n_{step})}) = 0
\end{aligned} \quad . \tag{B.2}$$

As shown in equation (B.2) and Figure B-1, the direction of the first sub-step $\mathbf{m}_{(1)}$ is estimated from the direction $\mathbf{m}_{(0)}$, which is normal to the yield surface at the trial stress ($\boldsymbol{\sigma}^{\mathrm{TR}}$). Then, the exact direction $\mathbf{m}_{(1)}$ can be obtained from the 1st sub-step nonlinear solution based on the Euler backward method. After solving for the 1st sub-

step, the new direction for the 2nd sub-step $\mathbf{m}_{(2)}$ is estimated from the direction $\mathbf{m}_{(1)}$ based on the 1st sub-step stress ($\boldsymbol{\sigma}_{(1)} = \boldsymbol{\sigma}^{\mathrm{TR}} - \lambda_{(1)}\mathbf{C}^{e}\mathbf{m}_{(1)}$) and so on. This procedure ends when $F = F_{(n_{step})} = 0$ and consequently ${}^{n+1}\boldsymbol{\sigma} \leftarrow \boldsymbol{\sigma}_{(n_{step})}$. Finally, the proportional logarithmic plastic strain remains normal to the yield surface at the final stress (${}^{n+1}\boldsymbol{\sigma}$), i.e.,

$$\Delta\boldsymbol{\varepsilon}^{p} = \Delta\bar{\varepsilon}^{p}\frac{\partial\bar{\sigma}}{\partial\,{}^{n+1}\boldsymbol{\sigma}}(\equiv \lambda_{(n_{step})}\ \mathbf{m}_{(n_{step})}) \tag{B.3}$$

Therefore, the normality condition of the incremental deformation theory is satisfied at the current state (n+1).

If the multiscale approach based on the FC Taylor model and interacting slip systems concept is used, the iteration procedure for any (k-th) step is given according with the guidelines given in section (4.5.2). In case of anisotropic yield functions, like Yld91 or Yld2004-18p, an interested reader should check Yoon et al. (1999a; 1999b), Cardoso (2002) or Yoon et al. (2006).

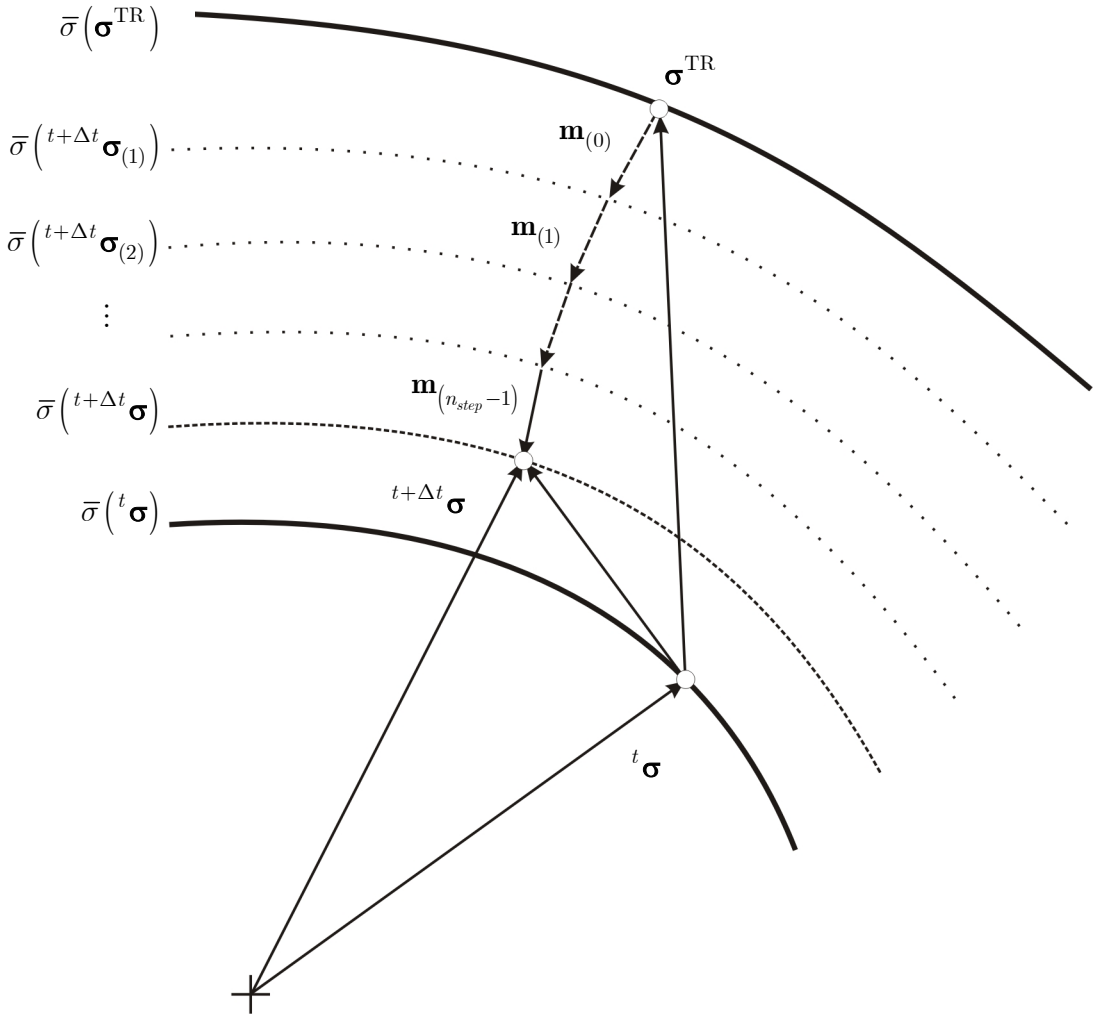

Figure B-1: Semi-implicit multistage return mapping

Appendix C

Pole Figures

There is a complex set of definitions associated to the construction and interpretation of pole figures, namely stereographic projections, material preferred textures, Orientation Distribution Functions and so on, which itself could be enough matter for an entire book. In the following lines, only some qualitative definitions are given for a reader that never had contact with this field. For a proper and complete explanation of all concepts on direct and inverse pole figures, please refer to Bunge (1982), Kocks et al. (1998) or Hosford (1993), to cite just a few references on the field.

Roughly speaking, a direct pole figure is a graphical representation of the angular distribution function of a chosen crystal direction, with respect to the sample coordinate system. Consider a cubic crystal in a rolled sheet sample with the axes as shown in Figure C-1.

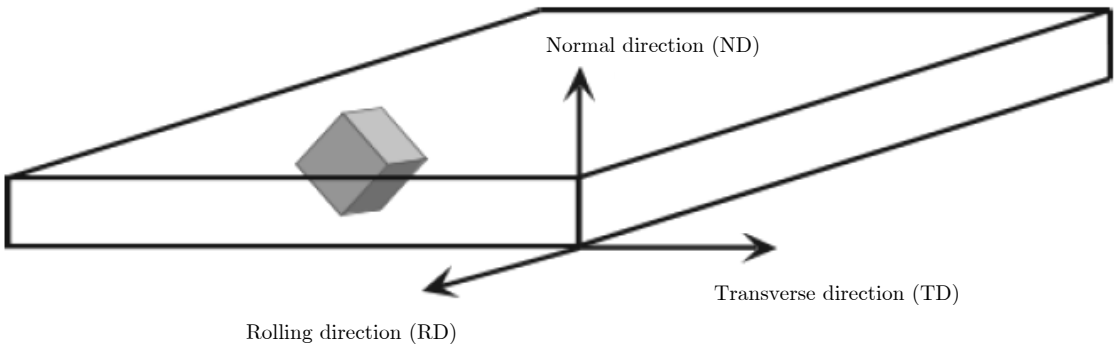

Figure C-1: Crystal orientation and sample coordinate system

All planes and directions of a crystal can be represented on a spherical surface by letting them pass through the center of a reference sphere and extending them until they intersect the reference sphere (Figure C-2a). Thus, a direction can be represented by two diametrically opposite points at which it intersects the sphere. A plane is represented by the great circle formed by its intersection with the reference sphere. Additionally, it can be also represented by its pole (normal to the plane passing on the center of the sphere), being plotted in this case like a direction.

Since plotting and measurement on a spherical surface would be a cumbersome job, it is convenient to map the sphere onto a plane (Figure C-2b). The most common mapping system is the stereographic projection (Bunge, 1982). Measurements can be made with the aid of trigonometry or using a Wulff net (Hosford, 1993).

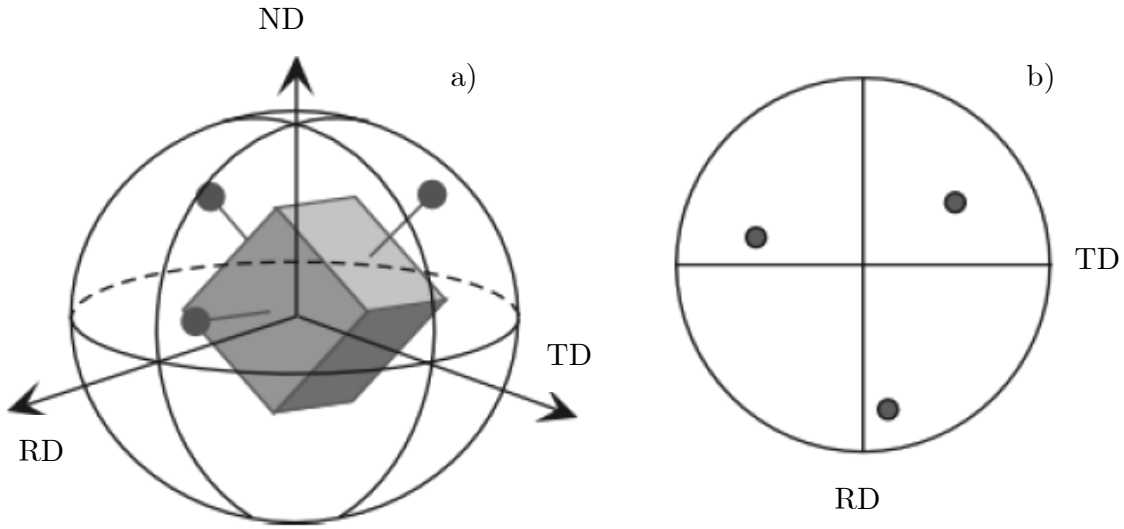

Figure C-2: a) Reference sphere; b) Stereographic projection (Texsem, 2006).

The example represented on Figure C-2 is a {001} pole figure. Note that the three points shown in the pole figure are for three symmetrically equivalent planes of the crystal.

On the other hand, the traces of {100} and {110} planes breakup the hemisphere into 24 equivalent spherical triangles, each one having <100>, <110> and <111> directions as corners, Figure C-3. Because all triangles are equivalent, the orientation of a single direction may be represented as a point in any triangle.

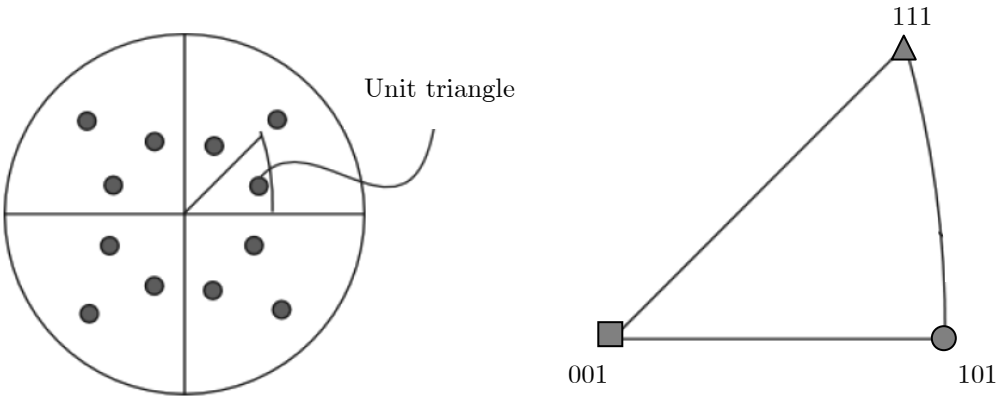

Figure C-3: Pole figure and unit triangle.

So far we have looked at stereographic projections for a single crystal/orientation. Extending the idea to polycrystalline materials, a set of poles can be plotted for each individual grain to produce a pole figure.

If the grains are randomly oriented, then we should expect to see the poles distributed regularly over the pole figure (Figure C-4a). More often the grains are not randomly oriented, but tend towards particular orientations depending on the alloy composition and processing history. This is called the "preferred" orientation, or crystallographic texture of the material (Figure C-4b). In this case the poles will be concentrated within certain areas of the pole figure.

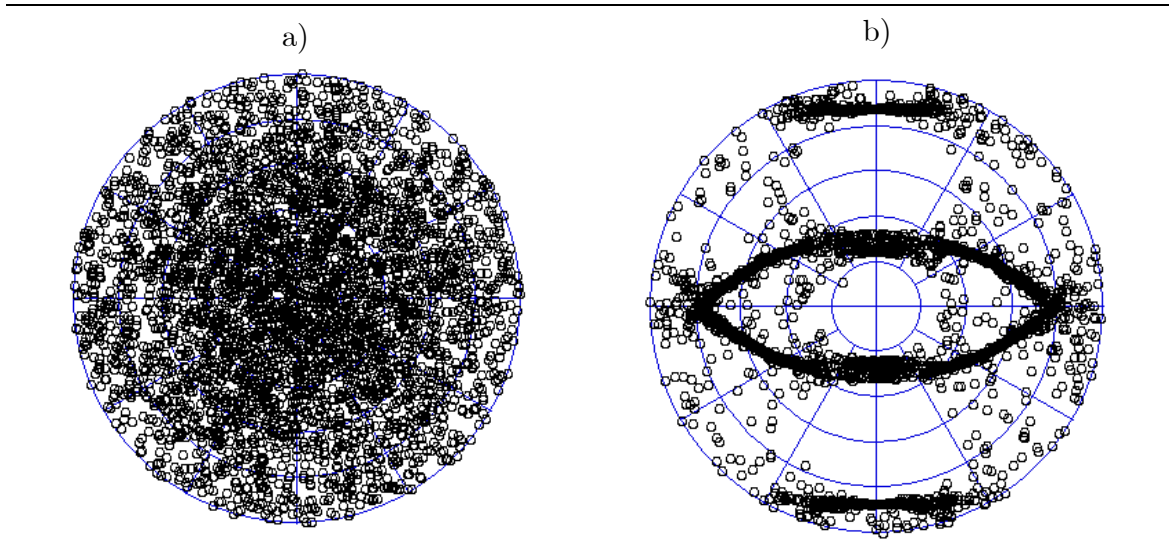

Figure C-4: {111} Pole figures. a) Random texture; b) Preferred orientation.

The alloy characteristics and its deformation path will determine its crystallographic texture. There are several types of preferred orientation in case of aluminum alloys (Table C-1, Figure C-5) , such as Cube, Goss, Copper, Brass, "S" and others (Kocks et al., 1998). Thus, a proper interpretation of pole figures it is a very useful instrument to evaluate the characteristics and deformation history of a material.

Cube	{001}<100>
Goss	{011}<100>
Brass	{011}<112>
Copper	{112}<111>
S	{123}<412>

Table C-1: Typical crystallographic textures of aluminum alloys.

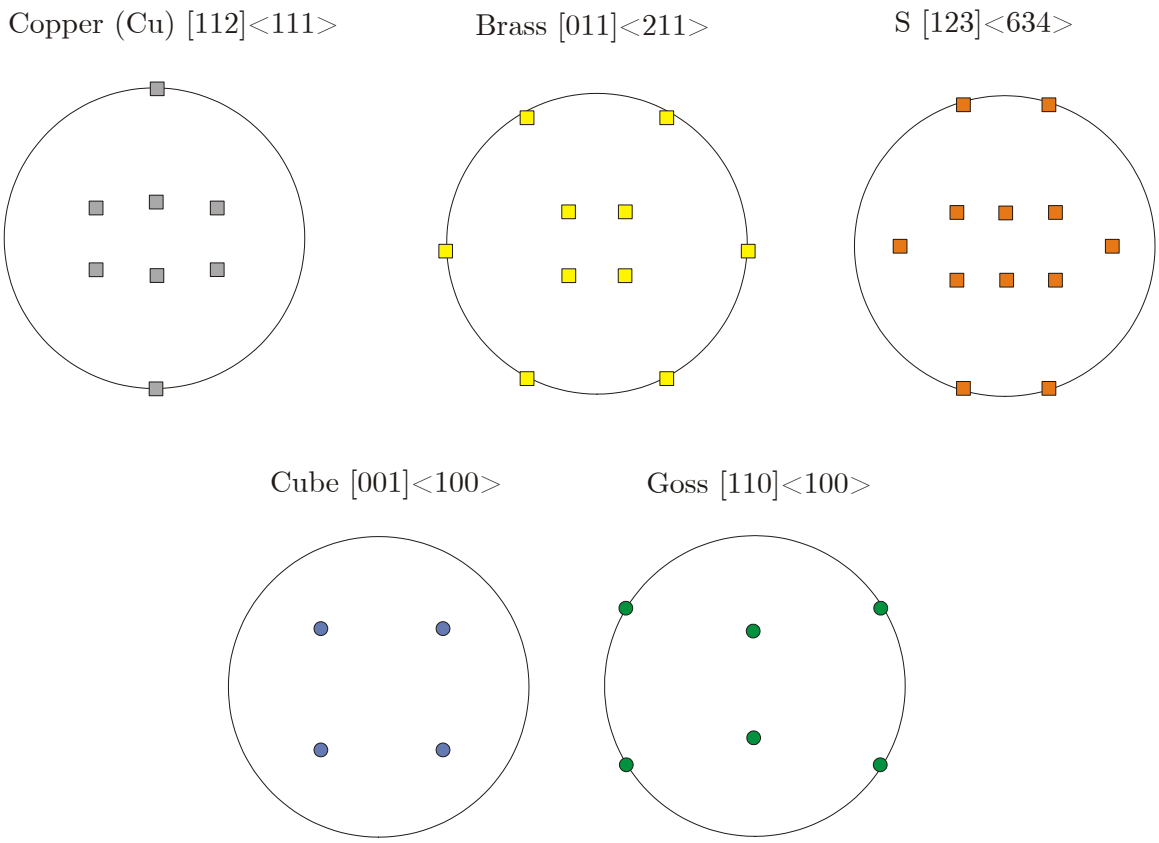

Figure C-5: Typical crystallographic textures of aluminum alloys (Simões, 2006).